# CVR JOURNAL
# OF
# SCIENCE & TECHNOLOGY

## Indexed by

- Google Scholar
- Directory of Research Journals Indexing (DRJI)
- Scientific Indexing Services (SIS)
- International Institute of Organised Research (I2OR)
- Scholar Impact -  Journal Index
- Citefactor



*Ranked in the 101-150 band by NIRF (MHRD) for the II Consecutive Time*
*Accredited by NAAC with 'A' GRADE*

# CVR COLLEGE OF ENGINEERING

# EDITORIAL

We are happy to bring out the Volume – 15 of the Biannual Journal- CVR Journal of Science and Technology, due in December 2018. This Volume is also brought out in time, with the co-operation of all the authors and editorial team. We are thankful to the Management Committee for supporting this activity, and permitting to publish the journal in colour print, using quality printing paper.

We are taking lot of care to see that quality is maintained in the papers published. Anti-Plagiarism Check is being done, in addition to review by senior professors. Teachers of English Department are also taking part in reviewing the papers. We are encouraging P.G. students also, to publish papers, with the help of their supervisors, based on, one year of Project work done by them. One will find some such articles from different departments in this issue. We hope the academic standards of P.G. programs and quality of project works done by the students improves in this way and helps the students in their career.

In this issue, an interesting article on Artificial Neural Networks (ANN) based on perception or Artificial Neuron is published. Also, one will find research articles pertaining to durability studies made on high strength concrete and also light weight, self – compacting concrete, Radiation effect on MHD stagnation – point Flow of a nanofluid, in a chemical reaction, and many other interesting research articles.

The Volume covers research articles in the branches of engineering and Mathematics. The breakup of papers among the various branches is:

**CIVIL – 4, CSE –2 , ECE – 6, EEE – 1, EIE– 2, MECH- 3,  H & S(Maths)-1.**

Some of the research articles accepted for publication in the forthcoming Volume.16 are also listed in the end.

We are very happy to share with our readers that CVR College of Engineering is **one among the TOP 3 institutions**, **in the State of Telangana,** as per the **NIRF MHRD rankings**. It is ranked in the **101-150 band** of rankings by the **NIRF,** consecutively for the II time. For a college which is about 17 years old, it is remarkable achievement. This made the management of the college to launch Mission 100, to be among the top 100 institutions in the country. Research activity plays an important role in this aspect. Hope the Journal and the contributors will help in improving the ranking of the institution. We are also happy to share with the readers that the college is **Accredited by NAAC with 'A' grade.** It is expected that the contributors will further enhance the reputation of the college through this Journal.

I am thankful to all the members of the Editorial Board for their help in reviewing and short listing the research papers for inclusion in the current Volume of the journal. I wish to thank **Dr.S.Venkateshwarlu, HOD, EEE and Associate Editor**, for the effort made in bringing out this Volume. Thanks are due to **HOD, H & S, Dr. G. Bhikshamaiah** and the staff of English Department for reviewing the papers to see that grammatical and typographical errors are corrected. I am also thankful to **Smt. A. Sreedevi**, **DTP Operator** in the Office of Dean Research for the effort put, in the preparation of the papers in Camera Ready form.

For further clarity on waveforms, graphs, circuit diagrams and figures, readers are requested to browse the soft copy of the journal, available on the college website **www.cvr.ac.in** wherein a link is provided.

**Prof.  K. Lal Kishore**
**Editor**

# CONTENTS          Page No

# Strength and Durability Studies on Light Weight Self-Compacting Concrete with LECA as Partial Replacement of Coarse Aggregate

N. Ramanjaneyulu[1], Kakustham Srigiri[2], and M.V. Seshagiri Rao[3]

[1]Research Scholar, JNTUA College of Engineering/Anantapuram and Asst. Professor, CVR College of Engineering/Civil Engineering Department, Hyderabad, India
Email: rams.613@gmail.com

[2]M. Tech Student, CVR College of Engineering/Civil Engineering Department, Hyderabad, India
Email: srigiri135@gmail.com

[3]Professor, CVR College of Engineering/Civil Engineering Department, Hyderabad, India
Email: rao_vs_meduri@yahoo.com

*Abstract:* **This paper presents the results of strength and durability studies on light weight aggregate Self Compacting Concrete (SCC) made with expanded clay aggregate (LECA) partially replacing conventional coarse aggregate. The grades of the concrete investigated are M20, M30, M40 and M60 which consist of low, standard and high strength concretes. The durability studies include sorptivity, acid and sulphate resistance. The densities of LWSCC varied from 1870 kg/m³ to 1950 kg/m³. The sorptivity was found to be more. Acid and sulphate resistance were found to be less in LWSCC. The paper describes the details of investigations and results on LECA based LWSCC.**

*Key words*: Light Weight Expanded Clay (LECA), Light weight Self-Compacting Concrete, VMA, and Superplasticizer.

## I. INTRODUCTION

Self-compacting concrete (SCC) is a special type concrete requiring no compaction and flow through congested reinforcement. The density of SCC is almost equivalent to that of normal concrete (NC). Light Weigh Concrete (LWC) has been developed to reduce the density of structures, which ranges from 300 to 2000 kg/m³ [6]. Light Weight Aggregate (LWA) concretes are one type of LWC which are produced using natural or artificial LWA. The advantages of LWC includes reduction of dead loads of structures which reduces foundation costs. At present, number of investigations are in progress to develop Light Weight Self Compacting Concrete (LWSCC) to derive the benefits LWC [8]. Investigations carried out by different researchers using some Light Weight Aggregates in SCC have proved that Light Weight Aggregate Self Compacting Concrete (LWASCC) can be manufactured and used by judiciously choosing the LWA type [9]. Keeping the above in mind, the present investigations are taken up to study the strength and durability characteristics of LWASCC of M20, M30, M40 and M60 grades partly replacing conventional coarse aggregate with light weight expanded clay aggregate LECA.

## II. LITERATURE REVIEW

Nan Su et.al (2001) proposed a mix design procedure for SCC. In this method, the amount of coarse aggregate content is determined, and the amount of finer material chemical admixtures and water are determined to satisfy the EFNARC guidelines for SCC. The SCC mixes produced, based on the above method are found to be satisfying the mechanical and durability properties of concrete [1].

M.V. Seshagiri Rao et al. (2013) developed a rational mix design method for SCC for designing SCC mixes of different grades. The rational mix design proposed, modified certain parameters of NaSu method and gives a direct mix design procedure for SCC to fix the CA, FA, fines admixture content and water/binder ratio. They developed W/b ratio various strength curves [5].

J. Alaxandare Bose et.al. (2012) investigated on Self compacting Light Weight Concrete (SWLC) with light weight aggregate available in Iberian Peninsula. The influences of different compositions of ingredients were studied and some limits were suggested. They concluded that SCLC of adequate stability and self compactibility can be produced for strength ranging from 3.7.4 to 60.8 MPa [3].

M.V. Seshagiri Rao et.al. (2013) studied the durability properties like Acid Strength Loss Factor (ASLF), Acid Attacking Factor (AAF), Acid Weight Loss Factor (AWLF) and Acid Durability Factor (ADLF) on different grades of SCC ranging from M20 to M70 and evaluated different factors and compared with normal concrete (NC). Sorptivity tests were also reported on SCC and NC [10].

P. Prakash et.al. (2015) reported the mechanical properties of M20 grade of LWC mud with CINDER and LECM as light weight aggregates mixed in different proportions. They have reported concrete

with densities of range 1750 to 1850 kg/m$^3$ can be produced without compromising the strength [8].

Abdurrahman Nava Lotfy et.al (2015) investigated the durability properties of LWCC using three types of LWA i.e. furnace slag (FS), Expanded Clay (EC) AND Expanded Shale (ES). They observed that FSLWSCC has shown high resistance to salt scaling due to lower porosity and absorption properties of the aggregates compared to EWLSCC. All LWSCC specimens behaved reasonably well after 2 weeks of exposure to sulfuric acid. She observed that the fresh, hardened and durability of LWSCC mixes are affected by the CA to FA ratio and total aggregate proportion of LWA [7].

Gopi Rajamanickanna et.al. (2016) studied the fresh and hardened properties of SCC using LECA as fine aggregate replacement. They observed that a maximum of 25% LECA as fine aggregate can be replaced [15].

### III. EXPERIMENTAL PROGRAMME

The experimental programme consisted of casting and testing of NWSCC and LWSCC specimens. The rational mix design was adopted. Several trails were made for producing NWSCC and LWSCC satisfying the EFNARC 2005 specifications. A total four grades of concrete were investigated consisting of M20, M30, M40 and M60 representing ordinary, standard and high- strength concrete, respectively. A total of 42 standard cubes of NWSCC and 96 cubes for LWSCC were cast to study the mechanical properties. 48 standard cubes for each NWSCC and LWSCC of size of 100mm*100mm*100mm were cast for acid attack.

Three specimens each for NWSCC and LWSCC were cast and tested for sorptivity. The properties of the constituent materials used in the present study investigations are given in table I.

TABLE I.
MATERIAL PROPERTIES OF INGREDIENTS USED FOR NWSCC AND LWSCC

| Property/unit | Value |
|---|---|
| Cement – OPC 53 grade Specific gravity | 3.10 |
| Normal consistency | 29.5% |
| Coarse aggregate (Gravel) Specific gravity | 2.65 |
| Bulk density: kg/m$^3$ | 1442 |
| Fineness modulus | 7.16 |
| Coarse aggregate (LECA) Specific gravity | 2.65 |
| Bulk density: kg/m$^3$ | 1442 |
| Fineness modulus | 7.16 |
| Super-plasticizer | Conplast SP 430 |
| Fine aggregate Specific gravity | 2.55 |
| Bulk density: kg/m$^3$ | 1713 |
| Fineness modulus | 2.19 |

### *Mix proportioning and Mechanical properties*

The details of mix proportion are shown in table II. Replacements of coarse aggregate fraction are shown in table III. The fresh properties of NWSCC and LWSCC are shown in table IV. The density and mechanical properties of NWSCC and LWSCC are shown in table V.

TABLE II.
MIX PROPORTIONS OF NWSCC

| Type of mix | Mix proportions | QUANTITIES kg/m$^3$ | | | | | |
|---|---|---|---|---|---|---|---|
| | | Cement | Flyash | Fine aggregate | Coarse aggregate | Water | SP |
| NWSCC-M20 | 1:1.2:3.4:2.6:0.9:0.021 | 258 | 310 | 900 | 685 | 240 | 5.67 |
| NWSCC-M30 | 1:0.8:2.5:1.9:0.5:0.022 | 360 | 300 | 900 | 700 | 180 | 8.05 |
| NWSCC-M40 | 1:0.7:1.8:1.4:0.51:0.026 | 468 | 350 | 885 | 700 | 240 | 12.2 |
| NWSCC-M60 | 1:0.4:1.2:1.1:0.39:0.013 | 660 | 310 | 850 | 730 | 260 | 9.02 |

TABLE III.
REPLACEMENT OF COARSE AGGREGATE IN kg/m$^3$

| Type of mix | Coarse Aggregate Replacement kg/m$^3$ | | | | | | | |
|---|---|---|---|---|---|---|---|---|
| | Gravel 90% | LECA 10% | Gravel 80% | LECA 20% | Gravel 70% | LECA 30% | Gravel 60% | LECA 40% |
| LWSCC-M20 | 614.5 | 22.7 | 546.2 | 45.5 | 477.9 | 68.2 | 409.6 | 91.0 |
| LWSCC-M30 | 629.8 | 23.3 | 559.8 | 46.6 | 489.8 | 69.9 | 419.8 | 93.3 |
| LWSCC-M40 | 629.8 | 23.3 | 559.8 | 46.6 | 489.8 | 69.9 | 419.8 | 93.3 |
| LWSCC-M60 | 656.1 | 24.3 | 583.2 | 48.6 | 510.3 | 72.9 | 437.4 | 97.2 |

TABLE IV.
FRESH AND HARDENED PROPERTIES OF NWSCC AND LWSCC

| Type of mixes | Grade Of Concrete | Coarse Aggregate % | | Fresh properties | | | Hardened properties | |
|---|---|---|---|---|---|---|---|---|
| | | Gravel % | LECA % | $T_{50}$ cm (2-5) sec | V-Funnel (6-12) sec | L-box ($H_2/H_1$) mm | 7 days (MPa) | 28 days (MPa) |
| NWSCC | M20 | 100 | - | 4 | 7 | 0.85 | 21.85 | 27.0 |
| | M30 | 100 | - | 5 | 8 | 1 | 24.7 | 38.8 |
| | M40 | 100 | - | 4 | 11 | 9.2 | 33.5 | 51.5 |
| | M60 | 100 | - | 3.9 | 10 | 8.9 | 46.9 | 68.8 |
| LWSCC | M20 | 90 | 10 | 4.2 | 9 | 1 | 13.3 | 21.3 |
| | M20 | 80 | 20 | 4.2 | 11 | 0.92 | 13.4 | 20.5 |
| | M20 | 70 | 30 | 4.4 | 8 | 0.92 | 12.6 | 20.4 |
| | M20 | 60 | 40 | 4.1 | 12 | 0.89 | 11.46 | 20.2 |
| | M30 | 90 | 10 | 4.2 | 11 | 0.95 | 24.6 | 37.3 |
| | M30 | 80 | 20 | 4.1 | 11.5 | 0.93 | 22.9 | 35.5 |
| | M30 | 70 | 30 | 4 | 12 | 0.92 | 18.9 | 33.0 |
| | M30 | 60 | 40 | 4.3 | 9 | 0.91 | 13.0 | 24.3 |
| | M40 | 90 | 10 | 3.4 | 9 | 1 | 31.9 | 49.1 |
| | M40 | 80 | 20 | 3.9 | 10.2 | 0.89 | 25.2 | 40.1 |
| | M40 | 70 | 30 | 4.3 | 9 | 0.89 | 25.1 | 37.8 |
| | M40 | 60 | 40 | 4.7 | 11.2 | 1 | 23.4 | 34.8 |
| | M60 | 90 | 10 | 4.3 | 10.3 | 1 | 46.2 | 60.6 |
| | M60 | 80 | 20 | 4.7 | 10.9 | 0.9 | 43.7 | 59.8 |
| | M60 | 70 | 30 | 4.6 | 12 | 0.96 | 40.6 | 57.1 |
| | M60 | 60 | 40 | 4 | 11 | 1 | 35.3 | 52.3 |

## Durability Tests On SCC

Durability is a very important engineering property of concrete. In the present investigations, some of the durability properties of the normal concrete SCC and light weight concrete SCC like chemical attack (acid attack and sulphate attack), capillary water absorption by sorptivity test were studied.

## Tests for Acid Attack on SCC

After the curing period of 28 days the cubes were tested for the weights and compressive strength. The cured NWSCC and LWSCC specimens of different grades viz. M20, M30, M40 and M60 were kept exposed to 5% solutions of both sulfuric acid, hydrochloric acids and sodium sulphate. Cubes were continuously immersed in solution for 28 days and 56 days.

The change in appearance, weight, compressive strength and dimensions of solid diagonals were measured. For determining the resistance of concrete specimens to environments such as acid attack, durability factors such as acid strength loss factor (ASLF), acid attacking factor (AAF), acid weight loss factor (AWLF) and acid durability loss factor. (ADLF) were calculated.

1) Acid strength loss factor (ASLF) is an indication of relative performance of concrete in strength, before and after immersion in a particular concentration of acid. This also depends on the period of immersion of the specimen.

$$ASLF = S_r * N/M$$

Where,
$S_r$ is the relative strength at N days (%), N is the number of days at which the durability factor is required.

M is the number of days at which the expose is determined.
A lower value of ASLF indicates greater stability towards acid attack.

2) Acid attacking factor (AAF) is an indication of diagonal loss of the specimen after immersion in acid for certain period of time. The extent of loss is determined as

AAF = (Loss of acid diagonal after immersion/ diagonal before immersion) * 100.

Higher value of it indicates that the dimensional stability is lower.

3) Acid weight loss factor (AWLF) is calculated as the % loss of weight of cubes by immersing the cubes in various types and concentration of acids for different immersion periods.

AWLF = (Loss of weight after immersion of cube / original weight of cube) * 100.

In order to determine the durability factor, these factors are combined, and it is termed as ADLF.

$$ADLF = ASLF*AAF*AWLF.$$

Table 9 shows AWLF for both the types of mixes. Table 10 shows AAF for both types of mixes. Table 11 shows the ASLF for both types of mixes and table 13 shows the ADLF for both types of mixes.

## Sorptivity

Sorptivity is the rate of absorption and transmission of water by capillary action. The sorptivity test was conducted

on 100 mm x 100 mm x100 mm cubes. The sorptivity measures the rate of penetration of water into the pores in the concrete by capillary suction.

Sorptivity coefficients are determined for normal concrete SCC and light weight concrete SCC.

Sorptivity test is done on the basis of Hall's method (Hall, 1989). After curing of specimens for 28 days in curing tank, the cubes are removed and dried. Paraffin wax is coated on four sides of the cube leaving the top and the bottom. The initial weights of the cubes are taken. Then, the cubes are immersed in water up to 6.6mm from the bottom.

The cube absorbs the water and transmits the water to upwards by capillary action. The weights of the specimens were measured at times of 1min, 5min, 10min, 15 min, 30 min, 1 h, 2 h, 4 h, 6 h, 24 h, 48 h and 72 h after the end of curing. The sorptivity studies were conducted continuously for 3 days.

Sorptivity test for normal concrete was carried out keeping one face of cube in water. For LECA concrete, the tests were done keeping both top and bottom faces of cubes in water separately. This is done as it is observed that LECA is floating due to low density is flowing and more LECA was observed on top surface.

The sorptivity coefficient (s) was obtained from the expression.

$$S = I / T1/2, \quad I = \nabla W/Ad$$

Where,

W is the amount of water absorbed (kg),

A is the cross section of specimen that was in contact with water ($m^2$)

d is the density of the medium in which the specimen was dipped (d = 1, as the medium used was water)

T = time (min).

The unit of S is kg/ ($m^2$ $min^{1/2}$).

The variation of i against $t^{1/2}$ was plotted.

Table VI shows the Sorptivity of NWSCC for different grades of concrete. Table VII shows the Sorptivity of LWSCC for different grades of concrete. Table 8 shows the LWSCC for Different Grades of Concrete with LECA portion immersed in water when compared to other parts of concrete.

TABLE V.
DENSITIES AND COMPRESSIVE STRENGTH OF NWSCC AND LWSCC

| Type of mixes | Grade Of Concrete | Coarse Aggregate % | | Average Densities kg/m³ | Compressive strength MPa | |
|---|---|---|---|---|---|---|
| | | Gravel % | LECA % | | 7-Days | 28-Days |
| NWSCC | M20 | 100 | - | 2430 | 21.8 | 27.0 |
| | M30 | 100 | - | 2450 | 24.7 | 38.8 |
| | M40 | 100 | - | 2440 | 33.5 | 51.5 |
| | M60 | 100 | - | 2460 | 46.9 | 68.8 |
| LWSCC | M20 | 90 | 10 | 2303 | 13.3 | 21.3 |
| | M20 | 80 | 20 | 2200 | 13.4 | 20.5 |
| | M20 | 70 | 30 | 2076 | 12.6 | 20.4 |
| | M20 | 60 | 40 | 1975 | 11.4 | 20.2 |
| | M30 | 90 | 10 | 2313 | 24.6 | 37.3 |
| | M30 | 80 | 20 | 2218 | 22.9 | 35.3 |
| | M30 | 70 | 30 | 2086 | 18.9 | 33 |
| | M30 | 60 | 40 | 1991 | 13 | 24.3 |
| | M40 | 90 | 10 | 2286 | 31.9 | 49.1 |
| | M40 | 80 | 20 | 2193 | 25.2 | 40.1 |
| | M40 | 70 | 30 | 2083 | 25.1 | 37.8 |
| | M40 | 60 | 40 | 1940 | 23.4 | 34.8 |
| | M60 | 90 | 10 | 2301 | 46.2 | 60.6 |
| | M60 | 80 | 20 | 2198 | 43.7 | 59.8 |
| | M60 | 70 | 30 | 2113 | 40.6 | 57.1 |
| | M60 | 60 | 40 | 1970 | 35.3 | 52.3 |

TABLE VI.
SORPTIVITY OF NWSCC FOR DIFFERENT GRADES OF
CONCRETE

| Sample no. | Time in Mins | Cumulative Water Absorption (Δw)Kg | | | | S=I/M0.5 Sorptivity value in $10^{-3}$ mm/min$^{0.5}$ | | | |
|---|---|---|---|---|---|---|---|---|---|
| | | M20 | M30 | M40 | M60 | M20 | M30 | M40 | M60 |
| 1 | 1 | 0 | 0 | 0 | 0 | 0 | 0 | 0 | 0 |
| 2 | 5 | 0.2 | 0.1 | 0.1 | 0 | 89.6 | 44.8 | 44.8 | 0 |
| 3 | 10 | 0.3 | 0.2 | 0.1 | 0.1 | 94.3 | 63.2 | 31.4 | 31.4 |
| 4 | 15 | 0.5 | 0.3 | 0.3 | 0.1 | 129.1 | 77.5 | 77.5 | 25.8 |
| 5 | 30 | 0.5 | 0.3 | 0.3 | 0.1 | 91.4 | 54.8 | 54.8 | 18.2 |
| 6 | 60 | 0.5 | 0.3 | 0.3 | 0.1 | 64.9 | 38.7 | 38.7 | 12.9 |
| 7 | 120 | 0.5 | 0.3 | 0.4 | 0.1 | 45.6 | 27.3 | 36.5 | 9.1 |
| 8 | 180 | 0.6 | 0.3 | 0.4 | 0.2 | 44.7 | 22.3 | 29.8 | 14.9 |
| 9 | 240 | 0.6 | 0.5 | 0.5 | 0.3 | 38.7 | 32.7 | 32.7 | 19.36 |
| 10 | 300 | 0.6 | 0.6 | 0.5 | 0.4 | 34.6 | 34.6 | 28.8 | 23.0 |
| 11 | 360 | 0.6 | 0.7 | 0.5 | 0.5 | 31.6 | 36.9 | 26.3 | 26.3 |
| 12 | 1440 | 0.7 | 0.7 | 0.5 | 0.5 | 18.4 | 18.4 | 13.1 | 13.1 |
| 13 | 2880 | 0.8 | 0.7 | 0.6 | 0.5 | 14.9 | 13.0 | 11.1 | 09.3 |
| 14 | 4320 | 0.8 | 0.7 | 0.6 | 0.5 | 12.1 | 10.6 | 09.1 | 07.6 |

TABLE VII.
SORPTIVITY OF LWSCC FOR DIFFERENT GRADES OF CONCRETE WHEN TOP PORTION (LECA) IMMERSED

| Sample no. | Time in Mins | Cumulative Water Absorption (Δw)Kg | | | | S=I/M0.5 Sorptivity value in $10^{-3}$ mm/min$^{0.5}$ | | | |
|---|---|---|---|---|---|---|---|---|---|
| | | M20 | M30 | M40 | M60 | M20 | M30 | M40 | M60 |
| 1 | 1 | 0.3 | 0.3 | 0.4 | 0.4 | 300 | 300 | 400 | 400 |
| 2 | 5 | 0.4 | 0.4 | 0.4 | 0.4 | 179.3 | 179.3 | 179.3 | 179.3 |
| 3 | 10 | 0.4 | 0.4 | 0.4 | 0.4 | 126.5 | 126.5 | 126.5 | 126.5 |
| 4 | 15 | 0.5 | 0.6 | 0.5 | 0.6 | 129.1 | 155 | 129.1 | 155 |
| 5 | 30 | 0.7 | 0.6 | 0.7 | 0.7 | 127.9 | 109.6 | 127.9 | 127.9 |
| 6 | 60 | 0.7 | 0.7 | 0.7 | 0.7 | 90.4 | 90.4 | 90.4 | 90.4 |
| 7 | 120 | 0.9 | 0.8 | 0.7 | 0.9 | 82.1 | 73.0 | 63.9 | 82.1 |
| 8 | 180 | 0.9 | 0.9 | 0.9 | 0.9 | 67.1 | 67.1 | 67.1 | 67.1 |
| 9 | 240 | 0.9 | 0.9 | 0.9 | 0.9 | 58.1 | 58.1 | 58.1 | 58.1 |
| 10 | 300 | 1.1 | 1.1 | 1.1 | 1.1 | 63.1 | 63.1 | 63.1 | 63.1 |
| 11 | 360 | 1.1 | 1.1 | 1.1 | 1.1 | 57.9 | 57.9 | 57.9 | 57.9 |
| 12 | 1440 | 1.1 | 1.2 | 1.1 | 1.2 | 28.9 | 31.6 | 28.9 | 31.6 |
| 13 | 2880 | 1.2 | 1.3 | 1.3 | 1.3 | 22.3 | 24.2 | 24.2 | 24.2 |
| 14 | 4320 | 1.3 | 1.3 | 1.3 | 1.4 | 19.7 | 19.7 | 19.7 | 21.3 |

TABLE VIII.
SORPTIVITY OF LWSCC FOR DIFFERENT GRADES OF CONCRETE WHEN BOTTOM PORTION IMMERSED

| Sample no. | Time in Mins | Cumulative Water Absorption (Δw) Kg | | | | S=I/M0.5 Sorptivity value in $10^{-3}$ mm/min$^{0.5}$ | | | |
|---|---|---|---|---|---|---|---|---|---|
| | | M20 | M30 | M40 | M60 | M20 | M30 | M40 | M60 |
| 1 | 1 | 0.2 | 0.2 | 0.2 | 0.2 | 200 | 200 | 200 | 200 |
| 2 | 5 | 0.3 | 0.3 | 0.3 | 0.3 | 134.5 | 134.5 | 134.5 | 134.5 |
| 3 | 10 | 0.4 | 0.4 | 0.3 | 0.4 | 126.5 | 126.5 | 94.9 | 126.5 |
| 4 | 15 | 0.4 | 0.4 | 0.3 | 0.4 | 103.3 | 103.3 | 77.5 | 103.3 |
| 5 | 30 | 0.4 | 0.4 | 0.4 | 0.4 | 73.1 | 73.1 | 73.1 | 73.1 |
| 6 | 60 | 0.4 | 0.4 | 0.4 | 0.4 | 51.6 | 51.6 | 51.6 | 51.6 |
| 7 | 120 | 0.5 | 0.4 | 0.4 | 0.5 | 45.6 | 36.5 | 36.5 | 45.6 |
| 8 | 180 | 0.6 | 0.5 | 0.4 | 0.5 | 44.7 | 37.2 | 29.8 | 37.2 |
| 9 | 240 | 0.7 | 0.5 | 0.5 | 0.6 | 45.1 | 32.2 | 32.2 | 38.7 |
| 10 | 300 | 0.7 | 0.6 | 0.5 | 0.6 | 40.4 | 36.6 | 28.8 | 34.6 |
| 11 | 360 | 0.7 | 0.6 | 0.6 | 0.6 | 36.9 | 31.6 | 31.6 | 31.6 |
| 12 | 1440 | 0.8 | 0.8 | 0.7 | 0.9 | 21.0 | 21.0 | 18.4 | 23.7 |
| 13 | 2880 | 1.0 | 0.9 | 0.8 | 0.9 | 18.6 | 16.7 | 14.9 | 16.7 |
| 14 | 4320 | 1.0 | 1.0 | 0.9 | 1.0 | 15.2 | 15.2 | 13.6 | 15.2 |

TABLE IX.
SORPTIVITY OF LWSCC FOR DIFFERENT GRADES OF CONCRETE

| Solution | ACID WEIGHT LOSS FACTOR (AWLF) -56 DAYS | | | | | | | |
|---|---|---|---|---|---|---|---|---|
| | NWSCC | | | | LWSCC | | | |
| | M20 | M30 | M40 | M60 | M20 | L30 | L40 | L60 |
| NA$_2$SO$_4$ - 5% | 1.69 | 1.71 | 1.27 | 1.28 | 1.53 | 1.61 | 1.54 | 1.52 |
| HCL - 5% | 10.72 | 9.91 | 9.74 | 9.4 | 17.25 | 14.07 | 10.71 | 9.84 |
| H$_2$S0$_4$ - 5% | 22.2 | 32.7 | 23.1 | 23.6 | 27.46 | 37.06 | 4105 | 43.29 |

TABLE X.
AAF OF NWSCC AND LWSCC FOR DIFFERENT GRADES OF CONCRETE

| Solution | ACID ATTACKING FACTOR (AAF) -56 DAYS | | | | | | | |
|---|---|---|---|---|---|---|---|---|
| | NWSCC | | | | LWSCC | | | |
| | M20 | M30 | M40 | M60 | M20 | L30 | L40 | L60 |
| NA$_2$SO$_4$ - 5% | 1.78 | 1.22 | 1.72 | 1.21 | 1.78 | 2.87 | 1.35 | 1.42 |
| HCL - 5% | 7.87 | 4.73 | 7.69 | 7.19 | 8.08 | 3.63 | 18.03 | 7.19 |
| H$_2$S0$_4$ − 5% | 18.56 | 19.09 | 18.03 | 15.78 | 20.54 | 17.67 | 12.49 | 13.47 |

TABLE XI.
ASLF OF NWSCC AND LWSCC FOR DIFFERENT GRADES OF CONCRETE

| Solution | ACID STRENGTH LOSS FACTORS (ASLF)-56 DAYS | | | | | | | |
|---|---|---|---|---|---|---|---|---|
| | NWSCC | | | | LWSCC | | | |
| | M20 | M30 | M40 | M60 | M20 | L30 | L40 | L60 |
| NA$_2$SO$_4$ - 5% | 8.8 | 6.95 | 4.3 | 5.3 | 2.4 | 6.17 | 4.8 | 1.3 |
| HCL - 5% | 16.29 | 19.84 | 18.1 | 25.2 | 23.29 | 19.85 | 21.5 | 32.5 |
| H$_2$S0$_4$ - 5% | 60.37 | 78.71 | 83.1 | 84.01 | 74.25 | 81.06 | 83.5 | 85.5 |

TABLE XII.
ADLF OF NWSCC AND LWSCC FOR DIFFERENT GRADES OF CONCRETE

| Solution | ACID DURABILITY LOSS FACTORS (ADLF)-56 DAYS | | | | | | | |
|---|---|---|---|---|---|---|---|---|
| | NWSCC | | | | LWSCC | | | |
| | M20 | M30 | M40 | M60 | M20 | L30 | L40 | L60 |
| NA$_2$SO$_4$ - 5% | 26.4 | 14.49 | 40.68 | 8.21 | 6.53 | 28.5 | 9.9 | 2.80 |
| HCL - 5% | 1376.3 | 929.9 | 1346.8 | 1709.24 | 3311.6 | 1008.7 | 999.35 | 1458.2 |
| H$_2$S0$_4$ - 5% | 24874.3 | 49134.1 | 34504.7 | 31285.9 | 41879.1 | 53855.6 | 37453 | 47348.3 |
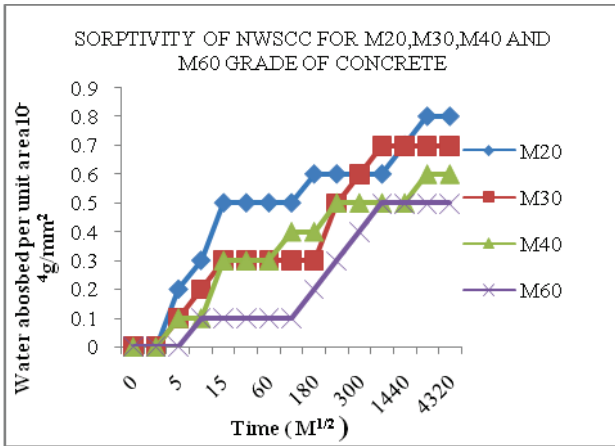
Figure 1. Sorptivity of NWSCC
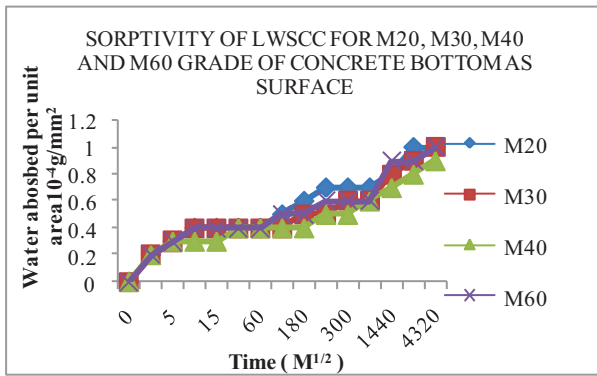


Figure 2. Sorptivity of LWSCC
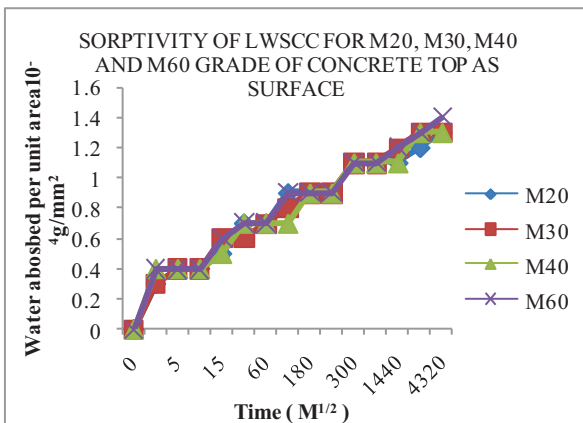


Figure 3. Sorptivity of LWSCC SCC with LECA portion is immersed in water when compared to other parts of concrete.



Figure 4. AWLF- 56 days



Figure 5. AAF- 56 days
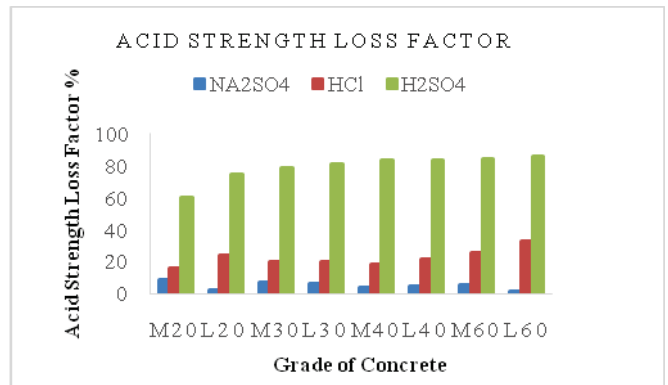


Figure 6. ASLF- 56 days
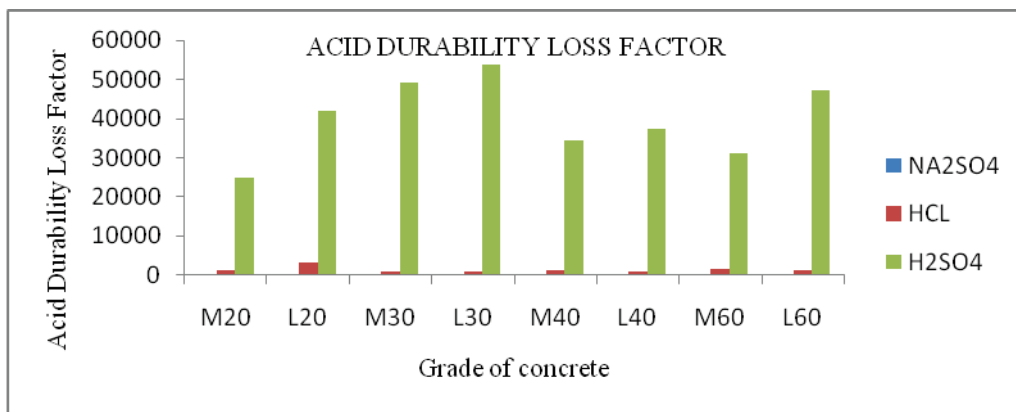
Figure 7. ADLF- 56 days

## IV. RESULTS

For M20, M30, M40 and M60 grade of concretes the fresh properties were satisfied. For M20, M30, M40 and M60 Grade of concrete the compressive strength for 7 days were 21.8, 24.7, 33.5, 46.9 and for 28 days were 27, 38.8, 51.5 and 68.8 N/mm$^2$. The densities of concrete are decreasing with the increase in the percentage replacement of coarse aggregate with LECA. The mechanical properties, it was observed that for M20 grade of concrete the replacement of coarse aggregate with 10%, 20%, 30% and 40% with LECA, the average compressive strength for 7 and 28 days in MPa were 13.3, 13.4, 12.6, 11.46 and 21.3, 20.5, 20.4, 20.2. It was observed that for M30 grade of concrete the replacement of coarse aggregate with 10%, 20%, 30% and 40% with LECA, the average compressive strength for 7 and 28 days in MPa were 24.6, 22.9, 18.9, 13 and 37.3, 35.5, 33, 24.3. It was observed that for M40 grade of concrete the replacement of coarse aggregate with 10%, 20%, 30% and 40% with LECA, the average compressive strength for 7 and 28 days in MPa were 31.9, 25.2, 25.1, 23.4 and 49.1, 40.1, 37.8, 34.8. For M60 grade of concrete the replacement of coarse aggregate with 10%, 20%, 30% and 40% with LECA the average compressive strength for 7 and 28 days in MPa were 46.2, 43.7, 40.6, 35.3 and 60.6, 59.8, 57.1, 52.3. It is observed that as the grade of the concrete increases, the rate of water absorption decreases. Also, the values of water absorption in SCC are much lower when compared to the LWSCC. The dimension loss is less in NWSCC when compared to LWSCC, both in acids and sulphate. For $Na_2SO_4$ 1.48 and 2.47, HCL 17.87 and 18.79 and, in $H_2SO_4$ 17.85 and 18.79. These are the average percentage loss for all grades of concrete for NWSCC and LWSCC. The weight loss is less in NWSCC when compare to LWSCC, both in acids and sulphate. For $Na_2SO_4$ 9.94 and 13.02, HCL 9.94 and 13.02 and $H_2SO_4$ 19.70 and 37.21. These are the percentage loss for all grades of concrete for NWSCC and LWSCC. The strength loss was less in NWSCC when compared to LWSCC, both in acids and sulphate. For $Na_2SO_4$ 6.33 and 7.51, HCL 19.88 and 24.37 and $H_2SO_4$ 76.56 and 81.09. These are the average percentage loss for all grades of concrete for NWSCC and LWSCC.

## V. CONCLUSIONS

1. Density of concrete is found to decrease with the increase in the percentage replacement of normal aggregate with LECA.

2. The density of light weight aggregate varied from 1870 Kg/m3 to 1950 Kg/m$^3$, which is less than the weight of conventional concrete having a density of 2450 Kg/m$^3$ as measured in lab.

3. Due to light weight, LECA was found to be floating on the surface of the concrete causing problems for the flow of SCC.

4. The passing ability of SCC with LECA was found to decrease with increase in the percentage of LECA due to its water absorption. However, this can be compensated by higher dosage of super plasticizer.

5. Compressive strength of light weight SCC with LECA was found to increase when LECA is immersed in water for 24 hours before making concrete.

6. The sorptivity of light weight SCC was found to be more when SCC with LECA portion is immersed in water when compared to other part of concrete.

7. Higher grade SCC has lower water absorption values than lower grades with conventional aggregate. However, in Light weight SCC they found to be same in all grades.

8. With the increase in duration of exposure to the acidic environment, the AAF was found to be increasing in both LWSCC and NWSCC, in both acids and sulphates. However, the dimension Loss is less in LWSCC when compared to NWSCC.

9. With the increase in duration of exposure to the acidic environment, the AWLF and ASLF are found to be increasing in both LWSCC and NWSCC, in both acids and sulphate. However, the loss of weight and loss of strength is more in LWSCC when compared to NWSCC.

10. When compare to the NWSCC the LWSCC was found to be less durable in both Acids and Sulphate.

## REFERENCES

[1] Nan su, Kung-Chung Hsu, His-Wen Chai (2001) "A Simple mix design method for Self Compacting concrete" cement and concrete research 31(2001) 1799-1807.

[2] Y.J. Kim, S.J. Jeon, M.S. Choi, Y.J. Kim, Y.W. Choi (2010) "The Quality Properties of Self-Consolidating Concrete Using Lightweight Aggregate"2010, Korea Concrete Institute, ISBN 978-89-5708-182-2.

[3] J. Alexandre Bogas, Augusto Gomes, M.F.C. Pereira (2012) "Self-Compacting Lightweight Concrete Produced with Expanded Clay Aggregate" Construction and Building Materials 35(2012) 1013-1022.

[4] Michala Hubertova, Rudolf Hela (2013) "Durability of Lightweight Expanded Clay Aggregate" Concrete and Concrete Structure 65(2013)2-6.

[5] S. Venkateswara Rao, Prof. M. V. Seshagiri Rao, Prof. D. Ramaseshu, P. Rathish Kumar (2013) "A Rational Mix Design Procedure for Self-Compacting Concrete" CWB-5/2013.

[6] Sachin Paul, Ganesh Babu (2014) "Mechanical Properties of Light Weight Aggregate Geopolymer Concrete Using Light Weight Expanded Clay Aggregate" Transactions on Engineering and Sciences ISSN: 2347-1964, Vol.2, Issue 10 October, 2014.

[7] Abdurrahmaan Lotfya, Khandaker M.A. Hossainb and Mohamed Lachemib (2015) "Mix Design and Properties of Lightweight Self-Consolidating Concretes Developed with Furnace Slag, Expanded Clay and Expanded Shale Aggregates" Cement-Based Materials, 2015.

[8] Mr. Anil Kumar R, Dr. P Prakash (2015) "Studies on Structural Light Weight Concrete by Blending Light Weight Aggregates" ISSN: 2350-0557, Volume-2, Issue-4, July-2015.

[9] T. Sonia1, R. Subashini1 (2015) "Experimental Investigation on Mechanical Properties of Light Weight Concrete Using Leca" ISSN (Online): 2319-7064 Index Copernicus Value (2015): 78.96.

[10] S. Venkateswara Rao, M. V. Seshagiri Rao, D. Ramaseshu, P. Rathish Kumar (2015) "Durability Performance of Self-Compacting Concrete" Magazine of Concrete Research, Volume 64, Issue 11.

[11] Anil Kumar R, Dr.P.Prakash (2015) "Mechanical Properties of Structural Light Weight Concrete by Blending Cinder & LECA" IARJSET Vol. 2, Issue 10, October 2015.

[12] Hanamanth Shebannavar, Maneeth P. D,Brijbhushan S (2015) "Comparative Study Of LECA As A Complete Replacement Of Coarse Aggregate By ACI Method With Equivalent Likeness Of Strength Of Is Method" IRJET Volume: 02 Issue: 08,Nov-2015.

[13] Prof. M. Mahdy (2016) "Structural Lightweight Concrete Using Cured Leca" IJEIT Volume 5, Issue 9, March 2016. Issn: 2277-3754.

[14] Abhijitsinh Parmar, Urvish Patel, Avadh Vaghashiya, AditiParmar, PayalParmar (2016) "Fresh Concrete Properties of Light Weight Concrete Using EPS and LECA As A Replacement Of Normal Aggregates" 2016 IJEDR, Volume 4, Issue 1, 2321-9939.

[15] Gopi Rajamanickam, Revathi Vaiyapuri (2016) "Self-compacting self-curing concrete with lightweight aggregates" JCE.1137.2014.

[16] M.shankar (2016) "Experimental Investigation on Self Compacting Concrete Using Light Weight Aggregates"Volume: 1, Issue: 1, June 2016, ISSN: 2455-9288.

# Elevated Temperature and Durability Studies on High Strength Concrete

P. Rukkun Vardhan[1] and T. Muralidhara Rao[2]

[1]M.Tech Student, CVR College of Engineering/Civil Engineering Department, Hyderabad, India.
Email: prv1484@gmail.com
[2]Professor, CVR College of Engineering/Civil Engineering Department, Hyderabad, India.
Email: tmuralidhararao@gmail.com

*Abstract:* **In this paper, an attempt was made to study the effect of elevated temperatures and durability studies on fifty one numbers of ten centimeter high strength concrete cubes prepared with ultrafine mineral admixture, Alccofine 1203. Trials were made with 0%, 5%, 10% and 15% replacement of cement with Alccofine. Optimum percentage of replacement of cement by Alccofine was found to be 10%. The maximum compressive strength achieved was 79.93MPa. Elevated temperature, Non-Destructive test and Durability studies were conducted. The percentage loss in weight was found to be decreased with the temperature increase from $100^0C$ to $900^0C$. Similar trend was observed for Compressive strength also with the temperature increase. But compressive strength was increased at $300^0C$. The weight and compressive strength was increased when immersed in Sulphate solution, Chloride solution, Alkali solution and Sea water.**

*Index Terms:* **Compressive strength, Weight, Elevated Temperatures, Sulphate Attack, Chloride Attack, Alkali Attack, Sorptivity.**

## I. Introduction

### A. High Strength concrete(HSC)

HSC is characterized by high compressive strength. HSC is more durable because the low water-to-cementitious materials ratio results in very low porosity. The main advantage of HSC is its high compressive strength. Other advantages include improved microstructure and homogeneity, high flexibility with the addition of fibers. Due to the high strength of the concrete, the thickness of concrete elements will be reduced, which results in materials saving and cost saving.

### B. Alccofine 1203

Alccofine1203 is a new generation slag of high glass content with high reactivity obtained through the process of controlled granulation having Ultra-fineness with optimized particle size distribution. Alccofine1203 is much finer than other hydraulic materials like cement, fly ash, silica etc. The use of Alccofine1203 leads to a reduction of the size of the crystalline compounds, particularly calcium hydroxide which results in a reduction of the thickness of the interfacial transition zone (ITZ). It also reduces the free lime (CH) to C-S-H. This, in turn, strengthens the interfacial transition zone width with C-S-H structures occupying the CH crystal spaces. Thus, allowing the concrete to sustain higher loads without cracking. The physical and chemical parameters are presented in Table I and Table II.

TABLE I.
PHYSICAL PARAMETERS OF ALCCOFINE1203

| Specific gravity | Bulk Density ($kg/m^3$) | Fineness ($Cm^2/gm$) | Specific Gravity | Particle size distribution ($\mu$) | | |
|---|---|---|---|---|---|---|
| 2.9 | 680 | 12000 | 2.86 | D10 | D50 | D90 |
| | | | | 1-2 | 4-5 | 8-9 |

TABLE II.
CHEMICAL PARAMETERS OF ALCCOFINE1203

| CaO | $Al_2O_3$ | $SiO_2$ | $Fe_2O_3$ | $SO_3$ | MgO | Glass content |
|---|---|---|---|---|---|---|
| 34.0% | 24.0% | 35.0% | 1.20% | 0.13% | 8.20% | >90% |

## II. Literature Review

High strength concrete was prepared using foundry slag as a partial substitute for fine aggregate in varying proportions. Alccofine was used in an optimum amount of 15% as a partial substitute for Portland pozzolana cement. Results showed increase in Ultrasonic pulse velocity and rebound number with increase in foundry slag content and age [1]. Durability tests were conducted on high performance concrete made with Alccofine and Fly ash. Alccofine enhanced the durability of concretes and reduced the chloride diffusion. Due to the more compactness and less permeability of concrete, effect of chloride attack was reduced [2]. Strength and durability performance of concrete with Alccofine as partial replacement was studied and observed that 20% replacement of cement with Alccofine increased the strength and durability of concrete at all the ages [3]. The behavior of high performance of concrete with Alccofine as a supplementary cementitious material was studied. It was observed that 10% replacement of cement with Alccofine gave an increase in the compressive strength and flexural strength [4]. Performance of concrete was studied by replacing the cement with supplementary cementitious material Alccofine. Under sulphate attack, it was found that the weight loss decreased with the increase in Alccofine addition [5].The behavior of Alccofine concrete was studied at different high range water reducing dosages with low water/binder ratios. The cost of concrete mix prepared with Alccofine was lesser than the concrete prepared without Alccofine [6]. Effect of elevated temperatures on compressive strength, Split tensile strength

and Flexural strength was studied between the temperatures $50^0C$ to $250^0C$. Compressive strength, Split tensile strength and Flexural strength were found to be decreased with the increased temperature [7].

### III. Experimental Programme

#### A. Materials
Cement, fine aggregate, coarse aggregate and water were used for the preparation of desired strength of concrete mix. In addition, Supplementary Cementitious Material (Alccofine 1203) was used to increase the strength of the concrete. Chemical admixture (ACE 30 JP) was also used to produce high workability in fresh concrete and to reduce water-cement ratio

#### B. Cement
Ordinary Portland Cement of 53 grade conforming to IS:8112-1989 was used in the present Project work. Specific gravity of cement was 3.10 and the cement was tested according to IS:1489-1991 (Part-I).

#### C. Fine Aggregate
Natural river sand was used as fine aggregate. Specific gravity of fine aggregate was 2.65. Fineness modulus is 2.87. Bulk density is 1778.26 kg/m$^3$.Testing of fine aggregate conforms to IS: 383-1970.

#### D. Coarse Aggregate
Coarse aggregate passing through 20mm sieve and retained on 10mm sieve and 4.75mm sieve was taken in 60% and 40% respectively. Specific gravity of Coarse aggregate was 2.70. Testing of coarse aggregate conforms to IS:383-1970.

#### E. Water
Potable water was used in the preparation of concrete. Water used conforms to IS:456-2000.

#### F. Superplasticizer
Superplasticizer used in the present study was Master Glenium BASF ACE30JP. Dosage of superplasticizer used was 1.27% by weight of binder. Chemical Admixture BASF ACE30JP is conforms to IS: 9103-1999.

#### G. Mineral Admixture
Alccofine1203 conforming to IS:12089-1987, IS:456-2000 (Clause No:5.2.2) and ASTM C989-99 [9] was used as a supplementary cementitious material. Its particle size is much finer than the cement particle size.

#### H. Compressive Strength
Mix proportions 1:0.556:1.629:0.25 and 1:0.617:1.644:0.25 were taken from the literature and trial castings were made to produce high strength concrete. Concrete cubes of 100mm x100mm x100 mm size were cast. Forty-eight hours after casting, cubes were demoulded and water cured for 28 days and tested using 3000kN Computerized Compression Testing Machine at right angle to the direction of casting for compressive strength of concrete as per IS: 516-1959 [10] as presented in Fig. 1.
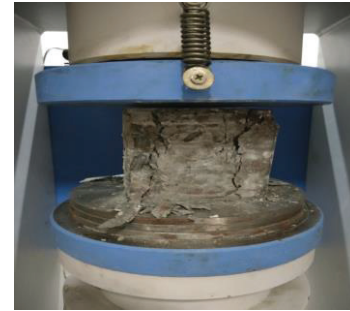


Figure 1. Cube testing under computerized Compression Testing Machine

Mix proportion 1:0.556:1.629:0.25 with 10% Alccofine 1203 yielded high strength compared to 1:0.617:1.644:0.25 mix proportion. The results obtained from the compressive strength of concrete with mix proportions 1:0.556:1.629:0.25 was presented in Table III.

TABLE III.
MIX PROPORTIONS AND COMPRESSIVE STRENGTH DETAILS OF
1:0.556:1.629:0.25

| Mix Proportion | Alccofine 1203 | Avg.Compressive Strength (MPa) |
|---|---|---|
| 1:0.556:1.629:0.25 | 5% | 69.71 |
| 1:0.556:1.629:0.25 | 10% | 79.93 |
| 1:0.556:1.629:0.25 | 15% | 63.55 |

#### I. Ultrasonic Pulse Velocity (UPV)
In the present work, pulse velocity was measured on 100 mm cubes according to IS 13311 (Part 1):1992 [8] by using PUNDIT (Portable Ultrasonic Non-destructive Digital Indicating Tester) Lab plus apparatus as presented in Fig. 2. Higher velocities were obtained when the quality of concrete in terms of density, homogeneity and uniformity is good. In case of poorer quality, lower velocities are obtained. The test results before and after removing from high temperature furnace are presented in Fig. 3.



Figure 2. Ultrasonic Pulse velocity measurement of cubes
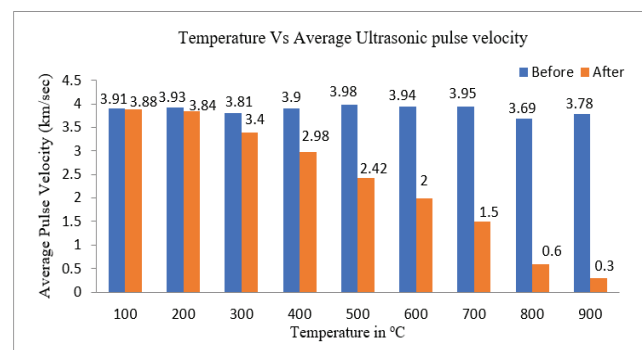


Figure 3. Average Ultrasonic pulse velocity of cubes before and after temperature studies.

### J. Elevated Temperature Studies

Fire accidents, sabotages or natural hazards are the situations where concrete is likely to get exposed to elevated temperatures. Exposure to elevated temperature causes Physical changes including large volume changes due to thermal dilations, thermal shrinkage and creep related to water loss. The volume changes can result in large internal stresses and lead to micro-cracking and fracture. Elevated temperatures also cause chemical and micro-structural changes such as water migration, increased dehydration, interfacial thermal incompatibility and the chemical decomposition of hardened cement past and aggregate. All these changes decrease the stiffness of concrete and increase the irrecoverable deformation.

In the present work, Cubes cast were kept in high temperature furnace for 02 hours duration at different temperatures from $100^0C$-$900^0C$ as presented in Fig .4. After 02 hours duration, cubes were taken out of the furnace and the Ultrasonic pulse velocity of cubes was measured using Portable Ultrasonic Non-destructive Digital Indicating Tester. The Percentage loss in weight of cubes and Residual compressive strength of the cubes were evaluated.

### K. Percentage loss in weight

The percentage of weight loss of cubes after taking out from high temperature furnace is presented in Table IV.

TABLE IV.
AVERAGE PERCENTAGE OF WEIGHT LOSS OF CUBES AFTER TAKING OUT FROM HIGH TEMPERATURE FURNACE

| Temperature ($^O$C) | Specimen designation | Weight of specimen before placing in HTF (W1) kg | Weight of specimen after taking out from HTF (W2) kg | Average percentage of weight loss = ((W1-W2)*100) /W1 |
|---|---|---|---|---|
| 100 | 10 BT | 2.41 | 2.40 | |
| | 18 BT | 2.46 | 2.36 | |
| | 19 BT | 2.48 | 2.47 | 1.63 |
| 200 | 2 BT | 2.55 | 2.50 | |
| | 3 BT | 2.41 | 2.35 | |
| | 24 BT | 2.46 | 2.41 | 2.02 |
| 300 | 6 BT | 2.49 | 2.40 | |
| | 20 BT | 2.44 | 2.33 | |
| | 22 BT | 2.45 | 2.35 | 4.06 |
| 400 | 1 BT | 2.46 | 2.33 | |
| | 12 BT | 2.45 | 2.32 | |
| | 25 BT | 2.47 | 2.35 | 5.28 |
| 500 | 7 BT | 2.41 | 2.27 | |
| | 17 BT | 2.47 | 2.35 | |
| | 21 BT | 2.45 | 2.30 | 5.73 |
| 600 | 9 BT | 2.47 | 2.33 | |
| | 23 BT | 2.46 | 2.29 | |
| | 26 BT | 2.47 | 2.32 | 6.09 |
| 700 | 11 BT | 2.49 | 2.32 | |
| | 15 BT | 2.46 | 2.33 | |
| | 4 BT | 2.49 | 2.32 | 6.45 |
| 800 | 13 BT | 2.43 | 2.25 | |
| | 16 BT | 2.48 | 2.33 | |
| | 27 BT | 2.44 | 2.27 | 6.93 |
| 900 | 8 BT | 2.50 | 2.32 | |
| | 73 BT | 2.48 | 2.30 | |
| | 77 BT | 2.50 | 2.33 | 7.22 |
| *HTF- High Temperature Furnace | | | | |

The percentage loss in weight of cubes was found to be increased up to $900^0C$. It was observed that there was an increase in percentage of weight loss with respect to increase in temperature.

### L. Compressive Strength

The compressive Strength of cubes before placing and after removing from high temperature furnace are presented in Table V.

TABLE V.
COMPRESSIVE STRENGTH OF CUBES SUBJECTED TO ELEVATED TEMPERATURE STUDIES

| Temperature ($^O$C) | Average compressive strength before placing in HTF (MPa) | Average residual compressive strength after taking out from HTF (MPa) | Average percentage loss in compressive strength |
|---|---|---|---|
| 100 | 78.06 | 63.06 | 19.34 |
| 200 | 78.69 | 56.93 | 27.72 |
| 300 | 77.55 | 91.9 | -18.55 |
| 400 | 78.86 | 68.3 | 11.74 |
| 500 | 77.39 | 62.1 | 19.71 |
| 600 | 78.52 | 57.4 | 26.809 |
| 700 | 77.83 | 52.76 | 32.15 |
| 800 | 77.98 | 37.36 | 52.06 |
| 900 | 79.44 | 23.96 | 69.83 |



Figure 4. Cubes in High High Temperature Furnace



Figure 5. Cube after 02 hrs.in Temperature Furnace at $100^0C$



Figure 6(a). Cube after 02 hrs. in High Temperature Furnace at $200^0C$



Figure 6(b). Cube after 02 hrs. in High Temperature Furnace at $300^0C$



Figure 7(a). Cube after 02 hrs. in High Temperature Furnace at $400^0C$



Figure 7(b). Cube after 02 hrs. in High Temperature Furnace at $500^0C$

Figure 8(a). Cube after 02 hrs. in High Temperature Furnace at $600^0$C


Figure 8(b). Cube after 02 hrs. in High Temperature Furnace at $700^0$C


Figure 9(a). Cube after 02 hrs. in High Temperature Furnace at $800^0$C


Figure 9(b). Cube after 02 hrs. in High Temperature Furnace at $900^0$C

No visible cracks and spalling were found up to $300^0$C as presented in Fig. 5, Fig. 6(a) and Fig. 6(b) respectively. Cracks were observed in the specimens tested to $400^0$C and $500^0$C as presented in Fig. 7(a) and Fig. 7(b). Cracks were observed as pronounced in the specimens subjected to $600^0$C, $700^0$C, $800^0$C and $900^0$C respectively as presented Fig. 8(a), Fig.8(b), Fig. 9(a) and Fig.9(b) respectively. Above $700^0$C, large crack widths and depths were observed in the specimens. The variation in color was observed with respect to the temperature increase. Up to $600^0$C, the concrete colour doesn't change noticeably. When the temperature was increased to $700^0$C, the color of cube was changed from normal to pink or red as presented in Fig. 8(b). When the temperature was increased above $700^0$C, the color of cube was changed to whitish grey as presented in Fig. 9(b).

*M. Durability Studies - Sulphate Attack Test*

Sulphate attack test was carried out on 100 mm x100 mm x100 mm concrete cubes. Total 03 cubes were casted and cured in water for 28 days. After 28 days curing, cubes were taken out and allowed for drying for 24 hours at $50^0$C and weights were taken before placing in the sulphate solution (2.5% $Na_2SO_4$ and 2.5% $MgSO_4$ by weight of water) as presented in Fig. 10. The concentration of the solution was maintained throughout this period by changing the solution periodically. The specimens were taken out from the sulphate solution after the prescribed period of continuous soaking and the surface of the cubes was cleaned, weighed & the average percentage of loss in weight was calculated at 7, 14, 28 and 56 days as presented in Fig. 11 and tested in the compressive testing machine at the end of 56 days and the compressive strength of the concrete cubes was calculated as per IS: 516-1959 [10].


Figure 10. Cubes immersed in $MgSo_4$ & $Na_2So_4$
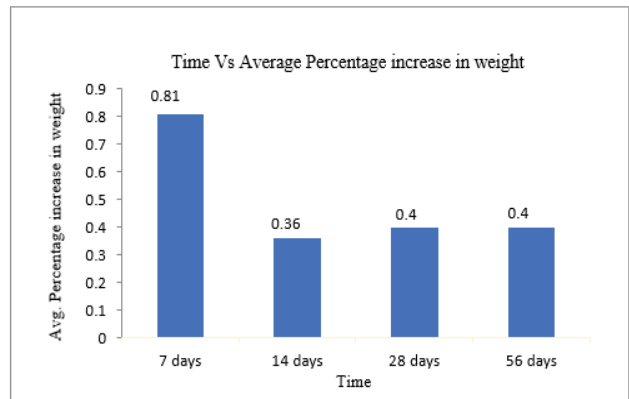

Figure 11. Variation of average percentage increase in weight of cubes taken out from $Mgso_4$ and $Na_2so_4$

*N. Chloride Attack Test*

Chloride resistance test was carried out on 100 mm x100 mm x100 mm concrete cubes. Total 03 cubes were casted and cured in water for 28 days. After 28 days curing, cubes were taken out and allowed for drying for 24 hours at $50^0$C and weights were taken before placing in the sodium chloride solution (5% of Nacl by weight of water) as presented in Fig. 12. The concentration of the solution was maintained throughout this period by changing the solution periodically. The specimens were taken out from the sodium chloride solution after the prescribed period of continuous soaking and the surface of the cubes was cleaned, weighed & the average percentage of loss in weight was calculated at 7, 14, 28 and 56 days as presented in Fig. 13 and tested in the compressive testing machine at the end of 56 days and the compressive strength of the concrete cubes was calculated as per IS: 516-1959.


Figure 12. Cubes immersed in Nacl
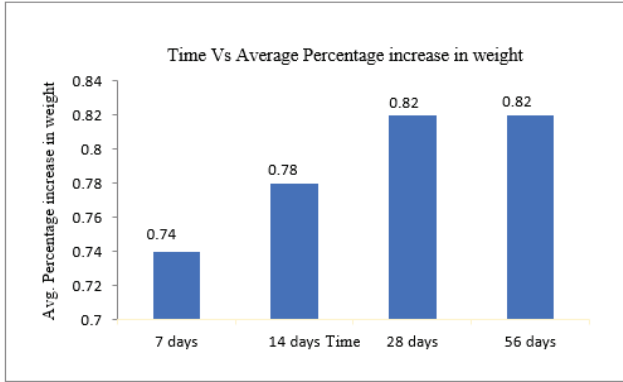
Figure 13. Variation of average percentage increase in weight of cubes taken out from Nacl

### O. Alkali Attack Test

Alkali attack test was carried out on 100 mm x100 mm x100 mm concrete cubes. Total 03 cubes were casted and cured in water for 28 days. After 28 days curing, cubes were taken out and allowed for drying for 24 hours at $50^{0}C$ and weights were taken before placing in the sodium hydroxide solution (5% of sodium hydroxide solution by weight of water) as presented in Fig.14. The concentration of the solution was maintained throughout this period by changing the solution periodically. The specimens were taken out from the sulphate solution after the prescribed period of continuous soaking and the surface of the cubes was cleaned, weighed & the average percentage of loss in weight was calculated at 7, 14, 28 and 56 days as presented in Fig.15 and tested in the compressive testing machine at the end of 56 days and the compressive strength of the concrete cubes was calculated as per IS: 516-1959.



Figure 14. Cubes immersed in NaoH
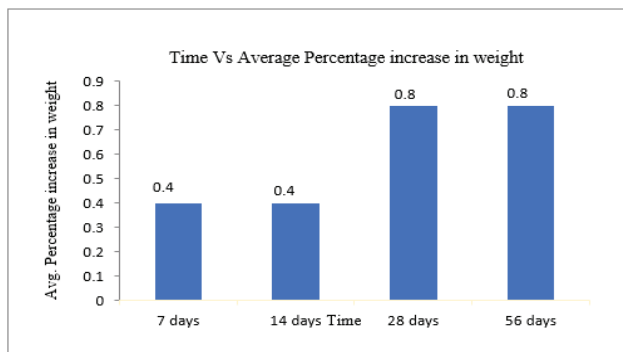


Figure 15. Variation of average percentage increase in weight of cubes taken out from NaoH

### P. Sea Water Test

Sea water was brought from Bay of Bengal and test was carried out on 100 mm x100 mm x100 mm concrete cubes. Total 03 cubes were casted and cured in water for 28 days. After 28 days curing, cubes were taken out and allowed for drying for 24 hours at $50^{0}C$ and weights were taken before placing in the sea water (5% of Sea water solution) as presented in Fig.16. The concentration of the solution was maintained throughout this period by changing the solution periodically. The specimens were taken out from the sulphate solution after the prescribed period of continuous soaking and the surface of the cubes was cleaned, weighed & the average percentage of loss in weight was calculated at 7, 14, 28 and 56 days as presented in Fig.17 and tested in the compressive testing machine at the end of 56 days and the compressive strength of the concrete cubes was calculated as per IS: 516-1959.



Figure 16. Cubes immersed in Sea Water
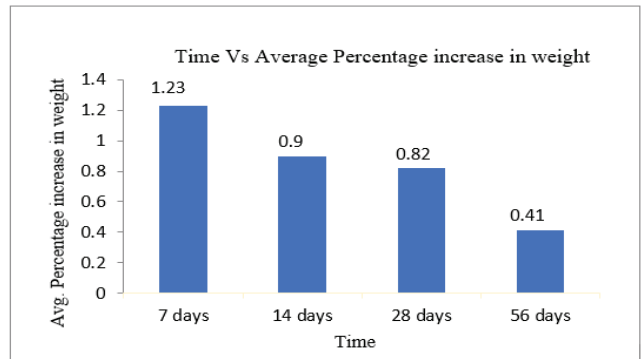


Figure 17. Variation of average percentage increase in weight of cubes taken out from Sea Water

### Q. Percentage Increase in Weight

The Percentage increase in weight for Nacl, NaoH, $MgSo_4$ & $Na_2So_4$ and Sea Water as presented in Fig.18.
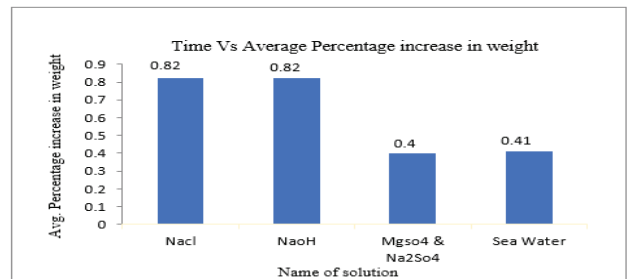


Figure 18. Comparison of percentage Increase in weight of cubes for different solutions at 56 days

## R. Compressive Strength

The Average Compressive Strength before placing and after removing from Nacl, NaoH, MgSo₄ & Na₂So₄ and Sea Water and percentage increase in compressive strength are presented in Table 6.

TABLE VI.
PERCENTAGE INCREASE IN COMPRESSIVE STRENGTH OF CUBES AT 56 DAYS

| Name of Solution | Average Compressive Strength when cured in potable water (MPa) | Average Compressive Strength after taking out from the chemical solutions (at 56days) (MPa) | Percentage Increase in Compressive strength |
|---|---|---|---|
| Nacl | 69.71 | 91.83 | 31.73 |
| NaoH | 79.93 | 94.6 | 18.35 |
| MgSo₄ & Na₂So₄ | 63.55 | 86.93 | 36.78 |
| Sea Water | 78.40 | 89.10 | 13.64 |

## S. Sorptivity Test

Sorptivity is the absorption and transmission of water through capillary action.

Before the specimen is placed in contact with water it was kept in oven at temperature of $50^0C$ for 03 days [9]. Cubes (10 cm) were placed as presented in Fig.19.

The absorption (I) due to capillary action is the change in mass divided by the product of the cross-sectional area of the test specimen and the density of water as in (1). The units of 'I' are mm.

$$I = \left( \frac{m_t}{a * d} \right) \qquad (1)$$

Where, I = absorption

Δw= change in weight = W2-W1

W1 = Oven dry weight of cube in grams

W2 = Weight of cube after the prescribed time

due to capillary suction of water in grams.

$m_t$ = change in specimen mass (in grams, at time t)
a   = exposed area of the specimen through
       which water penetrated (mm²)
d  = density of the water (g/mm³)

Sorptivity was calculated using the expression presented in (2).

$$\text{Sorptivity, S} = I/t^{1/2} \qquad (2)$$
Where, S = Sorptivity in mm/min$^{1/2}$
t = elapsed time in min.


Figure 19. Cubes under Sorptivity test

Sorptivity coefficient is calculated as $1.5873 \times 10^{-4}$ mm/min$^{0.5}$ from the graph presented in Fig.20.
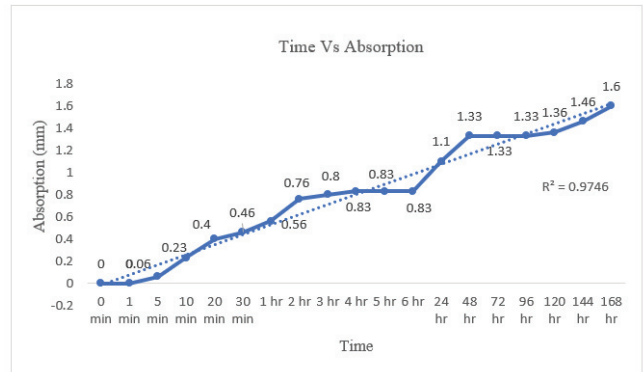

Figure 20. Variation of water absorption of cubes with respect to time

## IV. DISCUSSIONS AND CONCLUSIONS

The quality category of cubes before temperature studies as per IS:13311 (Part-I) was 'Good'. The Ultrasonic pulse velocity of high strength concrete cubes as per IS:13311 (Part-I) between $100^0C$-$900^0C$ in an interval of $100^0C$ was found to be 'Good' quality for $100^0C$, $200^0C$ and 'Medium' quality for $300^0C$ and 'Doubtful' quality for $400^0C$, $500^0C$, $600^0C$, $700^0C$, $800^0C$ and $900^0C$. Due to the weakened cohesion between the mixture constituents, path length of the Ultrasonic pulse velocity might have been increased and thereby decreasing the velocity. This might be the reason for the decrease in quality category of concrete cubes from 'Good' to 'Doubtful'.

The effect of elevated temperatures on weight of concrete cubes was studied between $100^0C$-$900^0C$ in an interval of $100^0C$. The percentage loss in weight of cubes was found to be increased from $100^0C$ to $900^0C$. This may be attributed to the continuous evaporation of moisture from the concrete cubes which might have weakened the bonding between the binder and the course aggregate.

The percentage difference in compressive strength between $100^0C$ to $900^0C$ in an interval of $100^0C$ was 19.34, 27.72, -18.55, 11.74, 19.71, 26.80, 32.15, 52.06, 69.83. The increase in strength at $300^0C$ might be attributed to the increase in surface forces between gel particles (Vander Waal forces) due to the removal of moisture content. The decrease in compressive strength at $800^0C$ may be attributed to decomposition of the cementing compound C-S-H with its different phases, dehydration of calcium hydroxide (CH) into free lime. These changes would have affected the volume occupied by these cementitious products and when combined with the weakened cohesion between the mixture constituents due to the different expansions experienced by each of them. The decrease in compressive strength at $900^0C$ may be attributed to the decomposition of calcium carbonate through the loss of $CO_2$ and all the free water might have lost.

The percentage variation in average weight of 10cm concrete cubes after 56 days of immersion in Nacl solution, NaoH solution, Mgso₄ plus Na₂so₄ solution and Sea water was found to be 0.82, 0.80, 0.40 and 0.41 respectively. The percentage variation in weight of cubes is very less and this might be due to the error in taking the measurements.

The percentage increase in compressive strength after taking out from the chemical solutions $Na_2SO_4$ and $MgSO_4$, Nacl, NaoH and Sea water at 56 days was found to be 31.73, 18.35, 36.78 and 13.64 respectively. The concentration of these solutions was not sufficient enough to affect the Compressive strength of concrete cubes.

More absorption of water due to capillary action might be attributed to the precondition of the concrete cubes at a temperature of $50^0C$ for 03 days as per ASTM:C1585-04.

Based on the above discussions, the use of Alccofine 1203 is recommended as a mineral admixture to prepare a concrete of high strength and durability.

### REFERENCES

[1] Devinder Sharma, Sanjay Sharma, Ajay Goyal,"Pre-diction of High Compressive Strength of Concreteusing Waste Foundry Slag and Alccofine by NDT,"International Journal of Engineering Research &Tech-Nology, ISSN: 2278-0181, vol.5, Issue 02, February-2016.

[2] Yatin, H., Patel, Patel, P.J., Jignesh, M., Patel, Patel, H.S., "Study on Durability of High PerformanceConcrete with Alccofine and Fly Ash," International Journal of Advanced Engineering Research and Studies, E-ISSN:2249- 8974, vol 2, Issue 03, April-June-2013.

[3] Narender, A., Reddy, Meena, T., "A Comprehensive Overview on Performance of Alcco fine Concrete," International Journal of Pharmacy & Technology, ISSN: 0975-766X, vol 9, Issue 01, April-2017.

[4] Vikram, K., Shadi, Banarase, M.A., "Experimental Study on Effect of Alccofine on Properties of Concrete- A Review," International Journal of Research in Engineering, Science and Technologies, ISSN: 2395-6453, vol 1, Number 8, December-2015.

[5] Gayathri, K., Ravichandran, K., Saravanan, J., "Durability and Cementing Efficiency of Alccofine in Concretes," International Journal of Research in Engineering and Technology, ISSN: 2278-0181, vol 5, Issue 05, May-2016.

[6] Saurabh Gupta, Sanjay Sharma, Devinder, E.R., Sharma, "A Review on Alccofine: A Supplementary Cementitious Material," International Journal of Modern Trends in Engineering and Research, ISSN: 2349-9745, vol 2, Issue 08, August-2015.

[7] Sreenivasulu, A., Srinivasa, K., Rao, "The Effect of Temperature on Mechanical Properties of M100 Concrete,' American Journal of Engineering Research, ISSN: 2320-0847, Vol 02, Issue 04, 2013.

[8] IS 13311 (Part 1): 1992 -Non-Destructive Testing of Concrete-Methods of Test (Part 1 Ultrasonic Pulse Velocity).

[9] ASTM: C1585-04, "Standard Test Method for Measurement of Rate of Absorption of Water by Hydraulic Cement Concretes", PP 1-5.

[10] IS :516-1959, "Method of Tests for Strength of Concrete, Bureau of Indian Standards.

# Geomorphological Instantaneous Unit Hydrograph (GIUH) for an Ungauged Watershed

B. N. Malleswara Rao

Professor, CVR College of Engineering/Civil Engineering Department, Hyderabad, India

Email: bnmrao@gmail.com

*Abstract:* In the present micro climate change conditions, there is a need for managing the available water resources and their optimum utilization for various purposes. This work aims at developing the Geomorphological Instantaneous Unit Hydrograph (GIUH) by using rainfall-runoff characteristics of an unguaged basin. The rainfall-runoff relationship can be developed using different empirical and conceptual methods. The empirical models are site specific. One has to develop separately for each basin. But earlier models were developed with few fixed parameters applicable to all the basins. A conceptual model developed by Rodriguez-Iturbe and Valdes relates the peak runoff and time to reach peak (unit hydrograph parameters) with the Geomorphological parameters of the basin. Remote sensing images and Survey of India toposheets are used to calculate these parameters in the present study. Basin parameters can be modified considering user needs with the help of GIS software. The study area chosen is the Khanapur watershed which is an unguaged lying in the mid Godavari basin. GIS database is developed using the basin parameters namely, drainage network map, slope map, land use / land cover map, and contour map in the analysis to find the Nash GIUH model parameters.

*Index Terms:* Unit hydrograph, unguaged, runoff, watershed, time of concentration, Geographic Information System, GIUH.

## I. INTRODUCTION

I. Rodriguez-Iturbe and Valdes [9] introduced the concept of the Geomorphologic Instantaneous Unit Hydrograph (GIUH) to link the hydrologic characteristics of a basin with the geomorphologic parameters. The GIUH method can be used for unguaged basins, wherein rainfall data is available but runoff data is not available. Also GIUH having advantage to the other methods, as it does not require rainfall and meteorological data of other catchments in the region. Earlier works of A. N. Strahler [2], F. F. Snyder [8], R. E. Horton [16], A. B. Taylor and Schwartz [1] have provided an understanding of basin geomorphology-hydrology relationship through empirical relations. Further

advancement was made by following researchers like C. O. Clark [6], J. E. Nash [11] and Koutsoyiannis and Xanthopoulos [14]. Literature study highlights the advantage of parametric approach for the derivation of unit hydrograph to establish a relationship between the Unit Hydrograph and basin characteristics.

A stream of a certain order with a linear response function was used in the derivation of the GIUH by following researchers like D. Ros [7], I. Rodriguez-Iturbe and Valdes [9], Kirshen and Bras [13], A. Rinaldo et al., [3], Jin [12], C. Fleurant et al., [5]. GIUH approach is applicable in situations where rainfall data is available but no runoff data is available. It is a more powerful technique for the estimation of peak run-off. The Nash-IUH model parameters and GIUH was linked by N. R. Bhaskar et al. [15]. GIUH technique is also useful in deriving the unit hydrograph (UH) using the geomorphologic characteristics (I. Rodriguez-Iturbe and Valdes [9], R. Rosso, [19], B. Sahoo et al., [4], R. Kumar et al., [17] and R. Kumar et. al. [18] studied the performance of Clark and Nash model by equating this model runoff peak to the peak runoff of GIUH model. This approach includes finding of Clark and Nash model parameters by assuming known peak runoff of GIUH model. In the present study, GIUH-based Nash model is used for the estimation of floods in unguaged watersheds with a reasonable degree of accuracy.

## II. STUDY AREA

Khanapur watershed of Adilabad district which is the study area is a sub-basin of middle Godavari basin, lies in west of Adilabad in Telangana, comprising of five villages namely Khanapur, Dilawarpur, Tarlapadu, Gandhinagar and Maskapur. Fig. 1 shows the study area. The total area of the basin is 55.753 km$^2$. Geographically it lies between the Longitudes of 78$^o$34'33"E to 78$^o$40'37"E and Latitudes of 19$^o$2'24"N to 19$^o$6'37"N.
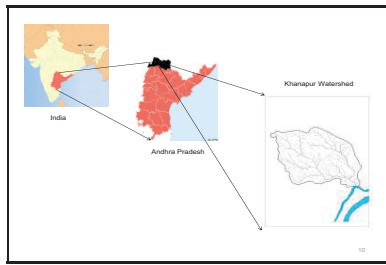
Figure 1. Location map for Khanapur watershed

## III. GIS Database Generation

*Drainage map*: Fig. 2 shows the drainage map. The study area drainage map consists of stream network and water bodies.

*Soil map:* Fig. 3 shows the soil map. It gives the information regarding different types of soils in the watershed. This data is useful in prediction of the runoff capability of different soils.

*Contour map:* Fig. 4 shows contour map. contour is an imaginary line joining the points of equal elevation, the highest elevation being +400 M.S.L.

All the above GIS maps will form the geographical data base of the watershed.
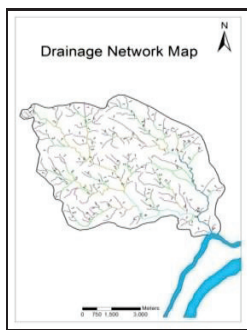


Figure 2. Drainage map
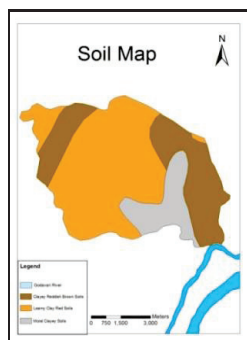


Figure 3. Soil Map
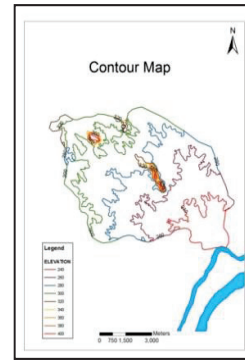


Figure 4. Contour Map

## IV. Derivation of Nash Model Parameters from $q_P$ and $t_P$ of GIUH

Total Number of streams of different orders    (N) = 209
Total area of the drainage basin (A) =55.75km$^2$
Total length of the all streams (L) =152.75km
Drainage density   (D) =A/L= 0.365 km$^2$/km
Horton's stream-bifurcation ratio ($R_B$) =2.98
Horton's stream-length ratio ($R_L$) =1.58
Horton's stream-area ratio ($R_A$) =2.60
Mean stream length of highest order ($L_W$) = 2.98km

Time of concentration of a basin is estimated using geomorphologic data by applying the equations (1) and (2). Velocity relationship given by equation (8) is useful in estimating time of concentration for a watershed by using mean slope and land cover characteristics. Equations (7) and (8) are used in arriving a relationship between velocity, flow length and mean slope characteristics of a watershed which is presented by equation (9).

$$t_c = 0.01947. L^{0.77}. S^{-0.385} \qquad (1)$$

$$t_c = \frac{1}{60} \left(\frac{L}{v}\right) \qquad (2)$$

$$V = 0.8562. L^{0.23}. S^{0.385} \qquad (3)$$

TABLE I.
MEASURED GEOMORPHOLOGICAL DATA

| Stream Order | Total number of Streams | Total Length of Streams (km) | Drainage Area (Km²) | |
|---|---|---|---|---|
| 1 | 144 | 88.1039 | 19.9757 | |
| 2 | 40 | 30.6626 | 14.7512 | |
| 3 | 18 | 22.1177 | 7.2726 | |
| 4 | 5 | 5.9093 | 4.3154 | |
| 5 | 2 | 5.9601 | 7.7953 | |

TABLE II.
DERIVED GEOMORPHOLOGICAL DATA

| Stream Order (W) | Mean Stream Length (km) | Mean Stream Area (Km$^2$) | Bifurcation Ratio ($R_B$) | Stream Length Ratio ($R_L$) | Stream Length Ratio ($R_A$) |
|---|---|---|---|---|---|
| 1 | 0.61 | 0.14 | 3.60 | -- | -- |
| 2 | 0.77 | 0.37 | 2.22 | 1.25 | 2.65 |
| 3 | 1.23 | 0.40 | 3.6 | 1.60 | 1.09 |
| 4 | 1.19 | 0.9 | 2.5 | 0.96 | 2.14 |
| 5 | 2.98 | 3.9 | -- | 2.52 | 4.52 |

Here $t_c$ = time of concentration in min.; L = length of the main stream length in meter and S = mean watershed slope (m/ m) and V = velocity in m / s.

J. E. Nash [10] suggested a conceptual model in which basin impulse response can be represented as the outflow obtained from routing the unit volume of the instantaneous excess rainfall input through a series of 'n' successive linear reservoirs having equal delay time. The following equation are given by Nash IUH model :

$$U(0,t) = \frac{1}{k} \times \frac{1}{\Gamma(n)} \times e^{\left(\frac{-t}{k}\right)} \times \left(\frac{t}{k}\right)^{n-1} \qquad (4)$$

Where  U (0, t)  =  ordinate of the IUH
　　　　Γ  =  gamma function
　　　　K  =  catchment storage coefficient (scale function)
and　　n  =  the number of linear reservoirs (shape parameter).

$$q_p \times t_p = \frac{(n-1)}{\Gamma(n)} \times e^{-(n-1)} \times (n-1)^{(n-1)} \qquad (5)$$

Eq. (5) is a function of Nash IUH model parameters n only.

The most important characteristic of an IUH are the peak $q_p$ and the time to peak $t_p$. I. Rodriguez-Iturbe and Valdes [9] noticed that $q_p$ and $t_p$ are simple related to the velocity v. This when simplified the following equations (6) and (7) were obtained.

$$q_p = \left(\frac{1.31}{L_W}\right) \times R_L^{0.43} \times v \qquad (6)$$

$$t_p = \left(\frac{0.44}{v}\right) \times L_W \times R_B^{0.55} \times R_A^{-0.55} R_L^{-0.38} \qquad (7)$$

By multiplying (6) and (7), we will get $q_p \times t_p$ in terms of geomorphological characteristics.

$$q_p \times t_p = 0.5764 \, R_B^{0.55} \times R_A^{-0.55} \times R_L^{0.05} \qquad (8)$$

Equating (5) and (8), we have

$$\frac{(n-1)}{\Gamma(n)} \times e^{-(n-1)} \times (n-1)^{(n-1)} 0.5764 \, R_B^{0.55} \times$$
$$R_A^{-0.55} \times R_L^{0.05} \qquad (9)$$

The n value which obtained from above equation may be substituted in the following equation which is derived from by combining (6) and (2) to get Nash model parameters K for a given velocity v

$$K = \frac{t_p}{n-1} = \frac{0.44}{v} \times L_W \times R_B^{0.55} \times R_A^{-0.55} \times$$
$$R_L^{-0.38} \times \frac{1}{n-1} \qquad (10)$$

TABLE III.
ORDINATES OF GIUH DERIVED FROM NASH MODEL PARAMETERS

| Time t (hours) | (t/k) | $e^{-t/k}$ | $(t/k)^{2.81}$ | U(t) cm/hr (i) | U(t) m$^3$/s (2.8 X A X (i) ) |
|---|---|---|---|---|---|
| 0 | 0 | 1 | 0 | 0 | 0 |
| 0.2 | 0.9 | 0.394 | 0.82 | 0.32 | 49.29 |
| 0.4 | 1.9 | 0.156 | 5.73 | 0.87 | 136.3 |
| 0.6 | 2.8 | 0.06 | 17.91 | 1.07 | 167.93 |
| 0.8 | 3.7 | 0.024 | 40.19 | 0.95 | 148.6 |
| 1.0 | 4.7 | 0.01 | 75.23 | 0.70 | 109.69 |
| 1.2 | 5.6 | 0.004 | 125.6 | 0.46 | 72.2 |
| 1.4 | 6.5 | 0.002 | 193.7 | 0.28 | 43.89 |
| 1.6 | 7.5 | 0.001 | 281.8 | 0.16 | 25.19 |
| 1.8 | 8.4 | 0.0002 | 392.4 | 0.09 | 13.83 |
| 2.0 | 9.3 | $1 \times 10^{-4}$ | 527.6 | 0.05 | 7.33 |
| 2.2 | 10.2 | $3 \times 10^{-4}$ | 689.6 | 0.02 | 3.78 |
| 2.4 | 11.2 | $1 \times 10^{-5}$ | 880.7 | 0.01 | 1.90 |
| 2.6 | 12.1 | $5 \times 10^{-6}$ | 1102.8 | 0.01 | 0.94 |

## V.  RESULTS OF GIUH

Equilibrium velocity

$$V = 0.8562 \cdot (14621.91)^{0.23} \cdot 0.02^{0.385}$$

$$V = 1.723 \text{ m/sec}$$

Area of the watershed     $A$   =   $55.753 km^2$
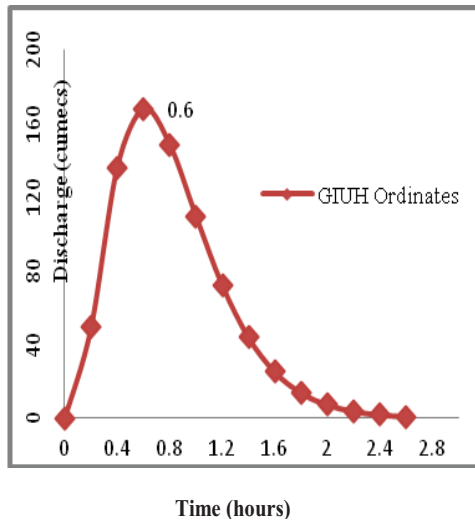


**Figure 5. Nash model IUH for Khanapur watershed**

On solving equation (7) and (8)

The Nash Parameters   $n$    =    3.81

                   $K$    =    0.24

The values can be utilized to derive the complete shape of GIUH using equation (4).

$$U(0,t) = \frac{1}{k} \times \frac{1}{\Gamma(n)} \times e^{\left(\frac{-t}{k}\right)} \times \left(\frac{t}{k}\right)^{n-1} \tag{11}$$

$$U(0,t) = 0.98 \times e^{\left(\frac{-t}{0.24}\right)} \times \left(\frac{t}{0.24}\right)^{2.81} \tag{12}$$

*Derived Values of GIUH:*
From the figure 5, we can derive that

Time to peak, $t_p$ = 0.6 hr

Base time, $t_b$ = 2.6 hrs

*Theoretical Values of GIUH:*

Main Stream Length (m) L       = 14621.91

Mean Slope of Watershed, S     =   2%

Velocity (m/s)    = $0.8562 \times L^{0.23} \times S^{0.385}$

               = 1.723 m/s

Peak discharge, $q_p = 1.31 \times R_L^{0.43} \times \left(\frac{v}{L\Omega}\right)$

$$= 1.31 \times (1.585)^{0.43} \times \left(\frac{1.723}{2.98}\right)$$

$$= 0.923 \ h^{-1}$$

Time to peak, $t_p = \left(\frac{0.44}{v}\right) \times L_\Omega \times (R_B/R_A)^{0.55} \times (R_L)^{-0.38}$

$$= \left(\frac{0.44}{1.723}\right) \times 2.98 \times (2.981/2.601)^{0.55} \times (1.585)^{-0.38}$$

$$= 0.7 \ hr$$

Base time, $t_b$     $= \frac{2}{q_p}$

$$= \frac{2}{0.923} = 2.2 \ hr$$

## VI. RESULTS AND CONCLUSIONS

1. The soil map prepared can be used in the generation of the land capability map. The land capability map thus prepared is used for preparing land adjustment map which gives the information on cropping pattern adjustment needed for better agricultural production.

2. The drainage map shows the drainage pattern of the area, stream density and existing tank details. It also gives the information on tank condition i.e., details like water spread area, silted portion etc. This information is helpful to prepare plans for restoration of these deteriorated tanks.

3. The hydrogeomorphological data base shows the different geological formations, lineaments, geological faults etc. This information is helpful in finding water potential zones which in turn is useful in preparation of land capability map.

4. The hydrogeomorphological data is used in geomorphological analyses of the study area. The different geomorphological parameters obtained from the present study are as follows:
Total number of streams of different orders,   N = 209
Total area of the drainage basin,   A   = 55.75km$^2$
Total length of all streams, L      = 152.75 km
Drainage density, A/L          = 0.365
Horton's stream-bifurcation ratio, $R_B$    = 2.98
Horton's stream-length ratio, $R_L$     = 1.58
Horton's stream-area ratio, $R_A$      = 2.60
Mean stream length of highest order, $L_w$ =2.98km

5. By using the geomorphological parameters, a Geomorphological Instantaneous Unit Hydrograph (GIUH) using Nash model parameters n and K values is developed.

6.This GIUH model is useful in development of runoff in an event where the rainfall data is known.

7.The GIS database can also be used by officials to understand the activities in the watershed and analyze the temporal variations in this area.

### REFERENCES

[1]  A.B.Taylor and H. E. Schwartz,"Unit-hydrograph lag and peak flow related to basin characteristics", *Trans. Amer. Geophys. Uni.,* vol. 33, pp. 235–246, 1952.

[2]  A.N. Strahler "Quantitative analysis of watershed geomorphology",Trans. Amer. Geophys. Uni.,vol.38,pp. 913-920, 1957.

[3]  A. Rinaldo, A. Marani and R. Rigon,"Geomorphological dispersion", *J. Water Resour. Res.*, vol. 27, pp. 513-525, 1991.

[4]  B. Sahoo, C. Chatterjee, N. S. Raghuwanshi, R. Singh and R. Kumar, "Flood estimation by GIUH based Clark and Nash models", *J. Hydrologic Engg.*, vol.11, pp. 515-525,

[5]  C. Fleurant,B. Kartiwa, B. Roland, "Analytical model for 2006. ageomorphological instantaneous unit hydrograph", *J. Hydrol. Process.* vol. 20, pp. 3879–3895, 2006.

[6]  C. O. Clark, "Storage and the unit hydrograph", *Trans. Am. Soc. Civ. Engr.*, pg. 110, 1945.

[7]  D. Ros, and M. Borga, "Use of digital elevation model data for the derivation of the geomorphological instantaneous unit hydrograph", *J. Hydrol. Process.*, vol. 11, pp. 13–33, 1997.

[8]  F. F. Snyder, "Synthetic unit graphs", *Trans. Amer. Geophys. Uni.*, vol.2, pg. 447, 1938.

[9]  I. Rodriguez –Iturbe and J. B. Valdes, "The geomorphologic structure of hydrologic response", *J. Water Resour. Res.*, vol. 15, pp. 1409-1420, 1979.

[10]  J.E. Nash,"The form of the instantaneous unithydrograph." *Intern .Assoc.of Sci e.and Hydr.,*Pub.45,vol.3, pp.114–121, 1957

[11]  J. E. Nash, "A unit hydrograph study, with particular reference to British catchments", *Proc. Inst. Civil Engg.*, vol. 17, pp. 249-282, 1960.

[12]  Jin,"A deterministic gamma-type geomorphologic instantaneous unit hydrograph based on path types", *J. Water Resour. Res.*, vol. 28, pp. 479-486, 1992.

[13]  Kirshen, and Bras,"The linear channel and its effect on the geomorphologic IUH",*J.Hydrol.*vol.65, pp.175-208, 1983.

[14]  Koutsoyiannis and Xanthopoulos,"On the parametric approach tunit hydrograph identification",*J. Water Res. Manage.*, vol. 3, pp. 107–128, 1989.

[15]  N. R. Bhaskar, B.P. Parida, and A.K. Nayak, "Flood estimation for ungauged catchments using the GIUH", *J.WaterResour. Plann. and Manage.* vol. 123, ASCE, 1997.

[16]  R.E. Horton, "Erosional development of streams and their drainage basins: Hydro physical approach to quantitative morphology", *Bull. Geol. Soc. Amer.*, vol. 56, pp.275–370,1945.

[17]  R. Kumar, C. Chatterjee, A. K. Lohani, S. Kumar, R. D. Singh "Sensitivity analysis of the GIUH based Clark modelfor a catchment", *J. Water Res. Manage.*, vol. 16, pp.263–278, 2002.

[18]  R. Kumar, C. Chatterjee, R. D. Singh, A. K. Lohani and S.Kumar, "Runoff estimation for an ungauged catchment using geomorphological instantaneous unit hydrograph (GIUH) model", *J. Hydrol. Process.*, vol. 21, pp. 1829-1840, 2007.

[19]  R. Rosso, "Nash model relation to Horton order ratios",*J. Water Resour.,* vol. 20, pp. 914–920, 1984.

# Twin Steel Helix Fiber Reinforced Concrete

P. Alekhya[1], R. Prashanth Kumar[2], N. Murali Krishna[3]

[1] M Tech Student, CVR College of Engineering/ Department of Civil Engineering, Hyderabad, India.
Email: alekhyapodila@gmail.com

[2]Assoc. Professor , MVSREC, Department of Civil Engineering, Hyderabad, India.
Email: prashanthkumarsharp@gmail.com

[3]Professor, CVR College of Engineering/ Department of Civil Engineering, Hyderabad, India
Email: nmuralikrishna 1956@gmail.com

*Abstract*: As on date the most widely used construction material is still Reinforced cement concrete. As concrete is strong in compression and week in tension, steel is placed in concrete where ever tension is anticipated. The process is proven to be cumbersome, time consuming and expensive. Fiber reinforced concrete has emerged as a consequence which offers improved tensile strength in addition to increased compressive strength. Twin steel helix fiber with more frictional resistance are added in concrete matrix to improve tensile strength of concrete. In this paper experimental results of compressive strength and tensile of different grade of concrete with different dosages of twin steel helix fibers are presented.

*Index Terms:* Twin steel helix Fiber reinforced concrete (TSHFRC), Tensile strength.

## I. INTRODUCTION

It's a well-known fact that even as on this date too, reinforced cement concrete is still the most widely used construction material all over the world. It is well known that concrete is strong in compression and weak in tension and as a reason steel is used at all locations where tensile stress develops in all structural elements. However, availability of a construction material which can resist both compression and tension and can be produced with equal ease as conventional concrete is most desirable. Such a construction material shall also be economically viable, easy for production, handling and placing and yet durable like conventional RCC. Twin steel helix fiber reinforced concrete (TSHFRC) as a construction material is the right choice meeting all the above requirements. TSHFRC consists of two tiny steel wires of 0.25mm diameter twisted together and cut into pieces of 20mm length added to cement concrete during mixing, replacing the rebar to some extent or in full to achieve higher crack resistance and structural strength throughout the concrete mass in all directions. The shape of cross section and the number of twists of steel and cement concrete. The steel wire, with its twisted profile is a far superior reinforcement and is a better improvement over fibers of any time. When concrete is stressed or bent, the fibers with smooth profile will slide-out with minimal possible friction. But the same fibers provided with deformation like a hooked end or corrugation adds friction and increases pullout force.

### A. TSHFRC-OTHER TYPES FRC

Ferro-cement is a composite material consisting of steel wool and cement mortar. It consists of closely spaced wire fabric which are impregnated with rice cement mortar mix. The steel wool is generally obtained from lathe machining job works, mechanical workshops, are usually 0.5-1.0mm wide with varying lengths. The structural orientation of the steel wool can be arbitrary. The steel wool is mixed with cement mortar of cement sand ratio 1:2 with water cement ratio 0.4-0.45 the thickness of Ferro-cement elements usually varies from 20mm-30mm. this material is found suitable in making special types structural elements like shelves which have strength through forms, and structures like roofs, silos, water tanks and pipe lines. The development of Ferro-cement depends on suitable casting techniques for required shape. Development of proper fabrication techniques for Ferro-cement is still not a widely explored. Areas and gaps need to be filled. Fiber reinforced concrete is a composite material consisting of cement mortar or concrete, discontinuous, discrete, uniformly dispersed fibers and steel reinforcement. It has been recognized long since that the additional of small, closely spaced and uniformly dispersed fibers to concrete would act as crack arrester and would substantially improve its static and dynamic properties. Unlike the Ferro-cement n fiber reinforced concretes, in which fibers s are used in addition to rebar, in TSH fiber reinforced concrete usage of rebars drastically reduced or avoided all together. The TSH fibers are twisted fibers made from electrogalvanized steel. The twist changes the failure mechanism from simple pulling out to torsion mode resulting in a more efficient use of steel fiber.

### B. ADVANTEGES OF TSH FIBER CONCRETE

1. Unlike rebar or mesh, helix increases the pre-crack modulus of rupture.

2. Adds post crack tensile strength.

3. Does not permit micro cracks to develop.

4. Works in all three dimensions and throughout the entire section of concrete.

5. Excellent shear protection.

These are three reasons engineering prefer to use helix

1. First crack prevention.

2. Post crack strength increase and

3. Overall cost reduction.

### C. OBJECTIVES OF THE PRESENT STUDY

1. To establish a stress strain relation of TSH fiber reinforced concrete in both compression and tension, that can well establish the overall stress strain behavior.

2. To develop moment carrying capacities of rectangular sections using both TSH fiber reinforced concrete and conventional reinforced concrete.

3. To develop equivalent rectangular stress block parameters for TSH fiber reinforced concrete in order to extend the concepts of stress block analysis to design structural member.

## II. LITERATURE REVIEW

**Antoine E, Naaman** (2003) described in this paper the usage and application of new generation of steel fibers for use in cement, ceramic and polymeric matrices [1].

**Flavio de Andrade silval et al** (2009) performed an experimental investigation to understand the sisal fiber pull out behavior from a cement matrix [2].

**Dong-joo kim et al** (2009) Provided the performance of an innovative slip hardening twisted steel fiber in the compression with other fibers including straight steel smooth fiber, high strength steel hooked fiber, SPECTRA (High molecular weight polyethylene) fiber and PVA fiber [3].

**Gustavo J Parra-Montesinos** (2005) investigated recent applications of tensile strain-hardening, high performance fiber reinforced cement composites (HPFRCCs) in earth-quake resistant structures is presented. [4]

**Min-yuan cheng et al** (2010) investigated effectiveness of steel fiber reinforced cement for increasing punching shear strength and ductility in slab subjected to monotonically increased concentrated loads are presented [5]

**The discovery of Vikant S. vairagade et al** (2013) is based on the laboratory experiment; cube and cylindrical specimens have been designed with metallic and non-metallic groups of fibers. In metallic fibers, steel fibers of hook end with 50, 60 aspect ratio and crimped round (copper coated) of 52.85 aspect ratio containing 0%and 0.5% volume fraction were used without adding admixtures [6]

## III. EXPERIMENTAL INVESTIGATION

In the present study the TSH fiber reinforced concrete elements of grades corresponding to M20, M25 and M30 with different percentages of helix mesh reinforcement are taken-up. The concrete mix design has been carried out using IS code method as per 10262-2009. The cement that is used in the concrete mix confirm to OPC 53grade of make ultra tech. the coarse aggregate size varies from 10mm to down below, belongs to the quarry Deshmukh located in Nalgonda district. The fine aggregate used is Rob sand belonging to the quarry Deshmukh located in Nalgonda district. Potable water is used for concrete making. Making use of above material, the mix design of concrete conforming to grades M20, M25 and M30 have been designed under controlled conditions in the laboratory environment using IS code method as per provisions of BS code 8110 no of cylinders of size 150mm diameter and 300mm long were prepared to carry out compression tests. The cylinders are prepared with percentages of helix fiber mesh varying from 0%, 0.15%, 0.30% and 0.45%. They are cured for 28days, before testing is carried out. Similarly, concrete prisms 500mm long with 100mm*100mm sectional dimensions are also prepared conforming to grades M20, M25 and M30 with helix fiber mesh varying from 0%, 0.15%, 0.3% and 0.45%. The concrete prisms are used for bending tests.

### A. COMPRESSION TEST

After having designed the concrete mix as described above, the concrete cylinders with 150mm diameter 300mm long have been casted. The compression test has been performed on the concrete cylinders to evaluate the compressive strength of fiber reinforced concrete. During the process of performing tests the relation between the stress and strain is also plotted. Concrete cubes were also prepared of sizes 150*150*150mm and were tested to evaluate for compressive strength after 28 days curing the test was performed as per IS516-1959.

### B. TENSION TEST

The tension test to evaluate the tensile strength of concrete and the stress strain variation in the concrete is performed using two methods.

1. Split tensile test

2. Uni-Axial direct tensile test

### 1. SPLIT TENSION TEST:

Split tensile strength on cylinders was carried out according to the procedure given in IS 516-1956. Immediately after the removal of cylindrical specimens from the water tank are kept on the test surface. The surfaces, which are to be in contact with the packing strips. The bearing surfaces of the testing machine were wiped

clean. The cylinder was placed horizontally in the centering with packing skip (wooden strip)/ or loading pieces carefully poisoned along the top and bottom of the plane of loading of the specimen. The wooden pieces were placed on top of the cylinder and bottom of the cylinder, so that the specimen is located centrally. The load was applied without shock and increased continuously at a normal rate with the rage 1.2N/mm2/min to 2.4N/mm2/min until failure of the specimen.

The maximum load applied was recorded at failure and the appearance of concrete and unused features in the type of failure was observed. The test result is presented in the table form, and then the splitting tensile strength of the specimen was calculated by using the following formula,

$$F_{ct}=2P/\pi*L*d$$

Where, P= Maximum load in newton applied to the specimen, L= length of the specimen in mm, D= cross sectional dimension of the specimen in mm

### 2. UNI-AXIAL DIRECT TENSION TEST (DOG BONE SHAPED SPECIMEN)

The uni-axial direct tensile test method is the method by which it can identify the key properties of FRC; such as strain hardening or strain softening, the elastic modulus, and stress verses strain relationships under tension. These are the constitution properties of FRC that are useful for the modeling and design of FRC structural member [Naaman, et al 2007]. However, currently there is no standard method for this test available in the U.S.

Some uni-axial tensile tests were carried out at UT-Arlington [Chao et al 2011]. The specimen was specifically designed so that a pin-pin loading condition is created at the ends. Both the ends have double dog bone geometry and are strengthened by the steel mesh to ensure that cracking would only occur in the central portion of the specimen, with in the gauge length. The double dog bone shape is used to provide a better transition to avoid stress concentration which resulted from the reduction of cross section. The central portion has a square cross section with a dimension of 4*4 inches. This dimension was selected to ensure more uniformly distributed fibers while maintaining a suitable weight for laboratory handling. The strains were measured by a pair of linear variable differential transformers (LVDTs) with a gauge length of approximately 6 inches. Tests were carried out by a closed-loop, servo-controlled machine with a loading rate of approximately 0.0002 inches/min.

Having performed the compression test and tension test on the concrete the information pertaining to its

1. Permissible compressive strength,

2. Permissible tensile strength,

3. The stress strain curve in compression and

4. The stress strain curve in tension.

## IV. DESIGN METHODOLOGY USING TSHFRC

### A. FLEXURAL ELEMENTS:

**The method of development is as described under:**

Let the sectional dimensions of the member be B and D, where B is the width and D is the depth of the section. As the member is subjected to bending moment the member bends causing maximum bending strains on the extreme fibers of the beam section. On one extreme edge it is tensile and on the other it is compressive, assuming zero value strain at a particular locationwithin the depth of the section. This location is referred as neutral layer. The strain along the depth of the section varies uniformly. The location where the strain is zero, the magnitude of the stress is obviously zero. In the zone of the tensile strain, the corresponding tensile stresses can be mapped, obtained from the relevant stress strain curve. Similarly, in the compressive strain zone the corresponding compressive stresses can be mapped, obtained from the stress-strain curve.

To begin our calculations, an arbitrary depth of neutral axis (corresponding to zero strain) is assumed. Depending on the nature of moment, compressive/ tensile strains develop on either sides of the neutral layer. Across the depth of the section, corresponding the strains, the respective compressive/tensile stresses are plotted, as explained above, obtained from the relevant stress-strain diagrams. The total force on the section on either side of the neutral layer is determined. The force on one side is compressive while on the other side is tensile. If our initial assumption for neutral axis depth id exact, the magnitude of the total forces on either side shall be the same, which is quite unlikely. Using an iterative procedure, the neutral axis depth is kept on altered until the total compressive force is equal to the total tensile force. This is the true depth of neutral axis. The locations of the center of gravities of the total compressive and total tensile from the neutral layer are worked-out. The sum of the distances, gives the lever arm for the section. The product of the lesser of the compressive/tensile forces with the lever arm gives the moment of resistance of the section.

### B. COLUMN ELEMENTS

The axial loads with Bi-axial moment carrying capacity of the section

Here, the columns are assumed to be short rectangular columns (buckling effects ignored). A trial section for the column (B*D) is assumed. Say, for example the results pertaining to axial force (P) and the biaxial moments ($M_{zz}$ and $M_{yy}$) for the member are obtained from the structural analysis.

Let A, $Z_{zz}$ and $Z_{yy}$ are the area of cross section, modulus of section about the stronger axis and modulus of the section about the weaker axis respectively. The maximum and minimum compressive stresses develop in the section are given by $\sigma_{max}=P/A+M_{zz}/Z_{zz}+M_{yy}/Z_{yy}$ and $\sigma_{min}=P/A-M_{zz}/Z_{zz}-M_{yy}/Z_{yy}$ respectively. The value of stress obtained for |max shall not be more than the maximum permissible compressive stress of the concrete for that grade and fibers ratio. Similarly, if the minimum happens to be tensile, it shall not be more than that of the maximum permissible tensile stress of concrete for that grade and fibers ratio.

## V. UTILITY OF PRESENT STUDY

The cost of the building structure (abstract estimate) with stabilized structural configuration is worked out using principles of estimation. The abstract estimate for the same structure as designed by staad pro package using limit state method is also worked out. The percentage difference between the abstract estimates of two different methods are worked out to emphasis the need of the present study. Three such building structures have been analyzed and the design using to methods to draw generalized conclusions. However, we are presently in the process of optimization program using genetic algorithm to propose safe economical column and beam sections for a proposal building frame. Once the output of the member forces available frame staad pro package.

## VI. SPECIMEN CALCULATIONS

In all the three buildings whose plans were enclosed at the end of the thesis were designed using RCC limit state method and TSHFRC concrete to substantiate the utility of the present study. In the present chapter, the specimen calculations pertaining to one building only had been presented.

The calculations enlisted below are with respective building plan figure 7.3. The structural configuration for the building plan figure 7.3 has been modeled using staad pro package. The sizes of the column are taken as per the architectural drawing the beams have been oriented in such a way that they all come under walls. Extra beams are also being provided to ensure that all slabs are either transfer load in one-way mechanism or two-way mechanism. The width of the beams was 230mm and depths of the beams vary as per the span of the beams (approximately $1/10^{th}$ of the span of the beam). M20 grade concrete was used to model the both beams and columns of the structure. The slab thickness was assumed to be 100mm on which a floor finishing load of $1.5KN/m^2$ was assumed. The imposed load on all slabs taken as $2KN/m^2$. The staad model developed as above is analyzed for load combinations due to dead load and imposed load only. The structural design of beams and columns as obtained from staad pro has been recorded. The member in forces for all beams and columns has been recorded. The cost of steel is separately calculated for

beams members and column members. Having obtained the member forces in all beams and columns using staad pro package as described above. The most optimal sectional dimensions for all beams and columns using TSHFRC is worked out. By optimal it implies the cost of concrete inclusive of the steel fiber content shall be lowest. Having proposed the optimal section for all buildings elements the analysis using staad pro is re-run. The sectional properties of the members are revised to suit.

## VII. RESULTS AND DISCUSSIONS

The present work includes: Performing experiments to determine in the laboratory to determine,

1. Stress-strain characteristics in compression.

2. Stress-strain characteristics in tension for fiber reinforced concrete made using helix fiber as the reinforcing material. It has already been reported that the concrete conforming to M20, M25 and M30 has been designed as per IS code method. The percentage of mesh has been varied from 0.15%, 0.3% and 0.45% of the area of cross section of the concrete element. Discard number of cubes of 150*150*150mm and cylinders of 150mm diameter and 300mm long. This apart, special tensile brisket was also prepared. The revised member end forces obtained from staad pro. The process is repeated until a situation of stability is arrived. A stable configuration is one in which the analysis is due to re-run of staad pro don't alter the member forces. For a stable state of structural configuration, the total cost of TSHFRC.

TABLE I.
MATERIAL REQUIRED FOR 1 CUBIC METER OF CONCRETE

| Grade | Cement | Fine aggregate | Coarse aggregate | water |
|---|---|---|---|---|
| | $Kg/m^3$ | Kg | Kg | $Kg/m^3$ |
| M20 | 380 | 1019 | 868 | 190 |
| M25 | 400 | 996 | 848 | 200 |
| M30 | 445 | 966 | 823 | 200 |

TABLE II.
DETAILS OF MIX DESIGN

| Sample ID | Details of mix design |
|---|---|
| CC-1 | Cement concrete using normal river sand |
| CC-2 | Cement concrete using robo sand |
| TSHFRC-1 | Cement concrete with robo sand & 0.15% of TSHFRC |
| TSHFRC-2 | Cement concrete with robo sand & 0.3% of TSHFRC |
| TSHFRC-3 | Cement concrete with robo sand & 0.45% of TSHFRC |

TABLE III.
RESULTS OF M20 GRADE CONCRETE

| M20 | | | | |
|---|---|---|---|---|
| Designation | Average compressive strength (mpa) | | Average split tensile strength (mpa) | |
| | First crack | Ultimate strength | First crack | Ultimate strength |
| CC-1 | 25.60 | 30.60 | 2.30 | 2.35 |
| CC-2 | 27.50 | 29.40 | 2.30 | 2.45 |
| TSHFRC-1 | 27.50 | 32.50 | 2.85 | 4.30 |
| TSHFRC-2 | 27.80 | 35.65 | 2.60 | 6.50 |
| TSHFRC-3 | 28.50 | 37.0 | 2.90 | 7.17 |

TABLE IV.
RESULTS OF M25 GRADE CONCRETE

| M25 | | | | |
|---|---|---|---|---|
| Designation | Average compressive strength (mpa) | | Average split tensile strength (mpa) | |
| | First crack | Ultimate strength | First crack | Ultimate strength |
| CC-1 | 29.00 | 30.60 | 2.60 | 2.85 |
| CC-2 | 29.50 | 32.75 | 2.58 | 2.73 |
| TSHFRC-1 | 28.50 | 37.50 | 2.88 | 6.25 |
| TSHFRC-2 | 28.00 | 38.35 | 3.10 | 7.00 |
| TSHFRC-3 | 29.35 | 38.00 | 3.06 | 7.15 |

TABLE V.
RESULTS OF M30 GRADE CONCRETE

| M30 | | | | |
|---|---|---|---|---|
| Designation | Average compressive strength (mpa) | | Average split tensile strength (mpa) | |
| | First crack | Ultimate strength | First crack | Ultimate strength |
| CC-1 | 31.34 | 35.7 | 2.8 | 3.25 |
| CC-2 | 32.50 | 34.5 | 2.88 | 3.28 |
| TSHFRC-1 | 32.15 | 40.12 | 3.25 | 6.50 |
| TSHFRC-2 | 33.70 | 40.50 | 3.64 | 7.35 |
| TSHFRC-3 | 32.64 | 41.50 | 3.45 | 7.23 |

**7.1 STRESS STRAIN GRAPHS**



Figure 7.1(a). Tension curve of M20 grade with 0.15% TSHFRC
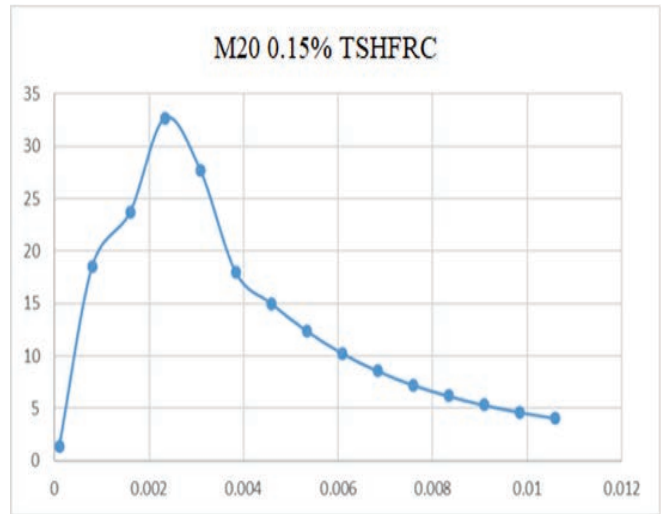


**Figure 7.1 (b) Compression curve of M20 grade with 0.15% TSHFRC**

**7.2 STRESS STRAIN DIAGRAM**
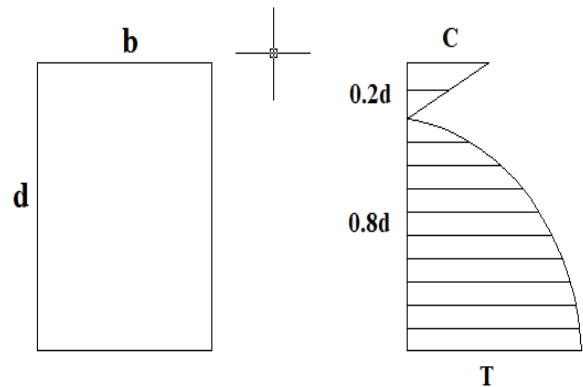


**Figure 7.2.  Stress Strain diagram**

**7.3 BUILDING PLANS AND STAAD MODEL**
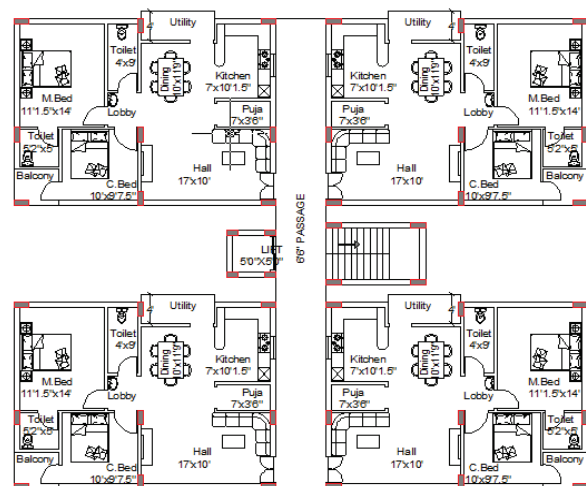


**Figure 7.3(a).  Building plan**
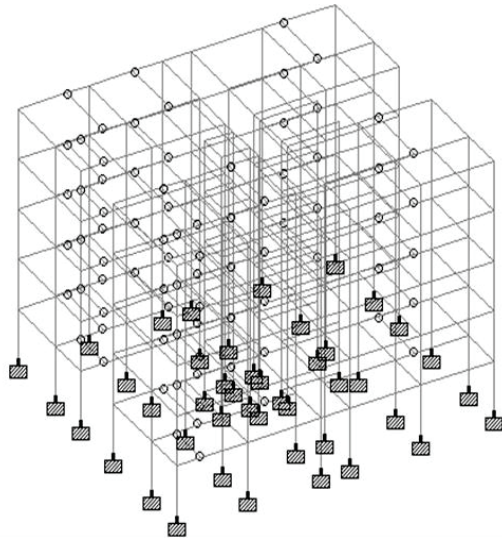
**Figure 7.3(b). Staad model**

TABLE VI
0.15% FIBERS M20 GRADE

| From graph | S.No | From graph | Avg tension | Y1 (d) | Avg*Y1 |
|---|---|---|---|---|---|
| Et=0.0025 | 0 | 0 | 0 | 0 | 0 |
| σt=3.25 | 1 | 0.5 | 0.25 | 0.7 | 0.19d |
| Ec=0.0025 *(0.2/0.8d) =0.000625d | 2 | 1 | 0.75 | 0.68 | 0.51d |
| From graph σc=15N/mm2 | 3 | 1.45 | 1.225 | 0.6 | 0.735d |
| C=b(1/2*0.2d*15 =1.5bd | 4 | 1.8 | 1.625 | 0.52 | 0.845d |
| Yc=h/3,h=0.2 =0.06666666667 | 5 | 2.2 | 2 | 0.44 | 0.88d |
|  | 6 | 2.45 | 2.325 | 0.3 | 0.837d |
|  | 7 | 2.75 | 2.6 | 0.2 | 0.728d |
|  | 8 | 3 | 2.875 | 0.2 | 0.575 |
|  | 9 | 3.2 | 3.1 | 0.1 | 0.372 |
|  | 10 | 3.25 | 3.225 | 0.04 | 0.129 |
|  |  |  | T= 19.97*0.08d |  | Total=5.801*0.08 |
|  |  |  | =1.598bd |  | =0.46bd |
| Yt=total/t |  |  |  |  |  |
| 0.287859825 |  |  |  |  |  |
| Lever arm=d-(0.290d+0.0667d) |  |  |  |  |  |
| 0.6433d |  |  |  |  |  |
| Mu=t*lever arm |  |  |  |  |  |
| 1.02799bd² |  |  |  |  |  |
| Mu=c*lever arm |  |  |  |  |  |
| 0.96495bd² |  |  |  |  |  |

TABLE VII (A)
BEAM CALCULATIONS

| 1 | 2 | 3 | 4 | 5 | 6 | 7 | 8 | 9 |
|---|---|---|---|---|---|---|---|---|
| 9 | 200 | 400 | 3350 | 35.07 | 45.9 | 59.5 | 0.7 | 2.7 |
| 118 | 200 | 500 | 1620 | 62.36 | 71.7 | 56.9 | 0.5 | 2.7 |
| 10 | 200 | 500 | 3050 | 62.32 | 71.7 | 69 | 0.6 | 2.7 |
| 133 | 200 | 500 | 2040 | 58.52 | 71.7 | 36.6 | 0.3 | 2.7 |
| 566 | 200 | 300 | 2010 | 23.53 | 25.8 | 13.1 | 0.2 | 2.7 |

1-Beam number from staad

2-Breadth in mm

3-Depth in mm

4-Length in mm

5-Moment obtained from staad

6-Moment capacity of TSH fibers

7-Flexural shear

8-Shear stress

9-Permissible tensile shear stress

TABLE VII (B)
BEAM COST CALCULATIONS

| 10 | 11 | 12 | 13 | 14 | 15 | 16 | 17 | 18 |
|---|---|---|---|---|---|---|---|---|
| 9 | 0.3 | M20 | Safe | 0.26 | 6.31 | 938 | 1262 | 2200 |
| 118 | 0.3 | M20 | Safe | 0.16 | 3.81 | 567 | 763 | 1330 |
| 10 | 0.3 | M20 | Safe | 0.30 | 7.18 | 1067 | 1436 | 2504 |
| 133 | 0.3 | M20 | Safe | 0.20 | 4.80 | 714 | 960 | 1674 |
| 566 | 0.3 | M20 | Safe | 0.12 | 2.84 | 422 | 568 | 990 |

10-Beam number from staad

11-Dosage of TSH fibers

12-Grade of concrete

13-Remarks

14-Volume of concrete in cubic meters

15-Quantity of TSH fibers in kgs

16-Cost of concrete in Rs

17-Cost of TSH fibers in Rs

18-Total cost in Rs

TABLE VIII (A)
COLUMN CALCULATIONS

| 1 | 2 | 3 | 4 | 5 | 6 | 7 | 8 | 9 |
|---|---|---|---|---|---|---|---|---|
| 11 | 200 | 400 | 3050 | 8000 | 722 | 17 | 2.85 | 10*10⁹ |
| 14 | 200 | 400 | 3050 | 8000 | 609 | 34 | 6.27 | 10*10⁹ |
| 17 | 200 | 400 | 3050 | 8000 | 447 | 40 | 7.39 | 10*10⁹ |
| 20 | 200 | 400 | 3050 | 8000 | 282 | 40 | 7.49 | 10*10⁹ |
| 23 | 200 | 400 | 3050 | 8000 | 115 | 47 | 8.27 | 10*10⁹ |

1-Column number from staad

2-Breadth in mm

3-Depth in mm

4-Height in mm

5-Area in mm

6-Axial load Pu in KN

7-Moment in z-direction KN/m$^2$

8- Moment in y-direction KN/m$^2$

9-Moment of inertia in z- direction

TABLE VIII (B)
COLUMN COST CALCULATIONS

| 10 | 11 | 12 | 13 | 14 | 15 | 16 |
|----|----|----|----|----|----|----|
| 11 | 266666666.7 | 13.28 | 15 | M20 | 0.15 | Safe |
| 14 | 266666666.7 | 16.47 | 18 | M20 | 0.3 | Safe |
| 17 | 266666666.7 | 15.9 | 17 | M20 | 0.45 | Safe |
| 20 | 266666666.7 | 13.8 | 15 | M20 | 0.15 | Safe |
| 23 | 266666666.7 | 13.42 | 15 | M20 | 0.15 | Safe |

10-Column number from staad

11- Moment of inertia in y- direction

12-Stress=$(P/A+M_{zz}/I_{zz}*D/2+M_{yy}/I_{yy}*B/2)$

13-Permissible maximum compressive stress

14-Grade of concrete

15-Doasage of TSH fibers

16-Remarks

TABLE VIII. (C)
CONTINUATION OF COLUMN COST CALCULATIONS

| 17 | 18 | 19 | 20 | 21 | 22 |
|----|----|----|----|----|----|
| 11 | 0.244 | 2.8731 | 854 | 574.62 | 1428.62 |
| 14 | 0.244 | 5.7462 | 854 | 1149.24 | 2003.24 |
| 17 | 0.244 | 8.6193 | 854 | 1723.86 | 2577.86 |
| 20 | 0.244 | 2.8731 | 854 | 574.62 | 1428.62 |
| 23 | 0.244 | 2.8731 | 854 | 574.62 | 1428.62 |

17-Column numbers from staad.

18-Volume of concrete in cubic meters

19-Quantity of TSH fibers in Kgs

20-Cost of concrete in Rs

21-Cost of TSH fibers in Rs

22-Total cost in Rs

TABLE IX
COST COMPARISON

| RCC building | | | | Helix fiber reinforced concrete building | | | |
|---|---|---|---|---|---|---|---|
| Building-1 | | | | Building-1 | | | |
| (Rs) | beam | Colu mn | T | (Rs) | beam | colu mn | T |
| Steel | 2231 60 | 12222 20 | 34538 0 | Steel | 1323 10 | 3830 0 | 1706 10 |
| Concr ete | 8050 0 | 43050 | 12355 0 | Concr ete | 1106 54 | 4563 9 | 1562 93 |
| total | 468930 | | | Total | 326903 | | |
| Building-2 | | | | Building-2 | | | |
| (Rs) | beam | Colu mn | T | (Rs) | beam | colu mn | T |
| Steel | 3345 30 | 14175 0 | 47628 0 | Steel | 2259 00 | 3821 2 | 2641 12 |
| Concr ete | 1445 50 | 43400 | 18795 0 | Concr ete | 1668 22 | 5180 7 | 2186 29 |
| total | 664230 | | | Total | 482741 | | |
| Building-3 | | | | Building-3 | | | |
| (Rs) | beam | Colu mn | T | (Rs) | beam | colu mn | T |
| Steel | 9668 40 | 59290 | 10261 30 | Steel | 4627 13 | 2556 58 | 7183 71 |
| Concr ete | 4452 00 | 29050 | 47425 0 | Concr ete | 3578 53 | 1733 01 | 5311 54 |
| total | 1500380 | | | Total | 1249525 | | |

## VIII. CONCLUSIONS

1. The inclusion of TSH fibers have considerably increased the compressive strength of concrete for all grades of concrete M20, M25 and M30 as can be seen from table no III to V

2. Similarly, the inclusion of TSH fibers have also substantially increased the tensile strength of concrete as can be seen from table no III to V

3. Even though not quantified, the addition TSH fibers have substantially increased the ductility of all grades of concrete.

4. The utility of the present study is amply demonstrated with the help of case studies on three number of RCC buildings. The results obtained are used for drawing following conclusions.

- The quantity of concrete consumed in making columns has increased by 5.6%, when TSH fiber concrete is used.

- The quantity of concrete consumed in making beams has also increased by 27.25%, when TSH fiber concrete is used.

- But the total amount of steel consumed in columns is reduced by 68.6%, when TSH fiber concrete is used.

- Similarly, the total amount of steel consumed in beams is reduced by 40.71%, when TSH fiber concrete is used.

- The overall cost of building is reduced by 30%, when TSH fiber concrete is used.

## REFERENCES

[1] Naaman, A.E., *"Engineered Steel Fibers with Optimal Properties for Reinforcement of Cement Composites,"* Journal of Advanced Concrete Technology, Japan Concrete Institute, Vol. 1, No. 3, November 2003, pp. 241 252.

[2] Dong-Joo Kim et al. *"High performance fiber reinforced cement composites with innovative slip hardening twisted steel fibers",* IJCSM vol.3, No 119-126, December 2009.

[3] Flavio de Andrade Silva et al, *"Bond mechanism in sisal fiber reinforced composite",* proceeding of the 11th international conference on non-conventional materials and technologies. September 2009, bath, UK.

[4] Parra-Montesinos, G., *"High Performance Fiber Reinforced Cement Composites: an Alternative for Seismic Design of Structures,"* ACI Structural Journal, Vol. 102, No. 5, Sept.-Oct. 2005, pp. 668-675.

[5] Min-yuan cheng et al *"Evaluation of steel fiber reinforcement Punching shear resistance in slab-column connections –part 1: monotonically increased load",* ACI structural journal 107(1), 2010.

[6] Vikrant S. Variegate et al *"Investigation of steel fiber reinforced concrete on compressive and tensile strength",* IJSTR Vol.1, issue 3, May 2012.

[7] Naaman, A.E., and Reinhardt, H.W., Co-Editors, *"High Performance Fiber Reinforced Cement Composites:* HPFRCC 2, RILEM, No. 31, E. & FN Spon, London, 1996, 505 pages.

[8] Balaguru, P., and Shah, S.P., *"Fiber Reinforced Cement Composites,"* McGraw Hill, New York, 1992.

[9] Bentur, A., and Mindess, S., *"Fiber Reinforced Cementitious Composites,"* Elsevier Applied Science, London, UK, 1990.

# A Hybrid Clustering Model to Evaluate Quality of Software Services on Cloud Environment

Dhanamma Jagli[1], N. Subhash Chandra[2], Seema Purohit[3]
[1]Research Scholar, JNTU /Hyderabad, India.
Email: dsjagli.vesit@gmail.com.
[2]Professor, CVR College of Engineering/ CSE Department, Hyderabad, India.
Email: subhashchandra.n.cse@gmail.com
[3]Professor, Kirti Engineering College/ CSE Department, University of Mumbai, India.
Email: supurohit@gmail.com.

*Abstract:* **Cloud computing is emerging as an innovative paradigm in the field of Internet-based services in many software and hardware industries. The benefits that it provides in terms of cost, flexibility, efficient technology and business ability represent a huge competitive advantage for an organization. This is proven to be an essential requirement for extending several existing applications. In order to utilize the entire rewards of the SaaS model proficiently and successfully, there should be a suitable quality model to evaluate the SaaS quality. In fact, service-providers must evaluate their services against needs of service-user to increase their services. The existing SaaS quality evaluation models lack focus on all aspects of quality and services together.**

**On the other hand, each cloud service user is unique that leads to a very huge variation in the requirements of the software services. Therefore, this paper presents a hybrid model to help service users to opt a better SaaS product to satisfy their environment and needs. The proposed Hybrid model is implemented by using a hybrid clustering algorithm to construct clusters of SaaS products.**

*Index Terms:* **Software as a Service (SaaS), K-Means Clustering, DBSCAN Clustering, Hybrid Clustering**

## I. INTRODUCTION

Cloud computing is the newest technology of computing as well as to provide numerous scalable resources dynamically and to virtualizes those resources as a service over the Internet. Three main cloud offering models are available in the cloud computing environment, they are Platform as a service (PaaS), Infrastructure as a Service (IaaS ) , and Software as a Service (SaaS ) . The SaaS model provides several applications for costumers without installing any application locally. So, one can use any virtual servers available on the web to make a cloud. SaaS is a model of delivering into centrally hosted applications of the Internet. SaaS applications run on a SaaS supplier's server. The advantage of SaaS is that the software or application can be accessed through the internet without installing them at the local system. The cloud service providers manage access to the application, including security, availability, and performance. SaaS business applications are regularly accessed by service users by means of a thin client via a web browser[1]. The private and public organizations and individuals are adopting SaaS products to utilize its profit. But, selection of right SaaS product from pool of products is a major problem for SaaS customer. In this context, a hybrid clustering model has been proposed to improve the quality of evaluation of SaaS products. The paper is organized as follows: Section II presents the literature review carried out towards SaaS product selection and identifies the gaps embedded in the existing models. Section III explains proposed hybrid model, Section IV discusses experimental results and compares with the results of existing models and Section V presents conclusion and future work.

## II. LITERATURE REVIEW

The work on SaaS evaluation is relatively very less till2005; later, analytical works have improved towards SaaS analysis. Chen Yiming, et.al, proposed a model by choosing the most effective SaaS vendor supported service principles instead of selecting SaaS Product[2]. Pang XiongPilar cyst, Li Dong, projected an advanced quality model that measures the safety, software quality of the SaaS and quality of service from the perspective of a service-provider[3,4,5.] Jae Yoo, et.al, proposed a top-quality methodology that may facilitate to look at the quality side of SaaS, supported the SaaS key features derived from primary SaaS options[4, 6]. They valued and assessed their proposed quality model for evaluating SaaS quality. However, they have not covered all the key features of SaaS like multi-tenancy etc. Manish Godse, Shrikant Maulik , proposed a replacement model based on Analytic Hierarchy Process (AHP ) approaches / approached for ranking the SaaS features like Functionality , Vendor name , Design , Usability , and Cost[7]. However, the proper ranking of SaaS products is not possible, as each feature plays a vital role in the SaaS. Authors Qian Tao etc. proposed a technique for all cloud services based on non-functional QoS attributes like reputation, reliability, security, time, price and availability[8,9,10]. They exploited the results by Partitioning around Medians (PAM) rule for all kinds of cloud services. However, its own limitations will effect the optimum solution[9]. The review of literature summarizes that, the researchers contributed their innovations and supported key options and quality attributes to evaluate SaaS products. But, all researchers considered vendor perspective attributes only. This paper addresses the gaps involved in evaluation of SaaS without considering user perspective attributes.

### III. Proposed Hybrid Clustering Model

To overcome the research gaps identified from literature review, a Hybrid clustering model is proposed and implemented on real time data sets with user's perspective attributes i.e.
•Product Name: the name with the SaaS product.
•Rating: Rating is a numeric value given by SaaS users on the scale of 1 to 10, 1 being the lowest and 10 highest.
•No. of Reviews: Reviews are a numeric attribute, which give no. of comments from SaaS users of that product.
•Category of SaaS: This is a categorical attribute that describes the category of SaaS.
This SaaS data set has been collected from Amazon public cloud and a few other sources. The proposed hybrid model consists of two phases. In the first phase K- means clustering algorithm applied to SaaS products data set. In the second phase, the DBSCAN algorithm applied to first phase results. The data flow in Hybrid Clustering model is as shown in Figure1.
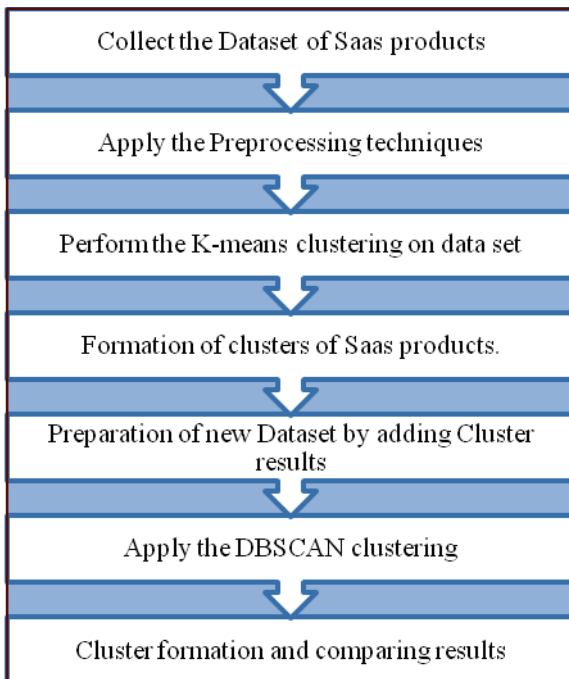


Figure 1. The Work flow of the Proposed Model

*K-means Clustering*

K-means clustering is "to classify objects of multiple groups such that, objects in the same cluster are as similar as possible, whereas objects of different clusters are as dissimilar as possible "[11]. In k-means clustering, every cluster is represented by means of its center or centroid that corresponds to the mean of data objects assigned to each cluster. K-means clustering model constructs four clusters of SaaS data set ratings and number of reviews. Different clusters are shown in Figure 2 and indicated in different colors.
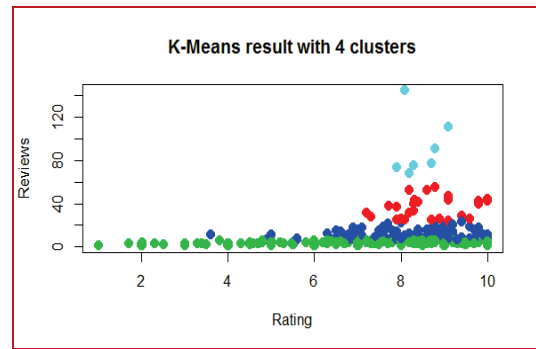


Figure 2.  K-means Cluster plot

Cluster 1 represents SaaS products of the highest rating, and highest number of reviews. • Cluster 2 represents SaaS products of the highest rating, and average number of reviews. • Cluster 3 represents SaaS products of average rating and average reviews. • Cluster 4 represents SaaS products that are below average rating, with a below average number of reviews.

*Limitations of K-Means:*

The limitations of K-means clustering algorithm is as follows: It can be applied only when the mean of a cluster is defined. User needs to specify k. The results obtained are sensitive to the initial random selection of cluster- centers. That means clustering is highly sensitive to outliers. K- means is not suitable for discovering clusters with any convex shapes or clusters of very different size. Hence, the Density Based Clustering Algorithm is implemented over K- means clusters data set, which does not require the user to specify the number of clusters to be generated. It can find any shape of clusters that can identify outliers.

*Density Based Clustering (DBSCAN)*

DBSCAN is a Density-Based Spatial Clustering and Application with Noise. It clusters together points that are close to each other based on spatial distance and minimum number of points[12,13]. This cluster model identifies clusters of any shape in a data set and handles noise and outliers within the data set. The steps involved in DBSCAN clustering algorithm are as shown in the Figure 3

For each data object or point Xi, compute the distance between Xi and the other points.

Find all neighbor data objects within distance eps of the starting data object (Xi).

Each data object, with a neighbor count greater than or equal to Minpts, is marked as core point or visited.

For each core point, If it's not already assigned to a cluster, create a new cluster.

Iterate through the remaining unvisited data objects in the data set.

Figure 3. DBSCAN Algorithm

The DBSCAN algorithm requires 2 parameters[14,15] i.e.
Eps: the minimum spatial distance between two points. If the distance between two points is less than or equal to this value (eps), then these points are considered neighbors.
MinPoints: the minimum number of points to form a cluster.
In conventional DBSCAN Algorithm, Eps and MinPts values were chosen on trial and error basis. To enhance the output of DBSCAN algorithm, the optimal Eps value has been generated by KNNdist in R Studio as 0.15 for a sample dataset, shown in Figure 4.



```
> dbscan::kNNdistplot(saassv, k = 5)
> abline(h = 0.15, lty = 2)
```
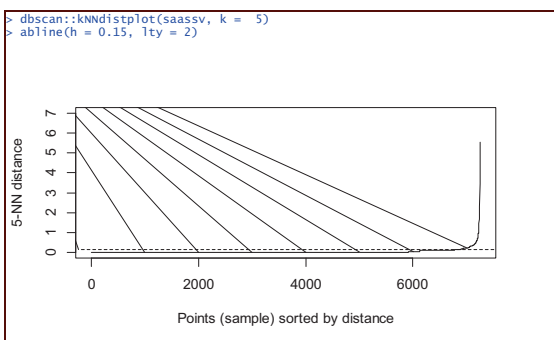
Figure 4. Optimal Eps value for DBSCAN Clustering

DBSCAN algorithm constructed seven different clusters of convex shape as shown in the Figure 5 and represented by different colors. The number of clusters varies according to datasets and it also impacts on no. of noise points. Taking this as a consideration, a cluster number as seven to reduce no. of noise points.
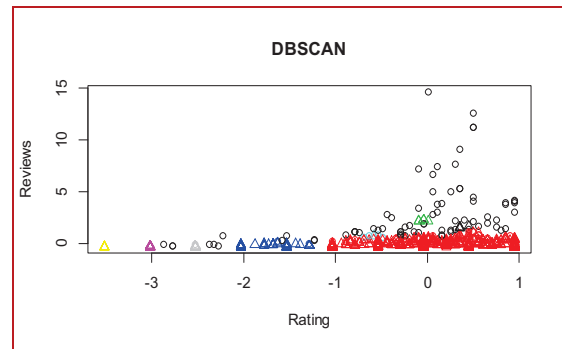


Figure 5. DBSCAN Cluster Plot

*Limitations of DBSCAN:*
DBSCAN fails to discover the clusters of varying densities and overlapping regions. It is not completely deterministic, so that, border points or data objects that are reachable from more than one cluster can be part of either cluster, depending on the order for data processing.

*Hybrid K-means -DBSCAN (KD) Clustering*
Each of the K-means and DBSCAN algorithms have their own limitations and benefits. To make use of the advantages of both clustering algorithms, hybrid clustering algorithm has been proposed to overcome the limitations of both clustering algorithms. The steps involved in the proposed Hybrid algorithm are as shown in Figure 6.
.



Compute k-means clustering

Create k-means cluster output as k-cluster dataset.

Compute the DBSCAN on k-cluster dataset.

Construct the clusters
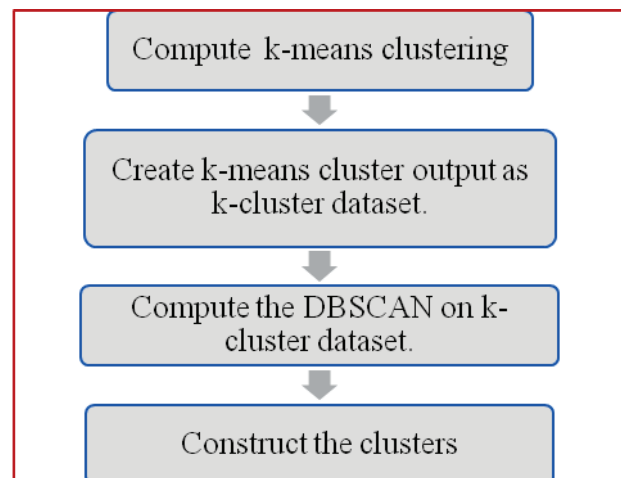
Figure 6. Proposed Hybrid KD Clustering Algorithm

### IV. RESULTS AND DISCUSSION

The Hybrid clustering algorithm has constructed 40 clusters and 277 noise points with Eps = 0.15 and minPts = 5 for 1460 objects. The clusters are shown in Figure 7 with different colors.
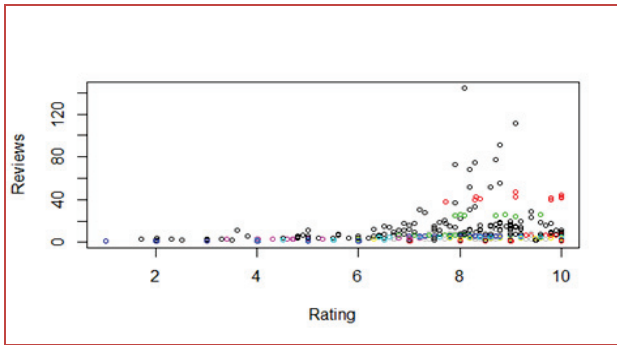
Figure 7.  Hybrid KD Cluster Plots

Silhouette value is considered as a performance measure to compare the results of K-means, DBSCAN and Hybrid Algorithms[16,17]. It indicates that, the similarity of an object is in its own cluster (cohesion) compared to alternative clusters (separation). The silhouette ranges from −1 to +1, the higher value indicates that the object is well suited to its own cluster and poorly matched to neighboring clusters. As per results, the proposed Hybrid clustering algorithm has produced comparatively better results than k-means and DBSCAN as shown in the Figure 8.
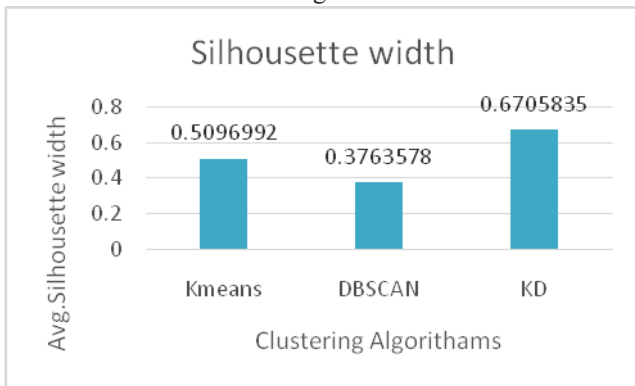

Figure 8.  Results Comparison table

### V. CONCLUSIONS

In summary, the proposed Hybrid model is one of the cloud offerings, Software as a Service (SaaS). This model provides a clear overview of different parameters of choices of SaaS consumers that can help to evaluate before using SaaS products. This proposed hybrid cluster model is considered attributes of software service from a user's perspective service that is feedback from service users in terms of ratings and reviews. This model provides SaaS product cluster groups so that service users can select any SaaS product of the group accordingly. Moreover, this model is implemented on live data set and produced better results compared to existing models.

### REFERENCES

[1] Benlian A, Koufaris M, Hess T. Service Quality in Software-as-a-Service: Developing the SaaS-Qual Measure and Examining Its Role in Usage Continuance. J Manag Inf Syst. 2012;28(3):85-126. doi:10.2753/MIS0742-1222280303.

[2] Goode S, Lin C, Tsai JC, Jiang JJ. Rethinking the role of security in client satisfaction with Software-as-a-Service (SaaS) providers. Decis Support Syst. 2015;70:73-85. doi:10.1016/j.dss.2014.12.005.

[3] Bott R, Zinn D, Hart Q, et al. The Analytic Hierarchy Process. In: Antonopoulos N, Gillam L, eds. Igarss 2014. Vol 5. Informatik im Fokus. IEEE; 2014:1-5. doi:10.1007/s13398-014-0173-7.2.

[4] Bott R, Huynh V-N, Pham SB, et al. An End-To-End QoS Mapping Approach for Cloud Service Selection. Antonopoulos N, Gillam L, eds. IEEE Ninth World Congr Serv. 2013;5(1):341-348. doi:10.1007/s13398-014-0173-7.2.

[5] Wen PX, Dong L. Quality Model for Evaluating SaaS Service. In: 2013 Fourth International Conference on Emerging Intelligent Data and Web Technologies. IEEE; 2013:83-87. doi:10.1109/EIDWT.2013.19.

[6] Lee JYJW. A Quality Model for Evaluating Software-as-a-Service in Cloud Computing. In: 2009 Seventh AC IS International Conference on Software Engineering Research, Management and Applications. IEEE; 2009:261-266.doi:10.1109/SERA.2009.43.

[7] Godse M, Mulik S. An approach for selecting Software-as-a-Service (SaaS) product. In: CLOUD 2009 - 2009 IEEE International Conference on Cloud Computing. ; 2009:155-158. doi:10.1109/CLOUD.2009.74.

[8] Tao Q, Chang H, Yi Y, Gu C. A trustworthy management approach for cloud services QoS data. In: Machine Learning and Cybernetics (ICMLC), 2010 International Conference on. Vol 4. ; 2010:1626-1631.

[9] He Q, Han J, Yang Y, Grundy J, Jin H. QoS-driven service selection for multi-tenant SaaS. Proc - 2012 IEEE 5th Int Conf Cloud Comput CLOUD 2012. 2012:566-573. doi:10.1109/CLOUD.2012.125.

[10] Liu F, Guo W, Zhao ZQ, Chou W. SaaS integration for software cloud. Proc - 2010 IEEE 3rd Int Conf Cloud Comput CLOUD 2010. 2010:402-409. doi:10.1109/CLOUD.2010.67.

[11] Jung HW, Kim SG, Chung CS. Measuring software product quality: A survey of ISO/IEC 9126. IEEE Softw. 2004;21(5):88-92. doi:10.1109/MS.2004.1331309.

[12] Desharnais J-M. Analysis of ISO/IEC 9126 and 25010. 2009.

[13] Pedram H, Moghaddam DK, Asheghi Z. Applying the ISO 9126 model to the evaluation of an e-learning system in Iran. Iran J Inf Process Manag. 2012;27(2):495-517.

[14] Parasuraman A, Berry LL, Zeithaml VA. Refinement and Reassessment of the SERVQUAL Scale. J Retail. 1991;67(4):420. doi:10.1111/j.1438-8677.2010.00335.x.

[15] Parasuraman a, Zeithaml V a, Berry LL. SERQUAL: A Multiple-Item Scale for Measuring Consumer Perceptions of Service Quality. Vol 64.; 1988:28. doi:10.1016/S0148-2963(99)00084-3.

[16] Dhanamma Jagli, Seema Purohit S, Chandra NSS, et al. SAASQUAL : A Quality Model For Evaluating SaaS on The Cloud. Adv Intell Syst Comput. 2015;654:1-6. doi:10.1007/978-981-10-6620-7_41.

[17] Dhanamma Jagli M, Purohit S, Chandra NS, et al. SaaS CloudQual: A Quality Model for Evaluating Software as a Service on the Cloud Computing Environment. In: ICICSE2016. Springer; 2016:2-5. doi:10.1007/978-981-10-3818-1.

# Fuzzy Analytical Hierarchy Process Based Optimal Work Station node prediction for Large Networks

M. Jaiganesh[1] and R.K. Selvakumar[2]
[1]Asso. Professor, CVR College of Engineering/CSE Department, Hyderabad, India.
Email: jaidevlingam@gmail.com
[2]Professor, CVR College of Engineering/CSE Department, Hyderabad, India.
Email: rkselvakumar@gmail.com

*Abstract:* **Cloud Computing is an emerging computing technology and delivering lots of services to the end users. In order to ensure the quality of cloud service, the service request ought to be ready to dynamically predict the optimal work station node. The research proposes an optimal work station node prediction in Hierarchical large networks using Fuzzy Analytical Hierarchical Process (AHP). This work is considered as a hierarchical model to explore each level and their sublevel based on the resource availability. The prediction of optimal workstation is dogged on the resource factors: Energy, Memory and Cost. Each work station periodically determines these factors with sub level work stations. The advantage of the proposed work is to predict the best workstation to serve an efficient cloud service for large networks. The proposed model simulated by using MATLAB tool, experiments has been conducted to prove the appropriateness of this novel approach.**

*Index Terms:* **Cloud computing, Quality of Service, Service analysis, Fuzzy Analytic Hierarchy Process (FAHP).**

## I. INTRODUCTION

Several computing paradigms have promised to deliver the utility computing vision and these include cluster computing, Grid computing, and more recently Cloud computing [1]. The utility computing capabilities are deliberated as software and hardware components in the large repository. Cloud computing is a paradigm for utility computing. It is a new era in making varieties of information carried through internet connections by using connective devices [8]. It offers its services in pay and use method for its clients. The Data center is a sophisticated high definition server, which runs applications virtually in cloud computing. It moves the client application, services and data to a centralized large pool called Big Data centers [7]. It enhances flexibility and enables data centers to be dynamic in nature. To provide better cloud service quality, it is essential to dynamically identify information processing of the particular service request. First, we need to supervise the service request data and we can identify whether it happens in a large network service request or not. Second, if the large network service request is produced, the size of the data and the stipulate for the resources and corresponding work station need to be predicted [13]. Existing cloud service prediction approaches were typically focused on cloud computing resource based quantities provided by the

service. In cloud computing scenario, specifically for large networks, the service is not only satisfied with resources but also considered with other constraints. The required work station is far away from the service request. To overcome this issue, this novel work applies Fuzzy Analytical Hierarchical Process (AHP) into a Hierarchical large network mode [14]. One of the most popular analytical techniques for complex decision-making is the Fuzzy Analytic Hierarchy Process (FAHP). Fuzzy AHP was developed by Laarhoven and Pedrycz [10] in the early 1983s. Fuzzy coupled with AHP as a decision method to ambiguity in levying the importance of feature and the performance ratings of alternative with esteem to features. Traditional multiple decision methods do not successfully feel problems with that vague data's.

The fuzzy AHP approach is a logical method for the choice and validation problems that incorporates the idea of fuzzy sets theory [11] and the hierarchical structure analysis. First step, here is rating issue describes many criteria. This criterion is also isolated into sub category. The outcome of fuzzy AHP is a main concern for ranking the overall choices, these alternatives lastly useful decision making to select the best method. The judgment needs to work the vagueness while evaluating the assessments of the choices. For judging these vagueness into believe ration fuzzy numbers are used as a substitute of crisp numbers [12].

FAHP [4, 10] is an extension of AHP. The assessment of different criteria requires the use of fuzzy membership function value. AHP is based on the use of crisp numbers [14]. A fuzzy member function [10] is related to a special fuzzy set $F = \{(x, \mu_f(x), x \in R\}$, where x takes its values on the real line, R: $-\infty \leq x \leq \infty$ and $\mu_f(x)$ is a continuous mapping from R to the closed interval [0, 1].

The contribution of paper

- This novel work proposes a cloud service forecast approach based on Fuzzy AHP method, which is used to predict the optimal workstation node in large networks.

- The approach efficiently constructs a hierarchical model to serve better cloud service paradigm for large networks.

## II. SYSTEM MODEL

Figure 1 illustrates the system architecture. In this model, there are fourteen work stations (depicted by a circle). It is a source to many destination scenarios. The environment is considered as large networks mapped into multi-cloud services. Each node represented as a Work Station (WS). Each edge is assigned as a next level work stations. The aim of this proposed architecture is to find optimal WS supporting for the cloud service request. Each work station maintains resource parameters such as Energy, Memory and cost. The method is starting from source WS (WS1) with the specified service request it travels to reach the optimal WS (WS13-Orange coloured arrows) to fully satisfy the service request. In that Figure 1, WS1 is assigned as the root node for the hierarchical architecture. The root WS is periodically updated with sub level Work Stations for their resource availability.
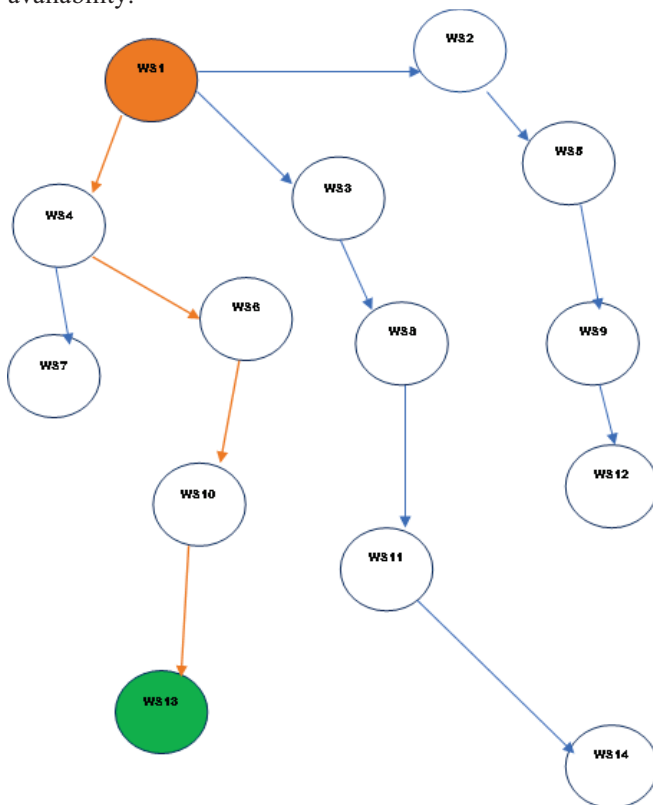


Figure1. Hierarchical Model

## III. PREDICTION OF OPTIMAL WORK STATION USING FUZZY AHP(FAHP)

### A. Step 1: Fuzzification

In this first step, the linguistic terms, criteria their quantifications are tabulated in Table3. Here, it is assumed more than one alternative and criteria. Because the limited number of factors are influencing for finding the best optimal path [5, 6]. Here, 3 –point scale is used to convert the fuzzy linguistic terms into crisp numbers. Table 2 shows the crisp data for corresponding fuzzy linguistic terms and matrix is known as Decision Making Matrix (DMM).

## Fuzzy System:

NumInputs=3NumOutputs=1NumRules=29
AndMethod='min'OrMethod='max'
ImpMethod='min'AggMethod='max'

DefuzzMethod='centroid'

Fuzzy trapezoid view of inputs Energy membership functions is defined in Equations (1)-(3).

**[Input1]='Energy'Range=[0 1]NumMFs=3**

MF1='Low':'trapmf', is defined in Equation (1)

$$\mu_{Low} = \begin{cases} 1 & if \ 0 \leq x \leq 0.201 \\ \frac{0.39921-x}{0.19821} & if \ 0.201 \leq x \leq 0.39921 \\ 0 & Otherwise \end{cases} \quad (1)$$

MF2='Medium':'trapmf',is defined in Equation (2)

$$\mu_{Medium} = \begin{cases} 0 & if \ 0 \leq x \leq 0.198 \\ \frac{x-0.198}{0.203} & if \ 0.198 \leq x \leq 0.401 \\ 1 & if \ 0.401 \leq x \leq 0.6 \\ \frac{0.8-x}{0.2} & if \ 0.6 \leq x \leq 0.8 \\ 0 & Otherwise \end{cases} \quad (2)$$

MF3='High':'trapmf',is defined in Equation (3)

$$\mu_{High} = \begin{cases} 0 & if \ 0 \leq x \leq 0.6 \\ \frac{0.8-x}{0.2} & if \ 0.6 \leq x \leq 0.8 \\ 1 & Otherwise \end{cases} \quad (3)$$

Fuzzy trapezoid view of inputs MemConsumption membership functions is defined in Equations (4)-(6).

**[Input2]='MemConsumption'Range=[0 1] NumMFs=3**

MF1='Small':'trapmf',is defined in Equation (4)

$$\mu_{Small} = \begin{cases} 1 & if \ 0 \leq x \leq 0.199 \\ \frac{0.4967-x}{0.2977} & if \ 0.199 \leq x \leq 0.4967 \\ 0 & Otherwise \end{cases} \quad (4)$$

MF2='Medium':'trapmf',is defined in Equation (5)

$$\mu_{Medium} = \begin{cases} 0 & if \ 0 \leq x \leq 0.1468 \\ \frac{x-0.1468}{0.3132} & if \ 0.1468 \leq x \leq 0.46 \\ 1 & if \ 0.46 \leq x \leq 0.54 \\ \frac{0.85-x}{0.31} & if \ 0.54 \leq x \leq 0.85 \\ 0 & Otherwise \end{cases} \quad (5)$$

MF3='Large':'trapmf',is defined in Equation (6)

$$\mu_{Large} = \begin{cases} 0 & if\ 0 \le x \le 0.4989 \\ \frac{0.803-x}{0.3041} & if\ 0.4989 \le x \le 0.803 \\ 1 & Otherwise \end{cases} \quad (6)$$

Fuzzy trapezoid view of inputsCost membership functions is defined in Equations (7)-(9).

**[Input3]='Cost'Range=[0 1]NumMFs=3**
MF1='Minimum':'trapmf',is defined in Equation (7)

$$\mu_{Minimum} = \begin{cases} 1 & if\ 0 \le x \le 0.303 \\ \frac{0.3505-x}{0.0475} & if\ 0.303 \le x \le 0.3505 \\ 0 & Otherwise \end{cases} \quad (7)$$

MF2='Moderate':'trapmf',is defined in Equation (8)

$$\mu_{Moderate} = \begin{cases} 0 & if\ 0 \le x \le 0.151 \\ \frac{x-0.151}{0.25} & if\ 0.151 \le x \le 0.401 \\ 1 & if\ 0.401 \le x \le 0.601 \\ \frac{0.8532-x}{0.2522} & if\ 0.601 \le x \le 0.8532 \\ 0 & Otherwise \end{cases} \quad (8)$$

MF3='Maximum':'trapmf',is defined in Equation (9)

$$\mu_{Maximum} = \begin{cases} 0 & if\ 0 \le x \le 0.652 \\ \frac{0.7037-x}{0.0517} & if\ 0.652 \le x \le 0.7037 \\ 1 & Otherwise \end{cases} \quad (9)$$

Fuzzy trapezoid view of output 'OptimalNeighbourNode'membership functions is defined in Equations (10)-(12).

**[Output1]='OptimalNeighbourNode'Range=[0 1]NumMFs=3**

MF1='Poor':'trapmf',is defined in Equation (10)

$$\mu_{Poor} = \begin{cases} 1 & if\ 0 \le x \le 0.206 \\ \frac{0.3028-x}{0.0968} & if\ 0.206 \le x \le 0.3028 \\ 0 & Otherwise \end{cases} \quad (10)$$

MF2='Fair':'trapmf',is defined in Equation (11)

$$\mu_{Fair} = \begin{cases} 0 & if\ 0 \le x \le 0.14 \\ \frac{x-0.14}{0.16} & if\ 0.14 \le x \le 0.3 \\ 1 & if\ 0.3 \le x \le 0.501 \\ \frac{0.6582-x}{0.1572} & if\ 0.501 \le x \le 0.6582 \\ 0 & Otherwise \end{cases} \quad (11)$$

MF3='Good':'trapmf',is defined in Equation (12)

$$\mu_{Good} = \begin{cases} 0 & if\ 0 \le x \le 0.5444 \\ \frac{0.696-x}{0.1516} & if\ 0.5444 \le x \le 0.696 \\ 1 & Otherwise \end{cases} \quad (12)$$
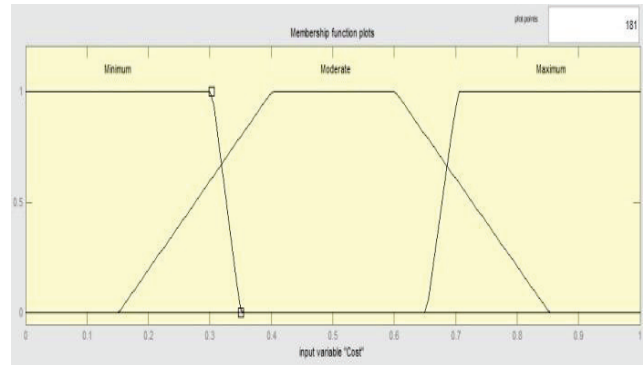


Figure 2.  Fuzzy trapezoid membership function for Cost

Figure 2 shows the fuzzification parameter –Cost with three fuzzy sets: Minimum- Moderate- Maximum and their corresponding membership functions.
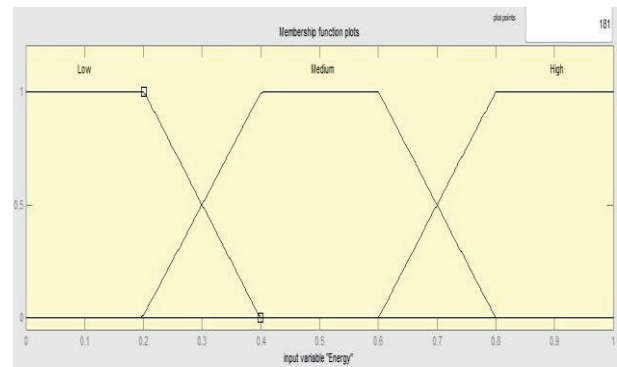


Figure 3.  Fuzzy trapezoid membership function for Energy

Figure 3 shows the fuzzification parameter –Energy with three fuzzy sets: Low- Medium- High and their corresponding membership functions.
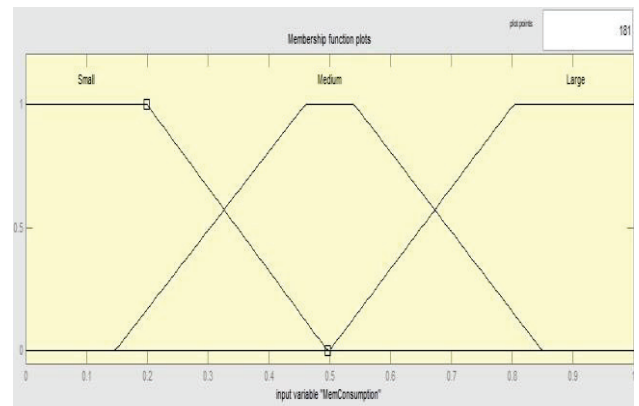


Figure 4. Fuzzy trapezoid membership function for Memory

Figure 4 shows the fuzzification parameter –Memory with three fuzzy sets: Small - Medium- Large and their corresponding membership functions.

The Table I displays the fuzzy values of neighbours of WS1 are WS2, WS 3 and WS 4 and the criteria Energy, memory and cost.

TABLE I.
FUZZY QUANTIFICATION NUMBER FOR CRISP VALUE

| Neighbour Node | Energy | Memory | Cost |
|---|---|---|---|
| WS 2 | 0.85 | 0.3251 | 1 |
| WS 4 | 0.76 | 1 | 0.6443 |
| WS 3 | 0.01 | 0.1452 | 1 |

TABLE II.
DECISION MAKING MATRIX FOR WORK STATION RANKING

| Neighbour Node | Fuzzy Score | Crisp Ranking |
|---|---|---|
| WS 2 | 0.725 | 2 |
| WS 4 | 0.801 | 1 |
| WS 3 | 0.385 | 3 |

TABLE III.
FUZZY AHP QUANTIFICATION OF CRITERIA AND ALTERNATIVES

| Fuzzy Range | Energy level of neighbours nodes | Consumption of memory | Cost of the path |
|---|---|---|---|
| FR1 | Low | Small | Minimum |
| FR2 | Medium | Medium | Moderate |
| FR3 | High | Large | Maximum |

*B . Step 2 Consistency checking*

It is used to check, and whether the allocating weights are based on the rule reasoning or not, regularly this value is less than 0.1.It implies the weights are reliable [2, 3].

A relative significant matrix to allocate weights for contrasting criteria with criteria is shown below, the matrix produced with diagonal elements are always zero. The criteria mapped with same to be one. $P_{ij}=P_{ji}$ where P is a factor of matrix

$$
\begin{array}{ccc}
 & E & M & C \\
\text{Energy} & 1 & 10 & 7 \\
\text{Memory} & \dfrac{1}{10} & 1 & \dfrac{1}{5} \\
\text{Cost} & \dfrac{1}{7} & 5 & 1
\end{array}
$$

By applying these values, it finds Geometric Mean (GM) is

GM1= (1*10*7)$^{1/3}$ = 4.1213
GM2= (1/10*1*1/5)$^{1/3}$ = 0.2714
GM3= (1/7*5*1)$^{1/3}$ = 0.8939

So, Total Geometric mean (GM) =
GM1 + GM2+ GM3= 5.2866

*C. Step 3: Prediction of normalized weights*

Weight $_1$ = 4.1213 /5.2866 = 0.7796,
Weight $_2$ = 0.2714/5.2866 = 0.0513and
Weight $_3$= 0.8939/5.2866 = 0.1690

Consistency can now be checked using following formula:

$$P3= (P1X\ P2) \tag{13}$$

Where P1 is relative importance matrix and P2 is weigh matrix obtained from equation (13).

$$P3=\begin{bmatrix} 1 & 10 & 7 \\ 1/10 & 1 & 1/5 \\ 1/7 & 5 & 1 \end{bmatrix}*\begin{bmatrix} 0.779 \\ 0.051 \\ 0.169 \end{bmatrix}=\begin{bmatrix} 2.47 \\ 0.16 \\ 0.53 \end{bmatrix}$$

Further,

$$P4 = P3/\ P2$$

$$\begin{bmatrix} 2.47 \\ 0.16 \\ 0.53 \end{bmatrix}/\begin{bmatrix} 0.779 \\ 0.051 \\ 0.169 \end{bmatrix}=\begin{bmatrix} 3.17 \\ 3.13 \\ 3.14 \end{bmatrix}$$

Finding Average of P4 i.e
$\lambda_{max}$= (3.17+3.13+3.14)/3
=3.144
Then Calculating Consistency Index(CI)
I = ($\lambda_{max}$ –n) / (n-1)
n is a size of matrix,
= (3.144-3)/2
CI = 0.072.
Consistency Ratio (CR) = CI/RI
=0.072/0.82
= 0.0878
0.0878<0.1

Here Random index already mentioned for particular collection of criteria, the value is 0.82. Hence, value of CR is less than 0.1, so the weights are reliable.

*D. Step 4:Pair wise comparison*

Pair wise assessment of alternative to alternative is achieved for each criterion as below:

| | WS2 | WS 3 | WS 4 |
|---|---|---|---|
| WS 2 | | | |
| WS 3 | 1 | 0.801 | 0.385 |
| | 1/0.801 | 1 | 0.385 |
| WS 4 | 1/0.385 | 1/0.385 | 1 |

By applying these values, it finds Geometric Mean (GM) is
GM1= (1*0.801*0.385)$^{1/3}$ = 0.675
GM2= (1/0.801*1*0.385)$^{1/3}$ = 0.783
GM3= (0.385*1/0.385*1)$^{1/3}$ = 0.998

So, Total Geometric mean (GM) =
                GM1 + GM2+ GM3= 2.456

Weight $_1$ =0.675 /2.456 = 0.274,
Weight $_2$ = 0.783/2.456 = 0.318and
Weight $_3$= 0.998/2.456 = 0.406

Consistency can now be checked using following formula:
                P3= (P1X P2)              (13)
Where P1 is relative importance matrix and P2 is weigh matrix obtained from equation (13).

$$P3= \begin{bmatrix} 1 & 0.801 & 0.385 \\ 1/0.801 & 1 & 0.385 \\ 1/0.385 & 1/0.385 & 1 \end{bmatrix} * \begin{bmatrix} 0.274 \\ 0.318 \\ 0.406 \end{bmatrix} = \begin{bmatrix} 0.684 \\ 0.769 \\ 1.937 \end{bmatrix}$$

Further,
                P4 = P3/ P2

$$\begin{bmatrix} 0.684 \\ 0.769 \\ 1.937 \end{bmatrix} / \begin{bmatrix} 0.274 \\ 0.318 \\ 0.406 \end{bmatrix} = \begin{bmatrix} 2.49 \\ 2.41 \\ 4.77 \end{bmatrix}$$

Finding Average of P4 i.e
$\lambda_{max}$= (2.49+2.41+4.77)/3
                =3.157

Then Calculating Consistency Index(CI)
I           = ($\lambda_{max}$ –n) / (n-1)
n is a size of matrix,
                = (3.157-3)/2
CI    = 0.0785
Consistency Ratio (CR) = CI/RI
                     =0.0785/0.82
                = 0.0957
                  0.957<0.1

Hence the weights are consistent.

### E.   Step 5:Judgement matrix

STEP 5:A matrix is formed with the help of obtained weights in case of pair-wise comparison matrix for three different criteria as calculated in step 4 is:-

$$\begin{bmatrix} 2.47 & 0.684 & 0.487 \\ 0.16 & 0.769 & 0.538 \\ 0.53 & 1.937 & 0894 \end{bmatrix}$$

So the final rank can be obtained as below:

$$\begin{bmatrix} 2.47 & 0.684 & 0.487 \\ 0.16 & 0.769 & 0.538 \\ 0.53 & 1.937 & 0.894 \end{bmatrix} X \begin{bmatrix} 0.274 \\ 0.318 \\ 0.406 \end{bmatrix} = \begin{bmatrix} 1.09 \\ 0.50 \\ 1.25 \end{bmatrix}$$

Deciding the rank according to the higher value of above matrix, hence ranking is WS4, WS 3 and WS 2.

$$\begin{bmatrix} 2.47 & 0.684 & 0.487 \\ 0.16 & 0.769 & 0.538 \\ 0.53 & 1.937 & 0894 \end{bmatrix}$$

## IV. PROPOSED ALGORITHM

```
 void Prediction _Work station (int G[MAX][MAX],int
M[MAX], int E[MAX],int n ,int SN, int FN)
 begin
  // G-Cost Matrix representation of the nodes of order n x n
  // M –Memory Consumption Vector representation of the
nodes of order n x 1
  // E- Energy Level Vector representation of the nodes of
order n x 1
  // n – Number of nodes in the network
  // SN – start node
  // FN – final node
  // MF1-MF12 – are Fuzzy Trapezoidal Membership
function
    int cost[MAX][MAX],distance[MAX],pred[MAX];
    int visited[MAX],count,mindistance,nextnode,i,j;

    //pred[] stores the predecessor of each node
    //count gives the number of nodes seen so far
    //create the cost matrix
    for i=0 to n-1 do
       for j=0 to n-1 do
         if(G[i,j]==0)
            cost[i,j]=INFINITY;
         else
            cost[i, j]=G[i,j];

    //initialize pred[],distance[] and visited[]
    for i=0 to n-1 do begin
       distance[i]=cost[SN, i];
       pred[i]=SN;
       visited[i]=0;
    end

    distance[SN]=0;
    visited[SN]=1;

   count=1;

    while(count<n-1) do
    begin
       mindistance=INFINITY;

       //nextnode gives the node at minimum distance
       for i=0 to n-1 do
         if(distance[i]<mindistance&&!visited[i])
         begin
            mindistance=distance[i];
            nextnode=i;
         end
```

```
        //check if a better path exists through
nextnode
        visited[nextnode]=1;
    for i= 0 to n-1 do begin
        if(!visited[i])
            if(mindistance+cost[nextnode][i]<dista
            nce[i] && max(MF10(
            max(MF1(M[nextnode]),
            MF4(E[nextnode]),
            MF7(G[nextnode][i])),
            MF11(max(MF2(M[nextnode]),MF5(E[ne
            xtnode]), MF8(G[nextnode][i])),
            MF12(max(MF3(M[nextnode]),MF6(E[ne
            xtnode]), MF9(G[nextnode][i])))>0.5
            begin

        distance[i]=mindistance+cost[nextnode][i];
                pred[i]=nextnode;
            end
        count++;
    end

    //print the path and distance of each node
    fori=0 to n-1 do
        if(i!=SN)
        begin
        printf("\nDistance of node%d=%d",i,distance[i]);
        printf("\nPath=%d",i);

        j=i;
        do
            j=pred[j];
            printf("<-%d",j);
        while(j!=FN);
        end
    end
```

## V. RESULTS AND DISCUSSIONS

The experiment is implemented in MATLAB Version R2014a with an Intel Dual Core Processor running at 1.86 GHz, 4GB of RAM. Among the three key variables, called Memory Consumption, Energy and Cost of path, the first step of the simulation performs on fuzzification by converting them into input membership functions. This is performed using the tool called as membership function editor provided in the MATLAB. Each criterion in the experiment is quantified into small, medium, and large for memory consumption; low, medium, and high for Energy, minimum, moderate and maximum for the Cost of path. The input variables are segregated because the comparison of the variability becomes effective and it helps in providing better results. The If-Then rules of the experiment are formulated using a rule editor depict in Figure 5.
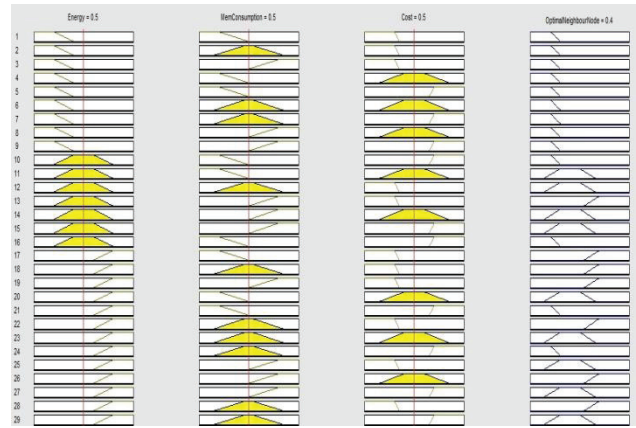


Figure 5. IF then rules –rule editor
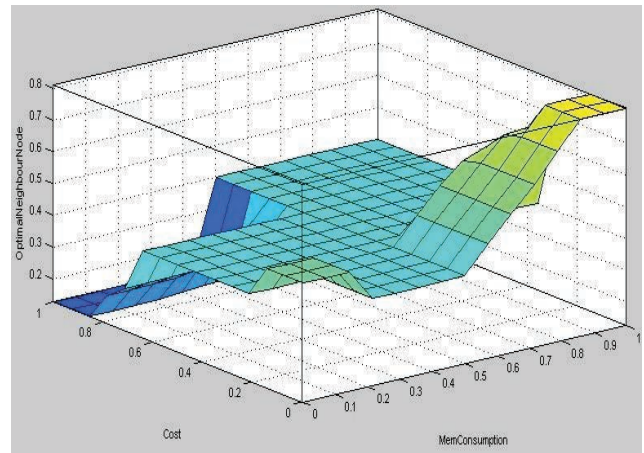


Figure 6. Output view of Memory and Cost Versus Prediction for Optimal Work station node.

The proposed work performed operation in FIS editor which handles the high-level issues. The membership function editor which defines the shapes of three membership function is associated with each criteria and rule editor for editing the list of rules. The surface viewer plots an output surface map of the system. The input vectors of the fuzzy inference engine as calculated by the simple attribute function are 0.414, 0.272, and 0.435, and the unique output generated by the Mamdani method is 0.931. All the rules have been depicted as 3D graphs called surface viewer in Figures 6, 7, and 8.
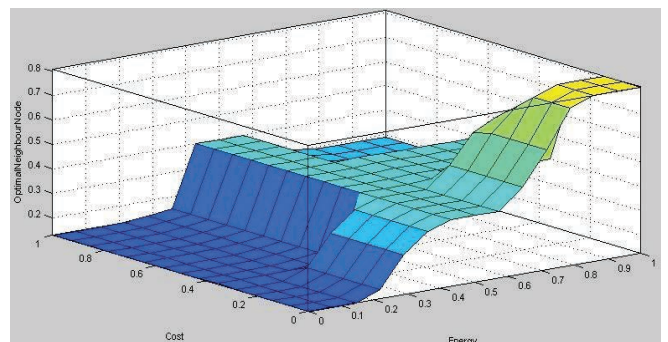


Figure 7 . Output view of Energy and Cost Versus Prediction for Optimal Work station neighbour node.
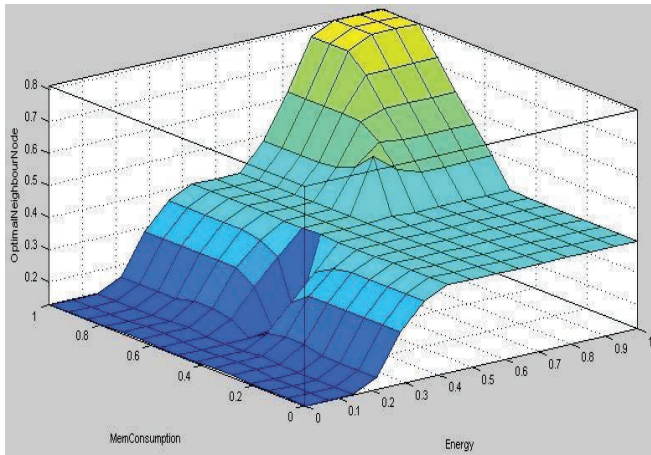
Figure 8. Output view of Energy and Memory Consumption Versus Prediction for Optimal Work station node.

## VI. CONCLUSIONS

The proposed model has applied the FAHP method, based on the node factors for successful prediction of work station for cloud service. This model considered the prediction of workstation nodes based on the factors: Energy, Memory and Cost. Fuzzy trapezoidal method is implemented to find membership function and developed rule based fuzzy inference system. The advantage of proposed system serves the best cloud service with maximum resource capability.

## REFERENCES

[1]  Butkiene R, G. Vilutis, I. Lagzdinyte-Budnike, D. Sandonavicius, K. Paulikas, "*The QoGS Method Application for Selection of Computing Resources in Intercloud*", ELEKTRONIKA IR ELEKTROTECHNIKA, vol.19, no. 7, 2013, pp 98-103.

[2]  Celik, M., Er, D., Ozok, F., "*Application of fuzzy extended AHP methodology on shipping registry selection: The case of Turkish maritime industry*", Experts Systems with Applications,2009, vol 36, (1), pp 190-198.

[3]  Cheng, Y.K., (2000), "*Development of a Fuzzy Multi-Criteria Decision Support System for Municipal Solid Waste Management*", Regina, Saskatchewan.

[4]  Enea, M., Piazza, T., 2004. *Project selection by constrained fuzzy AHP,* Fuzzy Optimization and Decision Making; 3: 39-62.

[5]  Gumus, A. T., 2009, "*Evaluation of hazardous wastetransportation firms by using a two step fuzzy-AHP and TOPSIS methodology*" Expert Systems with Applications, vol. 36 pp. 4067–4074.

[6]  Hota H.S., Sirigiri Pavani, P.V.S.S. Gangadhar, "*Evaluating Teachers Ranking Using Fuzzy AHP Technique*",International Journal of Soft Computing andEngineering (IJSCE) ISSN: 2231-2307, 2013, Volume-2, Issue-6, 485-488.

[7]  Jaiganesh, M & Vincent Anonykumar, 2013, "*B3: Fuzzy-based data center load optimization in cloud computing*", Mathematical Problems in Engineering 2013, 1-11.

[8]  Jaiganesh, M & Vincent Anonykumar, A 2014, "*Fuzzy ART based User behaviour trust in Cloud computing*", Seventh International Conference on artificial Intelligence and Evolutionary Algorithms in Engineering Systems, Advances in Soft computing, Volume 324, 2015, pp 341-348.

[9]  Kahraman, C, Ruan, D, Dogan, I., "*Fuzzy group decision making for facility location selection,*", Information Sciences, vol. 157, no. 14, pp. 135153, 2003.

[10] Saaty, T.L., 2005. "*The Analytic Hierarchy and Analytic Network Process for the mesurement of intangible criteria and for decision making In Multiple Criteria Decision Analysis: State of the Art Surveys.*" International series in operations research management science, Vol.78, Springer

[11] Tolga, E., Demircan, M. L., and Kahraman, C., (2005), *Operating System Selection Using Fuzzy Replacement Analysis and Analytic Hierarchy Process",*International Journal of Production Economics.97, 89-117.

[12] P.J.M. van Laarhoven, W.Pedrycz, "*A fuzzy extension of Saaty's priority theory*", Journal Fuzzy Sets and Systems. vol. 11, no. 1-3, pp.199-227, 1983.

[13] Pham Phuoc Hung, Tuan-Anh Bui, Kwon Soonil, Eui-Nam Huh, "A New Technique for Optimizing Resource Allocation andData Distribution in Mobile Cloud Computing",ELEKTRONIKA IR ELEKTROTECHNIKA, vol.22, no.1, pp. 73-80, 2016.

[14] Vendhan D, R.K.Selvakumar, "*Color Contrast Enhancement Based On Fuzzy Model For Thinprep Cervical CellImages*"Proceedings of the IEEE International Conference on Computational Intelligence and Computing Research, 2010.

# FPGA Realization of Hyperbolic Function

Subha Sri Lakshmi Thiruveedhi[1] and P. Viswanath[2]
[1]Asst. Professor, CVR College of Engineering/ ECE Department, Hyderabad, India
Email: rupashubha@gmail.com
[2] Professor, CVR College of Engineering/ ECE Department, Hyderabad, India
Email: panchagnulaviswanath@gmail.com

*Abstract:* **Machine Learning (ML) is applied in many real world applications. Artificial Neuron (AN) is the main building block of Artificial Neural Networks (ANN) which is the backbone of ML. ML algorithms for different applications like image and speech recognition etc., speech with large data are implemented on workstations with GPUs. However, the power of ML techniques for real time applications like monitoring, control and diagnostics, typical in power and process plant is still in nascent stage. Most of these applications require FPGA realization of ANNs. Realization of AN with both sigmoid and hyperbolic tangent activation functions along with results is reported in this paper. Design of building blocks consisting of Floating Point Unit (FPU) and Function approximation (FA) are presented. Implementation using Verilog HDL along with results of accuracy with simulated inputs and gate count and timing diagrams are presented.**

*Index Terms:* **Artificial Neuron, Floating Point Unit (FPU), Exponential Representation, Verilog HDL, Xilinx ISE.**

## I. INTRODUCTION

Rapid progress in Machine Learning in the last decade is opening opportunities for application of Deep Neural Networks and Machine Learning in real time control, monitoring and diagnostics of power and process applications. Enthalpy based real time control and sensor data reconciliation of power plants require repeated usage of steam and gas properties along with their Jacobian and Hessians. Steam and gas properties are, generally, represented in the form of complex Gibbs free energy or Helmholtz free energy equations. The properties are represented at discrete values and obtaining the function values and their derivatives is carried out by repeated calling of the above complex functions. This is computationally prohibitive. Krishna Dutt et al [1,2] reported a compact ANN representation of these properties for simultaneous obtaining of the properties and their derivatives along with their application to real time data reconciliation of power plant sensor data. Arash Ardakani et al [3] proposed an integer form of stochastic computation for an efficient implementation of a Deep Neural Network based on integral stochastic computing. The proposed architecture was demonstrated on a Virtex7 FPGA, resulting in 45% and 62% average reductions in area and latency. K.P. Sridhar et al [4] studied a testing method for VLSI based single neuron architecture with multiple inputs and one output for bench marking against ISCAS85-C17 circuit. Experimental results were reported on XILINX Spartan III FPGA. Bapuray.D. Yammenavar eta al [5] demonstrated an analog VLSI implementation with memory refresher circuits of a neural network; the design is adopted for digital operations like AND, OR and NOT. Focus of Jeremie Detrey et al [6] is on implementing floating-point elementary functions on FPGAs which is contemporary problem. They report trigonometric function approximation based on last bit accuracy. Derek Nowrouzezahrai et al [7] has presented a computationally efficient algorithm for cosine function based on Taylor's series approximation along with simulation results on Altera Stratix II FPGA. Series approximation is truncated based on accuracy in the last bit weight of the mantissas. P. Graf [8] designed and implemented a VLSI circuit for neural network for classification, particularly for image processing application, consisting of an array of 54 amplifiers with inputs and outputs interconnected through a matrix of resistive elements. All of the coupling elements are programmable resistive connection which can be turned on or off. Ranjeet Ranade [9] et al describes a technique to realize a novel digital multiplier used in Artificial Neural Network (ANN) and studied a generalized `Energy Function' for multiplier and its hardware realization by combining conventional digital hardware with a Neural Network. The design of Neurons, and the digital multiplier are described in this paper along with the simulation results. Valeriu Beiu [10] proposed a method to compute sigmoid function and its derivative in digital hardware by sum of steps and suggested that such algorithms are area-efficient. B.K. Bose [11] research was one of the earliest in floating point operation realizations in VLSI. Focus of research world over in the area of VLSI realization of ANN is on (a) efficient realization of floating point operations with real numbers (b) realization of efficient and accurate representation of functions (c) realization of artificial neuron and the feed forward ANN. Real time realization of the neural net with feed forward mode in FPGA is of recent interest to researchers. Both structural and behavioral models can be considered for implementation of ANN in FPGA. Behavioral Models and realization of an AN with different activation functions along with a floating point algebraic operator for real valued inputs, in FPGA environment is reported in this paper.

## II. ARTIFICIAL NEURON

Fundamental building block of Artificial Networks is Artificial Neuron, also called as Perceptron. Figure 1 describes a typical AN.
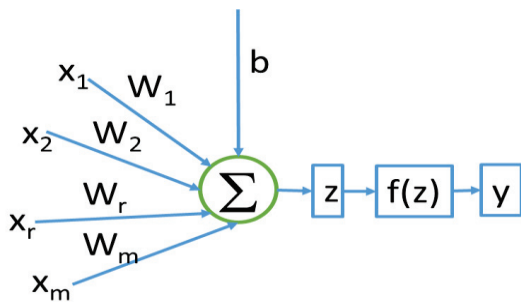
Figure 1. Structure of Artificial Neuron (AN)

AN structure consists of m inputs and their associated weights, a summer of weighted inputs and a mapping function that transforms the sum to an output. This function can be any differentiable function. Sigmoid, Tanh, ReLU are some of the widely used functions. Figure 2 shows the output of these two functions i.e., tanh(x) and sigmoid.

Equation (1) describes the functioning of an AN

$$Z = (\textstyle\sum w_i\, x_i + b) \qquad\qquad (1)$$
$$y = f(Z) \qquad\qquad\qquad\qquad (2)$$

In general, an AN has a multivariate input ($x_i$), weight vector and a mapping function. A summer block which (Z) a weight sum y the input vector ($x_i$). The mapping function (f) transforms the weighted input to the output (y). The mapping function can be any analytic function of at least first order continuity. The inputs (x) are normalized to be within (-1,1) or (0,1) band an application, however, the weights can be any real number. The output of y is obtained to be within (0,1) or (-1,1) for sigmoid or tanh respectively. There are many other possible functions of which ReLu has become very popular, particularly for dealing with binary inputs, where the above two functions are useful in case of real valued inputs. ReLu is generally used in deep beleif networks. Sigmoid is more popularly used in multi layer neural networks (MLP) or deep neural networks. The structure on learning functions of an AN is based on studies of biological neuron focus in mammalian brains. These biological neurons reveal that learning is either discriminative or generative in nature. A single AN tries to emulate these two capabilities through the learning function.
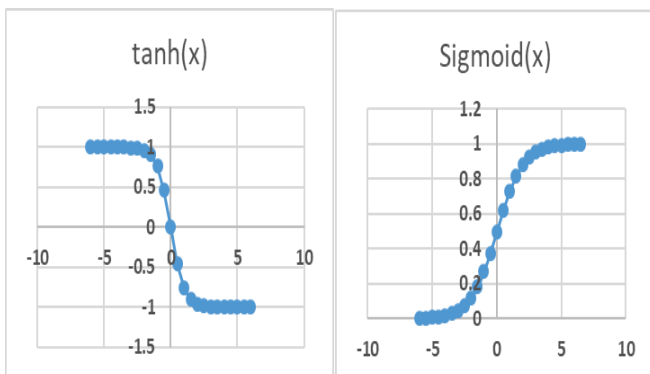
The output of these two functions is limited to [-1,1]. However, functions like ReLU, figure 3 does not limit the output to be within [-1,1]. From the above general purpose Floating Point Unit (FPU) with basic operations, multiplication, division, addition and subtraction, and a function mapping units are required for realization of an AN model in FPGA. Following describes design of these two with results obtained from the implementation in Verilog Code.
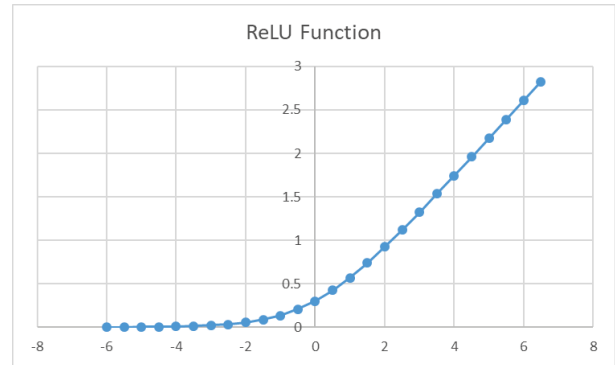


Figure 3. ReLU Activation Function.

## III. FLOATING POINT UNIT

Floating point unit is defined as math coprocessor. Mainly it is designed to perform various operations such as addition, subtraction, multiplication, division, square root and bit shifting etc. It even can perform other operations such as exponential & trigonometric operations which are defined as transcendental functions. In computer architecture applications one or more floating point units can be inserted within the central processing units (CPU's). Design and realization of FPU are based on IEEE 754 standard as shown in figure 4. Generally IEEE 754 standard specifies the interchange and arithmetic equation formats and methods for binary and decimal floating point arithmetic in computer & signal processing applications. Even this standard interchanges the bit strings that may be used to exchange the floating point data in an efficient form to compact form. Real number inputs (OP1,Op2) are converted to IEEE 754 representation and algebraic operators ADD, SUB, MULTI and DIV are operated on the converted operands. Figure 9 shows the summary details of device utilization, in which highest utilization is on number of slots (slices) to the extent of 35%, which can be considered reasonable.



Figure 2. Activation Functions of AN
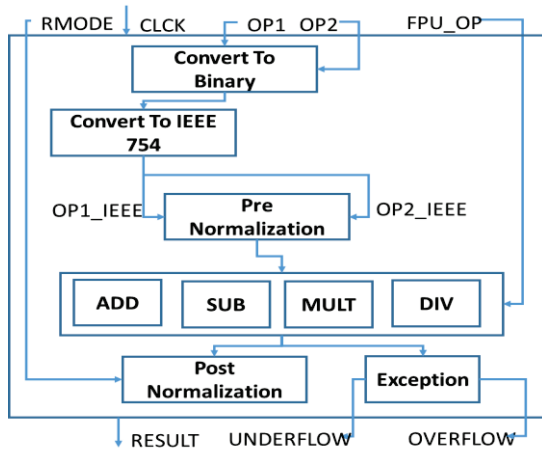
Figure 4. Block Diagram of Floating Point Unit

## IV. FUNCTION APPRIXIMATION

Both Sigmoid and tanh functions are modelled as below for realization in FPGA.

$$\text{Sigmoid}(z) = 1.0/(1.0+e^{-z}) \qquad (3a)$$

$$\tanh(z) = (e^z - e^{-z}) / (e^z + e^{-z}) \qquad (3b)$$

Common to both equations (3) and (4) is the function block exponentiation of the variable z. This is approximated as

$$e^z = 1 + z + \frac{z^2}{2} + \frac{z^3}{6} + \frac{z^4}{24} + \frac{z^5}{120} + \frac{z^6}{720} \qquad (3)$$

Equation 3(a), approximates the exponentiation with a maximum error of 0.04% at the maximum input range. This is considered reasonable approximation for AN. Based on this approximation, equations (1) and (2) are realized in FPGA as shown in figures 5 and 6, respectively.
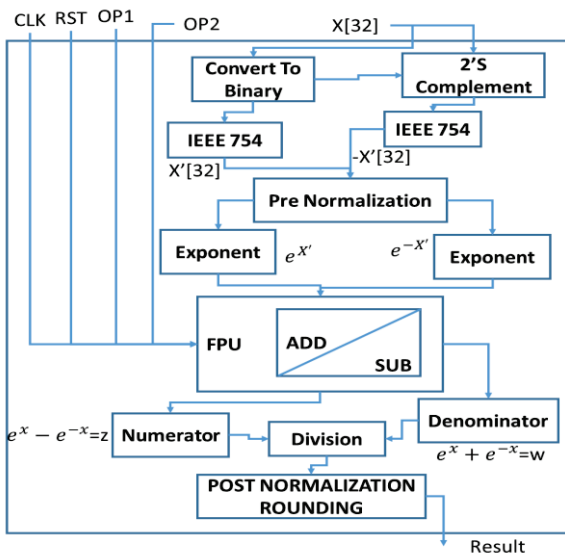


Figure 5. Internal Operational Structure of tanh Function Realization in FPGA
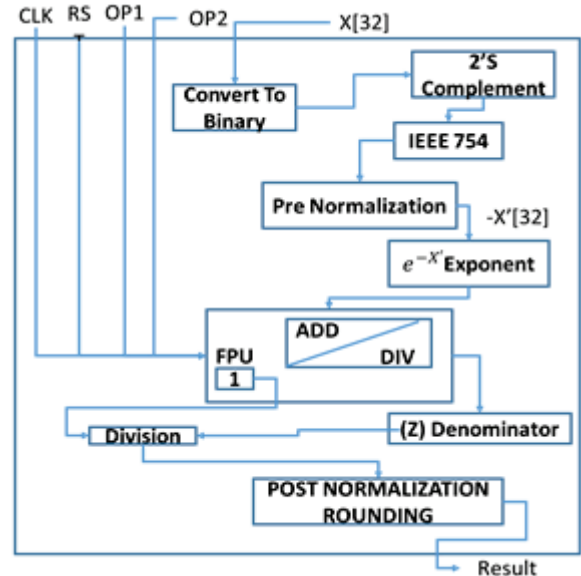


Figure 6. Internal Operational Structure of Sigmoid Function Realization in FPGA

The block level structures of tanh function and sigmoid function i.e., equation 3a and 3b are designed as shown in figures 7 and 8 respectively. The Floating point unit (FPU) is analyzed and designed by using Figure 4. The floating point operations are defined by parameter named as opcode. For example opcode = 00 indicates addition operation, 01 indicates subtraction operation, 11 indicates multiplication operation and finally 10 indicates division operation of floating point arithmetic unit. All the operands are defined in terms of floating point arithmetic and represented with IEEE 754 format.
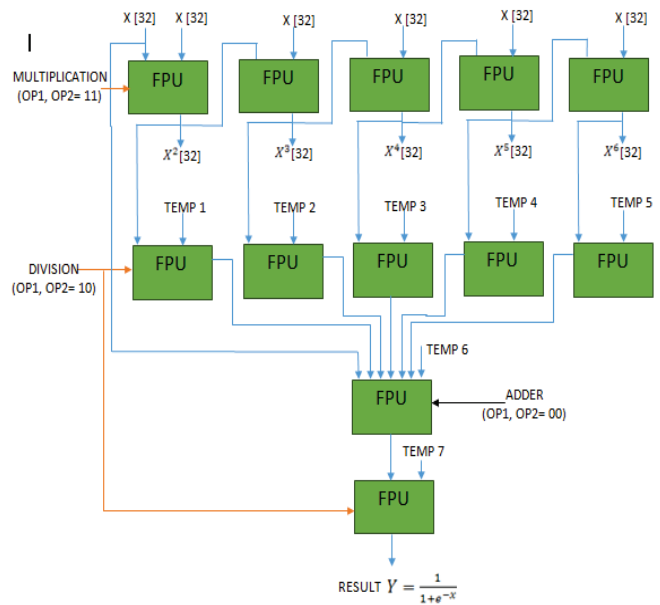


Figure 7.  Block Diagram of Sigmoid Function Realization
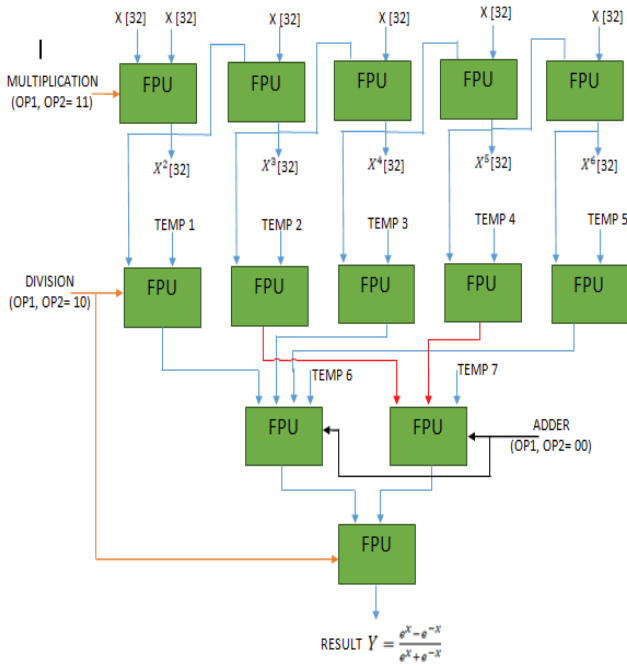
Figure 8. Block Diagram of tanh Function Realization in FPGA

All the TEMP variables in the above figures are defined as respectively, to derive the mathematical expressions such as equation (1), (2) & (3).

Temp 1= 2 -> 32'b 0000 0000 0000 0000 0000 0000 0000 0010
Temp 2= 6 -> 32'b 0000 0000 0000 0000 0000 0000 0000 0110
Temp 3= 24 -> 32'b 0000 0000 0000 0000 0000 0000 0001 1000
Temp 4= 120 -> 32'b 0000 0000 0000 0000 0000 0000 0111 1000
Temp 5= 720 -> 32'b 0000 0000 0000 0000 0000 0010 1101 0000
Temp 6 & Temp 7= 1 -> 32'b 0000 0000 0000 0000 0000 0000 0000 0001

## V. IMPLEMENTATION & RESULTS

All the blocks of Artificial Neuron i.e., Floating Point Unit (FPU), Tanh function and Sigmoid Function are designed using Verilog HDL and simulated using Xilinx ISE simulator of 14.7 versions. The device utilization for Floating Point Unit, Tanh and Sigmoid expressions are shown in the figures 9, 10 & 11 respectively. They are shown in terms of no. of slices & no. of Flip-flop's used in the design.



Figure 9. Device Utilization for FPU in FPGA



Figure 10. Device Utilization for Tanh Function in FPGA



Figure 11. Device Utilization for Sigmoid Function in FPGA

Simulation Waveforms are shown in the figures 12 & 13. Figure 12 shows the simulation waveform of floating point unit with multiplication operation. Input A[31:0] is defined as 01000000001000000000000000000000, input B[31:0] is defined as 01000000101000000000000000000000 and output is observed as

O[31:0]= 01000000110010000000000000000000



Figure 12. Simulation Waveform for FPU in FPGA

Figure 13 shows the Simulation analysis of Tanh mathematical expression in which x is defined in terms of floating point arithmetic values.
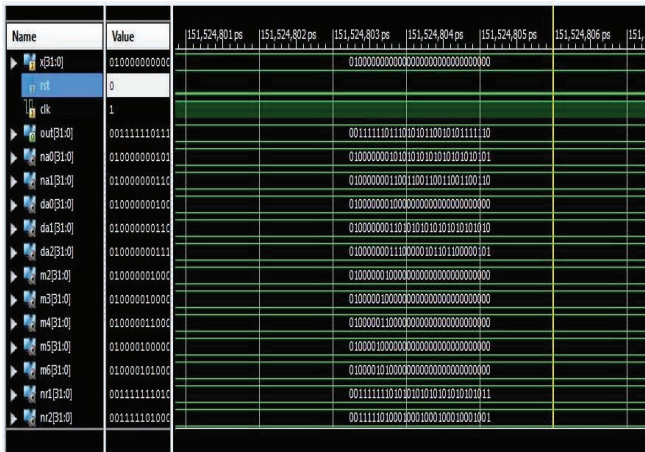
Figure 13. Simulation Waveform for Tanh Function in FPGA

Table 1 gives the details of Floating point unit, Sigmoid expression and tanh expression in terms of gate count (Number of Slices), CPU time and Power usage (in terms of watts).

All the blocks are implemented on FPGA with the respective specifications.
Family – Spartan 3
Device – XC3S400
Package – PQ208
Speed - -4/-5

TABLE I.
AREA VS CPU TIME VS POWER USAGE

| Blocks | Gate Count | CPU Time | Power Usage |
|---|---|---|---|
| Floating Point Unit | 2432 | 0.36 sec | 0.016 |
| Sigmoid Expression | 2826 | 0.39 sec | 0.019 |
| Tanh Expression | 2703 | 0.41 sec | 0.025 |

## VI. CONCLUSIONS

Realization of Hyperbolic Function in FPGA is demonstration through Verilog code in Xilinx, ISE 14.7, and simulation tool. Popularly known two activation functions, generally used with real number feature vector, are realized with an overall device utilization of 35%. The design is based on behavioral model. However, it is also possible to realize the Artificial Neuron based on structural model for improving the efficiency of device utilization. The function approximation is reported with an accuracy of 0.5. With an overall cycle time 0.41 seconds with a clock period of 100 MHz. The work reported is considered as building block for realizing a deep neural network of any number of hidden layers with each layer having a finite number of Artificial Neurons. The work can easily be extended to cover other activations functions like ReLU, used in deep belief networks.

## REFERENCES

[1] "Neural Nets for Thermodynamic properties", R.V.S Krishna Dutt, J Krishnaiah, Proceedings of the First International conference on Computational Intelligence and Informatics, Advances in Intelligent Systems and Computing, vol 507, Spinger, Singapore., 2017

[2] "System and Neural Net Methods for Signal Validation of Power Plant Measurement Data", R.V.S.Krishna Dutt, J.Krishnaih, Patent No.160123RD

[3] "VLSI Implementation of Deep Neural Network Using Integral Stochastic Computing", Arash Ardakani,, François Leduc-Primeau, Naoya Onizawa, Takahiro Hanyu, Warren J. Gross, arXiv:1509.08972v2 [cs.NE] 24 Aug 2016

[4] "Design and Implementation of Neural Network Based circuits for VLSI testing", K.P. Sridhar, B. Vignesh, S. Saravanan, M. Lavanya and V. Vaithiyanathan, World Applied Sciences Journal 29 (Data Mining and Soft Computing Techniques): 113-117, 2014.

[5] "Design and Analog VLSI Implementation of Artificial Neural Network", Bapuray.D.Yammenavar, Vadiraj.R.Gurunaik,Rakesh.N.Bevinagidad Vinayak.U.Gandage, International Journal of Artificial Intelligence & Applications (IJAIA), Vol.2, No.3, July 2011.

[6] "Floating Point Trigonometric Functions for FPGAS", Jeremie Detrey, Florent de Dinechin, IEEE, 2007.

[7] "Efficient Double-Precision Cosine Generation", Derek Nowrouzezahrai et al, Department of Electrical and Computer Engineering University of Waterloo, 2006.

[8] "VLSI implementation of a Neural Network Model", Hans P. Graf, Lawrence D. Jackel, and Wayne E. Hubbard AT&T Bell Laboratories, IEEE Computer, 1988

[9] "VLSI implementation of artificial neural network based digital multiplier and adder", Ranjeet Ranade, Sanjay Bhandari, A.N.Chandorkar, VLSID '96 Proceedings of the 9th International Conference on VLSI Design: VLSI in Mobile Communication, January 03 - 06, 1996

[10] "Close Approximations of Sigmoid Functions by Sum of Steps for VLSI Implementation of Neural Networks", Valeriu Beiu, Jan Peperstraete, Joos Vandewalle, Rudy Lauwereins, The Scientific Annals, Section: Informatics, vol. 40 (XXXX), no. 1, 1994.

[11] "VLSI Design Techniques for Floating Point Computation", B.K.Bose, Ph.D Thesis, UC Berkeley, 1988.

# A Compact UWB Circular Patch Antenna for X-Band and WLAN Applications

L. Nageswara Rao

Asst. Professor, CVR College of Engineering/ECE Department, Hyderabad, India

Email: lavurinagesh@gmail.com

*Abstract:* **A composite circular microstrip patch antenna (MPA) with aperture opening for UWB architecture is intended. Double recurrence circular patch configuration along aperture opening slot fed with a microstrip line are planned to achieve coupled recurrence task. The design involves the circular patch and space resonator. The moderation in the radio wire design for the auxiliary band is realized by a U – shaped resonator. The U-shaped aperture is employed in the ground plane to realize dual frequency operation. By modifying structure parameters, the patch works at the X-band (8.69 GHz) for satellite communications and parasitic - opening works at UNII band (5.15 GHz) for WLAN applications, the two resonators are transmitting with two diverse radiation designs. The designed antenna is small in size, less weight, reduced in cost and satisfactory confinement. The antenna analysis shows the desired return loss (<-10 dB), improved radiation pattern over working bands. To analyze the attainment of receiving wire, practical specifications, for example, reflection coefficient, data transmission and radiation design are resolved by the recreation of the designed model with HFSS. Designed antenna configuration is appropriate for ultra-wideband applications.**

*Index Terms:* **Microstrip Patch Antenna (MPA), dual frequency operation, microstrip feed line, UWB, WLAN.**

## I. Introduction

The fast advancement of wireless networks and developing the specifications for the restricted recurrence operation have incited the hindrance of radio-frequency (RF) ranges and obstruction among them. Multiband antenna assumes a fundamental part of wireless communication specifications and is utilized to meet the needs of various recurrence operation. The patch resonators [1] are in considerable request because of the fast improvement of remote correspondences for the WLAN applications. Consideration of designed antenna is reasonable because of patch resonator is small in size, less weight, reduced cost and satisfactory confinement. A patch antenna can be required to have a larger bandwidth. Different types MPAs such as circular, rectangular, squares with ring slot shapes [2]-[7] have been described in literature. Circular and rectangular patch antennas are having attractive features over the square and ring slot shapes.

The circular patch with aperture opening [8]-[9] is planned and designed for wireless communication systems that can support the UWB [10]-[11] applications. The double recurrence circular patch with space resonator configuration [3] is proposed to attain dual band frequency operation for UWB applications.

The expansive data transfer capacity designated to the all-inclusive band frameworks by FCC stretches out from 3.1 to 10.6 GHz, causes exceptionable obstruction with other tight band frameworks in this recurrence band, for example WLAN in the 5.1–5.75 GHz range and furthermore X-band satellite correspondence frameworks working in the 7.75–8.85 GHz space [10]. Therefore, UWB reception apparatuses fit for creating the required stop-bands are adorable. It is proposed to reconfigurable reception apparatuses with notched space for the ideal and effective utilizations of the UWB model [13]-[14].

UWB correspondence frameworks have gotten broad consideration on account of having particular preferences, for example, fast information rate, basic equipment arrangement, high-accuracy running, low power utilization, low intricacy, and ease. On the other hand, to plan UWB reception apparatuses, there are certain difficulties including high radiation productivity, the ultra-wideband execution, consistent gain, and so forth. The MPAs have accomplished extraordinary consideration for UWB reception apparatuses [15] because of a few striking highlights, including low dissemination misfortune, high radiation proficiency, different excitation systems, distinctive patch shapes, almost steady gain, and minimized patch size.

The designed model can be examined as the mix of MPA and other emanating resonator [12], such as a slot resonator. These two elements are tightly coupled together and oscillate at various frequencies. The radiation patterns have different performance levels for wireless communication applications. The WLAN has an essential part in applications, for instance, security frameworks, individual territory organize frameworks, mixed media courses, voice on web convention, cell phones and so forth. At the point when contrasted and old wired LAN arrangements, WLAN offers portability which makes the WLAN [16]-[18] frameworks more easy to understand.

Subsequently the resonator which can give great radiation execution at least two recurrence groups is more attractive and advantageous. In any case, the plan of multiband radio wires are testing and tedious when the span of the receiving wire should be decreased and the groups of task increases.

The prosperity patch antenna resonators in feeding systems need systematic knowledge to couple the resonators and components. However, the resonate encouraging framework set in these portrayed models, for example, microstrip sustained space, co planar space feed and CPW-sustained space course of action offers greater adaptability and is specifically good with various mounting surfaces. In this design, so as to maintain a strategic distance from by

means of gaps, the microstrip feed line is recommended [20]. The microstrip line set on a similar substrate of round fix that could be put straightforwardly finished the feed line. The microstrip feed is simple to model, easy to coordinate by controlling the inset feed position and simple to manufacture.

To emphasize the model, the circular patch configuration along aperture opening slot is planned. It consists of primary band (8.69 GHz) and lower band (5.1 GHz) ranges of the planned resonators are essentially reasonable by the MPA and aperture space consequently. Simulations have been performed using electromagnetic software HFSS provided from Ansys Corporation. The details of UWB antenna design are presented. The simulation results are introduced to feature the execution of the designed receiving wire.

## II. ANTENNA CONFIGURATION

The circular microstrip patch resonator with aperture opening fed by a microstrip line is designed. The hybrid model includes two different types of resonators; it consists of circular patch and slot. The proposed hybrid structure, the circular [8] patch antenna oscillates at 8.69 GHz and slot [9], oscillates at 5.1 GHz which is reasonable for UWB [10] applications. The design involves the circular patch and space resonator. By shifting the emanating resonators' position, a recurrence tunable MPA can be demonstrated. The feed line is placed at center of the substrate.

The designed model for wireless communications is exhibited in figure 1. The recommended structure has the dimensions of 40 mm × 40 mm × 1.6 mm, and a FR-4 with a relative permittivity of 4.4 is utilized as a substrate. It comprises of a compact MPA and an inside encouraged microstrip line which is imprinted on a FR-4 substrate. The ground plane is imprinted on the FR-4 substrate with a measurement of 40x40 (L x W) mm². The patch has a radius of R = 12.5 mm and offset distance $S_1$ = 18 mm as shown in Figure 1. The 50-Ω feeding line has a length of $L_f$ =21 mm and a width of $W_f$=3.0 mm.

The analytical operating frequency of the circular patch antenna is resolved [19] by the consequent equation and analogous to 8.69 GHz which is applicable for X- band applications.

$$a = \frac{F}{\left\{1 + \frac{2t}{\pi F \varepsilon_r}\left[ln\left(\frac{\pi F}{2t}\right) + 1.7726\right]\right\}^{1/2}} \quad (1)$$

Where,

$$F = \frac{8.791 \times 10^9}{f_r\sqrt{\varepsilon_r}}$$

$a$ = radius of the circular microstrip patch
$t$ = thickness of substrate
$\varepsilon_r$ = dielectric constant of substrate
$f_r$ = resonant frequency
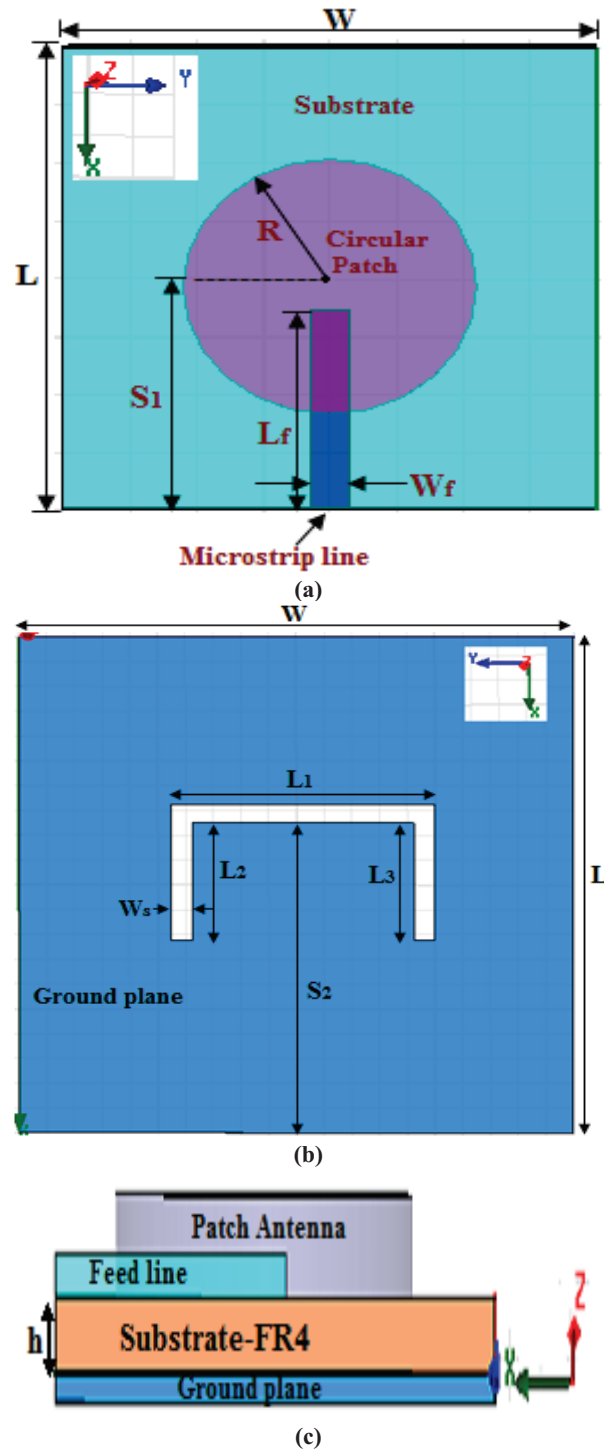


Figure 1. Proposed MPA with slot: (a) Top view;
(b) Bottom view; (c) Side view

In this model, a new type of resonator such as slot etched in ground plane is intended to achieve lower frequency (5.1 GHz) band. Fig. 1 exhibits the geometry of opening space. It is notable that by picking a high permittivity substrate, a more prominent size decrease can be accomplished. Thus, the substrate chose for the patch has been FR-4 ($\varepsilon_r$=4.4). By changing the opening measurements, the planned structure can works in two groups, and a good impedance coordinate for the working frequencies can be effectively achieved.

The design consideration for the lower excited slot antenna comprises of three rectangular spaces with different length and selected width $W_S$=0.5 mm as appeared in Figure 1, different rectangular space lengths are $L_1$=16 mm, $L_2$=5.5 mm, $L_3$=5.5 mm and counterbalance separation of opening is $S_2$ = 22 mm. By modifying the-opening parameters, the proposed structure can work in two groups, and a good impedance coordinate for the working frequencies can be effectively acquired. By adjusting the structure parameters, the circular patch and slot resonates at 8.69 GHz and 5.1 GHz respectively.   The shape of the structure has been chosen such that, it meets the necessity of data transmission and small in size consequently. The intended structure enables the affirmation of a dual band task without expanding the patch dimensions.

## III.  RESULTS AND DISCUSSIONS

Fig. 2 represents the simulated return loss of the intended MPA. The lower energized band is because of the space while the auxiliary band is because of the round microstrip fix radio wire. It represents -30 dB and -44 dB return loss at 5.1 GHz and 8.69 GHz consequently. Note that there are no frequencies to be evidently the nearness of indirect fix, that is, the full resound opening mode is started by the fix radio wire.

The arrival misfortune is another approach for expressing mismatch. It is a logarithmic proportion estimated in dB that thinks about the power reflected by the radio wire to the power that is sustained into the receiving wire from the transmission line.

The data transfer capacity basically characterizes the recurrence run over which a receiving wire meets a specific arrangement of determination execution criteria. The critical issue is to consider in regards to data transfer capacity is the execution tradeoffs between the majority of the execution properties portrayed previously.

The radiation example of the reproduced radio wire structure at 5.1 GHz and 8.69 GHz with phi=0 (deg) and phi = 90 (degree) are depicted in Fig. 3. The intended receiving wire transmits a most extreme in the broadside heading at 8.69 GHz and slot – opening resonator is radiating the waves in bidirectional at 5.1 GHz. The radiation examples of a radio wire give the data that depicts how the reception apparatus coordinates the vitality it transmits. Radiation designs are for the most part exhibited on a relative power dB scale.



(a)



(b)
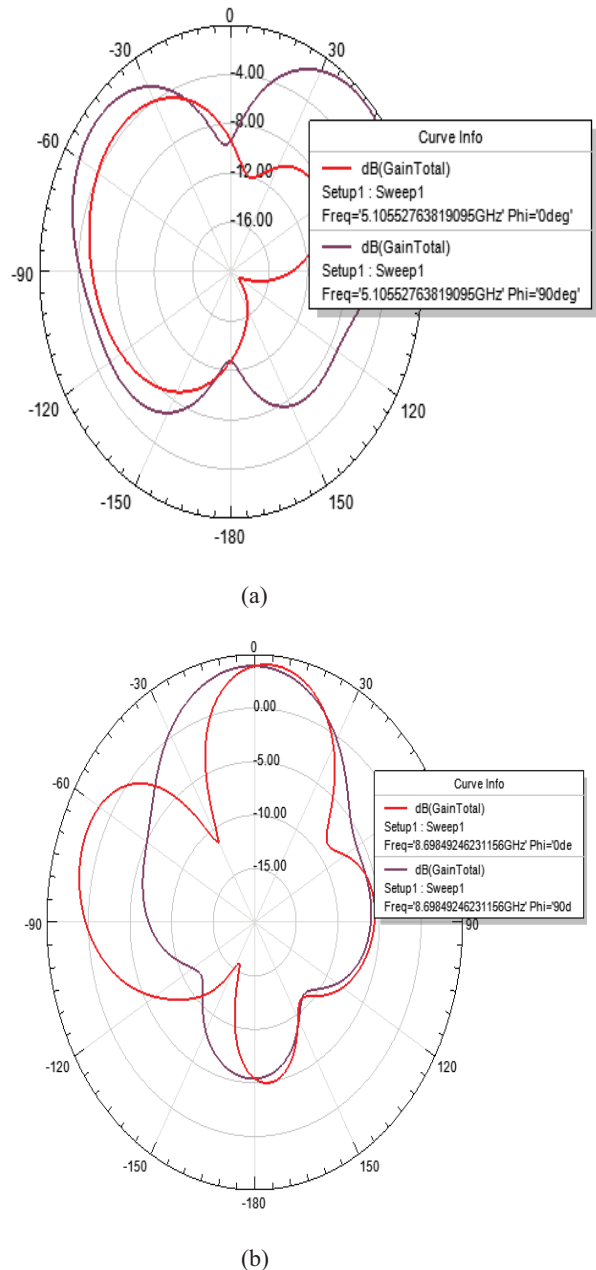
Figure 3. Radiation patterns at 5.1 GHz and 8.69 GHz

Fig. 4(a) and (b) represents the designed configuration gain at 5.1 GHz and 8.69 GHz as 4 dBi and 5.1 dBi consequently. The most extreme radiation is directed outside in both the recurrences.



Figure 2. Simulated return loss at 5.1 GHz and 8.69 GHz

(a)



(b)
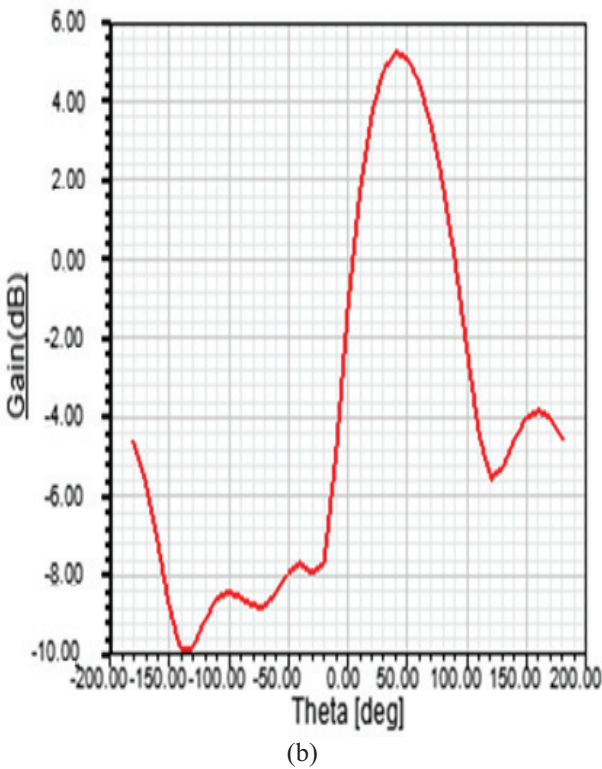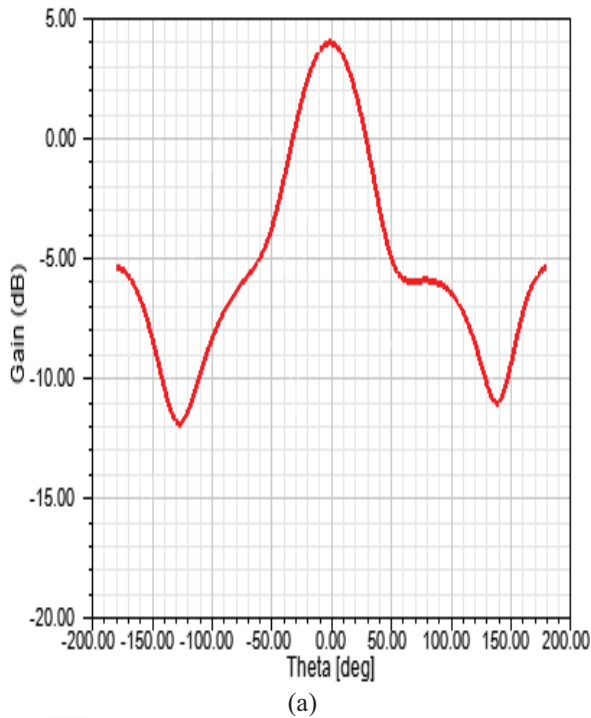
Figure 4. Simulated Gain at (a) 5.1 GHz and (b) 8.69 GHz



(a)



(b)

Figure 5. Simulated VSWR at (a) 5.1 GHz and (b) 8.69 GHz

## IV. CONCLUSIONS

A composite circular patch with aperture opening is intended for UWB systems. The planned circular patch structure with aperture space configuration is realized to procure the X- band (8.69 GHz) and WLAN (5.1 GHz) band. The recommended configuration is attainable and outline parameters are recognized by using description similarity. An intended model contour has been reproduced and it represents that return loss of -44 dB, -31 dB at the resonant recurrences of X-band (8.69 GHz) and WLAN band (5.1 GHz) correspondingly. The reconfigurable structure has the capacity of delivering recurrence indents for the UWB frameworks, to take out obstruction with WLAN (4.92– 5.2 GHz) and X-band of satellite correspondence frameworks (8.25– 8.81 GHz). The illustrated model takes a less volume, smaller size, basic shape and satisfactory operational data transfer capacity, with the end goal that it is appropriate for ultra - wideband applications.

Fig. 5(a) and (b) represents the VSWR of the intended model. It   depicts the analysis of the inclined line and load. For perfect case estimation the VSWR is 1. The investigated model has VSWR of 1.05 at 8.69 GHZ and 1.1 at 5.1 GHZ. The VSWR exhibit that how intently a radio wire's terminal impedance is composed to the trademark impedance of the slanted line.

## REFERENCES

[1] Sekhar M, S. N. Bhavanam, Dr. P. Siddaiah, "Triple Frequency Circular Patch Antenna",IEEE International Conference on Intelligence and computing Research, pp. 1-3, December 2014.

[2] R. Srivastava, S. Ayub, V. K. Singh, J. P. Saini, "Dual Band Rectangular and Circular Slot Loaded Microstrip Antenna for WLAN/GPS/WiMax Applications",Fourth International Conference on Communication Systems and Network Technologies,pp. 45-48, April 2014.

[3] S. I. Hussain Shah, S. Bashir, S. D. Hussain Shah, "Compact Multiband microstrip patch antenna using Defected Ground structure (DGS)",The 8th European Conference on Antennas and Propagation (EuCAP), pp. 2367-2370, April 2014.

[4] M. I. Sabran, S. K. A. Rahim, M. F. M. Yusof, A. A. Eteng1, M. Z. M. Nor, I. M. Ibrahim ,"Miniaturized Proximity Coupled Antenna with Slot Ring as Defected Ground Structure", IEEE Symposium on Wireless Technology and Applications (ISWTA), pp.81-85, Sept-oct 2014.

[5] Lakshmikanth, P., Takeshore, K., & Madhav, B. T. P. (2015). Printed log-periodic dipole antenna with notched filter at 2.45 GHz frequency for wireless communication applications. Journal of Engineering and Applied Sciences, 10(3), 40-44. doi:10.3923/jeasci.2015.40.44.

[6] M. H. Tariq, S. Rashid, F. A. Bhatti,"Dual Band Microstrip PatchAntenna for WiMAX and WLAN Applications", International journal of Multidisciplinary and Currentresearch, vol.2,pp. 104-108, Jan/Feb 2014.

[7] S. C. Gao, L. W. Li, T. S. Yeo, M. S. Leong,"Small Dual-Frequency Microstrip Antennas", *IEEE Transactions on VehicularTechnology*,vol.51,No.1,pp. 1916-1917, January 2002.

[8] Garima,D.Bhatangar,J.S.Saini,V.K.Saxena,L.M.Joshi, "Design of Broadband Circular Microstrip Patch Antenna With Diamond Shaped Slot",Indian Journal of Space And Physics,vol.40,pp.275-278,October 2011.

[9] J. A. Ansari, A. Mishra, N. P. Yadav,P. Singh , "Dualband Slot Loaded Circular Disk Patch Antenna for WLAN Application", International Journal Of Microwave And Optical Technology, vol.5, No.3, pp. 124-129, May 2010.

[10] Clementi, G., Fortino, N., Dauvignac, J.-Y.*, et al.*: 'Frequency and time domain analysis of different approaches to the backing of an UWB slot antenna', *IEEE Trans. Antennas Propag.*, 2012, 60, (7), pp. 3495–3498.

[11] Ojaroudi, N., Ojaroudi, M.: 'Novel design of dual band-notched monopole antenna with bandwidth enhancement for UWB applications', *IEEE Antennas Wirel. Propag. Lett.*, 2013, 12, pp. 698–701.

[12] G.P.Gao,M.Li,S.F.Niu,X.J.Li,B.N.Li,J.S.Zang, "Study Of Novel Wideband Circular Slot Antenna Having Frequency Band Notched Function",Progress In Electromagnetic Research(PIER)96,pp.141- 154,2009.

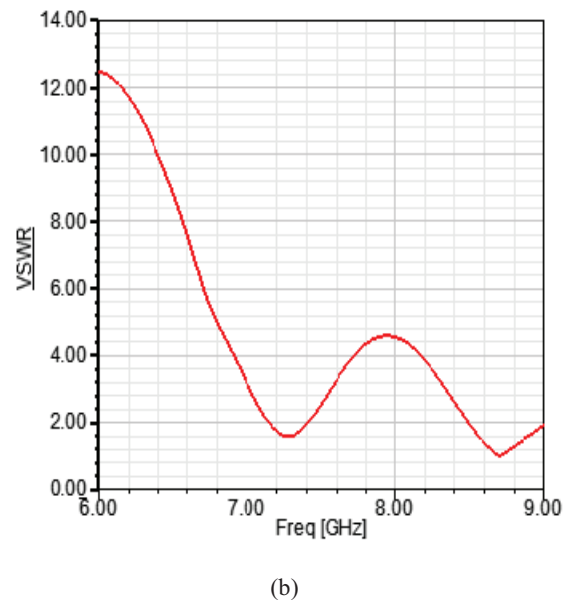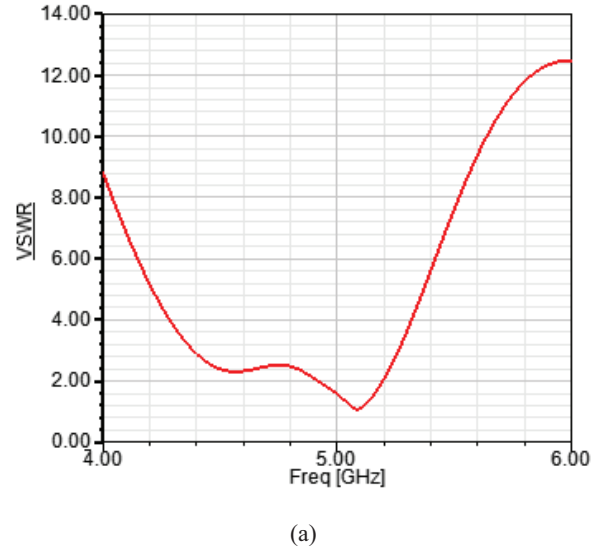[13] Ryu, K.S., Kishk, A.: 'UWB antenna with single or dual band-notches for lower WLAN band and upper WLAN band', *IEEE Trans. Antennas Propag.*, 2009, 57, (12), pp. 3942–3950.

[14] Li, Y., Li, W., Yu, W.*, et al.*: 'A small multi-function circular slot antenna for reconfigurable UWB communication applications'. *IEEE Antennas and Propagation Society Int. Symp*. (APSURSI), 2014, pp. 834–835.

[15] Kalteh, A.A., DadashZadeh, G.R., Naser-Moghadasi, M.*, et al.*: 'Ultrawideband circular slot antenna with reconfigurable notch band function', *IET Microw. Antennas Propag.*, 2012, 6, (1), pp. 108–112.

[16] Kishan Kumar K., Prasanth, Edward Stephen, A novel design approach and simulation of frequency reconfigurable microstrip patch antenna for Wi-Fi, WLAN and GPS applications, IEEE, International Conference on Robotics, Automation, Control and Embedded Systems, India, pp. 1-4, Feb. 2015.

[17] Xinghui Zhang, Dongya Shen, Lan Li, and Huiyun Liu., A Compact frequency reconfigurable antenna applied to WLAN/WiMAX, Shanghai, China , , pp. 1-7, Oct. 2011.

[18] Q. Zhong, Y. Li, H. Jiang, Y. Long,"Design of a Novel Dual-frequency Microstrip Patch Antenna for WLAN Applications",Antennas And Propogation Society International Symposium,vol.1, pp. 277-280,June 2004.

[19] C. A. Balanis,"Antenna Theory, Analysis and Design", Second edition, John Wiley andSons, NewYork, 1997.

[20] R. A. Kranenburg and S. A. Long, , "Microstrip Transmission Line Excitation of Dielectric Resonator Antennas," *Electron. Lett*. vol. 24, pp.1156-1157, 1988.

# Implementation of Image Processing Techniques using LabVIEW and MATLAB

B. Janardhana Rao

Assoc. Professor, CVR College of Engineering/ECE Department, Hyderabad, India
Email: janardhan.bitra@gmail.com

*Abstract*: **Image processing play a major role in day to day life. The implementation of image processing applications using MATLAB takes place in practice. The block based implementation of image processing applications can be done with LabVIEW (Laboratory Virtual Instrument Engineering Workbench). This paper discusses the basic operations on images like extraction of the RGB (Red, Green, and Blue) components in a color image, converting the gray scale image to binary image and the edge detection process in both MATLAB and LabVIEW. Based on the experimental results, the merits and demerits of programming languages are discussed.**

*Index Terms*: **MATLAB, LabVIEW, RGB and edge detection.**

## I. INTRODUCTION

LabVIEW is a visual programming language and well suits for hardware integration. LabVIEW code is much easier to debug and as a visual programming language it contains less number of bugs in the code. Most of the times LabVIEW runs on hardware than normal computer. LabVIEW will be used for multidisciplinary applications. MATLAB is text based programming language and it suits well for matrix algebra and data visualization. In general MATLAB is the best tool for image processing applications. In this paper, the basic image processing operations are implemented using LabVIEW and MATLAB. An image is a two dimensional matrix of pixel values. There are three types of images in general, hence three different types of pixel matrices. The black and white image (binary image) consists of pixel values as ones and zeros, ones indicate the brighter portions and zeros indicate the darker portions [1]. The gray scale image consists of pixel values as 0 to 255. Like gray scale image color image is also a matrix of pixels values from 0 to 255. Color image is also called as RGB image. RGB image is an overlap of matrices for red, green and blue components of size 256x256. Then the total image size becomes 256x256x3. Since the image is represented as matrix, any mathematical operations on images can be performed on image that can be done with a matrix [2].



Figure 1. Gray scale image matrix

The edge detection techniques are applicable only for black and white images, so in order to apply the edge detection to RGB or gray scale image first it should be converted into binary image. As it is not also possible to convert RGB images to black and white directly, first it is to be converted into gray scale then binary image.

There are different types of edge detection techniques which are Roberts, Prewitt, Sobel and Canny. In this paper canny edge detection is implemented.

## II. LabVIEW PROGRAMMING

LabVIEW is a graphical programming environment by National Instruments (NI). LabVIEW program consists of two major components: Front Panel (FP) and Block Diagram (BD). A front panel provides a graphical user interface and block diagram contains building blocks of a system resembling a flowchart [3], few icons used in this paper are given below [4]:



: IMAQ Create VI to create or edit new image.
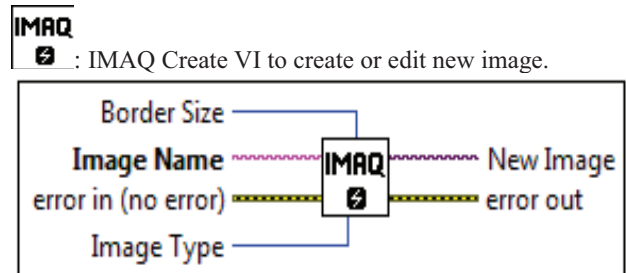




: Reads an image file, including any extra vision information saved with the image.
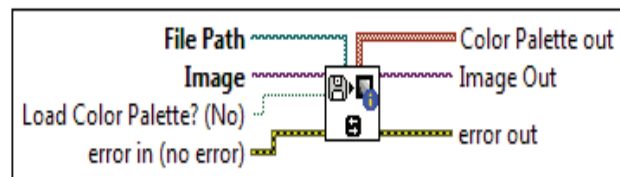




: Image Type to choose types of image (Gray Scale (U8), Gray Scale (I16), RGB (U32), HSL (U32)).



: File Path to choose the path of image (.png) only

 : Image information indicator to display the image

### III. IMPLEMENTATION USING MATLAB

The MATLAB (Matrix Laboratory) is a proprietary programming language developed by MathWorks. It contains thousands of built in functions for wide variety of concepts in different specializations. It includes more number of Toolboxes for solving the problems in various fields of research like Signal Processing, Image Processing, Communications, Fuzzy logic, Neural Networks etc. It contains the Graphical User Interface (GUI) for better understanding the solution of various problems [5].

In this paper MATLAB programming is implemented for basic operations on images using Image Processing toolbox which are extraction of RGB components from the RGB color image and canny edge detection method. These image processing concepts are implemented here for comparing the results with LabVIEW programming.

In RGB color image, the colors appear as spectral components of red, green and blue. The color of the pixels in RGB image is formed by the combination of red, green and blue components, these are called as color channels or color components [6]. The intensity values of the RGB color image is represented as

$$I_{RGB} = \left( I_R(x, y), I_G(x, y), I_B(x, y) \right)$$

Where $I_R(x, y)$ is intensity of the pixel at $(x, y)$ in the red channel, $I_G(x, y)$ is the intensity in the green channel and $I_B(x, y)$ is the intensity in the blue channel.

Figure 3, 4 and 5 shows the red, green and blue components of the input image shown in figure 2.
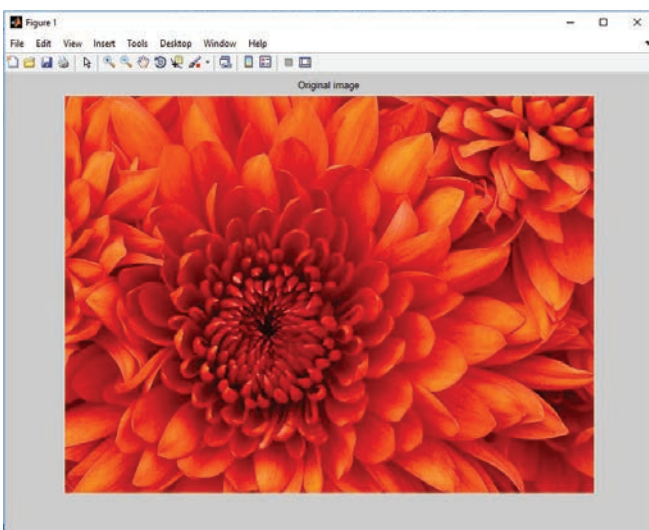


Figure 2. Input image
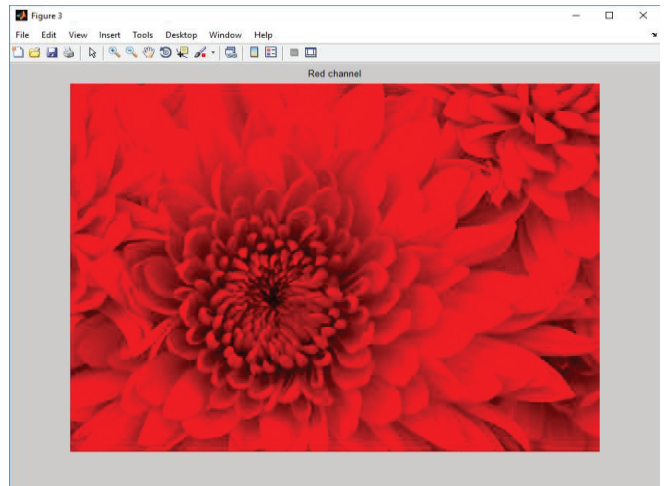


Figure 3. Red Component in RGB color image
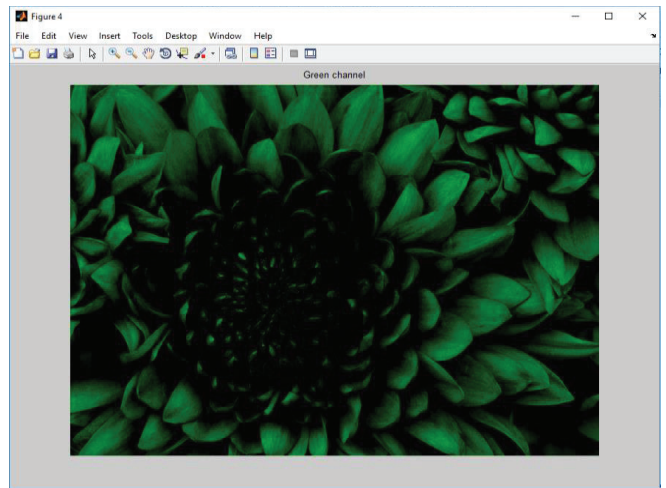


Figure 4. Green Component in RGB color image
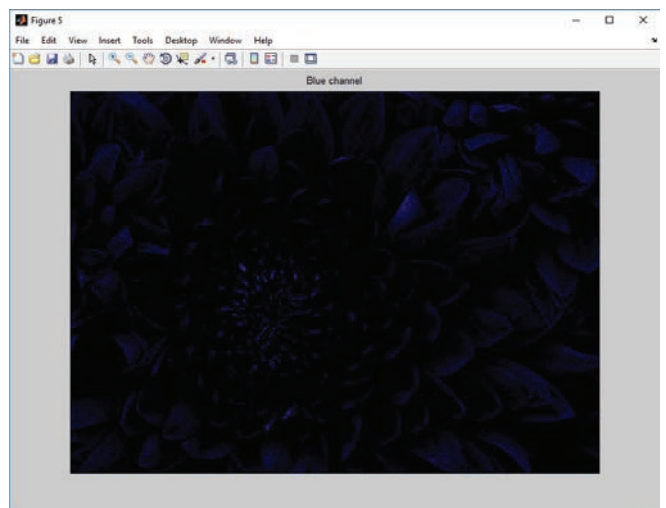


Figure 5. Blue Component in RGB color image

The edge detection of the images are used for many applications in the image processing [7]. The edge detection of the images is carried out by the flowchart shown in figure 6.
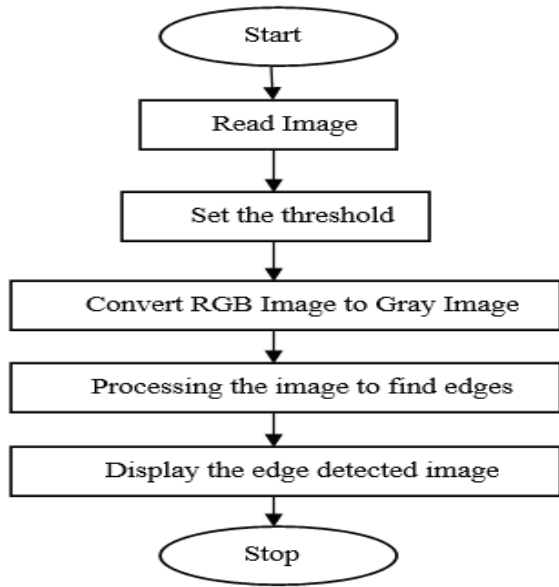
Figure 6. Flow chart for edge detection

There are different types of edge detection techniques and out of these canny edge detection technique gives the good results. Figure 8 shows the output image obtained by applying the canny edge detection technique to the input image shown in figure 7.
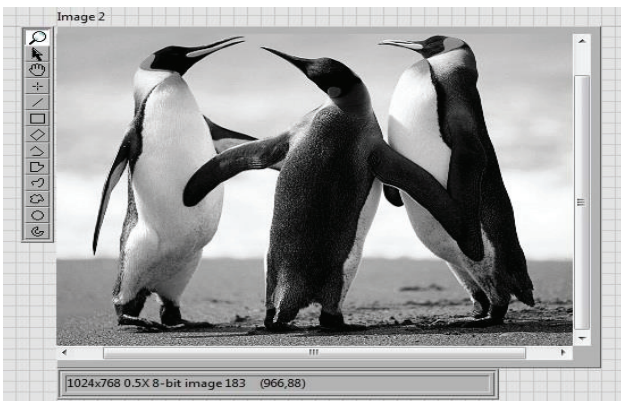


Figure 7. Input gray scale image
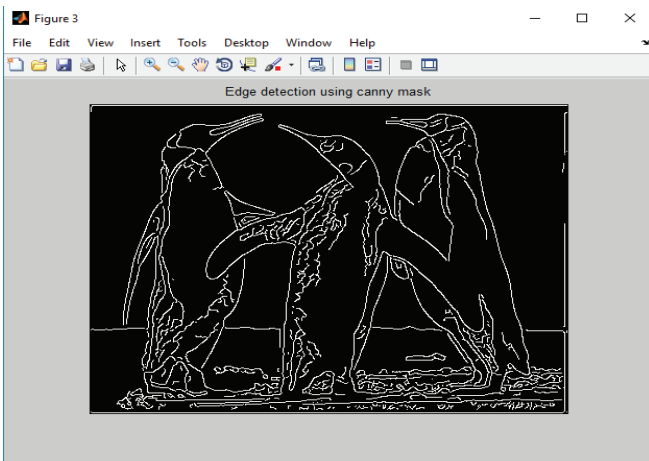


Figure 8. Output image from canny edge detection using MATLAB

## IV. IMPLEMENTATION USING LABVIEW

The Front panel view of LabVIEW is shown in figure 9. The applications of Digital Image Processing are implemented using LabVIEW toolkit 2015.
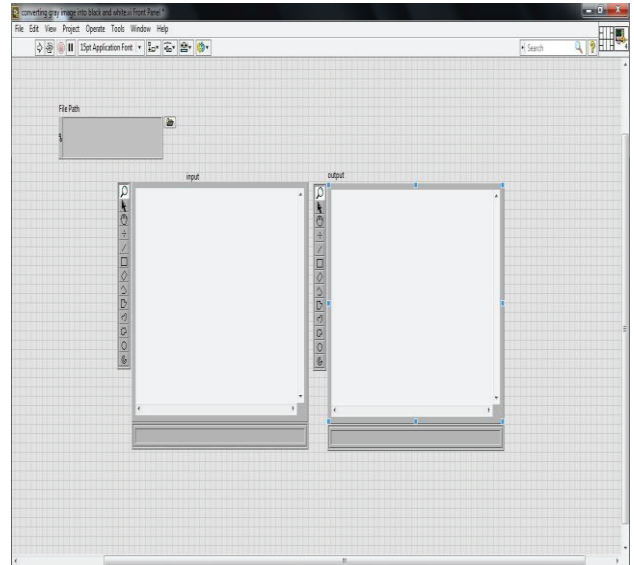


Figure 9. Front Panel of LabVIEW

The block diagram for extracting RGB components from the color image is shown in figure 10. Figure 11, 12 and 13 shows the red, green and blue components respectively obtained for the input image shown in figure 2.
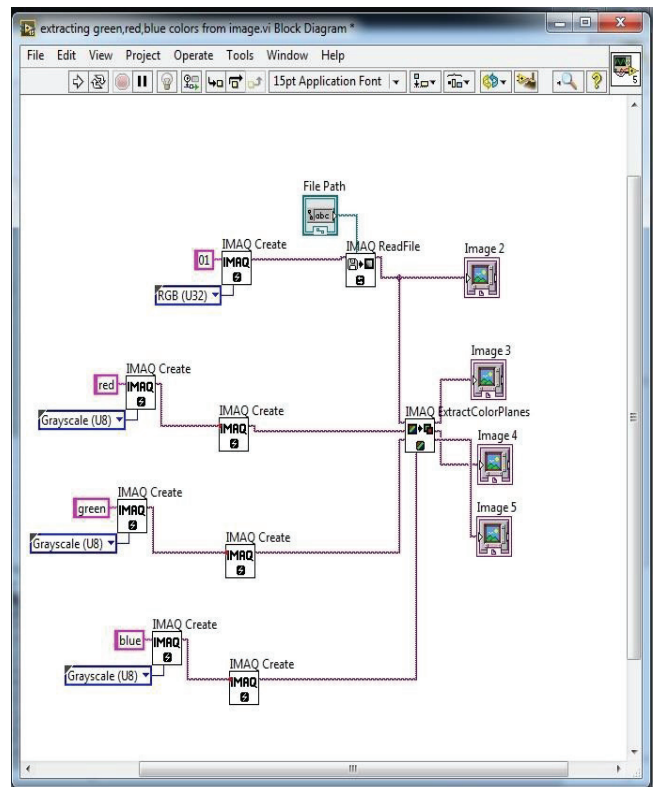


Figure 10. Block diagram for extracting RGB components
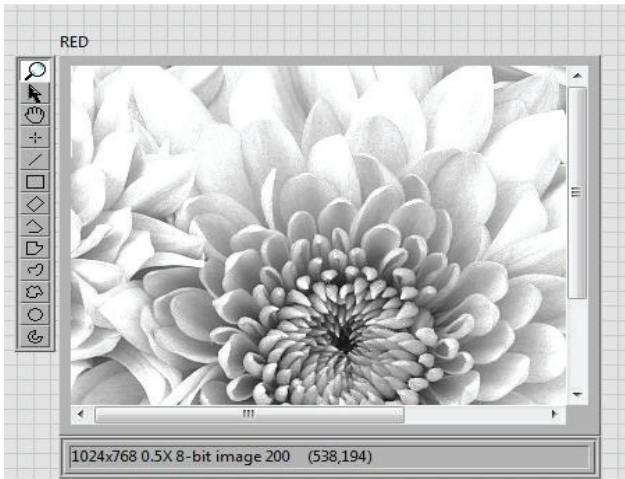
Figure 11. Red Component in color image
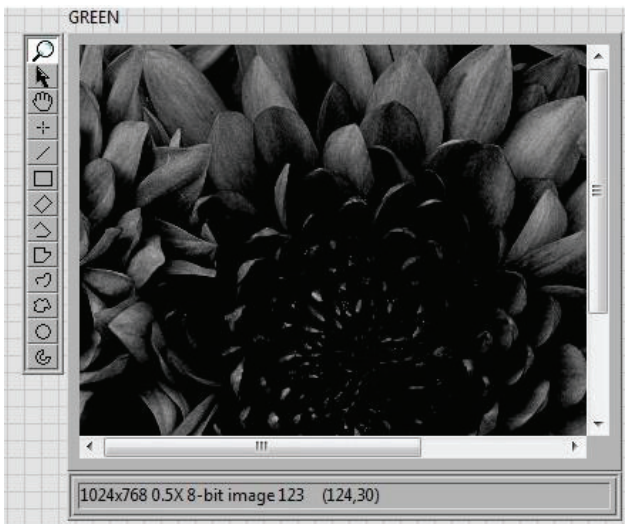


Figure 12. Green Component in color image
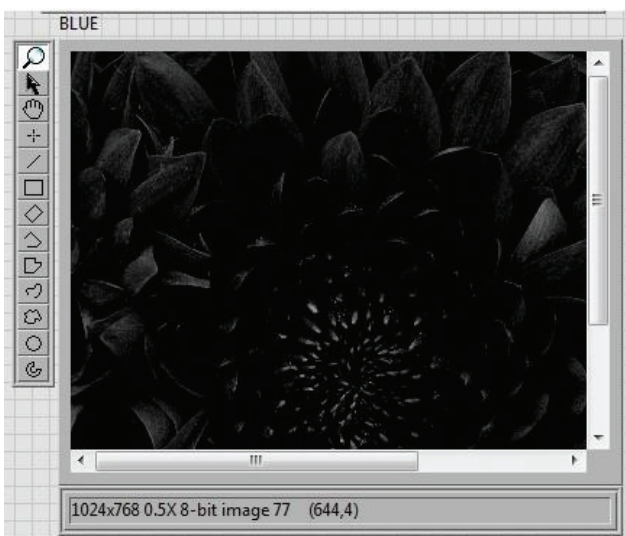


Figure 13.  Blue Component in color image

The block diagram for converting gray scale image to binary image is shown in figure 14.
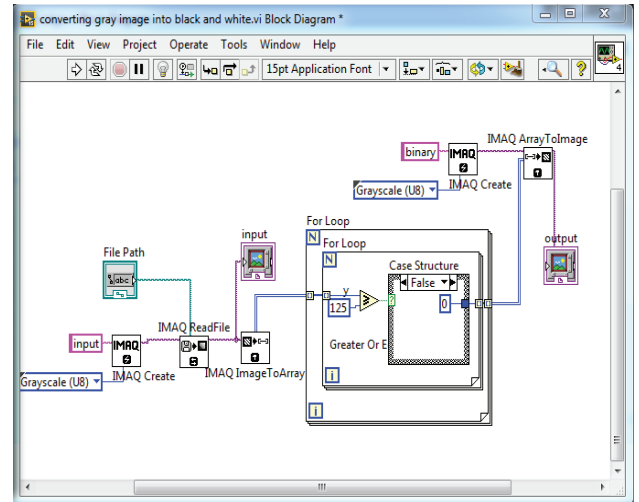


Figure 14.  Block diagram for converting gray scale image into binary image

By applying the image shown in figure 2 as input to the block diagram shown in figure 14 to convert the gray scale image into binary image, the output image obtained is shown in figure 15.
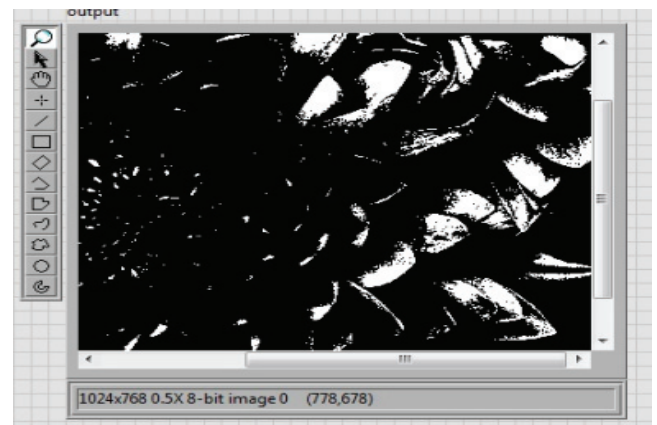


Figure 15. Binary image from grayscale image

The block diagram for implementation of edge detection for color image using canny edge detection method is shown in figure 16.
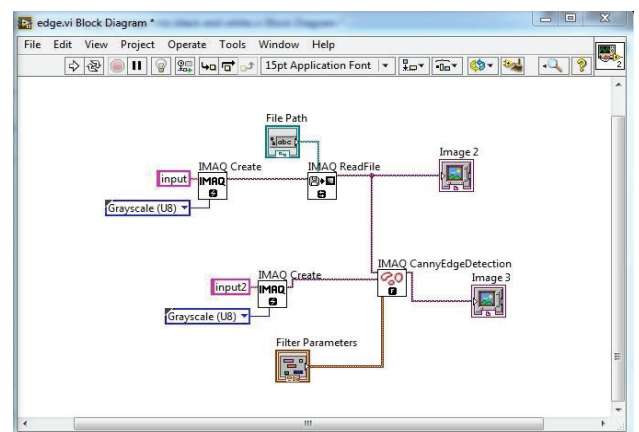


Figure 16. Block diagram for canny edge detection

The input image applied to the canny edge detection method implemented in figure 16 is shown in figure 7. The output image obtained from the canny edge detection method [8, 9] implemented in LabVIEW is shown in figure 17.
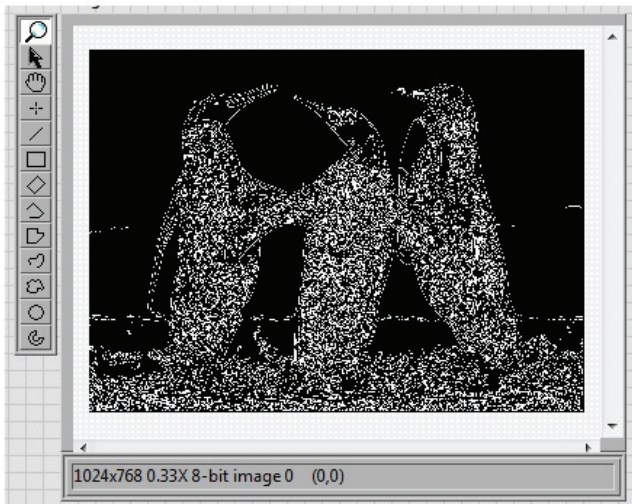


Figure 17. Output image from canny edge detection using LabVIEW

## V. CONCLUSIONS

In this paper the basic image processing applications are implemented using MATLAB and LabVIEW. The extraction of RGB components from RGB color image and canny edge detection technique is implemented using both MATLAB and LabVIEW programming. The conversion of gray scale image to binary image implemented using LabVIEW is also presented. From the experimental results it is concluded that the implementation of image processing applications is easy and more efficient in LabVIEW compared to MATLAB in real time applications. MATLAB programming takes more processing time compared to LABVIEW programming.

## REFERENCES

[1] Rafael C. Gonzalez (University of Tennessee), Richard E. Woods (MedData Interactive) and Steven L. Eddins (The MathWorks, Inc.), in '*Digital Image Processing Using MATLAB*' Second Edition, 2009 by Gatesmark, LLC.

[2] S.Sridhar, Digital Image Processing, Oxford University Press, 2011.

[3] N. Kim, N. Kehtarnavaz, and M. Torlak," LABVIEW Based Software Defined Radio: 4-QAM Modem*"*, Journal of Systemic, Cybernetics and Informatics (IIISCI), Vol. 4, No.3, ISSN 1690-4524, 2006.

[4] G. C. Panayi, ―Implementation of Digital Image Processing Functions Using LabVIEW, M.S. thesis, Dept. of Electrical and Computer Engineering, Univ. of Texas at Austin, May 1999.

[5] MATLAB and Simulink for Technical Computing, URL: http://www.mathworks.com, July 2010.

[6] Tarun Kumar, Karun Verma, "A Theory Based on Conversion of RGB image to Gray image", International Journal of Computer Applications (0975 – 8887) Volume 7– No.2, September 2010.

[7] X.L. Zhang ―Digital image edge detection with MATLAB I. Journal of Jilin institute of chemical technology. Vol.27, no.2, pp.59-61, 2010.

[8] Ravi Kumar A.V, Nataraj K.R, "Result Analysis of LabVIEW and MATLAB in Application of Image Edge Detection" International Journal of Computer Applications (0975 – 888) Volume 48– No.9, June 2012

[9] Edge Detection‖, chapter of ―NI Vision Concepts Help, online Resource.

# Analysis of Variation in Relative Mobility with Traffic Load in Wireless Mobile Network

Gaurav Sharma[1] and Manjeet Kharub[2]

[1]Asst. Professor, CVR College of Engineering/ECE Department, Hyderabad, India
Email: ergaurav209@yahoo.co.in
[2]Asst. Professor, CVR College of Engineering/ Mechanical Engineering Department, Hyderabad, India
Email: manjeetkharub@gmail.com

*Abstract:* **Call blocking and calls dropping in cellular communication system are the critical issues. Sometimes it occurs due to less network coverage, and handoff mechanism. Handoff is the process of moving from one cell to another cell, when the call is in the progress. This paper presents one of the handoff mechanism using different pathloss models to avoid the call blocking and call dropping probability using Gaussian noise and hysteresis margin. Due to small size of the cell, more handovers occur. Since, capacity of the network increases due to small size of the cell. It also increases the delay and switching load in the network. Quality of Service (QoS) also depends on the quick handoff mechanism, as unnecessary handoffs affect the QoS and should be avoided. In this paper, the proposed scheme supports better QoS and grade of Service (GoS).**

*Index Terms:* **Cellular network, Heterogeneous Network, Handoff, QoS, GoS.**

## I. INTRODUCTION

In wireless mobile communication, coverage and connectivity are the main issues that should be handled by the service provider, due to poor coverage and connectivity, the QoS degrades [1]. The user needs full service irrespective of any area. In cellular communication system, limited bandwidth is provided to the service providers. It is necessary for the service providers to manage all the communication within this limited bandwidth [2, 3]. Therefore, the frequency reuse concept is being used to make it possible. To achieve this, the coverage region is distributed into the smaller area called cells. By using the frequency reuse concept, the capacity is also increased. More number of users can avail the service; hence coverage and connectivity are increased. But due to increased capacity, interference may be increased [4, 5].

In each smaller region, transmitter and receiver are used to serve the users within its coverage. Transmitter and receiver of each cell are connected through wireless link. To provide the constant service, ongoing calls can be transferred from the presently serving cell to different cell when the users move in between the cells [1, 3, 6]. Heavy traffic flow in the network is generated due to large number of users in the network. When such a large number of users are present simultaneously in the particular cell, then that cell becomes hot spot cell. Therefore, it is necessary to design such a mechanism, which can handle the traffic routing properly, and allow the users to automatically move from the congested cell to make the network balance [2-4]. Network balancing [7] is the ability to balance the traffic

between two links without using complex routing protocols. This capability balances network sessions like Web, email, etc. over multiple connections in order to spread out the amount of bandwidth used by each user, thus increasing the total amount of bandwidth available [5]. In this paper, analysis of variation in relative mobility with traffic load in heterogeneous mobile network has been carried out. To balance the traffic load in the hotspot cell, an algorithm is proposed in this paper.

## II. HETEROGENOUS NETWORK AND HANDOFF MECHANISM

In cellular system, mobile station and base station are the basic units. These both units have different processing power, memory, communication range, power, etc. which make the system Heterogeneous Network commonly called as HetNets. Several mobile users are served by the single base station, due to which base station is having some high processing capabilities. On the other hand, homogeneous networks are the networks in which processing power, memory, communication range, etc. are kept same. But it is not usually considered in cellular systems [8, 9, 10]. As the traffic demand grows and the number of RF chains change, the network relies on cell splitting or additional carriers to overcome capacity and link budget limitations and maintain uniform user experience. This deployment process is complex and iterative [7]. A more flexible deployment model is needed for operators to improve broadband user experience in a ubiquitous and cost-effective way. Continuous service from the base station depends on the location of the mobile user and its mobility i.e. whether it is in the coverage range of the base station or not. If it moves out from the coverage range of the present serving cell, then it is not guaranteed to provide continuous service. Operations in HetNets are somewhat critical due to managing different parameters.

However portable administrators are hoping to embrace the heterogeneous cell arrangement, HetNet is the way to deal with, empower them to attain their objectives for coverage and capacity [11, 12].

A handoff alludes to the way toward exchanging an ongoing call or information session from one serving cell in a cellular network to different or starting with one direct in a phone then onto the next. An all-Around actualized handoff is essential for conveying continuous support of a guest or information session client. In Europe and different nations, a

handoff is known as a handover. Cell systems are made out of cells, each of which is equipped for giving broadcast communications administration to supporters meandering inside them [2, 7]. Every cell can just serve up to a specific region and number of endorsers. Consequently, when any of these two cutoff points is achieved, a handoff follows.

For example, if an endorser takes off the service from present serving cell or moves out of the coverage zone of a specific cell while entering another, a handoff happens between the two cells [4]. The duties of the cell that served the call previous to the handoff is exchanged to the second cell [12, 13]. A handoff may likewise be activated when the number of subscribers utilizing a specific cell has just achieved the cell's most extreme breaking point (capacity). Each time a mobile user goes starting with one cell then onto the next, the system naturally switches the obligation of coverage from one serving cell to other. It is called, "Hand Off" mechanism [8].

With the appearance of CDMA (Code Division Multiple Access) frameworks where same kind of networks can be utilized by a few mobiles and where it is conceivable to nearby base stations or cell segments to utilize a similar recurrence channel there are various diverse sorts of handoff that can be executed. For the most part, handoff in versatile systems can be arranged into two kinds [1]:

- Hard handoff

- Soft handoff

Although these types of handovers empower the mobile users to be associated with an alternate base station or distinctive cell part, they are accomplished in marginally extraordinary ways and are accessible under various situations.

At a time, two connections can be maintained; such type of technology is performed in 3G CDMA, where neighbouring cell provides the connection to the new incoming mobile users before their connection break from the old base station. Since, the neighbouring cell also works on similar frequency, due to which soft handoff is possible. In this type of channel accessing technique, to avoid the interference from the neighbouring cells, unique codes are used for each mobile user [7].

## III. CDMA System and Handoff Measurement Procedure

CDMA (Code-Division Multiple Access) is the multiplexing technique that is used to access the channel. In CDMA, a large frequency set is used by the wireless channel to access it by using a code of n bits, where n is large number greater than 50. The unique codes consist of binary digits such as 1s and 0s. In CDMA system, ultra-high-frequency (UHF) of frequency range between 800 MHz to 1.9 GHz is used by the users to make the accessible speed faster and transmission without interference [1, 3]. In this interference is very less from the neighbouring cells due to use of the unique code by the mobile users.

The CDMA system mainly uses direct sequence spread spectrum and efficient error control codes. In this technique,

all the information is transmitted at same frequency at same time with different codes, due to which inter cell and intra cell interference becomes very less. By using physical layer schemes, it is possible to use the frequency again in the cells unlike the other multiple access techniques. To minimize the inter cell interference, fast power control mechanism is used. The forward channel in CDMA is between the base station and mobile station. In this forward channel, QPSK (Quadrature Phase Shift Keying) modulation is used. In CDMA, the air interface is by far the most complex of all multiple access techniques [11, 12]. This technique uses spreading code methodology to spread the symbols before sending these codes from transmitter. On the receiver side, these codes are de-spread using correlator to generate the original message signal. However, CDMA uses the unique codes for the information transmission; due to it in CDMA soft handoff is employed.

The handoff system can be divided into three stages: measurement, decision and execution phases as shown in Fig. 1. In the measurement phase, measurement of the information required for handoff is carried out. Typically, it is measured by the mobile station by calculating the $E_c / I_0$ of the Common Pilot Channel (CPICH) of its present serving cell and alternate neighbouring cells. In the second phase of handoff procedure, first step results (measurement results) are compared with the predefined threshold values, that is decided by the mobile whether the handoff should be initiated or not. In the execution phase, based on the decision performed by decision phase, handoff process is completed. As soon as the process is completed, different parameters are changed according to the handoff type i.e. hard handoff or soft handoff.
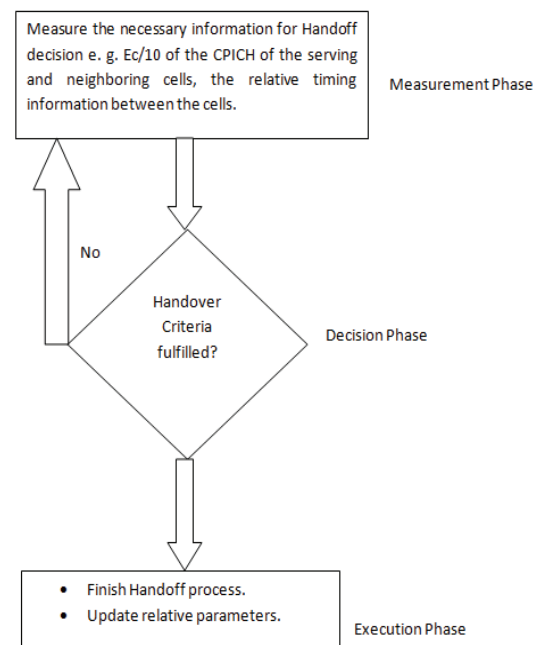


Figure 1. Different phases of handoff initiation.

In the CDMA system, soft handoff mechanism is used as discussed already. But it is necessary for the system to control the handoff initiation time. It means there should not be too early or too late handoff. Since too early or too late handoff affects the QoS of the system. Therefore to mitigate

this problem, RSS (received signal strength) threshold has been used in this paper. RSS threshold provides the enough time to the mobile users to initiate the handoff process [5, 12, 13].

It is also necessary to choose the threshold value very carefully in order to control the handoff time. By considering this factor, QoS has been improved and avoids too early and too late handoff initiation. This factor is called as adaptive RSS threshold (*Thresmin*). If any mobile user moves out of the serving cell's coverage region, then *Thresmin* helps in determining the handoff decision. This complete process is carried out with in very less time, due to which call dropping probability is decreased.

Quality of service (QoS) is measured in terms of call blocking probability and call dropping probability. The call is blocked if there are no available channels. The blocking probability can be obtained from the analysis of an M/M/n/n queue. In general, the first M indicates call arrivals are modeled as Poison process with arrival rates of λ call/s, the second M refers to exponential service time with mean $1/\mu$ s/call, the first n refers to the number of channels, and finally, the second n refers to maximum number of acceptable users before blocking occurs. The famous Erlang-B equation (also called blocked calls cleared formula) [10] under the conditions of M/M/n/n is given by:

$$P_B = \frac{\left(\lambda/\mu\right)^n / n!}{\sum_{k=0}^{n} \left(\lambda/\mu\right)^k / k!} \tag{1}$$

## IV. SIMULATION RESULTS AND PERFORMANCE MEASURE

The simulations of the proposed algorithm are performed in MATLAB, following assumptions and parameters are taken for simulation, as tabulated in Table I.

TABLE I.
SIMULATION PARAMETERS

| Parameters | Values |
|---|---|
| Number of users | 70 |
| Radius of cell | 1.5 km |
| Neighboring cells | 8 |
| Carrier Frequency | 500 MHz to 1000 MHz |
| Mobile Station Height | 1 m to 10m |
| Capacity of serving cell | 1 to 8 |
| Antenna Heights | 30m to 200 m |
| Radio propagation model | Hata Okumura path loss model and free space path loss model |
| Distance between base station and mobile station | 1km to 15 km |
| *hre* | 2 m |
| *hte* | 100 m |
| *sdA* | 3.5 |
| Gaussian noise | 3 dB |
| Hystersis margin | -5 dB |
| *sdB* | 1 |
| Environment | Urban Environment |
| Base Station Antenna Height | 50 m to 100 m |

Probabilities of call blocking (CB) and handoff call dropping (HCD) are analyzed for urban area. Analysis is carried out by keeping the channels reserved with respect to relative mobility.
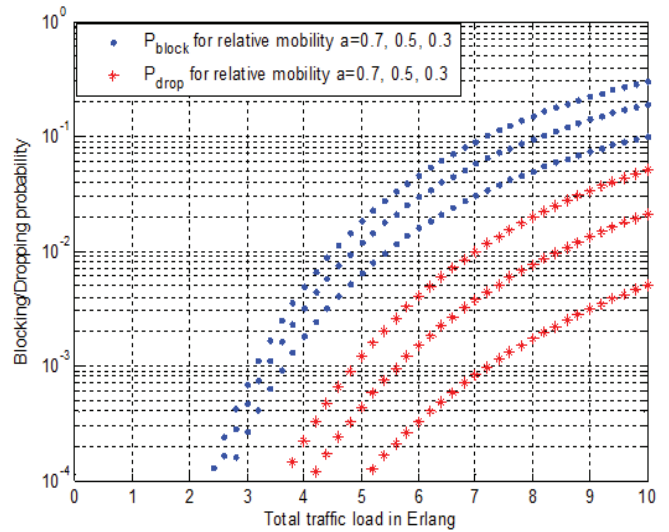


Figure 2. CB and HCD probabilities for different relative mobility (Reserved Channels=3)

Call blocking (CB) probability is measured as the probability of call blocked when any user tries to attempt it. It can be easily realized that at a reasonable increase in traffic load, both the new blocking and handoff dropping probability will increase significantly. Also a decrease in relative mobility will decrease blocking and dropping probabilities of ongoing calls. It can also be observed as the number of reserved channels decreased, call blocking probability is also comparatively improved.
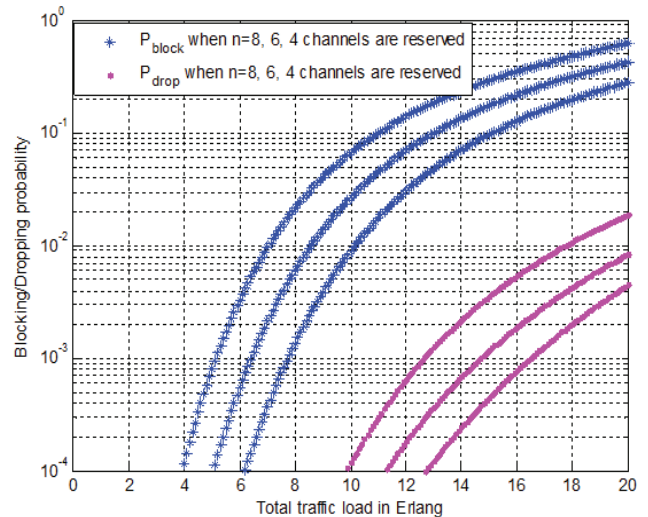


Figure 3. CB and HCD probabilities for different reserved channels for relative mobility *a* =0.7

Simulations have been carried out in MATLAB software with different values of relative mobility to measure the call blocking (CB) and handoff call dropping (HCD) probability. Call dropping probability is the measure of the probability when any ongoing call terminates. It is due to the reasons of

handover failure. It is measured in the form of metric as handover blocking probability.

Traffic intensity across the entire radio system is known as traffic load. It is measured in Erlangs. It measures the number of handoff per call. If relative mobility increases, number of handoff per call also increases [5, 9].

In some cases, the results have been analyzed when some of the channels are kept reserved. Total traffic load is measured in Erlang, Relative mobility and total number of channels are represented by $a$ and $\eta$ respectively. Results obtained are shown in Fig. 2, Fig. 3, Fig. 4, and Fig. 5.

It can be observed that there is trade-off between call blocking (CB) and handoff call dropping (HCD). If service provider has the main concern for low handoff call dropping, then it is required to keep more channels reserved for it. If more channels are reserved for handoff call dropping, then the probability of blocking of new calls is increased.
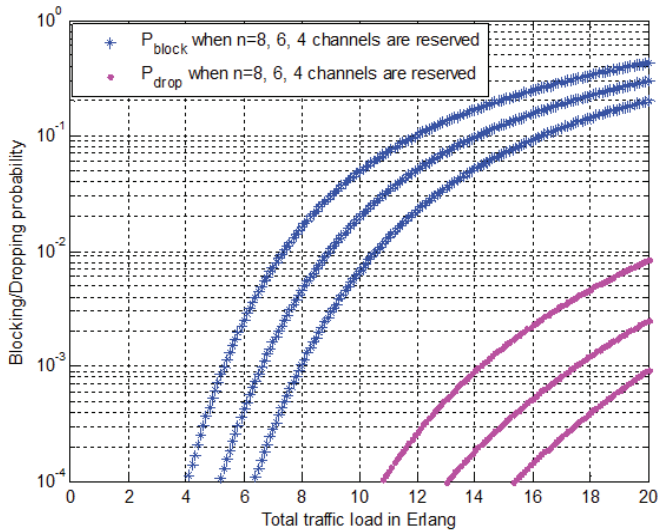


Figure 4. CB and HCD probabilities for different reserved channels for relative mobility $a$ =0.4
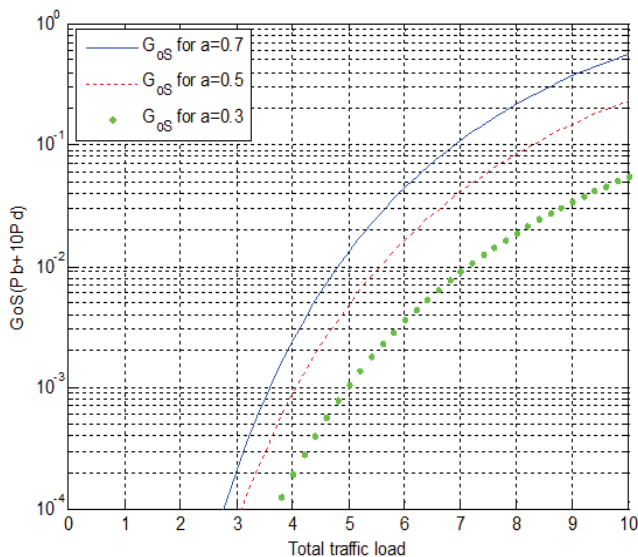


Figure 5. GoS for different relative mobility (3 channels are kept reserved)

In the dense population area, service provider divides the region into smaller cells to increase the capacity. As the number of cells and handoff are directly proportional to each other. A mobile user has to cross many boundaries of the cell for smaller cells and handoff occurred frequently. This type of scenario is happened in dense urban area. Therefore, this frequent handoff process degrades the QoS and increased the CB and HCD. The performance is measured by evaluating the blocking probability of the calls which is going to be start and dropping of the calls which are ongoing. Grade of Service (GoS) is a measure of congestion which is determined as the likelihood of a call being blocked, or the likelihood of a call being deferred past a specific measure of time [7], which is shown in Fig. 5.

TABLE II.
CALL BLOCKING CONDITIONS

| Signal Condition \ Channel Condition | 1 | 2 | 3 | 4 |
|---|---|---|---|---|
| G | SL | SL | SL | BL |
| N | SL | SL | BL | BL |
| H | SL | BL | SL | BL |
| R | BL | BL | BL | BL |

Table II shows the possible cases of the blocked new calls attempt. The number of blocked new call attempts (NB) can be read as follows:

BL: Blocked, SL: Successful

G: Mobile user receives the signals from both base station i.e. BS1 and BS2.
N: BS1's signal is acceptable but BS2 is not acceptable.
H: BS2's signal is acceptable but BS1 is not acceptable.
R: Signals from BS1 and BS2 are not acceptable.

1: Channel available at BS1 and BS2.
2: Channel available at BS1 but not available at BS2.
3: Channel available at BS1 but not available at BS2.
4: No channels are available either at BS1 or at BS2.

Therefore, the calls which are observed as blocked can be calculated as:

$$NB = NM4 + NO3 + NO4 + NH2 + NH4 + NJ1 + NJ2 + NJ3 + NJ4 \qquad (2)$$

The blocking probability (PB) is defined by:

$$PB = \frac{NB}{NG} \qquad (3)$$

Here, *NG* represents the new calls attempts that are generated for establish new connection.

Table III shows all the possible cases in which the ongoing call is dropped due to too late initiation of handoff or improper handoff.

DP: Drop, ND: Not dropped

K: Ongoing serving link quality is acceptable.

U: Ongoing serving link quality is not acceptable or up to the mark, but alternative link quality is good.

T: Neither ongoing link quality nor alternative link's quality is acceptable.

1: Handoff process is initiated with availability of the channels in alternative BS.

2: Handoff process is initiated when there is no channel available in the neighboring cell's base station.

3: Handoff process is not started.

TABLE III.
HCD CONDITIONS

| Initiation and Channel Condition / Signal Condition | 1 | 2 | 3 |
|---|---|---|---|
| K | ND | ND | ND |
| U | ND | DP | DP |
| T | DP | DP | DP |

Therefore, the number of ongoing calls which are observed as dropped due to improper handoff can be calculated as:

$$ND = NF2 + NF3 + NG1 + NG2 + NG3 \qquad (4)$$

The forced termination probability (*PFT)* is defined by:

$$PFT = \frac{ND}{(NG - NB)} \qquad (5)$$

The simulation observations show that CB and HCD probabilities are increased with increase in traffic load. As there is more traffic load, the more channels become busy. It can also be observed from the simulation results that CB and HCD probability are decreased with increase in relative mobility, even after keeping the traffic load constant. It shows that relative mobility also affects the system performance, as more mobility results in more handoff; due to which handoff mechanism is not performed well especially in the areas where the coverage is less. It can be seen that the constrained end likelihood abatements and watches out for a base level as the offered traffic diminishes. At the point when the offered traffic is low, the constrained terminations are fundamental because of handoff starts.

## V. CONCLUSIONS

In this paper, variation in relative mobility with traffic load in wireless mobile network has been analyzed, which balances the traffic load according to the relative mobility in heterogeneous mobile network. It can be observed that there is trade-off between call blocking (CB) and handoff call dropping (HCD). If service provider is having the main concern for low handoff call dropping, then it is required to keep more channels reserved for it. If more channels are reserved for handoff call dropping, then the probability of blocking of new calls is increased. As a result, capacity of the serving cell is decreased. It can also be easily realized that GOS decreases with increase in traffic load, because with the increase of traffic load, more channels are required for keeping the call blocking and call dropping probability low.

## REFERENCES

[1] A.E. Xhafa and O.K. Tonguz, "Handover performance of priority schemes in networks" *IEEE Trans. Vehicular Tech.*, vol. 57, no. 1, pp. 565-577, Jan. 2008.

[2] G. Sharma and A. Kumar, "Fuzzy logic based 3D localization in wireless sensor networks using invasive weed and bacterial foraging optimization," Telecommunication Systems, vol. 67, no. 2, pp. 149–162, May 2017.

[3] G. Sharma and A. Kumar, "Modified Energy-Efficient Range-Free Localization Using Teaching–Learning-Based Optimization for Wireless Sensor Networks," IETE Journal of Research, vol. 64, no. 1, pp. 124–138, Jul. 2017.

[4] Kim, D., Sawhney, M. and Yoon, H., "An effective traffic management scheme using adaptive handovertime in next generation cellular networks" Int. Journal of Network Management, pp. 139-154, 2007.

[5] K. I. Itoh and S. Watanabe and J. S. Shih and T. Sato, "Performance of handoff algorithm based on distance and RSSI measurements," *IEEE Trans. Vehicular Technology,* vol. 51, no. 6, pp. 1460-1468, Nov. 2002.

[6] G. P. Pollini, "Trends in handover design," *IEEE Comm. Magazine,* vol. 34, pp. 82-90, March.1996.

[7] D. K. Panwar and L. Shyam, "Coverage analysis of hand off algorithm with adaptive hysteresis margin, "Proc.of 10th International Conference on Information Technology, pp. 133-138, Dec. 2007.

[8] S. H. Wie, J.-S. Jang, B.-C. Shin and D.-H. Cho, "Hand off analysis of the hierarchical cellular system," *IEEE Trans. Vehicular Technology*, vol. 49, no. 5, pp. 2027-2036, Sept. 2000.

[9] G. Sharma, & A. Kumar, "Improved DV-Hop localization algorithm using teaching learning based optimization for wireless sensor networks". Telecommunication Systems, vol. 67, no. 2, pp. 163-178, 2017.

[10] M. Ruggieri, F. Graziosi and F. Santucci, "Modeling of the handover dwell time in cellular mobile communications Systems," *IEEE Trans. Vehicular Technology*, vol. 47, no.3, pp. 489-498, May. 1998

[11] G. Sharma, & A. Kumar,"Dynamic Range Normal Bisector Localization Al gorithm for Wireless Sensor Networks". Wireless Personal Communications, vol. 9, no. 3, pp. 4529-4549, 2017.

[12] R. Verdone and A. Zanella, "Performance of Received Power and Traffic-Driven Handover Algorithms in Urban Cellular networks", *IEEE Wireless Communication,* pp. 60-71, February 2002.

[13] Nandakumar S., Singh Rahul & Singh Sanjeet, "Traffic Driven & Received Signal Strength Adaptive Handoff Scheme," Int. Journal of Comp. App. (0975-8887), vol. 21, no.6, May 2011.

# High Performance ALU Using Carry Look-ahead Adder

V.Silpa kesav[1] G.Sai Srinadh[2] Shaik Javeed[3]
Asst. Professor, CVR College of Engineering/ECE Department, Hyderabad, India
Email: shilpakesav@gmail.com
M.Tech student, CVR College of Engineering /ECE Department, Hyderabad, India
Email: saisrinathraju@gmail.com,
M.Tech student, CVR College of Engineering /ECE Department, Hyderabad, India
Email: javeed.shaik249@gmail.com

*Abstract:* **A Low Power 8-bit Arithmetic Logic unit (ALU) using a Carry look-ahead adder (CLA) and placing Low $V_t$ ($LV_t$) cells in Critical path is anticipated. The ALU is designed in 90nm CMOS technology. ALU is the most essential circuit in any processor. It consists of AE, LE, CLA and CE. This ALU is designed to calculate Arithmetic and Logical operations. Power and Delay values of different 8-bit adders like CLA, Sparse and Ripple Carry Adder (RCA) are designed and compared. The simulation results show that the design of ALU using CLA and incorporating High $V_t$ and Low $V_t$ cells in the CLA gives more power and delay efficient than with only Standard threshold voltage cells.**

*Index Terms:* **Arithmetic Extender, Logic Extender, Carry Extender, Carry Look-ahead Adder, ALU.**

## I. INTRODUCTION

ALU is the major power hungry block in any microprocessor and micro controller. It performs both arithmetic and logical operations. Conventional ALU consists of Arithmetic Extender, Logical Extender, Carry Extender and Ripple carry adder. An Adder is an integral part of the ALU and it is a power density block in ALU. Hence, to improve the performance of ALU in terms of Power and delay, High $V_t$ Cells are utilized. The three different types of transistors are

1. Low $V_t$ transistor ($LV_t$)
   The low $V_t$ transistor type is used for applications where the speed is of primary importance. The disadvantage of this type of transistors is that, due to low threshold Voltage ($V_t$), the static power is very high.
2. Standard $V_t$ Transistors ($SV_t$)
   The standard $V_t$ transistor type is used when delay and static power has been traded off.
3. High Vth Transistor ($HV_t$)
   The High Vth transistor is a favor for extremely low static power consumption.

For reducing power and delay High $V_t$ cells are used in entire ALU and in critical path of CLA, Low $V_t$ transistors are used. The reference [5] and [6] explains about the power reduction of the design using PTL and Gate diffusion

technique and [7]-[10] shows the concept of low power techniques in various Arithmetic circuits.

Here the design of an eight bit ALU with three select lines for performing eight operations are shown in Figure-1. Out of these eight operations, four operations are logical and four operations are arithmetic operations. The design includes four basic blocks: They are CLA, Logic Extender (LE), Arithmetic Extender (AE), and Carry Extender (CE). The function of LE is to operate logic operations, AE is to operate arithmetic operations, CE is for carry operations and CLA is for actual arithmetic operations.

## II. CONVENTIONAL ALU

The Arithmetic Logic Unit (ALU) is the further most significant block in microprocessor [1]. This one is used on behalf of executing arithmetic and logic operations alike addition, Subtraction, Logical OR and Logical AND. In the Conventional ALU, Ripple carry adder (RCA) is used, and the delay and power values are more. So, instead of the RCA, Carry look-ahead adder has been selected. Since, ALU requires high speed and Low power. The overall circuit for 4-bit ALU is shown in figure1 [2]. The two different Combinational circuits in front of CLA are LE and AE.
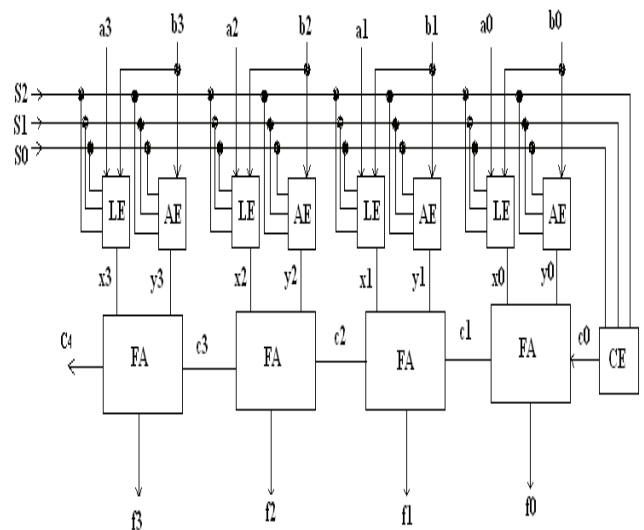


Figure 1. Existing ALU System.

TABLE I.
ALU FUNCTION TABLE

| S2 | S1 | S0 | Operation Name | Operation | X(LE) | Y(AE) | C0(CE) |
|----|----|----|----------------|-----------|-------|-------|--------|
| 0 | 0 | 0 | Pass | Pass A to output | A | 0 | 0 |
| 0 | 0 | 1 | AND | A AND B | A AND B | 0 | 0 |
| 0 | 1 | 0 | OR | A OR B | A OR B | 0 | 0 |
| 0 | 1 | 1 | NOT | A` | A` | 0 | 0 |
| 1 | 0 | 0 | Addition | A + B | A | B | 0 |
| 1 | 0 | 1 | Subtraction | A – B | A | B` | 1 |
| 1 | 1 | 0 | Increment | A + 1 | A | 0 | 1 |
| 1 | 1 | 1 | Decrement | A – 1 | A | 1 | 0 |

From the functional operation of ALU shown in table-1 the selection input S2 is the main important parameter for selecting Arithmetic operations and Logical operations. When the selection line S2 is '0', then Arithmetic operations are performed and when S2 is '1' then Logical operations are performed. S0 and S1 are going to select any one of the operations.

TABLE II.
TRUTH TABLE FOR LE

| S2 | S1 | S0 | $X_i$ |
|----|----|----|----|
| 0 | 0 | 0 | $a_i$ |
| 0 | 0 | 1 | $a_i.b_i$ |
| 0 | 1 | 0 | $a_i+b_i$ |
| 0 | 1 | 1 | $a_i'$ |
| 1 | X | X | $a_i$ |



Figure 2. Schematic of LE

In LE and AE blocks all types of logical and arithmetic operations will be carried out. The operands $a_i$ and $b_i$ are inputs to LE and AE. The LE performs the operation based on selection lines (S0, S1, and S2) and inputs $a_i$ and $b_i$. The schematic diagram and truth table of LE is shown in figure-2 and table-2 respectively.

TABLE III.
TRUTH TABLE OF AE

| S2 | S1 | S0 | bi | Yi |
|----|----|----|----|----|
| 0 | X | X | X | 0 |
| 1 | 0 | 0 | 0 | 0 |
| 1 | 0 | 0 | 1 | 1 |
| 1 | 0 | 1 | 0 | 1 |
| 1 | 0 | 1 | 1 | 0 |
| 1 | 1 | 0 | 0 | 0 |
| 1 | 1 | 0 | 1 | 0 |
| 1 | 1 | 1 | 0 | 1 |
| 1 | 1 | 1 | 1 | 1 |



Figure 3. Schematic of AE

TABLE IV.
TRUTH TABLE FOR CE

| S2 | S1 | S0 | C0 |
|----|----|----|----|
| 0 | X | X | 0 |
| 1 | 0 | 0 | 0 |
| 1 | 0 | 1 | 1 |
| 1 | 1 | 0 | 1 |
| 1 | 1 | 1 | 0 |



Figure 4. Schematic of CE

AE performs the operation based on selection lines and secondary input bi. It does not depend upon the primary input $a_i$. The schematic diagram and truth table of AE is shown in figure.3 and table.3. The Carry Extender is another important block in ALU. It depends on selection lines and gives the output of CE to CLA. The schematic diagram and truth table of CE is shown in figure-4 and table-4 respectively. Now the simulation outputs of LE and AE are $x_i$ and $y_i$ respectively. These $x_i$ and $y_i$ act as inputs to the CLA and give the simulation outputs as sum and carry. The selection lines S0, S1 and S2 are three selection lines for 8-bit ALU used to select outputs of LE and AE are $x_i$ and $y_i$
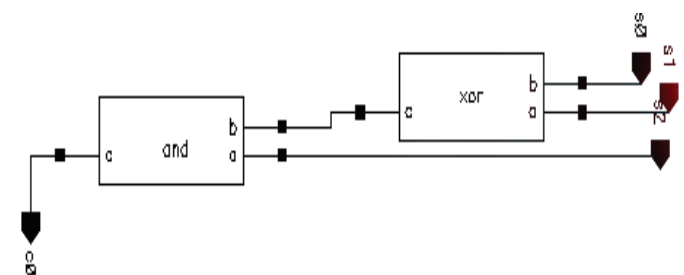
respectively. The operation of ALU through the selection lines are shown in table-I.

## III. DESIGN OF CLA

In ripple carry adder each carry-in signal is reliant on the carry out signal from the preceding full adder. The full-adder delay is very extreme. But the carry look-ahead adder [1] doesn't depend on the previous carryout signal. The equations for Carry look-ahead adder from full adder equation [1] is

$$C_{i+1} = x_i y_i + c_i(x_i + y_i) \qquad - (1)$$

From the above equation let $g_i = x_i y_i$ and $p_i = x_i + y_i$

Then equation- (1) can be written as

$$C_{i+1} = g_i + c_i p_i \qquad - (2)$$

Using equation - (2) expand the expression for designing 4-bit Carry look ahead adder.

For getting $C_1$ Substitute i=0 in the equation (2),

$$C_1 = g_0 + c_0 p_0 \qquad - (3)$$

For $C_2$ substitute i=1 in the equation -(2)

$$C_2 = g_i + c_1 p_1 \qquad - (4)$$

But $C_1 = g_0 + c_0 p_0$, so substitute equation-(3) in the equation -(4)

Then $C_2 = g_1 + p_1(g_0 + p_0 c_0)$

$$= g_1 + p_1 g_0 + p_1 p_0 c_0 \qquad - (5)$$

For getting $C_3$ Substitute i=2 in the equation - (2)

$$C_3 = g_2 + p_2 c_2 \qquad - (6)$$

And $C_2 = g_i + c_1 p_1$. Hence, Substitute $C_2$ in the equation – (6)

$$C_3 = g_2 + p_2(g_1 + p_1 g_0 + p_1 p_0 c_0)$$
$$= g_2 + p_2 g_1 + p_2 p_1 g_0 + p_2 p_1 p_0 c_0) \qquad - (7)$$

For getting $C_4$ Substitute i=3 in the equation – (2)

$$C_4 = g_3 + p_3 c_3 \qquad - (8)$$

But $C_3 = g_2 + p_2(g_1 + p_1 g_0 + p_1 p_0 c_0)$.Hence,

Substitute equation – (7) in the equation – (8).

And $C_4 = g_3 + p_3(g_2 + p_2 g_1 + p_2 p_1 g_0 + p_2 p_1 p_0 c_0$
$= g_3 + p_3 g_2 + p_3 p_2 g_1 + p_3 p_2 p_1 g_0 + p_3 p_2 p_1 p_0 c_0 \qquad - (9)$

Using the overhead carry equations, the carry look ahead adder signals from $C_1$ to $C_4$ have been produced. The outputs of two input xor gates are sums of CLA. The four bit CLA is shown in Figure.5.
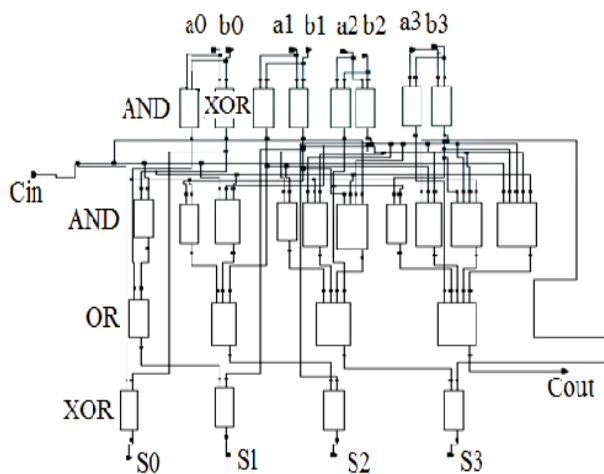


Figure 5. Schematic of 4-bit CLA

## IV. PROPOSED CLA

In this paper three 8-bit Ripple carry adder (RCA), sparse adder and Carry look ahead adder are designed and the power and delay values are calculated. Table- V shows that CLA gives best power and delay values than the other two adders.

The aim of the paper is to reduce the power and delay of the ALU. So CLA has chosen instead of RCA. Since, CLA is a key block of ALU, in order to reduce power and delay, the proposed 4-bit CLA using the High $V_t$ cell concept has been shown. In the present technology, there are different types of MOS transistors. Those are Low $V_t$ cells, High $V_t$ cells and Standard $V_t$ cells etc. The concept of High $V_t$ cells is explained here.

### 4.1 High $V_t$ Cell concept

The region just below $V_t$ of a transistor is called the sub-threshold region [4]. After the gate to source voltage $V_{gs}$ is less than threshold Voltage $V_t$, then the leakage current

$$I_{leakage} = \mu(W/L) e^{(-qV_t/\eta KT)} \qquad - (10)$$

Where μ = mobility
W = width of MOSFET
L = Length of MOSFET
K = Boltzmann's constant
T = Temperature
q = Charge of an electron
$V_t$= Threshold Voltage
η=Sub-threshold switching Coefficient

This indicates that the parameters μ, K, q are constants and only $V_t$ and W are dependent on $I_{leakage}$. As the width of MOSFET rises, leakage current also rises and as $V_t$ increases, the leakage current decreases exponentially. This, in turn lessens leakage power. So in this circuit all blocks of the Carry Look-ahead adder are designed and PMOS transistors are replaced with High $V_t$ (HV$_t$) cells. So the MOSFETs will be operated at their threshold voltage. Because of this, delay increases and power dissipation is reduced greatly.
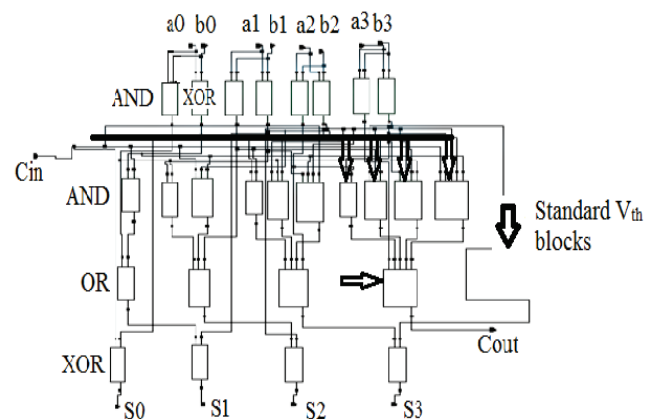


Figure 6. Proposed CLA

This justifies the usage of high $V_t$ devices for low power applications in this design. The aim of this paper is to reduce power and delay. So the combination of these cells will give better performance than using the Standard $V_t$ cells. In this topic, to reduce the delay and power, using Standard $V_t$ cells and High $V_t$ cells has been explained. Hence, in this 4-bit CLA, finding the critical path is quite important. The definition of Critical path has been given below.

Critical path: The longest delay path between inputs to output.

Here, the proposed 4-bit CLA the critical path is shown in Figure.6. It is $C_{in} \rightarrow$ Four AND gates $\rightarrow$ OR gate. So to reduce delay, critical path blocks are designed with Low $V_t$ cells. Next, to reduce power all remaining blocks are designed with High $V_t$ cells.

### 4.2 Design of 8-bit CLA

The proposed 8-bit CLA is designed with cascading two 4-bit CLA as shown in figure-7. The Carry out waveform of first CLA is connected to the $C_{in}$ of next CLA as shown in figure.7. The output waveform of the 8-bit CLA is shown in Figure-8 and Figure-9
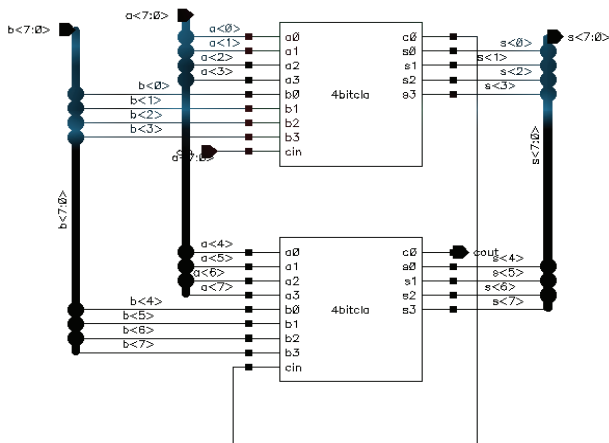


Figure 7. Schematic diagram of 8-bit CLA
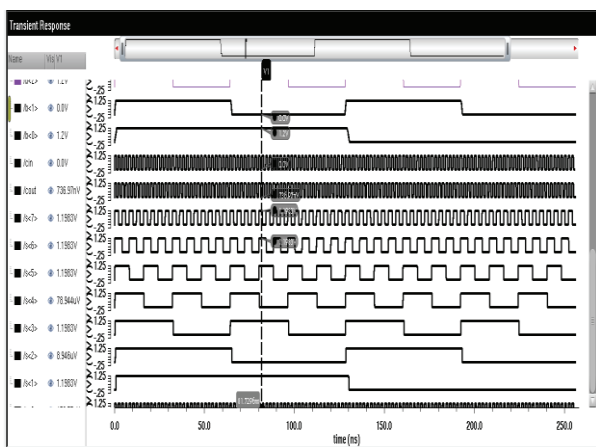


Figure 8. Simulation waveform of CLA-I
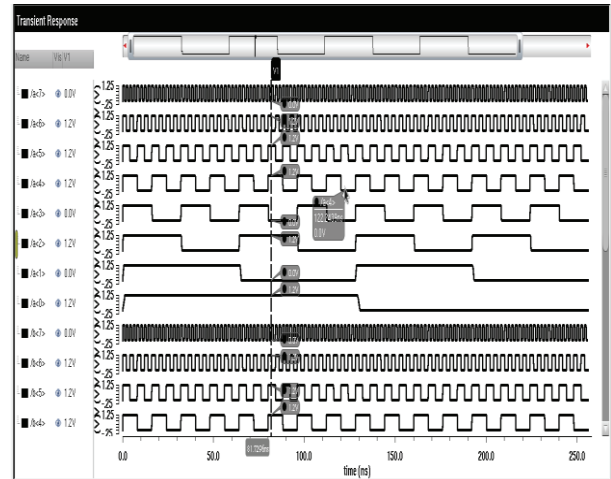


Figure 9. Simulation waveform of CLA-II

The proposed 8-bit ALU is shown in Figure.10. It has three selection lines, two 8-bit inputs a<7:0>, b<7:0> and outputs are Sum<7:0> and Carry. The internal blocks are Logical Extender, Arithmetic Extender and Carry Extender respectively. The simulation waveform of 8-bit ALU is shown in figure.11.
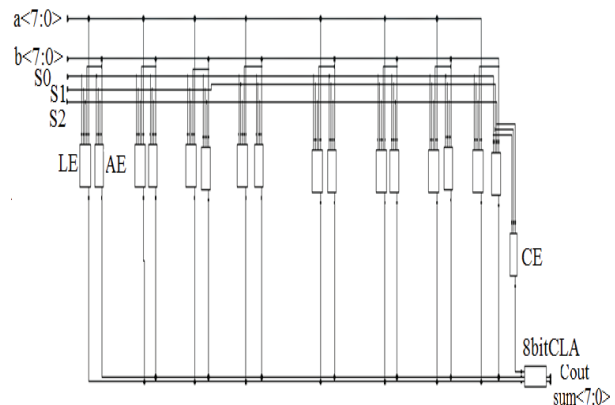


Figure 10. Proposed 8-bit ALU
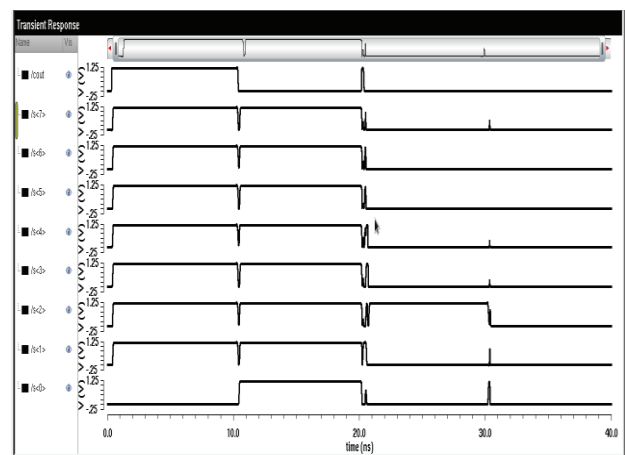


Figure 11. Simulation waveform of ALU

## V.  SIMULATION RESULTS

TABLE V.
COMPARISON TABLE OF ADDERS

| Parameter | Power($\mu$W) | Delay(pS) |
|---|---|---|
| Ripple Carry adder | 24.22 | 64800 |
| Sparse adder | 34.97 | 62400 |
| Carry Look- ahead adder | 22.92 | 81.7 |

Table –V shows the power and delay values of the Ripple Carry adder, sparse adder and Carry look-ahead adder. In the above mention adders Carry Look ahead adder gives Low power and delay.

TABLE VI.
PERFORMANCE PARAMETERS OF CARRY LOOK-AHEAD ADDER

| Parameter | Power($\mu$W) | Delay(pS) |
|---|---|---|
| Using Standard Vt Cells | 5.619 | 89.13 |
| Using High Vt Cells | 3.81 | 136.9 |
| Applying Low Vt cells in Critical Path | 3.92 | 102.2 |

Table.VI shows that the performance of CLA using Standard $V_t$ cells, using High $V_t$ cells and after applying Low $V_t$ cells in the Critical path. The average power dissipation of the Carry look-ahead adder (CLA) is 5.61$\mu$W. After applying High $V_t$ cells in all P- MOSFETs, power consumption was reduced to 3.81 $\mu$W and delay was increased to 136.9pS. I.e. 47% of power consumption was reduced and 53% of delay was increased. In this ALU design, delay is also an important parameter. So, further reducing the delay, critical path was identified and placed in all the cells in the critical path to Standard $V_t$ cells. Then 2.8% of power consumption was increased and 33.9% of delay was reduced. Hence, this high performance of CLA is used in the ALU.

TABLE VII.
PERFORMANCE OF 8 BIT ALU

| Parameter | Power($\mu$W) | Delay(pS) |
|---|---|---|
| 8bit ALU using Standard $V_t$ Cells | 50.8 | 246.3 |
| 8 bit ALU using High $V_t$ cells in CLA | 44.32 | 296.24 |
| 8bit ALU Applying Low $V_t$ in Critical Path of CLA | 43.58 | 258.5 |

Table-VII shows the performance of 8 bit ALU when it is designed with Standard $V_t$ cells, High $V_t$ cells and after applying Low $V_t$ cells in the Critical path of CLA. The average power consumption and delay of ALU is 50.8 $\mu$W and 246.3pS respectively. After placing HV$_t$ cells in CLA 14.6% of average power consumption was reduced and 20%

of delay was increased. So, to further reduce the power and delay Low $V_t$ cells are placed in critical path of CLA. Then 1.69% of power consumption was reduced and 14.5% of delay was reduced. This shows the best performance of power and delay of 8-bit ALU.

## VI. CONCLUSIONS

The main goal of this paper is to reduce power and delay. The key element in the 8-bit ALU is the 8-bit Carry look-ahead adder. So, to reduce power High $V_t$ cells are used in the P-MOSFET's of Logic gates, and to reduce delay standard $V_t$ Cells are used in logic gates of critical path. After applying the High $V_t$ Cell concept in CLA, power reduction in ALU was 14.6%, and the delay reduction was 14.5% after placing Low $V_t$ cells in the Critical path of CLA. This 8-bit ALU can be designed for other than these eight operations. This ALU can be extended to 16-bit also. This 8-bit ALU is can operate all Arithmetic and Logical operations. The total 8-bit ALU is designed in 90nm CMOS technology using Cadence tools.

### REFERENCES

[1]  Microprocessors Design Principles and Practices with VHDL by Enoch .O.Hwang.
[2]  R.Durga Bhavani, V. Silpakesav "Efficient design of Low – power 4 bit ALU using HVT Cell Concept" in CVR Journal of Science and Technology, Volume 9, December 2015, ISSN 2277-3916, pp-61-65., India.
[3]  T. Ester Rani, Dr. M. Asha Rani, Dr. Rameshwarrao, "Area Optimized Low Power Arithmetic and Logic Unit", 3rd International Conference on Electronics Computer Technology (ICECT 2011), V3-224-228.
[4]  Silpakesav, K.S. Nayanathara, B.K.Madhavi.: 'Design of Low Power SAR ADC for ECG Using 45nm CMOS', International Journal of VLSI design & Communication Systems (VLSICS) Vol.8, No.1, pp. 19-29, February 2017.
[5]  P.Satyamoorthy, S.Vijya Lakshmi and A.Daneil Raj "Efficient Design of Low power ALU using PTL-GDI Logic Full adder", in IJCA Dec 2013.
[6]  Lakshmi Swetha and K.Kalpana "An Efficient Design and Implementation of ALU using Gated Diffusion Index", in IJECS Volume 4 Issue 5 May 2015.
[7]  Amit Singh Gaur, Jyoti Budakoti, "Energy Efficient Advanced Low Power CMOS Design to reduce power consumption in Deep submicron Technologies in CMOS circuit for VLSI Design", IJARCCE, Vol.3, Issue 6, June 2014.
[8]  N.Weste and K.Eshragian, principles of CMOS VLSI Design: A Systems Perspective, Pearson/Addison Wesley Publishers, 2005.
[9]  P.Chandrakasan, S.Sheng, and R.W.Broderson, "Low-Power CMOS digital design", IEEE Solid- state circuits, Vol.27, pp.473-483; April.1992.
[10] Bellaouar.A and Elmasry.M,"Low-Power Digital VLSI Design: Circuits and Systems Boston, Massachusetts: Kluwer Academic Publishers, 1995.

# An Efficient and Automated Classification Scheme for Diagnosing Fatty Liver Disorder using Ultrasonic Images

Rajesh A
Assoc. Professor, CVR College of Engineering/ECE Department, Hyderabad,India.
Email: drrajesha86@gmail.com

*Abstract:* In the treatment of abdominal diseases like fatty liver disorder, ultrasonic images-based investigation is considered as the primary step of diagnosis. But, the noisy feature of ultrasonic images combined with the least contrasting features introduces maximum complexity during the process of automated classification. This paper contributes an Improved Active Contour Segmentation scheme for effective segmentation. Then Gray Level Co-occurrence Matrix (GLCM) and fractal features are extracted from the segmented ultrasonic images and the classification is achieved using an enhanced forest classification incorporated in the artificial neural networks (ANN) for accurate detection. The results of the proposed automated approach are investigated using classification accuracy, mean classification accuracy, true positive rate, false positive rate and true negative rate . The results of the proposed scheme also infers a classification accuracy rate of 98.73% and a mean classification accuracy rate of 97.65% compared to the baseline automated liver disorder classification techniques.

*Index Terms:* Fatty liver disorder, Improved isocontour Segmentation, Graph cuts, Taguchi Method, Fractal features

## I. INTRODUCTION

Computer-based automated diagnosis of diseases from biomedical images is considered as the potential field of research that integrates the benefits of Medical and Engineering domain [1]. The non-invasive, soft tissue visualization and economical characteristics of ultrasonic images has made them suitable for diagnosing the abdominal organs such as liver, spleen, pancreases and gall bladder [2]. In specific, liver diseases like heterogeneous liver and fatty liver can be effectively diagnosed by ultrasound images [3-4]. Heterogeneous liver belongs to the category of focal liver diseases that results in the swelling and inflammation of the organ due to pus formation caused by the infection of bacteria. Fatty liver disease relates to the category of diffused liver diseases that is caused due to the enormous deposit of triglycerides and other fat types in the liver cells. Inspite of the potential characteristics of ultrasonic images, the activity involved in classifying the normal cells from infected cells of the liver is influenced by minimum contrast, close appearances and hazy nature of images [5-7]. Inherently, the ultrasonic image of one liver disease may closely resemble the image of other liver disease or the similar ultrasonic images of the same liver disorder may exhibit different textures. This resembles of ultrasonic images result in a varying decision of the liver disorder made by the diagnosing radiologists [8]. Further, the diagnosis of this liver disease is influenced by the comfort and experience of the radiologist who are responsible for establishing the contrast and gain setting during the capture of ultrasonic images [9]. Furthermore, the patients' body condition, probe application and the absence of quality ultrasonic machine also impacts the quality and reassemblies of the images [10]. Hence, an automated classification scheme that is capable of handling texture and wavelet features in diagnosing liver diseases with improved accuracy becomes essential. In this paper, a novel texture and wavelet features-based automated liver disease diagnosis mechanism that uses improved active contour for segmentation, shift variant bi-orthogonal wavelet transform for filtering and an integrated random forest-based classification is proposed. The core objective of the proposed liver disease diagnosis scheme focusses on the enhancement of accuracy during classification such that diagnosis is achieved at a rapid rate with reliability.

The subsequent sections of this paper are ordered as follows. Section 2 highlights on the literature review conducted for elucidating the merits and limitations of the existing liver disease diagnosis schemes. Section 3 presents the outline of the proposed methodology and detailed explanation about each and every of the implemented automatic liver disease diagnosis scheme. Section 4 reveals the simulation results and analyses of the proposed liver disease diagnosis scheme in terms of Accuracy, Mean Accuracy and True Positive Rate. Section 5 presents the major contributions of the proposed scheme with possible scope of focus on the future enhancement.

## II. LITERATURE REVIEW

Traditionally, accurate classification between liver diseases is achieved based on the selection of potential features and Region of Interest (ROI) determination. But, the process of estimating the ROI region automatically from the ultrasound images leads to complexity since they do not possess continuous or definite boundaries in the diseased liver part used for analysis. Initially, an automated approach for liver disease detection is facilitated by utilizing the square ROI of 30X30 pixel dimension [11]. This method of liver disease diagnosis used 50 images that contained 30 fatty diseased liver images and the normal dis-infected liver images. It also used and integrated nearly seven textures during the fusion of the segmented images in order to ensure

the significant classification rate of 96%. Then Alivar et al. [12] devoted a scheme that used ROI size of 64X64 pixels during segmentation. Then ROI images are carefully used for determining different quantifiable wavelet packet, Gray Level Co-occurrence Matrix and Gabor Transform for phenomenal feature extraction. These triple level methods of feature extraction are essential for achieving a significant classification rate. The Authors used a dataset of 45 ultrasonic image samples out of which 35 are dis-infected liver samples and the remaining are infected liver samples for identifying and improving the classification accuracy based on K-nearest technique.

Further, an integrated mechanism-based on the integration of discrete wavelet transform and contrast improvement was proposed in [13] for preventing speckle noise from the images. The data set used for speckle image removal consisted of 35 dis-infected liver images, 35 decompensated liver images and 30 compensated images. This classification process utilized the K-mean clustering scheme for classification as it proved to optimize the performance of the diagnosis based on estimated minimum Euclidean distance. The classification accuracy of this system is also verified to be 97.32 compared to the benchmarked approaches. Then, an optimal feature extraction scheme was contributed in [14] for diagnosing different level of liver disorders. This computer automated scheme used the concept of forward selection for accurate classification in the dataset that contained ultrasonic images that possessed two image parameters, three medical-oriented features and one laboratory-inspired features for extracting. In this scheme, total 97 number of samples related to dis-infected liver, carcinoma-based liver disease, chronic hepatitis and steatosis was used during classification. This classification of ultrasonic images proved a classification accuracy of 97.89% during its utilization of Support Vector Machine and K-mean clustering scheme.

Furthermore, an automated liver disease classification scheme was proposed by Minhas et al. [15] with integrated statistical features and wavelet packet transform for feature extraction. This automated detection scheme used support vector machine based multi-objective scheme for classification. The classification rate of this scheme was also confirmed to be greater than 97% since it used the ROI segmentation of 64x64 pixel dimensions. The tenfold strategy used during classification was also responsible for improving the classification accuracy over 97%. Finally, another automated liver disease automation scheme was proposed in [16] with improved classification rate of 98%. This method was formulated for handling data sets that possesses highly un-correlated ultrasonic images and that fail to possess standard boundaries.

From the thorough investigation of the aforementioned automated liver diagnostic approaches, the base induction for the formulation of the proposed work is determined.

## III. THE PROPOSED WORK

This proposed scheme starts with the process of image acquisition, which is followed by improving active contour segmentation. Then shift-invariant bi-orthogonal wavelet transform is enforced on the segmented images for deriving diagonal, horizontal and vertical components based on which the component images are derived. Further, the Gray-Level Run-Length Matrix (GRLM) feature extraction is achieved from the derived component images and then the classification is performed using the method of random forests. The classification process using random forests is also improved through the incorporation of tenfold validation procedure. Further, the results obtained from the classification of the utilized GLRLM features and the benchmarked GLCM, intensity histogram and invariant moments are compared to validate the potential of the proposed diagnosis scheme.

### A) Improved active contour-based segmentation

Initially, the image is divided into unique regions that contain pixels of similar attributes are segregated during the segmentation process. For achieving segmentation, improved active contour approach is used for separating the boundaries of the object from the utilized image based on the enforcement of constraints. The classical active contour method is improved by initially defining a false edge. When the basic process of active contour is facilitated then the reference point of each determined regions are checked. If the gradient value pertaining to the pixel of the segmented regions is very small then the false point is assigned to the reference point. The collection of these false points constitutes the false edges. Then the force is enforced on the false edges in the tangential direction which is upright until true edge is visible. Thus, this method can be used for the ultrasonic images since they do not possess a standard boundary and further, the existing boundary may also merge into the neighbourhood regions. Further, this improved active contour is also furthermore based on the contributed work of Chan and Vese [17] that focusses on reducing the energy level. Hence the proposed scheme is proving to be meritorious as it eliminates the limitations of the traditional segmentation schemes existing in the literature. In addition, the gradient is not used as the constraint for determining the boundaries of the regions and hence they are suitable for its application in the segmentation process of blurred and noisy images like the ultrasonic images.

This Chan and Vese-based scheme uses two terms $F_1(C)$ and $F_2(C)$ for fitting energy as depicted using Equation (1) and (2)

$$E_{Fit} = F_1(C) + F_2(C) \int_{in(c)} |O_I - l_1|^2 dydx + \int_{out(c)} |O_I - l_2|^2 dydx \quad (1)$$

With

$$\inf_C [F_1(C) + F_2(C)] \approx 0 \approx F_1(C) + F_2(C) \quad (2)$$

Where $l_1$ and $l_2$ refers to the mean outside and inside of $O_I$ the image that contains regions related to the piecewise intensity constants with $C$ as the evolutionary curve.

Then the fitting energy expressed in Equation (1) is minimized by incorporating two terms pertaining to the area and the length of the evolutionary curve as depicted in Equation (2). This segment also uses the level set method for solving the specific case of minimum partitioning issue that always evolve during the application of improved active contour scheme of Chan and Vese method

### B) Shift Variant Bi-Orthogonal Wavelet Decomposition

The Shift Variant Bi-Orthogonal Wavelet Decomposition used in this automated approach aids in capturing the frequency and temporal data related to the utilized images' signal that comprises of multiple resolution scaling. This Shift Variant Bi-Orthogonal Wavelet Decomposition is used for investigating the signals of the image and prevents them from generating spurious information that are general in the image analysis. In this analysis, the signals of the image are investigated using varying number of least scales and translations. Initially, the segmented images are converted into four numbers of shift sets viz., $S_S = \{(0.0),(0,1),(1,0),(1,1)\}$ for the determination of image pairs. Then the individual image pairs results in four sub-images during the process of decomposition achieved using Equation (3) through the incorporation of filters $f_1$ and $f_2$.

$$I_{i-1,k} = \sum_k g_k I_{i,2l+k} f_{(i-1,k)} \qquad (3)$$

The resulting sub-images correspond to three higher wavelet-co-efficient-based frequency sub-images and one approximation lower frequency sub-images. Further, the mixing operation of the lower frequency sub-images are performed based on shift sets using origin point such that aids in better approximation of the originally used image. This process of mixing and shifting is performed upto '$k$' levels, such that better multiple scale representations of the original image are achieved. Then compute the co-efficients of approximation related to each of the resultant sub-images using Equation (4) and determine the wavelet co-efficient of the original image based on varying levels of intensity through Equation (5).

$$M_k^0(a,b) = \frac{(A_k^0(a,b) + B_k^0(a,b))}{2} \qquad (4)$$

and

$$D_i^e(a,,b) = \sum_{a,b \subseteq k}^n w^e(a^1,b^1)[E_i^e(a+a^1,b+b^1)]^2 \quad (5)$$

Then estimate the similarity of the original images using the derived multiple scale representations using the Equation (6)

$$M_{i,AB}^e(a,b) = 2\frac{\sum_{a,b \subseteq k} w^e(a^1,b^1)E_{i,A}^e(a+a^1,b+b^1)E_{i,B}^e(a+a^1,b+b^1)}{F_{i,A}^e(a,b) + F_{i,B}^e(a,b)} \qquad (6)$$

Furthermore, estimate the weights of the co-efficient using Equation (7) and (8) and then perform the verification process of consistency using for achieving the weights that could be used for decision process during testing and training.

$$\alpha_{i,A}^e = \sum_{a^1,b^1} w^e(a^1,b^1)\alpha_{i,A}^e(a+a^1,b+b^1) \qquad (7)$$

$$\alpha_{i,B}^e(D_i^e(a,b)) = \frac{1}{2} + \frac{1}{2}\left(\frac{1 - D_{i,AB}^e(a,b)}{1 - F_M}\right) \qquad (8)$$

and

$$E_{i,F}^e(a,b) = \alpha_{i,A}^e(a,b).E_{i,A}^e(a,b) + \alpha_{i,B}^e(a,b)E_{i,B}^e \qquad (9)$$

Finally, determine the wavelet co-efficient of the decomposed image using Equation (9) that performs the mean operation using the shift sets.

### C) Feature Extraction using GLRLM

In this scheme, nearly 11 features such as short-run emphasis, long-run emphasis, run percentage, run-length non-uniformity, gray-level non-uniformity, low gray level run emphasis, high gray level run emphasis, long run, low gray level run emphasis, long run high gray level run emphasis, short run low gray level run emphasis and short run high gray level run emphasis are extracted. Further, features related to Euclidean shape, color and to some extent texture contribute to the last level in this automated scheme of liver disease detection. The feature is extracted using GLRLM mainly for collecting potential values of the image pixels for classification by enforcing significant constraints in implementation. This GLRLM-based feature extraction scheme is confirmed to gather a better diversity of features even in the gray scale, hazy and appearance of ultrasonic images of liver. This automated approach possesses a better discrimination rate in classifying normal ultrasonic images of liver from diseased liver ultrasonic images in the spatial field. The proposed scheme is also compared with the classical detection techniques like invariant moments and intensity histogram techniques.

### D) Enhanced Random Forest Learning-based classification scheme

In this automated fatty liver diagnosis system, the enhanced Random Forest Learning-based classification scheme is used for four important reasons viz., a) It is capable of resolving multiple-class dimensional problem of classification, b) It is significant in generating decision tree that enables individual voting process that transforms each input of classification into its most feasible probability classification label, c) It is fast and possess the potential of

determining non linear data structures based on the the estimation of reliable ensemble parameter and d) it eliminates the degree of data over fitting even when the count of decision trees appended to the forests is increased. This proposed automated fatty liver diagnosis approach use the merits of three entities such as an improved instance filter, multi-perspective attribute estimator and forest classifier algorithm for effective and reliable classification. In this classification process, initially, three attributes quantification parameters pertaining to the uncertainty of correlation features, symmetric uncertainty and gain ration are used for better contextual selection that improves the degree of training for choosing the most related attributes for optimal classification. Then, an enhanced instance filter is mainly used for reliable balancing of multiple-class dimensional attribute classification since the data distribution need to be re-sampled when they are not uniformly distributed in order to enhance the efficiency of the classification process. In addition, the classical Random Forest Classification method is finally used over the transformed uniformly distributed data which is derived as the output of the incorporated instance filter phase. Hence, the classification accuracy of the proposed automated fatty liver diagnosis system is 98.72% compared to the classification schemes used for investigation.

## IV. RESULT ANALYSIS AND DISCUSSIONS

The performance of the proposed automated fatty liver disease diagnosis scheme is investigated using MATLAB R2013a based on evaluation parameters like classification accuracy and false positive rate.

The investigated result of the proposed automated diseased liver detection scheme is conducted using the data set that consists of 500 images classified under four categories collected from the scan centers of Chennai. The images are resized uniformly to the resolution of 512x512 such that the process of classification can be potentially improved. This proposed scheme was simulated using MATLAB R2013a with Weka for knowledge analysis. Nearly 500 iterations are carried out for separating the ROI from the images gathered for investigation and 100 iterations is used for segmenting out the smaller regions of ROI from the utilized original images. The GLRLM features are extracted with orientations viz., 0,45, 90 and 135 degrees such that 44 features are collected from 176 features involved in shift variant bi-orthogonal wavelet decomposition. The significance of the proposed approach is investigated using overall accuracy, mean accuracy and true positive rate.

Figure 1 and 2 portrays the input liver image before segmentation and liver image after Chen Vese segmentation
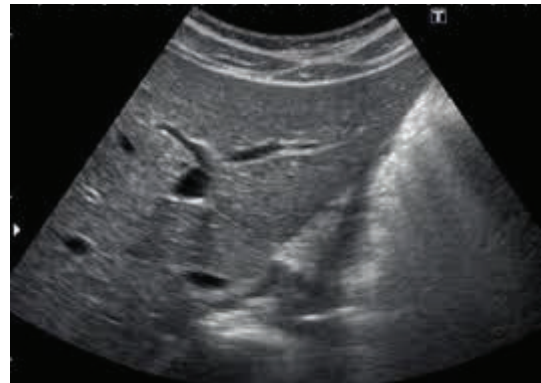


Figure 1. Input ultrasonic liver image used for detection
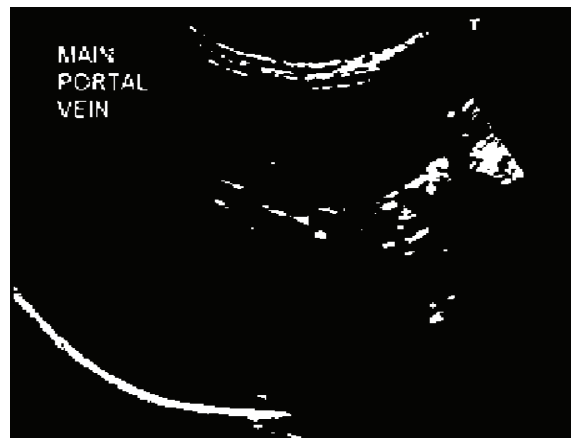


Figure 2. Chen Vese segmentation of liver image
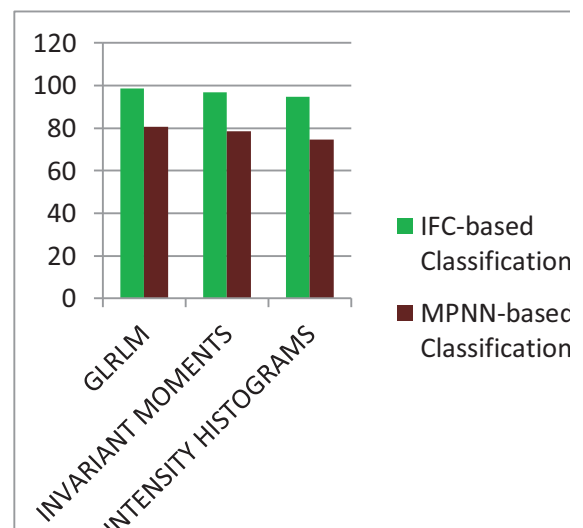


Figure 3. Classification accuracy percentage of IFC

Figures 3 presents the overall classification accuracy of the incorporated random forests and compared multilayer perceptron neural network. The overall accuracy of Improved Forest Classifiers(IFC) used in this automated detection technique seems to improve its classification

accuracy by 19% predominant to the investigated MultiLayer Perceptron Neural Network (MPNN). Similarly, Figure 4 portrays the performance of the utilized IFC based on mean classification accuracy. The mean classification accuracy is also confirmed to be better by 23% superior to the comparable MPNN used for classification.
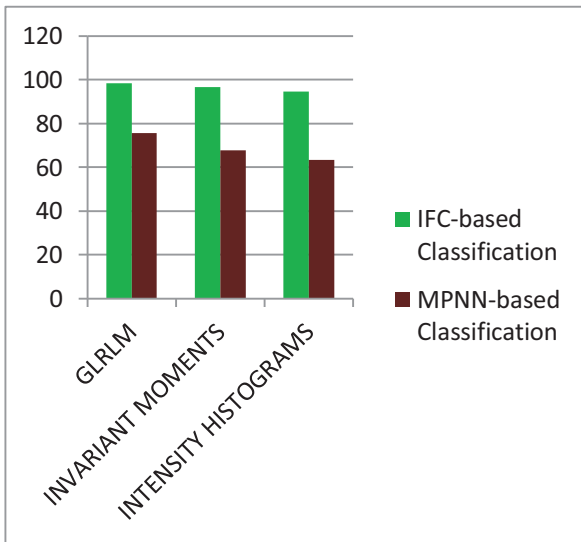


Figure 4. Mean Classification accuracy of IFC

Likewise, Figures 5 presents the true positive rate of random forests and compared MPNN. The true positive rate of IFC used in this automated detection technique is conformed to infer an excellent classification accuracy of 22% better to the compared multi-layer perceptron neural network.
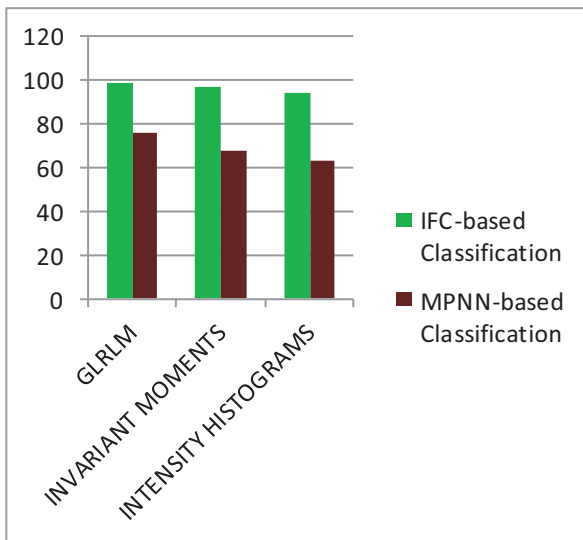


Figure 5. True positive rate of IFC

This improvement in true positive rate of this proposed automated scheme is due to eleven different GLRLM features extracted and the hybrid classification module used during deployment.

Furthermore, the performance of the proposed automated liver disease diagnosis system is investigated based on the significance of the system with instance filter, system without instance filter, system to Chen Vese Method and system without Chen Vese Method is presented in Table 1 .

TABLE 1.
PERFORMANCE OF AUTOMATED LIVER DETECTION SCHEME.

| Schemes of comparison | Decrease in False Positive Rate | Increase in True Negative Rate |
|---|---|---|
| Proposed Forest classifier based detection with instance filter | 18.13% | 27.25% |
| Proposed Forest classifier based detection without instance filter | 14.12% | 20.43% |
| Segmentation with Chen Vese method [17] | 21.12% | 29.21% |
| Segmentation without Chen Vese method [18] | 13.21% | 20.65% |

Table 1 clearly portrays that the proposed scheme is highly potent due to the incorporated Chen Vese method of segmentation and Enhanced Forest Classification Technique in its detection methodology. The proposed IFC method with the Chen Vese method of segmentation is proven to decrease the false positive rate by 8 % and increase the true negative rate by 8.64% superior to the benchmarked liver detection schemes used for investigation.

## V. CONCLUSIONS

The exhibited novel texture and wavelet features-based automated liver disease diagnosis mechanism improves the accuracy, mean accuracy and true positive rate by 19%, 23% and 22% compared to the benchmarked approaches considered for investigation. The utilization of shift variant bio-orthogonal wavelet transforms is confirmed to increase the contrast during the diagnosis of liver disorders. The results of the proposed liver disease detection scheme confirmed better classification accuracy of 98.56% better to the baseline liver disease automated techniques used for comparison. The true positive rate of the proposed scheme is also inferred to be better by 22% predominate to the comparative techniques under the evaluation using the features extracted using GLRLM, invariant moments and intensity histograms. In addition, the proposed IFC method with the Chen Vese method of segmentation is proven to decrease the false positive rate by 8 % and increase the true negative rate by 8.64%

## REFERENCES

[1] A.Alivar, H.Danyali, and M.S.Helfroush,"Hierarchical classification of normal, fatty and heterogeneous liver diseases from ultrasound images using serial and parallel feature fusion,". Biocybernetics and Biomedical Engineering, Vol.36(4), pp.697-707, 2016.

[2] A.F Costa, G. Humpire-Mamani, and A.J.Traina,"An Efficient Algorithm for Fractal Analysis of Textures,". 25th SIBGRAPI Conference on Graphics, Patterns and Images,Vol. 1(2),pp.23-35.

[3] K.Kalyan, B.Jakhia, R.D.Lele, M.Joshi, and A.Chowdhary,"Artificial Neural Network Application in the Diagnosis of Disease Conditions with Liver Ultrasound Images," Advances in Bioinformatics,Vol.2,pp.1-14,2014.

[4] K.Venkatalakshmi and S.Mercy Shalinie,"Classification of multispectral images using neuro-statistical classifier based on decision fusion and feature fusion," International Conference on Intelligent Sensing and Information Processing, Proceedings of, Vol.2(1), pp.45-54,2004

[5] A.Zaim,T.Yi, and R.Keck, "Feature-Based Classification of Prostate Ultrasound Images using Multiwavelet and Kernel Support Vector Machines,"International Joint Conference on Neural Networks, Vol.2(1),pp.34-43.2007.

[6] M.S.Uddin, K.K Halder, M. Tahtali, A.J. Lambert, and M.R.Pickering, " Speckle reduction and deblurring of ultrasound images using artificial neural network," Picture Coding Symposium (PCS),Vol. 2, pp.529-551, pp.45-67.(1).

[7] J.Virmani, V.Kumar,N.Kalra,and N. Khandelwal,"SVM-based characterization of liver cirrhosis by singular value decomposition of GLCM matrix," International Journal of Artificial Intelligence and Soft Computing, Vol.3,pp.276(3).

.[8] T.Kitamura, S.Takeuchi, and S.Abe,"Feature selection and fast training of subspace based support vector machines". International Joint Conference on Neural Networks (IJCNN),Vol. 2(1), Vol.23-34.2010.

[9] R.Rastghalam and H.Pourghassem,"Breast cancer detection using MRF-based probable texture feature and decision-level fusion-based classification using HMM on thermography images," Pattern Recognition,Vol. 51(2),pp.176-186.

[10] B.Thangaparvathi,D.Anandhavalli, and S.M.Shalinie,"A high speed decision tree classifier algorithm for huge dataset".International Conference on Recent Trends in Information Technology (ICRTIT), Vol.3(1),pp. 56-65. 2011.

[11] M.Singh,S.Singh, and S. Gupta,"An information fusion based method for liver classification using texture analysis of ultrasound images. Information Fusion, Vol.19(1), pp.91-96,2014.

[12] A.Alivar, H.Daniali, and M.S. Helfroush,"Classification of liver diseases using ultrasound images based on feature combination,4th International Conference on Computer and Knowledge Engineering (ICCKE), Vol.2(1),pp.23-36,2014.

[13] K.Raghesh Krishnan, and R.Sudhakar,"Automatic Classification of Liver Diseases from Ultrasound Images Using GLRLM Texture Features,"Soft Computing Applications, Vol.2(2), pp.611-624,2013.

[14] M.Owjimehr, H.Danyali, M.S.Helfroush,and A.Shakibafard, "Staging of Fatty Liver Diseases Based on Hierarchical Classification and Feature Fusion for Back-Scan–Converted Ultrasound Images", Ultrasonic Imaging, Vol.39(2), 79-95,2016.

[15] F.U.Minhas,D.Sabih,andM.Hussain,"Automated Classification of Liver Disorders using Ultrasound Images," Journal of Medical Systems, Vol.36(5), pp.3163-3172.

[16] R.Suganya, and S.Rajaram,"Classification of liver diseases from ultrasound images using a hybrid kohonen SOM and LPND speckle reduction method", IEEE International Conference on Signal Processing, Computing and Control, Vol.2(1), 45-56,2012.

[17] S.K.Siri, and M.V.Latte,"Universal Liver Extraction Algorithm: An Improved Chan–Vese Model," Journal of Intelligent Systems, 1(1), 34-46,2018.

[18] J.Virmani, V.Kumar, N.Kalra, and N.Khandelwal,"Prediction of liver cirrhosis based on multi-resolution texture descriptors from B-mode ultrasound. International Journal of Convergence Computing",Vol.1(1), pp.19-29,2013.

# Optimal Allocation of Electric Power Distributed Generation on Distributed Network Using Elephant Herding Optimization Technique

R. Vijay
Assoc. Professor, CVR College of Engineering/ EEE Department, Hyderabad, India
Email: vijai.mtp@cvr.ac.in

*Abstract:* **This paper deals with optimal allocation of distributed generation in the electrical distribution system. Due to rapidly increasing energy demand on the distribution network, the system is experiencing disturbances like equipment overloading, voltage sags and swell. In this paper, the thermal and power loss constraints are considered for optimal operation. Elephant Herding Optimization (EHO) technique is applied for optimal placement and sizing of distributed generation on electric distribution network. The conventional optimization technique fails due to its complexity while solving the nonlinear problems. The EHO technique is tested on 5 bus radial distribution system. The intelligent and precise allocation of distributed generation in electric distribution network by using EHO reduces the overloading of the equipment, voltage swell & sag, active power, reactive power and production cost of electricity. Furthermore, the suggested optimization technique is expanded to 24 bus radial distribution and practical Indian system.**

*Index Terms*: **distributed generation, optimal allocation, renewable energy sources, market liberalization, elephant herding optimization**

## I. Introduction

Recently the initiatives on smart grid and sustainable energy Distributed Generations (DG) are playing an important role in electric power systems. In order to overcome energy demand, the advantages of DG [1] are used to their potential. The future active network will effectively and efficiently link small and medium scale electric power sources with consumer demands. Due to rapidly increasing energy demand on the distribution network, the system is experiencing disturbances like overloading the equipment's, voltage sags & swell, thermal constraints and power loss.

The current development in small-sized and modulated power generation technologies have led to large-scale deployment of distributed generation in electrical distribution network [2]. The optimal allocation of distributed generation may provide enormous techno economic and social benefits such as minimized power/energy loss. The optimal location of distributed generation [3] in the electric distribution network is a nonlinear optimization problem, generally comprised of number, location and sizes.

The optimal placement, size and location in the distributed generation have been developed and effectively employed using conventional methods [4, 5]. These methods have experienced slow convergence rate in concerned search space. Both real as well as reactive power loss minimization

are the objectives for the DG placement [6] by using analytical methods. The conventional analytical methods [7] are not appropriate for solving complex problems. A boundary-based algorithm is used to obtain distributed generation regulates the individual best by snubbing the consequence of other objectives [8]. The allocation of distributed generation in electrical distributed network problem becomes a multi objective optimization [9] problem in which two or more objectives are optimized. The objective is inconsistent, so multiple objectives are converted into a single-objective problem by assigning weights.

Meta-heuristic and heuristic methods suggest the new practicable and streamlined elucidation. The Heuristic optimization algorithm is introduced to solve the optimal allocation of electrical distributed generation on distributed networks. Genetic algorithm [10] is used to abide generation, so that loss expenses and network disruption are minimized. Meanwhile the rating of the generator becomes exploited. The various optimization techniques such as Tabu Search (TS) [11], Particle swarm Optimization (PSO) [12], Artificial Bee Colony (ABC) [13], Bat Motivated Optimization (BMO) [14], Ant Colony Optimization (ACO) [15], Bacterial Swarm Optimization (BSO) [16,17], Enriched Biogeography Based Optimization (EBBO) Algorithm [18] are introduced to elucidate the optimal allocation in distribution network successfully. The hybrid optimization algorithm is comprised of Improved Multi-Objective Harmony Search (IMOHS) [19] and is applied to assess the sway of DG placement for an optimal arrangement of a distribution system.

The above revealed heuristic approach is used to determine the optimal location and sizing of DG from an investment point of view. In these literatures, the Short Circuit Bound (SCB) restrictions are not deliberated. The emphasis of the objective function is to optimize cost preferably than increasing renewable energy resources. In this paper this SCB and capital investment in new renewable distributed generation units are considered for optimal operation.

A new simple nature inspired optimization technique called the Elephant Herding Optimization (EHO) [20] algorithm stimulated by the elephant herding behavior is used. The EHO method is inspired by the herding behavior of male and matriarch (female) elephant. The food and shelter searching technique is the foremost inspirations in this algorithm. This EHO method is smeared to solve the optimal placement of distributed generation on electrical

distributed network. In this paper, 5 bus radial distribution networks are deliberated and unraveled for optimal site in the distribution network.

The fragmentations of this paper are alienated into five sections, Section 2 explains about the optimal placement of distributed generation problem formulation. Section 3 presents the overview of the proposed EHO algorithm. Section 4 discusses the application of EHO for optimal placement of distributed generation. Section 5 deals with detailed results and discussion followed by conclusion in Section 6.

## II. Problem Formulation

Embedded Generation is the small capacity generation and is not associated to the transmission system. Recently more amount of generation is being coupled at distribution level. This leads to change the features of the power system network. To increase the amount of power generation, change in the planning and design of the electrical distribution network is prerequisite.

Most of embedded generation is from renewable energy sources. The optimal usage of the prevailing power system network leads to cost operative method. Electric power generation capability should be apportioned across the buses, allowing for all the practical restrictions. The electric power generation capacity should be maximized [3]. Hence the proposed impartial function is taken as

$$J = \sum_{n=1}^{N} P_{DGn} \qquad (1)$$

Where $P_{DGn}$ is the DG power generation capability at the $n^{th}$ bus and without loss, presumed that there is a generator fulfilling every bus. The impartial function $J$ (MW) is maximized subject to the restrictions.

### A. Thermal Constraint:

The rated $I$ of the transmission lines need not to be surpassed

$$I_n < I_n^{rated}, n \forall N \qquad (2)$$

Where $I$ is the current circulated from the generator to bus and $I^{rated}$ is the maximum line current.

### B. Equipment Ratings:

The following ratings considered here are transformer capacity, short circuit bound, short circuit proportion and voltage rise outcome, the detailed explanations as follows

### Transformer Capacity:

The amount of power generation associated minus varying peak seasonal (summer) load didn't surpass the higher voltage evaluation of the transformer.

$$P_{Tr} \le P_{TrCap} \qquad (3)$$

Where $P_{Tr}$ indicates the power flow through substation transformer and $P_{TrCap}$ directs the rating of transformer taken.

### Short Circuit Bound:

The short circuit ratings are calculated and mentioned in the distribution code. The SCB calculation is derived to fortify that this constraint has not transcended the installed capacity. The restriction is specified by

$$SCB_{TX} < SCB_{Rated} \qquad (4)$$

$SCB_{rated}$ is the maximum current that breaks the switchgear securely in the abnormal condition. The endowment of power generation at each bus to SCB is resolved by short circuit analysis. The SCB endowment of power generation at each bus are consolidated into an algebraic equation as follows

$$\sum_{m=1}^{N} \zeta_{mTx} P_{DGm} + \sigma T_x \le SCB_{rated} \qquad (5)$$

Where $\zeta_{mTx}$ is the dependence of the SCB at the transmission substation to power inoculation at bus $m$ and $\sigma T_x$ is the inceptive SCB of the transmission bus.

### Short Circuit Proportion (SCP):

The SCP is defined as a proportion of the power generated $P_{DG}$ (MW) at every individual bus to the Short Circuit Level at every individual bus. The voltage dip near the generator due to outage of feeder is indicated. When induction motors are placed in the circuit it leads to voltage instability.

$$\frac{P_{DGn}}{SCB_n \cdot \cos(\varphi)} * 100 \le 10\%, n \forall N \qquad (6)$$

Where $SCB_n$ refers to the SCB at the $n^{th}$ bus and $\cos(\phi)$ is the power factor of the generator. The base value for the SCB at $n^{th}$ bus is calculated with no power generation. The SCB at the $n^{th}$ bus is

$$SCB_n = \sigma_n + \sum_{m=1}^{N} \zeta_{mn} P_{DGm}, i \ne j, n \forall N \qquad (7)$$

$$P_{DGn} - 0.1\cos(\varphi) \sum_{m=1}^{N} \zeta_{mn} P_{DGm} \le 0.1\cos(\varphi) * \delta_i \qquad (8)$$

### Voltage Rise Outcome (VRO):

The voltage at the generator is specified by below mentioned eqn.

$$V_G = V_L + \frac{RP_L + XQ_L}{V_L} + j \frac{XP_L - RQ_l}{V_L} \qquad (9)$$

$P_L$ and $Q_L$ are active and reactive power at the bus, $V_G$ is the voltage at the generator and $V_L$ is the voltage at the respective bus. Thus, it is comprehended that the generator voltage is the bus or load voltage and the rate associated with line impedance and power flow through the transmission line.

The active power flow through the electric distribution system has a large influence on voltage for the reason that the distributed network is high resistance compared to other

transmission lines. This steers to approximately higher X/R value compared to transmission networks. The system voltage of each bus must lie within standard limits.

$$V_n^{\min} \leq V_n \leq V_n^{\max} \qquad (10)$$

Where $V_n^{\min}$ and $V_n^{\max}$ indicates the minimum and maximum voltage boundaries at the $n^{th}$ bus. The attributes of voltage and power inoculations at every bus is resolute.

$$\mu_n P_{DGn} + \beta_n + \sum_{m=1}^{N} \mu_{mn} P_{DGn} \leq V_n^{\max} \, n \forall N \qquad (11)$$

Here $\mu_i$ is the dominion of the voltage level at bus $n$ taking place on power inoculations at bus $n$. That is the slope of the generated voltage vs power inoculation attributes of the $n^{th}$ bus. $\beta_n$ mentions the inceptive voltage level at the $n^{th}$ bus with no generation and $\mu_{nm}$ refers to the reliance of the voltage level at bus on power injections at bus.

This dissection is accomplished under minimum load conditions as it is the worst condition for voltage rise.

## III. ELEPHANT HERDING OPTIMIZATION

The EHO [21] search method is based on the steering elephant clans. In existing biosphere, the elephants associated with dissimilar clans stay organized under the directorship of female elephant; while the males when they grow leaves their elephant family groups.

The elephant behavior in search of food and shelter is modeled in two ways. These include clan apprising machinist and unraveling machinist. The current position of every group is updated by the matriarch, this process is known as clan apprising machinist. The enactment of the clan unraveling machinist enhances the elephant population miscellany in the whole search space.

Elephant herding optimization is implemented by the following procedure

- The elephant population is tranquil in some clans and every fraternity has fixed numbers.
- The male elephants move away from their clan and live distant from their clan at every iteration.
- The elephants in every group stay organized beneath the directorship of matriarch.

### Clan updating operator:

The elephant location in clan $C_n$ is effected by matriarch $C_n$ in all iterations. The elephant $m$ in clan $C_n$, is restructured by the following equation

$$e_{new,cn,m} = e_{cn,m} + \lambda \cdot (e_{best,cn} - e_{cn,m}) \cdot r \qquad (12)$$

From the above equation $e_{new,cn,m}$ is recently rationalized location of elephant $m$ in clan $C_n$ and $e_{cn,m}$ is the old location of elephant $m$ in group $C_n$ respectively. $\lambda$ is the surmounting factor that regulates the impact of matriarch

$C_n$ on $e_{cn,m}$ and the assessment of $\lambda$ lies between [0,1]. $e_{best,cn}$ represents the female elephant $C_n$ which is the fittest distinct elephant in clan $C_n$, $r$ represents the stochastic and uniform distribution in the assortment [0,1]. The fittest elephant in each clan is updated by eqn.(12), i.e. $e_{cn,m} = e_{best,cn}$. If the global optimal solution is not satisfied then again compute eqn. (13)

The fittest elephant is again rationalized by the below equation

$$e_{new,cn,m} = \kappa \cdot e_{center,cn} \qquad (13)$$

Where $\kappa$ governs the effect of the $e_{center,cn}$ on $e_{center,cnm}$. The new position $e_{new,cn,m}$ shown in eqn. (13) is determined from the information of the elephants in clan $C_n$. $e_{center,cn}$ is the center of elephant group $C_n$ and for the $x^{th}$ dimension it is premeditated by

$$e_{center,cnx} = \frac{1}{n} * \sum_{m=1}^{N} e_{cn,m,x} \qquad (14)$$

Where $1 \leq x \leq X$ indicates the $x^{th}$ dimension and $X$ is its total dimension. $N$ is the number of elephant population in group $C_n$. $e_{cn,m,x}$ is the $x^{th}$ dimension of the individual elephant. The Centre of clan $C_n$, $e_{center,cn}$ is calculated by eqn.(14).

### Clan Separating Operator:

In the elephant's clan male elephants move away from their family group and live solitary. This process is modeled as clan separating & updating operator, which is used for cracking optimizing hitches. The poorest fitness elephant is eliminated from the clan at each iteration, so that the search ability of EHO method is improved. This worst fitness elephant group is calculated by

$$e_{worst,cn} = e_{\min} + (e_{\max} - e_{\min} + 1) * r \qquad (15)$$

Where $e_{\max}$ and $e_{\min}$ are maximum bound and minimum bound of each individual location. $e_{worst,cn}$ is the poorest individual location in the clan $C_n$. $r \in [0,1]$ is the stochastic and uniform distribution in the range [0,1].

### Pseudo Code - Clan Updating Machinist:

*For*

*{*

$C_n$ *= 1 to* $N_{clan}$ *(all groups in elephant population) do*

    *For*

    *{*

        *m = 1 to* $N_{cn}$ *(for entire elephant in group* $C_i$ *) do*

*Acquaint* $e_{cn,m}$ *and generate* $e_{new,cn,m}$ *by eqn. (12)*

    *If*

    *{*

    $e_{cn} = e_{best,cn}$ *then*

    *Apprise* $e_{cn,m}$ *and produce* $e_{new,cn,m}$ *by eqn.(13)*

    *}*

    *End if*

  *}*

  *End for j*

*}*

*End for* $C_n$


### Pseudo Code - Separating Machinist:

*For*

*{*

  $C_n = 1$ *to* $N_{clan}$ *(all clans in elephant population)*

  *do*

  *Replace the worst elephant in clan* $C_n$ *by eqn.(15)*

  *End for* $C_n$

*}*


### Pseudo Code - EHO Algorithm:

*Initialize the population; Fix generation counter* $t = 1$*;*

*Maximum Generation MaxGen*

*While*

  *{*

  *t, Max Gen do*

  *Sort all the elephants according to their fitness.*

  *Implement clan updating operator*

  *Implement separating operator as shown*

  *Evaluate population by the newly updated positions*

  *T = t + 1*

  *}*

*End while*

## IV. IMPLEMENTATION OF EHO FOR OPTIMAL ALLOCATION OF DISTRIBUTED GENERATION ON DISTRIBUTION NETWORK

Usually elephants form some groups and move in search for food and shelter. In this context, the elephant movement from one location to another location is considered as power flow from one bus to another bus. They update their position and location status. Correspondingly, the optimal allocation problem is related to the bus location and bus data.

Elephants communicate with each other by low frequency vibrations. When they find the worst case of disturbances in the search space, in a particular place, they communicate with each other's in the clan (groups). Meanwhile, low voltage and high voltage fluctuations are the main cause of disturbance and losses in the distribution network. In a distribution network due to unexpected change in load, the bus voltage starts fluctuating. Depending on the voltage fluctuations, the weaker buses are identified.

The best position treasure by the elephant is the best bus (voltage profile) location. The position of the elephant location with more disturbances is the best position for placement of distributed generation.

The following steps explain the implementation of EHO for optimal DG allocation in distributed networks

Step 1: Set max number of elephants, no of elephants, no of buses, bus data node voltages, short circuit bound, $\lambda$ and $\kappa$.

Step 2: Update the best and worst position of the elephant, i.e., best and worst bus voltage.

Step 3: Update the worst position of elephant i.e., worst bus voltage.

Step 4: Elephants will communicate with others to update the current worst position (Local Solution) among the iteration.

Step 5: Now the elephants will keep on herding to find the global best position (Worst Location). By discovering the worst position, the voltage profile is enriched by employing distributed generations in the weak bus.
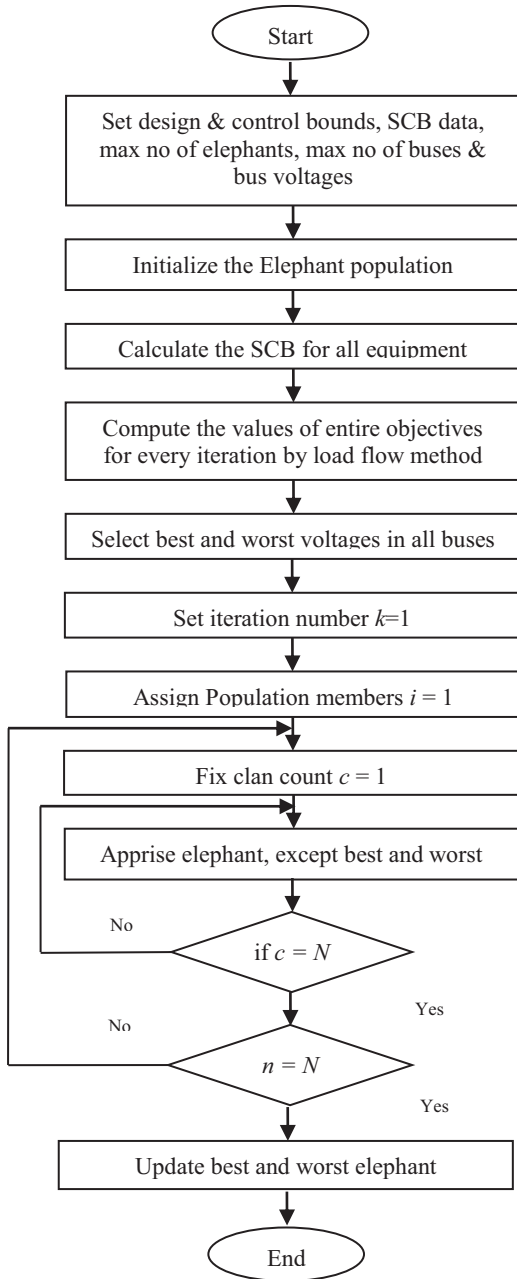
Figure 1. Flowchart of Implementing EHO to optimal placement of distributed generation



Figure 2. 38 KV 5 Bus Radial Distribution Network Diagram

By injecting power at various buses, the solitary voltage sensitive attributes are formed and presented in Fig.3.
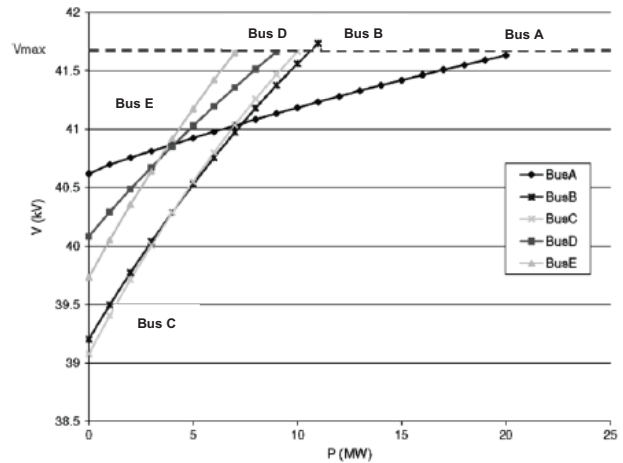


Figure 3. Generated Power Injections at respective Buses and its Voltage Compassions

By using the solitary voltage sensitive attributes, it is found that bus A is slight profound to power instillations at different buses. The bus A is slightly profound due to the location which is very near to 38/110 kV station. The bus B & C have analogous characteristics because those buses connected separately as of the distribution network.

## V. RESULTS AND DISCUSSION

The elephant herding optimization technique is tested on 5 bus radial distribution systems [3]. The tail fed 38/110 kV station with 5 buses is shown in Fig. 2. The EHO is verified to test on practical heftier networks. This segment discusses the result illustrations and demonstrates the potential for network sterilization.

TABLE I.
VOLTAGE INTERDEPENDENCIES OF 5 BUS SYSTEM

| $\mu$ (kV/MW) | $A^{th}$ Bus | $B^{th}$ Bus | $C^{th}$ Bus | $D^{th}$ Bus | $E^{th}$ Bus |
|---|---|---|---|---|---|
| $A^{th}$ Bus | 0.053 | 0.008 | 0.007 | 0.021 | 0.016 |
| $B^{th}$ Bus | 0.012 | 0.218 | 0.18 | 0.009 | 0.007 |
| $C^{th}$ Bus | 0.012 | 0.191 | 0.238 | 0.009 | 0.007 |
| $D^{th}$ Bus | 0.026 | 0.008 | 0.007 | 0.162 | 0.11 |
| $E^{th}$ Bus | 0.026 | 0.008 | 0.007 | 0.135 | 0.234 |

The values of $\mu_n (kV/MW)$ are determined from Fig.3. Where $\mu_n$ is the reliance of voltage in the bus $n$ on the power inoculation at bus $n$. The gradient voltage vs power

inoculation attributes of $n^{th}$ bus, the values of $\mu_n$ are presented diagonally in Table I.

The values of $\mu_{nm}$ are presented in Table I as off diagonal elements. Where $\mu_{nm}$ is the voltage reliance at bus $n$ on the power inoculation at bus $m$.

The individual sensitivity of SCB at 38/110kV substation to power injection at distinct bus is premeditated and presented in Fig.4.



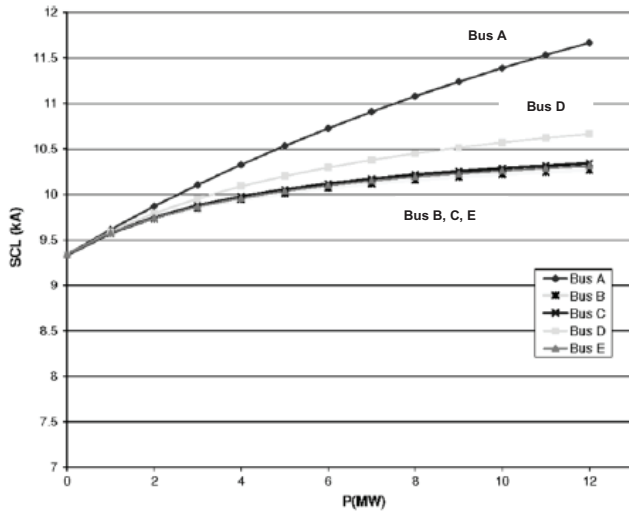Figure 4.   SCB at 38/110 kV substation vs. Power Injections at Individual Buses

The effect of bus on the SCB at 38/110kV substation is reliant on the remoteness from the substation. The influence of SCB is very high to bus A as the position of bus A is close to 110kV substation.

TABLE II.
$SCB_{Tx}$ DEPENDENCIES OF 5 BUS SYSTEMS

| Dependency Factor/ Bus | Bus A | Bus B | Bus C | Bus D | Bus E |
|---|---|---|---|---|---|
| $\zeta_{Tx}$ (kA/MW) | 0.18 | 0.11 | 0.10 | 0.14 | 0.11 |

The values of $\zeta_{nTX}$ (kA/MW) are revealed in Table II. Where $\zeta_{nTX}$ is SCB reliance at the substation to power inoculation at bus $m$. The slope of SCB vs. power inoculation attributes of the $m^{th}$ bus is revealed in Fig.4.

*Case 1: Consumer power generation on $E^{th}$ bus*

In this case, 7MW of consumer power generation is apportioned to bus E. Using EHO algorithm, sensitivity values of the maximum apportionment are indomitable, after 20 epochs the power generation inclines to 10.6 MW and is exposed in Table III.

*Case 2: Without preallocated generation*

In this case no generation is prior apportioned. The EHO is smeared and the whole allocation after 20 epochs is resolute as 20.65MW.

TABLE III.
OPTIMAL ALLOCATION OF DG IN DIFFERENT CASES CONSIDERED

| Bus No | Linear Programming Algorithm [3] | | EHO (Proposed) | |
|---|---|---|---|---|
| | Case 1 | Case 2 | Case 1 | Case 2 |
| | Actual Power in bus (MW) | Power Injected (MW) | Power Injected (MW) | Power Injected (MW) |
| $A^{th}$ Bus | 0 | 4.06 | 0 | 3.95 |
| $B^{th}$ Bus | 0 | 4.30 | 0 | 3.82 |
| $C^{th}$ Bus | 3.60 | 5.95 | 3.60 | 5.27 |
| $D^{th}$ Bus | 0 | 5.31 | 0 | 4.86 |
| $E^{th}$ Bus* | 7.60 | 3.12 | 7.00 | 2.85 |
| Total Power Injected | 11.20 | 22.74 | 10.60 | 20.65 |

*7.6 & 7.00 MW are the power injected by consumer at Bus E*

The EHO technique works on the radially functioned distribution system. The intensity of system decontamination diverges mutually between the buses. The distributed system structure is demonstrated in this literature with high level of dependency. In standby feeding circumstances entire five buses are associated to the transmission bus through the single bus. In a loftier power network, many numbers of transmission lines are connecting buses to the transmission bus with typical open points unscrambling sectors. This lessens the whole interdependence in the voltage levels, nevertheless none of SCB. Therefore, the possibility for power system decontamination is concentrated.

From Table III, it is clear that the proposed EHO technique outperforms the Linear Programming Algorithm by the means of the power injection considered in case 2. By using the EHO technique the power injected in the bus E and with respect to all other buses is also diminished comparatively, which shows the superiority of the proposed optimization technique. By using this EHO technique 9.19% power injected is reduced, which is distinct from the Table III. Meanwhile, the charge incurred in the particular DG will be saved.

The EHO determines the optimal allocation from the capital asset and helps the distribution companies to identify the possibility of faults. The projected technique also reduces the dependency of the individual bus. Moreover, the DG allocation at the particular bus is optimized and improves the stability of the system.

## VI. CONCLUSIONS

This paper proposes the elephant herding optimization technique for optimal allocation and sizing of distributed generation on electrical distribution networks. DG is the impeccable elucidation of recent and time ahead challenges

of modern electric power generation and distribution system. This might encounter the challenging desires of the consumers parsimoniously and ecologically by curtailing the charge, intricacy allied with on-site power generation, transmission and distribution. The proposed technique is applied on 5 bus radial power distribution system and the outcomes are presented. The result clearly indicates that the proposed EHO algorithm gives the optimal results. The proposed EHO technique is capable of producing higher quality results in terms of optimal allocation and sizing of distributed generation. The proposed EHO technique outperforms the conventional technique and the power injected by the DG in the weaker bus is also reduced considerably. The proper allocation and sizing of DG reduces the fuel cost to the distribution companies. Furthermore, this considered optimization technique may apply to the impending maneuver of the Indian Power distribution network for the proper constituting electric system.

## REFERENCES

[1] El-Khattam and Walid, "Optimal investment planning for distributed generation in a competitive electricity market," *IEEE Transactions on power systems*, vol. 19, no. 3, pp. 1674-1684, 2004.

[2] G.P.Harrison and A. R. Wallace, "Optimal power flow evaluation of distribution network capacity for the connection of distributed generation," *IEEE Proceedings Generation, Transmission and Distribution,* vol. 152, no. 1, pp. 115-122, 2004.

[3] K.Andrew and Mark O'Malley, "Optimal allocation of embedded generation on distribution networks," *IEEE Transactions on Power Systems*, vol. 20, no. 3, pp. 1640-1646, 2005.

[4] S.K.Pandey, S.R.Mohanty and N.Kishor, "A literature survey on load–frequency control for conventional and distribution generation power systems," *Renewable and Sustainable Energy Reviews*, vol. 25, pp. 318-334. 2013

[5] R.Vijay and C.S. Ravichandran. "A detailed investigation on conventional and meta-heuristic optimization algorithms for economic power scheduling problems," *International Journal of Engineering Trends and Applications*, vol. 3, no. 4, pp. 40-53, 2016.

[6] P.S. Georgilakis and N.D. Hatziargyriou, "Optimal distributed generation placement in power distribution networks:models, methods, and future research," *IEEE Transactions on Power Systems*, vol. 28, no. 3, pp. 3420-3428. 2013

[7] Paliwal.Priyanka, N. P. Patidar, and R. K. Nema, "A comprehensive survey of optimization techniques used for distributed generator siting and sizing," *Southeastcon, Proceedings of IEEE*. 2012.

[8] A. Zangeneh, S. Jadid, and A. Rahimi-Kian, "Normal boundary intersection and benefit cost ratio for distributed generation planning," *Int. Trans.Elect. Energy Syst.*, vol. 20, no. 2, pp. 97-113, 2010.

[9] S. N. Naik, D. K. Khatod, and M. P. Sharma, "Analytical approach for optimal siting and sizing of distributed generation in radial distribution networks," *IET Generation, Transmission, Distribution.*, vol. 9, no. 3, pp. 209-20, 2014.

[10] M. H. Moradi and M. Abedini, "A combination of genetic algorithm and particle swarm optimization for optimal DG location and sizing in distribution systems," *Int. J. Elect. Power Energy Syst.*, vol. 34, no. 1, pp. 66-74, Jan. 2012

[11] M.Gandomkar, M.Vakilian and M.Ehsan, "A genetic based tabu search algorithm for optimal DG allocation in distribution networks. *Electric Power Components and Systems*, vol. 33, no. 12, pp. 1351-1362, 2005.

[12] M.Nazari-Heris, S. Madadi, M.P.Hajiabbas and B.Mohammadi-Ivatloo, "Optimal distributed generation allocation using quantum inspired particle swarm optimization," *In Quantum Computing: An Environment for Intelligent Large Scale Real Application* .pp. 419-432, 2018.

[13] R.Vijay and R.Sowmya, "Optimal sitting of PV-wind-energy storage system integrated micro grid using artificial bee colony optimization technique," *International Journal of Innovative Research in Computer and Communication Engineering,* Vol. 80, 2017.

[14] R.Vijay and C.S. Ravichandran, "Optimal placement and sizing of distributed power sources in micro grid for power loss minimization using bat motivated optimization algorithm" *Asian Journal of Research in Social Sciences and Humanities,* Vol. 6, No.8, pp. 252-266, 2017.

[15] R.Vijay and J. Durga Devi. "Optimal placement and sizing of wind-PV integrated power generation by ant colony optimization technique," *International Journal of Recent Trends in Engineering & Research*, vol. 03, no. 5, pp. 2455-1457, 2017.

[16] R.Vijay, "Quorum sensing driven bacterial swarm optimization to solve practical dynamic power ecological emission economic dispatch," *International Journal of Computational Methods*, vol. *15,* no. 03, pp.1850089-24,2018.

[17] R.Vijay and C.S. Ravichandran, "Scheduling practical generating system using an improved bacterial swarm optimization," *Technical Gazette*, vol. 23, no. 5, pp. 1307-1315, 2016.

[18] V.Raviprabakaran "Optimal and stable operation of microgrid using enriched biogeography based optimization algorithm," *Journal of Electrical Engineering,* vol. 17, no. 4, pp. 1-11, 2018.

[19] K.Nekooei, M.M. Farsangi, H. Nezamabadi-Pour and K.Y.Lee, "An improved multi-objective harmony search for optimal placement of dgs in distribution systems," *IEEE Transactions on smart grid*, vol. 4, no. 1, pp. 557-567, 2013.

[20] Wang, Gai-Ge, Suash Deb and Leandro dos S. Coelho. "Elephant herding optimization," *Computational and Business Intelligence (ISCBI),* 3rd *International Symposium on IEEE*, 2015.

[21] N.K.Meena, S.Parashar, A.Swarnkar, N.Gupta and K.R.Niazi, "Improved elephant herding optimization for multiobjective DER accommodation in distribution systems", *IEEE Transactions on Industrial Informatics*, vol. 14, no. 3, pp.1029-1039, 2018.

# Design and Implementation of FIR Filter using Low Power and High-Speed Multiplier and Adders

O. Venkata Krishna
Assoc. Professor, CVR College of Engineering/EIE Department, Hyderabad, India
Email: venkatakrishna.odugu@gmail.com

*Abstract:* **The Finite Impulse Response (FIR) filter is robust and high stable architecture rather than Infinite Impulse Response (IIR) Filter for the speech and image processing applications. In this paper, a high speed and low power FIR filter is designed and implemented using Radix-4 modified Booth Multiplier and Carry Look Ahead (CLA) adder. The Booth multiplier reduces the accumulation computation time in the multiplication of filter inputs and coefficients. CLA is used to reduce the critical path delay of the normal Ripple carry adder, which is used for the addition for the FIR filter. The 8-tap direct form FIR filter is implemented using Booth multiplier and CLA, and it is simulated and synthesized. The delay and power corresponding to these blocks are computed and presented. The utilization summary with respect to target FPGA of the each block is presented.**

*Index Terms:* **FIR, CLA, Booth multiplier, FPGA, HDL, Verilog and Low Power.**

## I. INTRODUCTION

Digital filters are most frequently used for the speech processing, image processing and video processing applications. These digital filters are of two types Finite Impulse Response (FIR) filters and Infinite Impulse Response (IIR) filters. The FIR filter is preferred for the above applications due to the simplicity of the design and of high stability. The following expression (1) represents the N-tap FIR filter.

$$y[n] = a_0 x[n] + a_1 x[n-1] + a_2 x[n-2] + \cdots \qquad (1)$$

Where $a_0$, $a_1 \ldots a_n$ are the coefficients of the filter and $x[n]$ and $y[n]$ are the input and outputs of the FIR filter respectively. This FIR filter can be designed in many ways, like such as direct form, transpose form and hybrid forms. The block diagram of direct form FIR filter is shown in figure.1
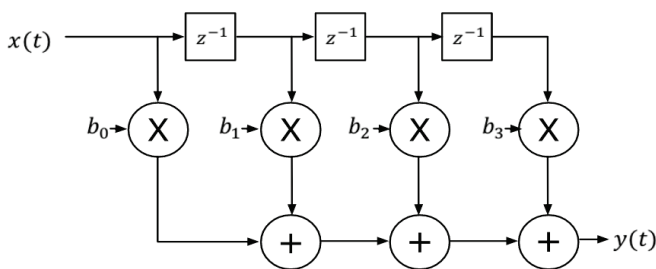


Figure 1. Block diagram of FIR filter

One of the important hardware blocks in the FIR filter is multiplier, this is used to generate the product of filter coefficients and inputs. There are different types of multipliers such as, Array multiplier, Booth's multiplier and Wallace tree multiplier, which are mostly used for the VLSI design. The other blocks are adders and delay elements. The D Flip-flops are used as delay elements in the filter, the adders are basically, Carry Look Ahead Adder (CLA) and Carry Save adders (CSA) are used in the implementation of the FIR architecture.

For the low power and high performance, the optimization can be done in block level. The optimized multiplier and adders can reduce the delay and power as well as area also. For the low power, the CLA adder and Booth multipliers are used in this work.

## II. BOOTH MULTIPLIER IMPLEMENTATION

The performance of the FIR filter depends mainly on multiplier. Hence, the optimized multiplier is implemented in this section. For the low power and less area, the booth multiplier is selected for the implementation. This approach reduces half of the accumulations and hence overall area, delay reduced.

Generally, the multiplication of two binary numbers requires partial product generation, reduction of partial products and final addition of partial products. For these operations, multiplier takes long time and more hardware. The Booth multiplier which is based on the Booth's Algorithm introduced by "Andrew Donald Booth" can be used for the reduction of delay [1]. There are radix-2 and radix-4 Booth multipliers available. The radix-2 Booth multiplier requires more additions compared to radix-4 multiplier. In this work radix-4 Booth multiplier (Modified Booth multiplier) is implemented and used for the design of FIR filter.

The Booth's concept is applicable for both signed and unsigned numbers. The figures 2 and figure 3 shows the flowchart of the radix-4 Booth's algorithm for unsigned and signed numbers respectively.

The booth multiplier multiplies two binary words with length of N x N or any length. Both the numbers signed or unsigned and combination of two types of numbers can be applied as the inputs for the multiplier. Multiplication means partial product generation, shifting and final addition. The Radix-4 modified Booth Multiplier reduces the number of partial products into half [2] [3].
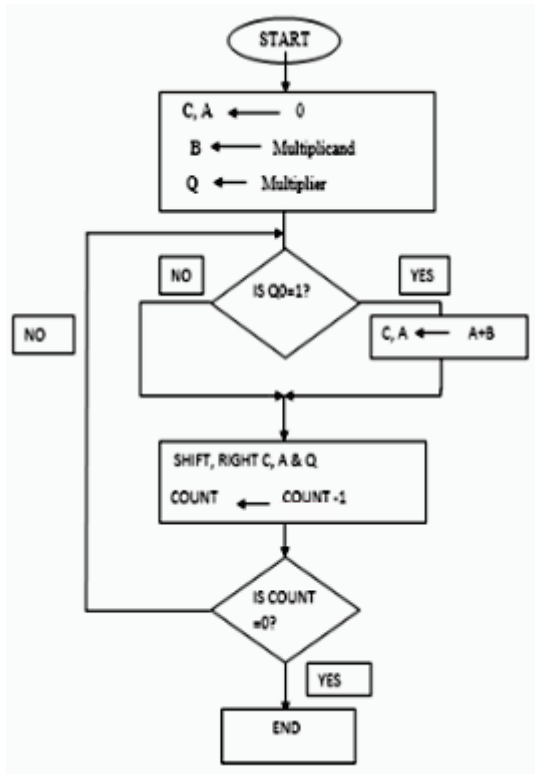
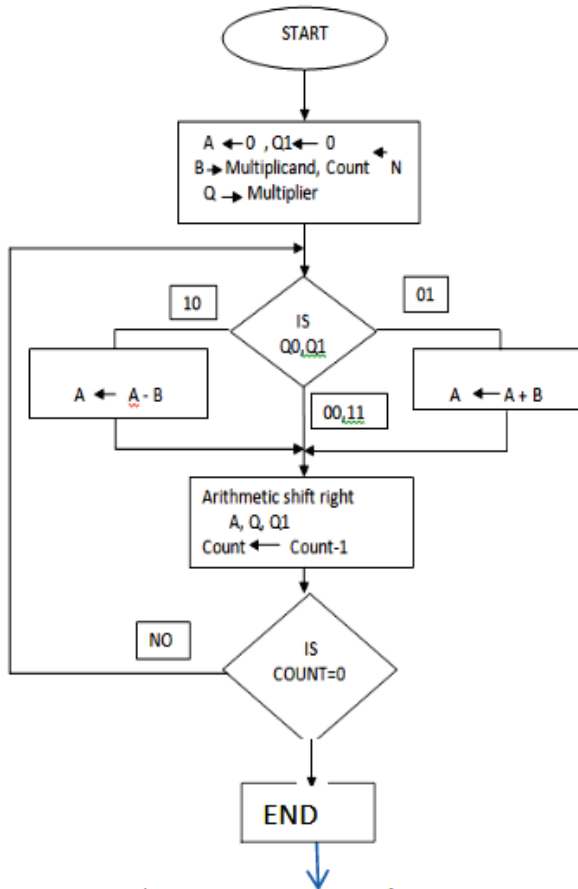Figure 2. Booth's algorithm flowchart for the unsigned numbers.

The flow charts are converted into the logic structure, which consists of control logic, 2's compliment logic circuit, partial product register, adder and shifting circuits. The hardware structure of the radix-4 modified Booth multiplier [4] [5], is shown in figure 4. The same structure is also implemented and synthesized using Xilinx ISE tool. The RTL schematic view is shown in the figure 5.
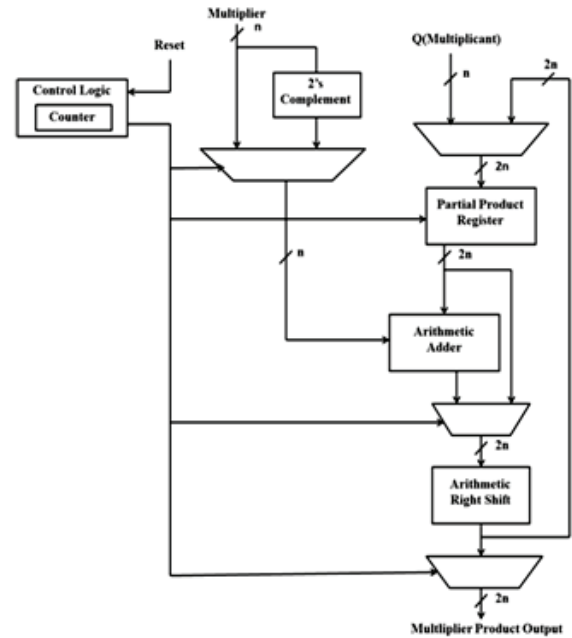


Figure 4. General architecture of Radix-4 Booth multiplier



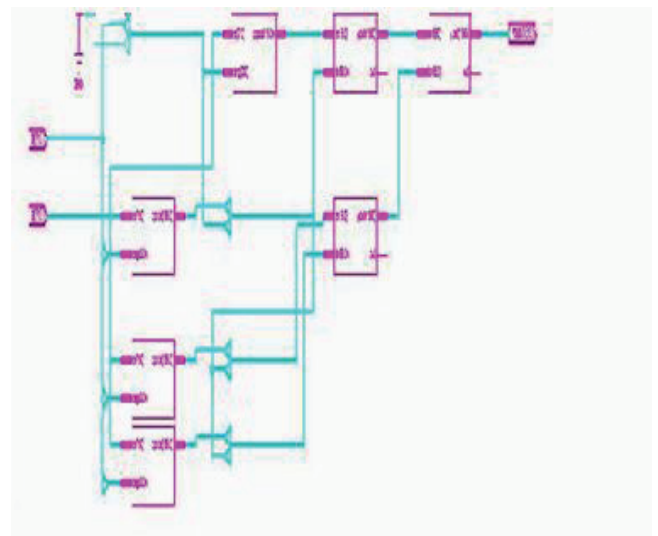Figure 5. RTL view of Radix-4 Booth multiplier

The synthesis report of the radix-4 Booth multiplier is represented in the table I this tables reports the hardware utilization for the Booth multiplier with respect to target device as Vertex Pro FPGA. The delay and power values for the Booth Multiplier are shown in the results section.



Figure 3. Booth's Algorithm in flow chart for the signed numbers.

TABLE I.
DEVICE UTILIZATION SUMMARY OF BOOTH MULTIPLIER FOR THE
TARGET DEVICE VERTEX PRO FPGA

| Device Utilization Summary (estimated values) | | | |
|---|---|---|---|
| Logic Utilization | Used | Available | Utilization |
| Number of Slice Registers | 75 | 64000 | 0% |
| Number of Slice LUTs | 278 | 64000 | 0% |
| Number of fully used LUT-FF pairs | 74 | 193 | 38% |
| Number of bonded IOBs | 132 | 640 | 20% |
| Number of BUFG/BUFGCTRLs | 3 | 32 | 9% |
| Number of DSP48Es | 80 | 256 | 31% |

## III. IMPLEMENATION OF CLA

Many High-speed adder architectures are available for the implementation of Addition, such as Carry Select, Carry Save, Carry Skip and Carry Look Ahead adders (CLA). The CLA is a robust structure that reduces the hardware and improves the speed.

The CLA overcomes the carry rippling delay, and also overcomes the latency problem in normal Ripple carry adder. The CLA adder depends on the carry generating term and carry propagate terms of the Full adder. In this, the carry is calculated for the possible carry bits and next it calculates the sum using appropriate hardware. Hence the delay is reduced with respect to the addition computation [6]. The architecture of the 4-Bit CLA is shown in the figure6.

The CLA operation depends on the propagate terms and generate terms of the full adder. The propagate and generate terms of the full adder is considered as given in the equations (2) and (3).

$$Pi = Ai \oplus Bi \qquad (2)$$

$$Gi = Ai.Bi \qquad (3)$$

The modified full adder sum and carry out are calculated with the help of the following equations (4) and (5) in CLA adder [7] [8].

$$Ci + 1 = Gi + (Pi.Ci) \qquad (4)$$

$$Si = Pi \oplus Ci \qquad (5)$$

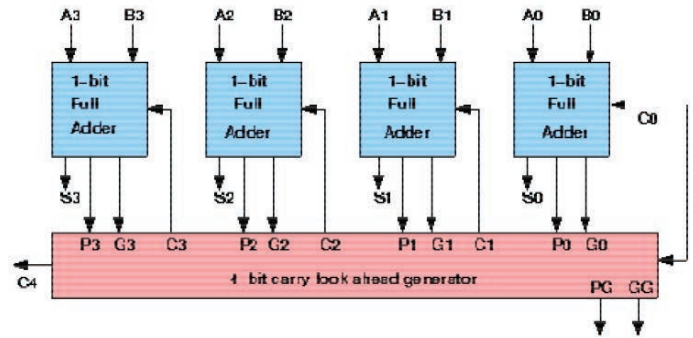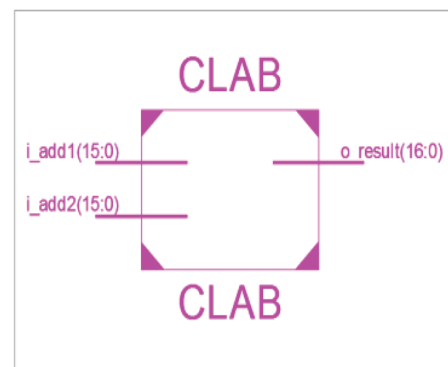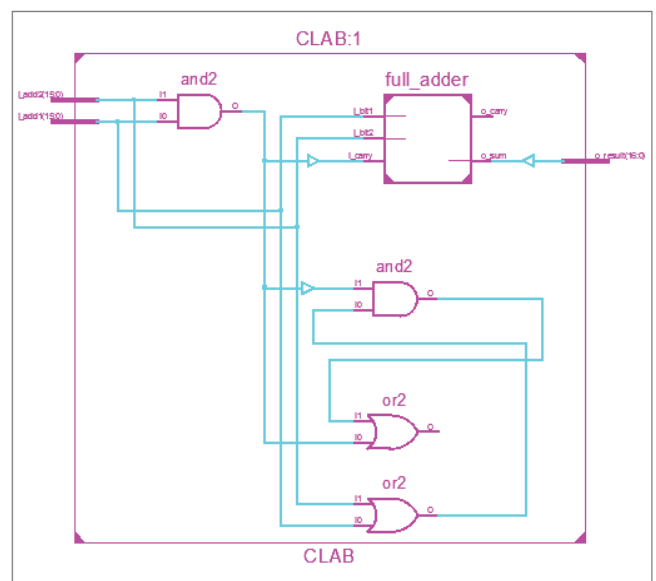Figure 6. General Architecture of the CLA

As per the above architecture, the HDL code is written to design the 16- bit CLA and simulated. The same HDL code is also synthesized using Xilinx ISE Tool. The RTL view of the 16-bit CLA as shown in the figure 7. The synthesis report of the CLA is shown in the table II.

(a)

(b)

Figure 7. RTL view of (a) the 16-bit CLA symbol (b) internal RTL view of 16-bit CLA

TABLE II.
DEVICE UTILIZATION SUMMARY OF CLA FOR THE TARGET DEVICE
VERTEX PRO FPGA

| Device Utilization Summary (estimated values) | | | |
|---|---|---|---|
| Logic Utilization | Used | Available | Utilization |
| Number of Slice LUTs | 29 | 64000 | 0% |
| Number of fully used LUT-FF pairs | 0 | 193 | 0% |
| Number of bonded IOBs | 132 | 640 | 20% |

## IV. IMPLEMENTATION OF FIR FILTER

The 8-Tap FIR filter is designed and implemented using Booth multiplier and CLA. The block based direct form FIR architecture [9] [10] selected and coded using HDL in Xilinx ISE tool and synthesized. The block-based concept is introduced for the parallel proceeding for the FIR filter to reduce the delay [11]. In this work 4 inputs are grouped as block and applied to filter input [12] [13]. The parallel processing also reduces the power consumption of the FIR filter [14]. The RTL view and the simulated output of the FIR filter is shown in the figure 8 and figure 9 respectively.
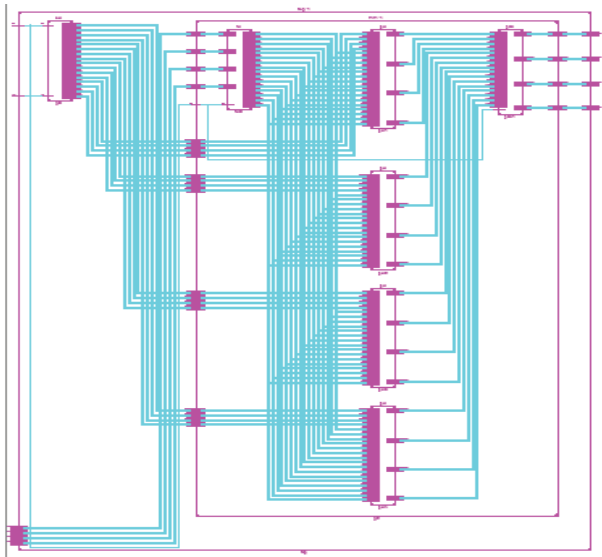


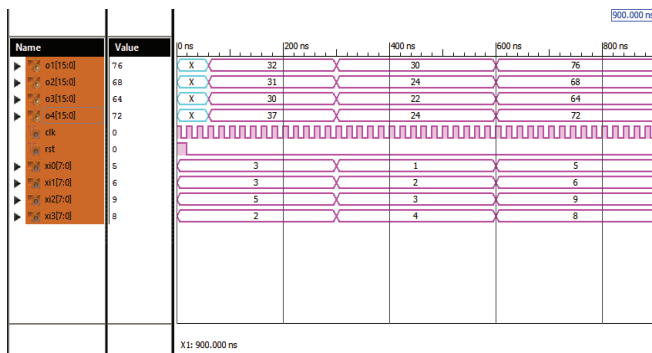Figure 8. RTL Schenatic view of 8-tap FIR Filter



Figure 9. Simulated output results of FIR Filter for the random inputs.

The utilization summary report of the 8-tap block-based FIR filter using Xilinx software is shown in the table III. Total 80 DSP blocks are required for the entire FIR filter. The total LUTs and LUT-FF pairs are 192 and 128 utilized for the 8-tap FIR filter. The input output blocks are 98 in total.

TABLE III.
DEVICE UTILIZATION SUMMARY OF FIR FILTER FOR TARGET DEVICE
VERTEX PRO FPGA

| Device Utilization Summary (estimated values) | | | |
|---|---|---|---|
| Logic Utilization | Used | Available | Utilization |
| Number of Slice Registers | 129 | 64000 | 0% |
| Number of Slice LUTs | 192 | 64000 | 0% |
| Number of fully used LUT-FF pairs | 128 | 193 | 66% |
| Number of bonded IOBs | 98 | 640 | 15% |
| Number of BUFG/BUFGCTRLs | 1 | 32 | 3% |
| Number of DSP48Es | 80 | 256 | 31% |

## V. RESULTS

In this section, the Radix-4 Booth multiplier and 16-bit CLA power consumption, area and delay are tabulated. The proposed 8-tap FIR Filter architecture is based on Booth multiplier and CLA adder power consumption, area and delay are computed using RTL compiler from CADENCE Tools. The TSMC 180nm CMOS technology is also used for synthesis of the FIR filter. Here, the same Xilinx HDL code is also synthesized using RTL compiler and it can be optimized. The RTL complier also generates the area, power and delay reports of the proposed 8 tap FIR filter. The table IV shows the area, delay and power of the FIR filter and important blocks of the FIR filter. In the previous section, Xilinx results corresponding to 8-tap FIR filter are discussed.

TABLE IV.
VLSI PARAMETERS OF FIR FILTER AND OTHER INTERNAL BLOCKS.

| Name of the structure | Area ($\mu m^2$) | Delay (ns) | Power ($\mu W$) |
|---|---|---|---|
| CLA Adder | 24544 | 8.371 | 6076 |
| Booth Multiplier | 38659 | 27.198 | 8906 |
| 8-tap FIR Filter | 91925 | 35.391 | 16967 |

## VI. Conclusions

The 8-tap FIR filter is designed and implemented using high speed adder and high-speed multiplier. The Radix-4 modified Booth multiplier and 16-bit CLA adder is considered for the implementation of high speed block based direct form 8-tap FIR filter, which is used for the digital signal processing applications. The VLSI parameters, such as area, delay and power for the optimized 8-tap FIR filter are calculated and presented. The summary report of the hardware utilization with respect to target FPGA also generated and presented in this paper for Booth multiplier, CLA adder and FIR filter. The HDL code is written and simulated, synthesized using Xilinx and RTL Compiler from CADENCE also.

## References

[1] Oscal T. -C. Chen, Sandy Wang, and Yi-Wen Wu, "Minimization of Switching Activities of Partial Products for Designing Low-Power Multipliers", IEEE Transactions on VLSI Systems, vol. 11, no. 3, June 2003.

[2] Shiann-Rong Kuang and Jiun-Ping Wang "Design of power efficient configurable booth multiplier" IEEE Trans. Circuits Syst. I Regular Papers vol. 57, no.3, pp. 568-580, March2010.

[3] TusharV.More, Dr.R.V.Kshirsagar, "Design of Low Power Column Bypass Multiplier using FPGA" IEEE journal of solid-state, circuits, vol 31,pp 1535-1546,July 2011.

[4] Akanksha Sharma, Akriti Srivastava, Anchal Agarwal, Divya Rana, Sonali Bansa "Design and Implementation of Booth Multiplier and Its Application Using VHDL. International Journal of Scientific Engineering and Technology, Volume No.3 Issue No.5, pp: 561 –563, May2014.

[5] A.RamaVasantha, M.Sai Satya Sri" Design and Implementation of FPGA Radix-4 Booth Multiplication Algorithm" in International Journal of Research in Computer and Communication Technology, Vol 3, Issue 9, September – 2014.

[6] Jagannath Samanta, Mousam Halder, Bishnu Prasad De "Performance Analysis of High Speed Low Power Carry Look-Ahead Adder" International Journal of Soft Computing and Engineering (IJSCE) ISSN: 2231-2307, Volume-2, Issue-6, Jan-2013.

[7] Fu -Chiung Cheng Stephen H. Unger "Delay - Insensitive Carry - Look ahead Adders" Manoj Kumar, Sandeep K. Aryaand Sujata Pandey "Single bit full adder design using 8 transistors" International Journal of VLSI design & Communication Systems (VLSICS) Vol.2, No.4, December 2011.

[8] M.C.B. Osorio, C.A. Sampaio, A. I. Reis, R.P. Ribas., etc.al. "Enhanced 32 - bit Carry Look Ahead Adder using Multiple Output Enable-Disable CMOS Differential Logic". SBCCI, pp. 181-185, 2004.

[9] A. Umasankar and N. Vasudevan," Design a and Analysis of Various Slice Reduction Algorithm for Low Power and Area Efficient FIR Filter", ICCTET13, IEEE Conf. July 2013.

[10] R. Mahesh and A. P. Vinod, "New reconfigurable architectures for implementing FIR filters with low complexity," IEEE Trans. Computer-Aided Design Integr. Circuits Syst., vol. 29, no. 2, pp. 275–288, Feb. 2010.

[11] S. Y. Park and P. K. Meher, "Efficient FPGA and ASIC realizations of a DA-based reconfigurable FIR digital filter," IEEE Trans. Circuits Syst. II, Exp. Briefs, vol. 61, no. 7, pp. 511–515, Jul. 2014.

[12] B. K. Mohanty and P. K. Meher, "A high- performance FIR Filter Architecture for Fixed and Reconfigurable Applications," IEEE Trans. on VLSI systems, vol. 24, issue 2, pp.444 –452, 2016.

[13] A. P. Vinod and E. M. Lai, "Low power and high-speed implementation of FIR filters for software defined radio receivers," IEEE Trans. Wireless Commun., vol. 7, no. 5, pp. 1669–1675, Jul. 2006.

[14] J. Park, W. Jeong, H. Mahmoodi-Meimand, Y. Wang, H. Choo, and K. Roy, "Computation sharing programmable FIR filter for low-power and high-performance applications," IEEE J. Solid State Circuits, vol. 39, no. 2, pp. 348–357, Feb. 2004.

# Implementation of Low Power Sigma Delta ADC for Broadband Communications

B Satish[1] and Prabhu G Benakop[2]

[1]Assoc. Professor, CVR College of Engineering/EIE Department, Hyderabad, India
Email: satishbojjawar78@gmail.com
[2]Principal, INDUR Institute of Engineering & Technology/ECE Department, Siddipet, India
Email: pgbenakop@rediffmail.com

*Abstract:* **For the broadband communication systems, the high data rate converters are required to achieve high accuracy and higher bandwidth. The mixed signal approach using CMOS technology is mostly preferred for these applications. Now a days, the ΣΔ converters are gaining popularity with their robustness. This design is implemented mainly in digital domain with small analog content. In this paper, a high speed 14-bit ΣΔ modulator with 2 MHz signal bandwidth with low oversampling ratio is designed. To increase the resolution, the dual quantization technique is used. It simplified the design and reduced the hardware circuitry and power consumption.**

*Index Terms:* ΣΔ modulator, ADC, DAC, quantization, Over Sampling, Low power and CMOS.

## I. INTRODUCTION

The high performance data converters require accuracy and high resolution of 12 to 16 bits, higher bandwidth with less production cost for broadband applications. The ΣΔ converters are mostly preferred for pipelining because of oversampling and robustness of the converter. The CMOS implementation of ΣΔ converter increases the inherent complexity but, improves the speed of the conversion process.

A high speed ΣΔ modulator for signal bandwidth of 2MHz is implemented in deep sub-micron 45 nm CMOS technology. The fourth order ΣΔ architecture is considered for the design [1]. The fourth order ΣΔ modulator consists of four integrators, comparator and amplifiers, ADC and DAC circuits. The amplifier and comparator are the analog blocks, and the remaining blocks are implemented in the digital form. Hence the mixed signal approach is used for the implementation of ΣΔ modulator in this paper.

The specifications of the ΣΔ modulator are considered for the applications of broad band communications. The table.1 represents all the specifications of important building blocks used in the modulator.

## II. BUILDING BLOCKS OF ΣΔ MODULATOR

In this section, the important building blocks of ΣΔ modulator are designed and implemented in the 45nm CMOS technology. All these blocks are operated at the power supply of 1 Volt.

### A. Front-end Amplifier

It is difficult to achieve specifications simultaneously, high gain and high speed due to degradation of output conductance in short channel transistors. By including a cascade stage, a better compromise between speed and gain is obtained, so the DC gain of the transistors with minimum length is increased to 80 dB and the gain bandwidth product of 250 MHz, with 37 mW power consumption.

TABLE I.
SPECIFICATIONS OF BUILDING BLOCKS FOR ΣΔ ADC

| Modulator | Clock Frequency | 60 MHz |
|---|---|---|
| | Differential Reference Voltage | 1V |
| | Oversampling ratio | 16 |
| | Clock jitter | 15ps (0.1%) |
| | Dual quantization | 1bit /4 bit |
| Front-End Integrator | Sampling capacitor | 0.5pF |
| | Switch on resistance | 250Ω |
| | Capacitor non-linearity | 25ppm/V |
| Amplifier | Open Loop DC gain | 2500 |
| | Slew rate | 380V/μs |
| | Gain bandwidth product | 235MHz |
| Comparators | Offset | ±10mV |
| | Hysteresis | 10mV |
| | Resolution time | 3.5ns |
| ADC and DAC | Resolution | 4-bit |
| | DAC INL | 0.4% FS |

Figure 1 shows a two stage operational amplifier (OpAmp1) with Miller compensation is used to achieve high gain; and high bandwidth is achieved. Miller compensation converts an internal pole pertaining to specific node, to become dominant pole by adding a small physical capacitance, which will be simulated as a large capacitance due to Miller effect and brings the effect of pole with low frequency. This technique is used for the transistors M12 and M13, so that high bandwidth as well as high speed can be achieved.

One more compensation technique called nulling resistor along with miller capacitor can be used to improve stability [2] [3]. The nulling resistor eliminates the zero present in the right half of s-plane. It even brings the zero present on RH side into LH side, so that excellent stability can be obtained. But nulling resistor implemented with MOSFET when coupled through miller capacitor degrades the transient response of integrator, as the output voltage will be reduced

due to compensation capacitor. This technique is used in this implementation as it needs less power to implement and is more stable with temperature and process variations.
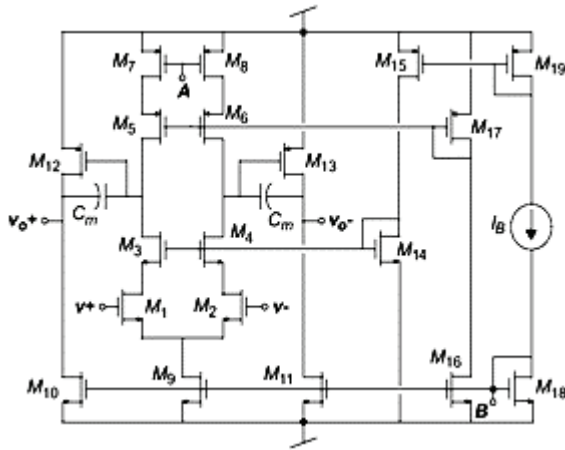


Figure 1. Two stage operational amplifier (OpAmp1) internal diagram with Miller compensation.

The weights used in implementing integrators strongly influences the output swing of the amplifier, when the reference voltage is fixed.

The transient response of the two stage Operational Amplifier used as a front-end integrator in the modulator is presented in the figure 2 [4]. It behaves like a first order system and it settles properly in the given time slot.
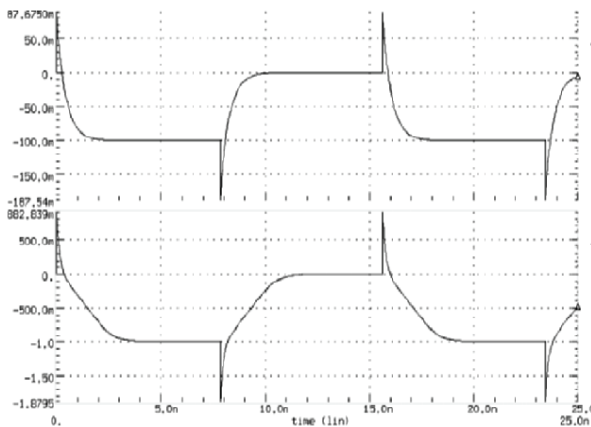


Figure 2. Transient response of two stage operational amplifier (OpAmp1)

The biasing requirement of an amplifier is fulfilled by transistors M14 to M19. The amplifier biasing stage is implemented by transistors $M_{14}$ to $M_{19}$. A dynamic CMFB net is used to minimize the power consumption to zero static power dissipation. Note that an inverting stage ($M_{20}$, $M_{21}$) is added to the basic SC net in order to implement the negative common-mode feedback.

B. Amplifiers other than stage 1

The second stage and next stage integrators require medium DC gain amplifiers. Hence, a cascade single stage

amplifiers are used. Telescopic operational amplifiers has advantage of providing signal path by only NMOS transistors, non-existence of mirror poles and a small bias current is required to operate with expected output voltage swing of 1 volt. The disadvantage of telescopic Op-Amp is that its common mode voltage levels at the both inputs must be different and also it requires a precisely controllable voltage reference to get stable and large voltage swing. A folded cascade operational amplifier is used in this design [5]. It has more advantages than telescopic Op-Amp such as, superior frequency response, better PSRR. However both consume equal power.
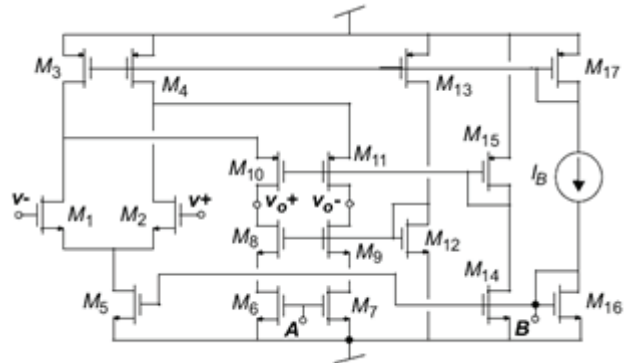


Figure 3. Schematic of Folded-Cascode Amplifier (OpAmp2, OpAmp3, OpAmp4).

The simulated output results of the OpAmp1, OpAmp2, OpAmp3 and OpAmp4 are presented in the table 2. The order of the ΣΔ modulator refers to the number of loops with integrator. These four Operational Amplifiers are used as four integrators in the fourth order ΣΔ modulator. The power consumption, gain and some important parameters are compared among all the operational amplifiers.

The power consumption of OpAmp4 is higher when compared with OpAmp2 and OpAmp3. The reason is that the OpAmp4 has larger load capacitance.

TABLE II.
SIMALTAED OUTPUT PARAMETERS OF THE FOUR AMPLIFIERS

| Parameters | OpAmp1 | OpAmp2 | OpAmp3 | OpAmp4 |
|---|---|---|---|---|
| DC gain (dB) | 80.0 | 62.8 | 55.7 | 62 |
| GB (MHz) | 250 | 311 | 261 | 167 |
| PM (Degrees) | 67 | 65 | 71 | 79 |
| SR (V/µs) | 390 | 410 | 320 | 185 |
| Input Noise (nV/√Hz) | 5 | 3.2 | 4.1 | 3.8 |
| OS (Volts) | ±2.5 | ±3.1 | ±2.9 | ±3.1 |
| Power (mV) | 38.5 | 4.5 | 4.0 | 6.6 |

The figure 4 shows the simulated output waveform of the second integrator, which is also used for third and fourth integrators in the modulator implementation. The output is linear but has limited slew rate as the applied input is a large step signal. This is tolerable for this design as it reduced the power dissipation.
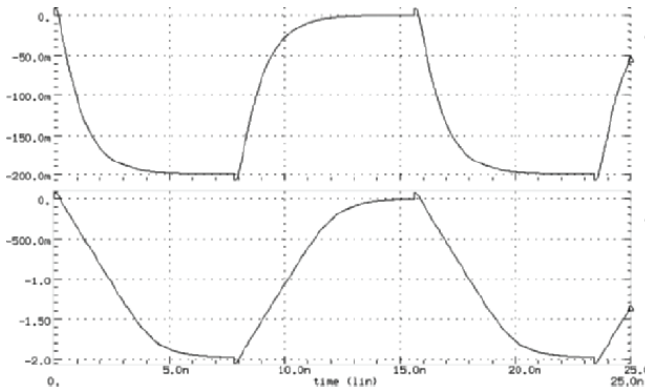
Figure 4.Simulated small- and large-signal transient response of the fourth integrator.

### C. Comparators

The comparators used in this design needs low resolution time with large hysteresis voltage of up to 10 mV. Generally, this can be implemented with traditional comparator with pre-amplifier stage, positive feedback circuit used as decision making circuit and output buffer. But it takes large area and more power required for implementation. Instead a dynamic comparator with regenerative latch is used as it does not require the pre-amplification stage and has zero static power dissipation. The regenerative latch used acts as decision making circuit while comparing the two inputs.

Figure 5 shows the architecture employed for the implementation of comparators [6], which has been widely used in $\Sigma\Delta$ modulator design. In practice, this topology is capable of achieving resolutions that required with no pre-amplifying stage.
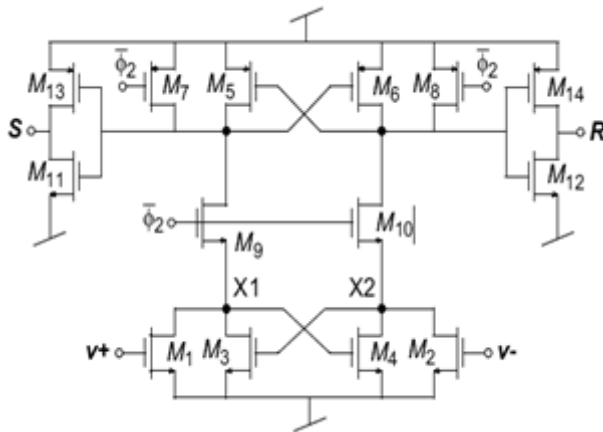


Figure 5.Dynamic comparator with Regenerative latch

The important features obtained after simulating the comparator are shown in the below table III.

TABLE III.
COMPARATOR RESULTS AFTER SIMULATION

| Hysteresis | < 10 mV |
|---|---|
| Resolution time, LH | 2.5 ns |
| Resolution time, HL | 2.3 ns |
| Power consumption | 0.65 mW |

## III. PROGRAMMABLE A/D/A CONVERTER

The switched capacitor 4-bit A-D-A converter is implemented and discussed in this section. It can also be used for 2 or 3 bit resolutions. A fully differential parallel ADC is designed and used to compare the differential voltage as illustrated in the figure.6

### A. A/D converter

The fully differential flash architecture is used for A to D converter, which compares the differential input voltage with the reference voltages [7]. The reference voltages are produced by DAC. During the $\Phi_1$phase, Vref positive and Vref negative values are stored in the input capacitors, which are then used to compute the difference during phase $\Phi_2$. At the end of $\Phi_2$, comparators are activated to find the sign of that difference. The thermometer output code of the 15 comparators is then translated to a code using AND gates.

Comparators in the ADC are identical to those used in the 1st and 2nd stage. Multi-metal sandwich capacitors of value are used and the analog switches are identical to those in the SC. The timing scheme of the switches has been adapted to reduce the capacitive load to the fourth integrator. Nevertheless, it suffers from input dependent charge injection from switches controlled by $\Phi_2$. This problem has been overcome by making these switches considerably smaller (for both NMOS and PMOS), with no degradation of the converter performance.
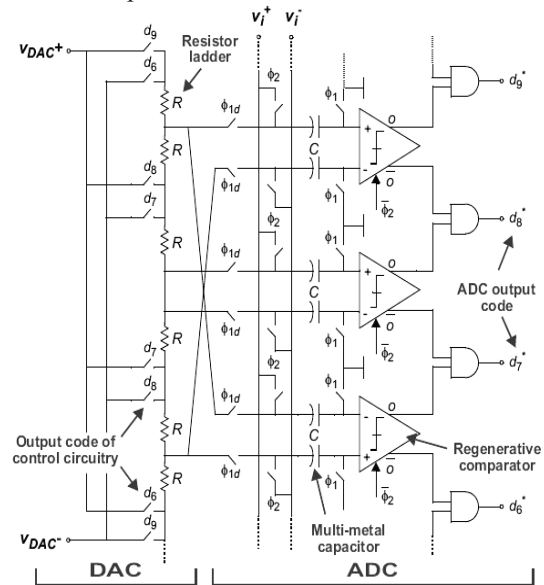


Figure 6. Programmable A/D/A converter: Partial view of the Switched Capacitor implementation.

### B. D/A Converter

For the proposed ADC, the ladder type DAC is used. This DAC provides the reference voltage for the ADC. The same DAC is also used for the conversion of digital voltage to analog output voltage in overall A/D/A converter. The ladder resistor network will generate the equivalent output analog voltage based on the selection of resistors corresponding to digital code.

The Resistor ladder network comprises of 30 unit resistors, which are connected between positive and negative reference voltages, +Vref and –Vref respectively. The value of each unit resistor is 50Ω and differential full scale current is 1.33mA. The resistors are implemented by un-silicided poly layers to provide high resistivity, good matching and is independent on variations of temperature. It also provides small settling error.

### C. Control Circuitry

The 4 bit A/D/A converter provides 2 or 3 bit resolution with the help of digital control circuitry, which is shown in the figure 7. The selection of the desired resolution is done with two signals, $S_{3b}$ and $S_{2b}$. The partial view of the digital control circuitry, which is used in the programmable A/D/A converter is shown in the figure 8.
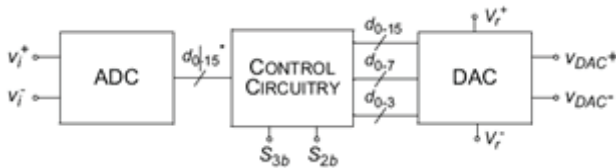


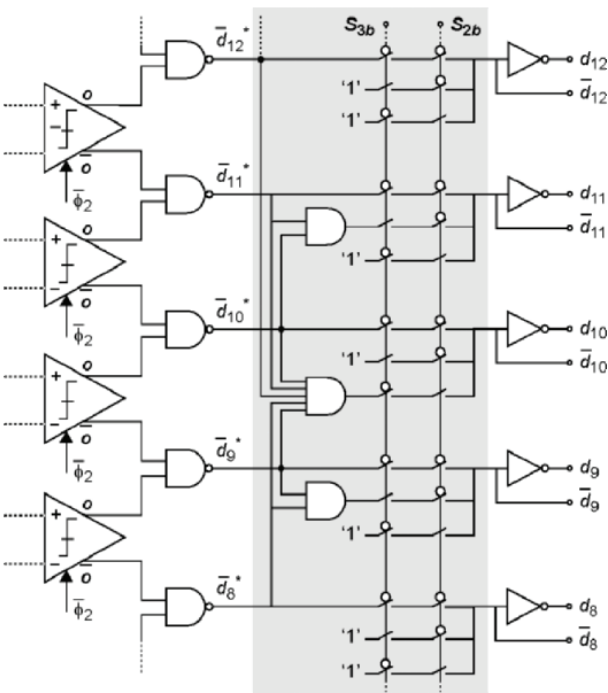Figure 7. Block diagram of the programmable A/D/A converter.



Figure 8. Partial view of the control circuitry.

### D. Clock phase generator

The different clock phases are generated using the circuit diagram shown in the figure 9 from external clock. The delayed version of these clock phases are used to reduce signal dependent charge injection [8]. The complimentary cock signals for the phases also generated by this circuit.
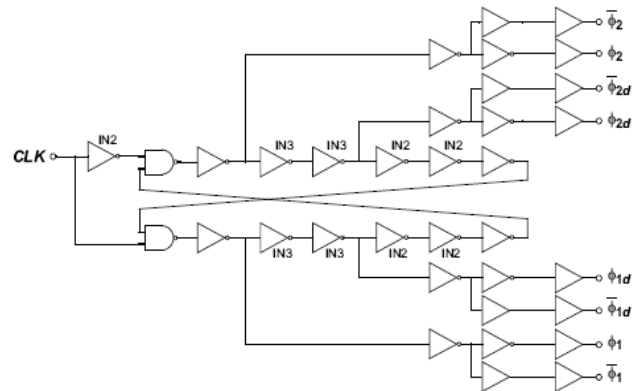


Figure 9. Clock phase generator and drivers.

The complete timing of the different clock phases are used in the ΣΔ modulator as shown in the figure.10
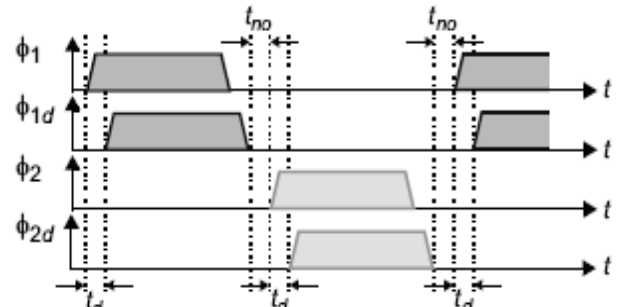


Figure 10. Timing of the clock phases in the ΣΔ modulator.

## IV. RESULTS

The functionality of the entire A/D/A converter operation is tested and measured using specific samples. The ADC, DAC and clock driver is also measured using specific test samples.

The code histogram method of sinewaves is used to measure the ADC performance [9]. An amplitude of 1 volt and 103 KHz frequency was applied to the ADC. The corresponding digital codes for 100 input periods were measured by digital tester. The analog and digital voltages are estimated from the 16 bit digital output code.

The 16-bit digital code is applied using digital tester to DAC and measures the performance, and the corresponding analog output voltages of DAC using high accuracy multi meter [10]. The performance measurement results are shown in the table 4. From that table we can conclude that the proposed ΣΔ modulator meets the specifications.

TABLE IV.
PERFORMANCE MEASUREMENTS OF THE A/D/A CONVERTER

| Parameter | ADC | | DAC | |
|---|---|---|---|---|
| | %FS | LSB | %FS | LSB |
| Offset error | -2.014 | -0.203 | 0.302 | 0.045 |
| Gain error | 4.595 | 0.659 | -0.633 | -0.098 |
| DNL | 2.894 | 0.453 | 0.153 | 0.016 |
| INL | 1.652 | 0.256 | 0.156 | 0.018 |

## V. CONCLUSIONS

In this paper, the low power ΣΔ modulator is implemented with resolution of 14 bits for the ADC with signal bandwidth of 2MHz. A 2-1-1 ΣΔ Modulator with $4^{th}$ order 3 stage cascade topology employing dual-quantization was selected. The dual quantization is only used in the last stages of modulator. The quantization power was reduced without any change in the linearity of the modulator. All the building blocks of the modulator are implemented in SC form using CAD tools. The topology of all the blocks and designs in transistor and gate level are described in this paper.

The entire modulator is implemented in the CMOS technology with power supply voltage of 1V. The low $V_t$ and multi metal capacitors, gates and switches with thick oxide are used to reduce the power in the modulator

## REFERENCES

[1]  Karema T., Ritoniemi T., and Tenhunen H., "Fourth Order Sigma-Delta Modulator Circuit for Digital Audio and ISDN Applications", Proc. of European Circuit Theory and Design Conference, 1989, pp 223-227.

[2]  D.A. Johns, K.Martin, Analog Integrated Circuit Design. John Wiley & Sons, 1997.

[3]  B.Razavi, Design of Analog CMOS Integrated Circuits. McGraw-Hill, 2000

[4]  Henil Langalia, Sarthak Lad, Mangesh Lolge, Surendra Rathod, "Analysis of two-stage CMOS Op-Amp for Single-Event Transients", International Conference on Communication Information & Technology (ICCICT), pp. 1-4, Oct. 19–20, 2012

[5]  S. C. Liu, K. T. Tang, "A low-voltage low-power Sigma-delta modulator for bio-potential signals", 2011 IEEE/NIH Life Science Systems and Applications Workshop (LiSSA), pp. 24-27, 7–8 April 2011.

[6]  Yukawa, "Analysis and Design of 2nd order sigma-delta modulator for audio applications". IEEE conference on Advances in computing, communications and informatics, at New Delhi, India, Dec2014.

[7]  Xian Tang , Kong Pang Pun, "New fully-differential amplifier-less pipelined ADC with wide power scalability and ERBW, Analog Integrated Circuits and Signal Processing", v.80 n.3, p.427-435, September 2014

[8]  Y. B. Hsieh, Y. H. Kao, "A fully integrated spread spectrum clock generator using two-point delta-sigma modulation", Proc. IEEE International Symposium. Circuits Systems, pp. 2156-2159, May 2007.

[9]  A.R. Feldman, B.E. Boser, and P.R. Gray, "A 13-Bit, 1.4-MS/s Sigma-Delta Modulator for RF Baseband Channel Applications". IEEE Journal of Solid-State Circuits, vol. 33, pp. 1462-1469, October 1998.

[10] K. Bult, G.J.G.M. Geelen, "A Fast-Settling CMOS Op Amp for SC Circuits with 90-dB DC Gain". IEEE Journal of Solid-State Circuits, vol. 25, pp. 1379-1384, December 1990.

# Design and Analysis of Welding Fixture for Elementary Weld Joints

Neeraj Kumar Jha[1] and Raghu Prem B[2]
[1]Assoc. Professor, CVR College of Engineering/ Mechanical Department, Hyderabad, India
Email: neerajjha.me@gmail.com
[2]Senior Engineer, Voltas Limited/ Mumbai, India
Email: premraghu63@gmail.com

*Abstract:* Fixtures are tools and contributes to increasing manufacturing efficiency and productivity. They are utilized in various manufacturing processes to rest, support and locate the workpiece. Welding fixtures are utilized in fabrication shops. They are specifically utilized to hold and locate the metallic plates and piece parts for permanent joining. They appear simple in construction but to develop an effective welding fixture, deep knowledge of design and manufacturing is required. Welding fixtures can be under static load from the workpiece they are supporting as well as under thermal stresses due to heat liberated by the particular welding process. The purpose of this paper is to provide a model and analyze a compact welding fixture and to illustrate few weld joints for small metal plates. The same model can be utilized efficiently to weld metal plates with variations in dimensions within some range. Software used for modeling of parts is CATIA V5R20 and that for the analysis is ANSYS 16.0

*Index Terms:* Fixture, Welding, Manufacturing efficiency, Productivity, Static load, Thermal stress, Weld joints, CATIA V5R20, ANSYS 16.0

## I. INTRODUCTION

Welding is process of joining metal parts in the presence of heat. Pressure is also applied in some processes of welding. Melting point, thermal conductivity, electric resistance and surface condition of the metal to be joined are those factors which must be studied well before designing a welded joint [1]. A lot of controlled parameters contribute to a defect free weld joint. Otherwise defects are unavoidable either in weldment or in welded joints. The correct welding technique is another important aspect to be taken care of while obtaining a weld joint. Defects like excess fusion, lap, undercut, improper fusions etc. are outcomes of a poor welding technique. Other defects like distortion or warpage is also observed in a welded joint which is a combined contribution of poor welding techniques and behavior of metal against thermal expansion and contraction. Once a weld joint is designed, it is the task of the welder to accomplish the joint, based on his skill with the available equipments. Proper work alignment is additional task which is to be taken care by a welder. With improper workholding and misaligned piece parts, a proper weld joints cannot be obtained.

To overcome the problems occurring in welded parts due to improper workholding, especially designed tools called welding fixtures are introduced in fabrication industries. A welding fixture is used to have proper provision of locating the piece parts and holding them firmly, so that these parts can be joined permanently by a suitable welding process. A welding fixture is a special purpose tool which is used to obtain one type of weld part usually. These fixtures are used at various stages in a fabrication shop to join various shapes, sizes and types of metals. Use of welding fixtures eases job setting work of a welder. These are economically used in mass production and especially when to be joined part profile is very complex. Based on the part geometry and design of welded joint, design of welding fixture can also be complicated to complex.

In the past there was limited research and applications in the welding sector. But, due to importance of welding for sheet metal in automobile and aerospace industries, the importance of welding has received special attention from designers, manufacturers and researchers. A weld fixture is often developed to reduce the deformation of each workpiece due to heat and residual stress in the welding process to reduce the dimensional variation of the assembly. Thus deformation analysis must be done to enhance the ability of the fixture on deformation controlling [2, 3].

While designing a welding fixture the following points must be considered [4]:

1. Expansion of heated workpiece and resultant distortion should not affect proper location, clamping, loading unloading and melting. Thus adequate clearance must be provided between workpiece and locators.
2. Welding spatters should not be allowed to fall on the threaded parts of the clamping elements. Thus the toggle clamps without threaded parts should be used in welding fixtures.
3. Provision for spatter grooves should be there below the line of welding.
4. Care should be taken to check that the joined workpiece does not get stuck or locked in the welding fixture.
5. For workpiece which need welding from a number of sides, a provision for easy tilting or rotating the fixture should be made, to simplify welding from various sides.

Based on above mentioned design considerations, this paper aims at designing and analyzing a compact welding fixture which can be used suitably to prepare Lap, Butt and T-weld joints on mild steel plates within the dimension range of 50 X 50 X 5 mm to 50 X 100 X 20 mm.
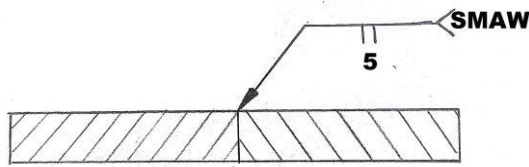
## II. JOINT DESIGN



Figure 1. Butt Joint Design

Figure 1 indicates joint design for square butt weld for butt joint. Figure 2 indicates joint design for fillet weld for lap joint. T- Joint to be obtained by fillet weld is indicated in Figure 3. Size of weld is 5mm and considered plate size for the joint is 50 X 100 X 5mm. Shielded metal arc welding (SMAW) is considered as welding process for further design considerations and analysis.
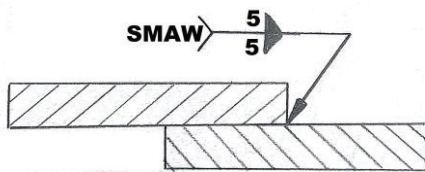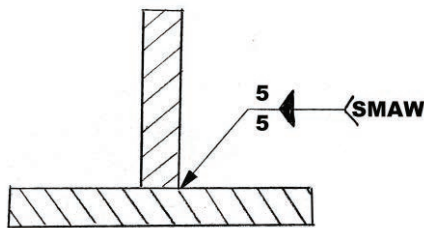


Figure 2. Lap Joint Design



Figure 3. T- joint Design

Table I represents few process variables related to SMAW process [5]. Current setting, polarity, electrode diameter and flux composition are among a few parameters which must be set properly to obtain a good quality weldment with good appearance by SMAW process. Otherwise weldment with non-uniform temperature and excess of spatters can be observed. These factors lead to defected, weak weld joints which are poor in appearance.

TABLE I.
PROCESS PARAMETERS RELATED TO SWAW

| Heat Source | Electric Arc |
|---|---|
| Electrode Type | Consumable |
| Operating Current | 30-300A |
| Operating Voltage | 15-45 V |
| Max. Temperature | 5000°C |
| Optimum Welding Speed | 75-150 mm/ min |
| Position Of Weld | All |
| Mode Of Operation | Manual |
| Weld Quality | Average |

As the plates to be joined are considered 5mm thick and SMAW gives deposition at high temperature, without beveling of the edges sufficient depth of penetration can be ensured for butt weld joint. But for good depth of penetration, the surfaces are assumed clean and free from any layer of scale, rust and lubricant.

Material selection is an inseparable part of the design. For analysis it is another important aspect to consider in design phase. Mild Steel (MS) is selected for the purpose of fixture design due to its own advantages. Mild steel is a ductile metal at room temperature. It has adequate strength against loads as well as it is not costly. Thus for moderate strength mild steel can be easily used. Few of the important characteristics of mild steel are enlisted in Table II [5].

TABLE II.
MATERIAL SPECIFICATION
MILD STEEL (MS)

| Density | 7800-7900 kg/m³ |
|---|---|
| Melting Point | 1370 °C |
| Carbon Content | 0.08-0.25% wt |
| Elasticity Modulus | $2.1 \times 10^5$ MPa |
| Elongation | 26-47 % |
| Yield Strength | 250-395 MPa |
| Tensile Strength | 345-580 MPa |
| Coefficient of Thermal Expansion | $7.2 \times 10^6/$ °C |
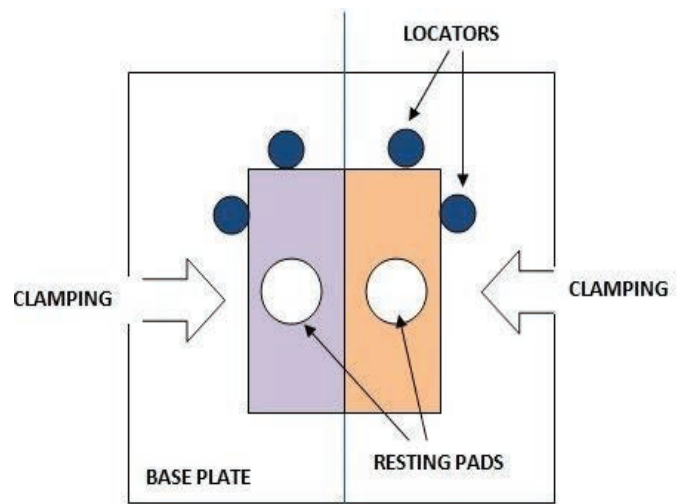


Figure 4. Base Plate Size Estimation

## III. DESIGN ESTIMATIONS AND FIXTURE DESIGN

Based on design considerations and the to be welded plate size, base plate dimension is estimated as 254 X 254mm and the same is shown in Figure 4. Estimation of plate size is important because not only it has to rest and locate the weld plates but the same plate has to accommodate the clamping devices also.

There are three main structural components in a fixture viz. locator, clamp and support. Locator is a stationary part unlike clamp which is movable. The locator can be a pin or a surface. Clamps are specifically designed mechanisms to apply force to grip the workpiece. Support is mostly stable on fixture, it holds the work piece and it helps the work

piece in keeping its geometry under thermal stresses. Thermal stresses rises because of heat output of welding process. [6].

Overall dimension estimated for base plate is 254 X 254mm and it can accommodate upto 150mm long MS plates for welding. Figure 4 further indicates feasible positions of resting and location. Locators are required in all manufacturing processes as their work is to overcome complex alignment of the workpiece [7].
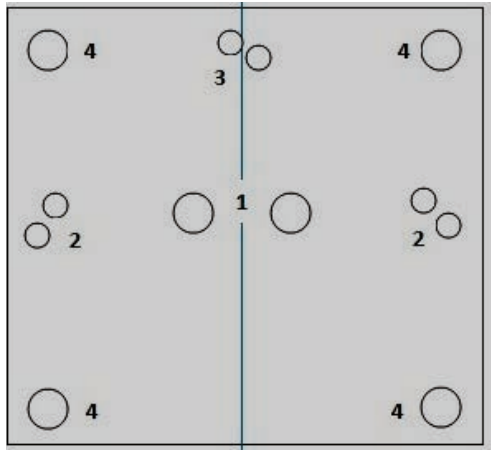


Figure 5. Reference Positions in Base Plate

In Figure 5, hole positions represented by 1 indicates position of rest pads to support weld plates in lap and butt arrangement. Holes indicated by 2 are for clamping devices.
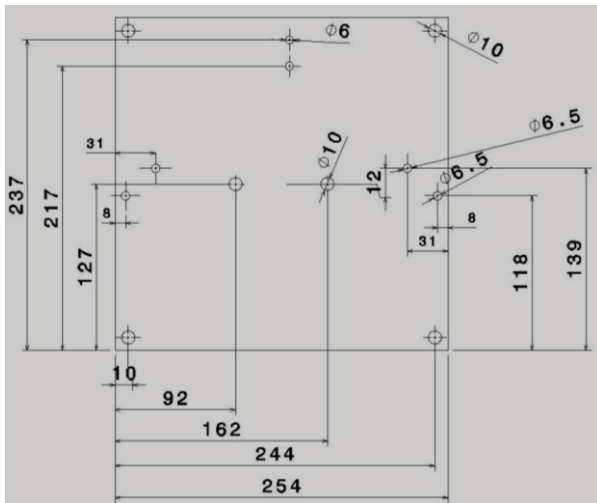


Figure 6. Base Plate Drafting (all dimensions are in mm)

Position 3 indicates place for bracket which is special attachment for T- joint. Positions indicated by 4 are support for base plate. Dimensional representation for base plate is in Figure 6.

Flat machined rest pads are implemented for resting of weld plates. They are adjustable in nature. When these pads have to rest weld plates for butt joint, they will be in contact with the surface of the base plate. Weld plates at this position will be facing each other. Same position can be utilized if there is requirement of groove weld on plates of various thicknesses. There is ample gap between rest pads to dissipate heat liberated by welding as well as for collection of spatters.
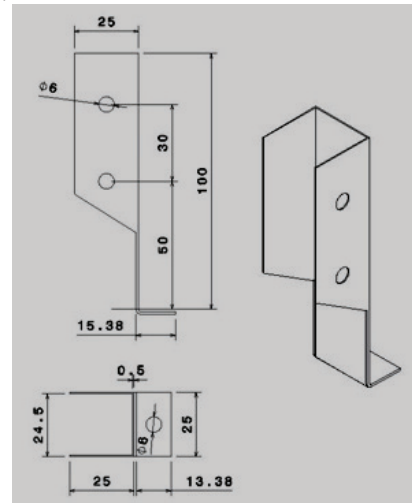


Figure 7. T-joint Bracket Drafting (all dimensions are in mm)

When there is a requirement of lap joint, one rest pad will be lifted to plate thickness height so that the plates can overlap.

For T-joint, a formed bracket is installed at one end of base plate. It is planned and designed such that it can support vertical plate upto 20 mm thickness over 40 mm thick plate in T position. This bracket is shown in Figure 7.

Bases on design consideration, lift type toggle clamps are used for holding weld plates. Freedom of adjustments are achieved with bolts and wing nuts of various dimensions. Assembled welding fixture model is shown in Figure 8.



Figure 8. Designed Welding Fixture Model

Part description of the designed fixture is shown in Table III. Proper view of assembly to indicate all of its parts is represented in Figure 9.

TABLE III.
BILL OF MATERIAL
WELDING FIXTURE

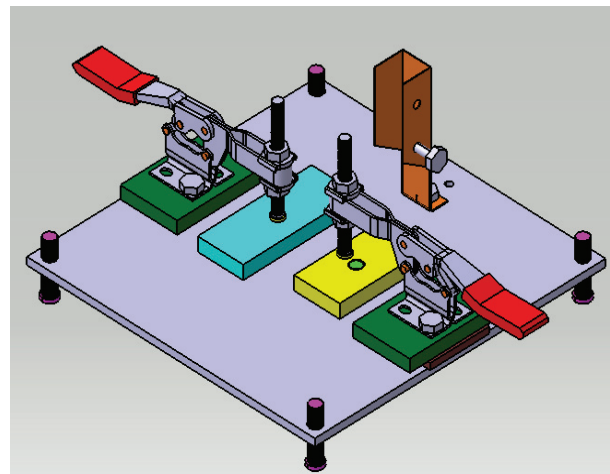| S.No. | Component Name | Material | Dimension | Qty. |
|---|---|---|---|---|
| 1 | Base Plate | MS | 254 x 254 x 6 mm | 1 |
| 2 | Toggle Clamps | Standard | Clamping Force upto 25 N | 2 |
| 3 | Nuts and Bolts | MS | M6 | 5 |
| 4 | Nuts and Bolts | MS | M10 | 6 |
| 5 | Clamps Support | MS | 80 x 50 x 10 mm | 2 |
| 6 | T- joint  bracket | MS | 25 x 25 x 115mm | 1 |
| 7 | Rest Pad - 1 | MS | 70 x 40 x 11 mm | 1 |
| 8 | Rest Pad - 2 | MS | 100 x 40 x 11 mm | 1 |
| 9 | Wingnut | MS | M6 | 1 |
| 10 | Wingnut | MS | M10 | 2 |

Numbers of parts used in welding fixture are kept low. Less number of parts ensures lesser maintenance requirement for fixture as well as less overall weight of the fixture. Indirectly, compactness of the model is ensured by less number of parts.
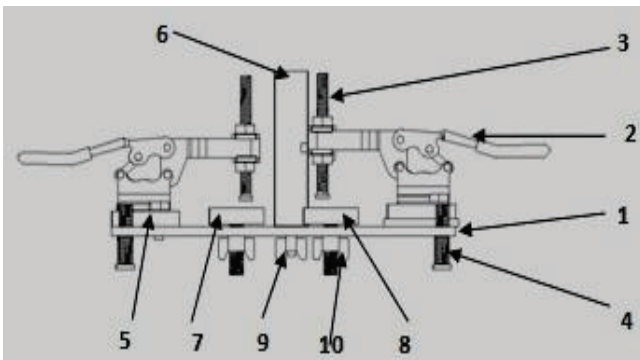


Figure 9. Welding Fixture Assembly (indicating all parts)

*A. Fixture Design:  Butt Joint*

To obtain butt joint, rest pads are in contact with the base plate. Weld plates are butt together and gripped against toggle clamps on rest pads as shown in Figure 10. Mounting and removal of weld parts are simple as well as plates of variable thicknesses can also be welded in this setup.
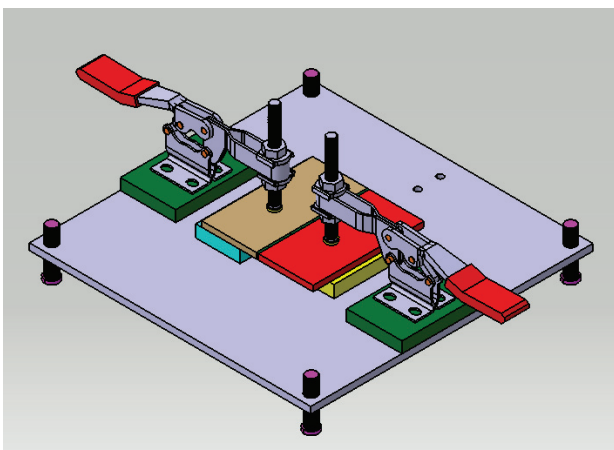


Figure 10. Designed Welding Fixture: Butt Joint

*B. Fixture Design:  LapJoint*

To obtain designed lap joint, one rest pad is to be lifted to the height of weld plate. Then the weld plates can overlap upto required length and can be gripped by toggle clamps as shown in Figure 11.  For fillet weld on the other side, plates have to be unmounted. After inverting them again, they can be gripped under toggle clamp to perform fillet weld.
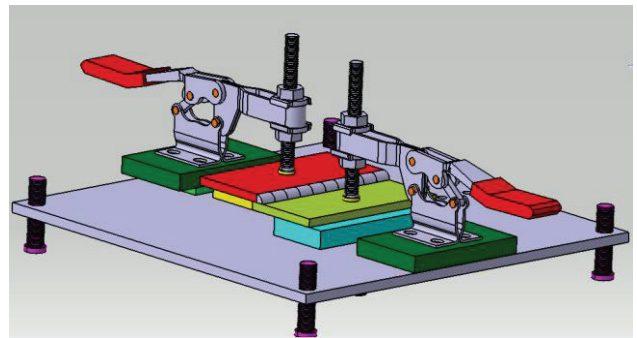


Figure 11. Designed Welding Fixture: Lap Joint

*C. Fixture Design:  T-Joint*

To obtain T- joint, designed bracket is to be attached to the base plate.  Horizontal plate may rest over rest pads but the vertical plate is to be rested in bracket by properly aligning in bracket. The horizontal plate can be gripped against clamp and the vertical plate will be held with fasteners in the bracket, as shown in Figure12.
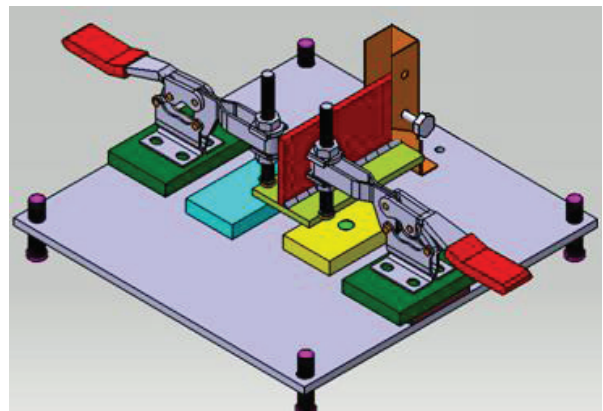


Figure 12. Designed Welding Fixture: T-Joint

## IV.  ANALYSIS

Static load and thermal analysis are performed on the designed fixture in order to ensure feasibility of designed fixture. ANSYS 16.0 is utilized for this purpose.

*A.  Static Load Analysis*

Static load analysis helps us to know deformation pattern of designed fixture under applied static loads. This analysis may further help us to estimate size and weight of workpiece to be accommodated over the fixture.

Static load analysis is performed on butt joint arrangement of the fixture. The similar loading situation and obtained result can be approximated for lap and T-joint.

Loading condition includes weight of plate and clamping force. Loading condition is indicated in Figure 13.
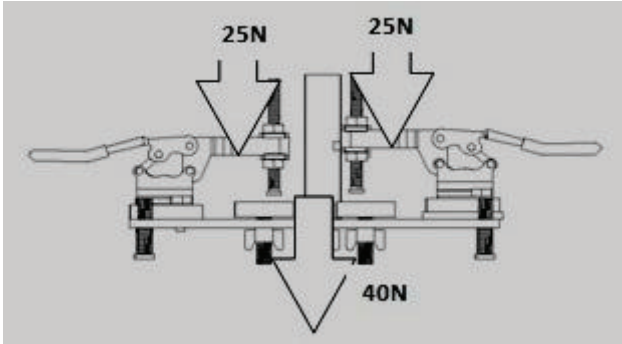


Figure 13. Loading Condition for Static Load Analysis

Based on loading condition Von Mises Stress analysis and deformation analysis is done for butt joint. Figure 14 and Figure 15 indicates results obtained for Von Mises stress and deformation analysis respectively. Observations are listed in Table IV.
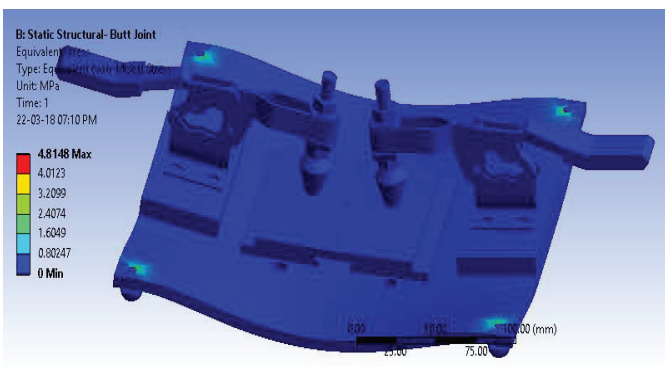


Figure 14. Von Mises Stress During Butt Joint

TABLE IV.
ANALYTICAL OBSERVATIONS
STATIC LOAD ANALYSIS BUTT JOINT

| Minimum Stress | 0 MPa |
|---|---|
| Maximum stress | 4.8148 MPa |
| Minimum Stress on | Support |
| Maximum stress on | Clamp |
| Minimum Deformation | 0 mm |
| Maximum Deformation | 0.0028164 mm |
| Minimum Deformation on | Support |
| Maximum Deformation on | Clamp |

*B. Thermal Analysis*

Thermal analysis is necessary here to know the effect of heat liberated by the process of welding on the fixture setup.



Figure 15. Total Deformation During Butt Joint

Usually in SMAW width of arc is wide. A wide arc zone contributes to wide heat affected zone and this widely dispersed amount of heat may harm other fixture parts in long production run.

Transient thermal analysis is done using ANSYS 16.0 to estimate temperature distribution on fixture surface. Thermal analysis on welding fixture for butt joint arrangement is shown in Figure 16. Figure 17 and Figure 18 are indicating thermal analysis results in lap and T-joint condition. Observations of the thermal analysis are indicated in Table V.
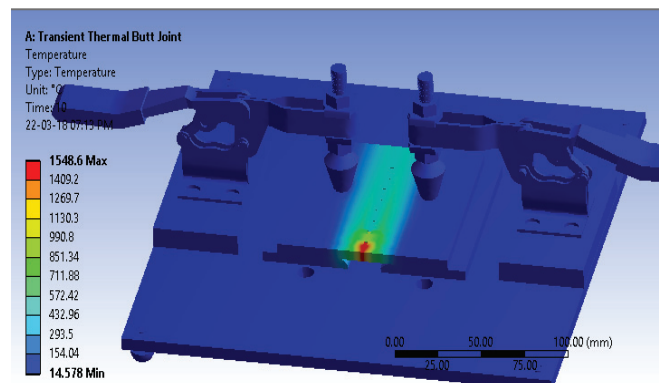


Figure 16. Thermal Analysis During Butt Joint



Figure 17. Thermal Analysis During Lap Joint

Figure 18. Thermal Analysis During Lap Joint

TABLE V.
ANALYTICAL OBSERVATIONS
THERMAL ANALYSIS ON JOINTS

| Parameters / joints | Butt Joint | Lap Joint | T-joint |
|---|---|---|---|
| Min.Temperature | 14.578°C | 21.191°C | 21.584°C |
| Max.Temperature | 1548.6°C | 1519.2°C | 1576.1°C |
| Min.Temperature on | Weld Plates | Weld Plates | Weld Plates |
| Max.Temperature on | Weld Plates | Weld Plates | Weld Plates |

Obtained results clearly indicate that there is no distortion on weld plate, thus the designed fixture is able to overcome the problem of distortion in the welded plates.

Similarly thermal analysis in case of various welded joints shows that the parts of fixture are not much affected by heat liberated in the process of welding

## V. CONCLUSIONS
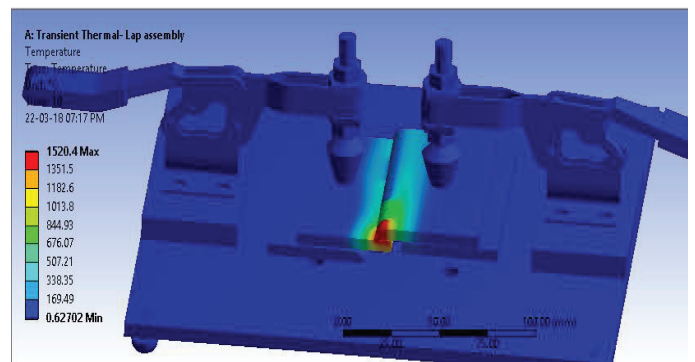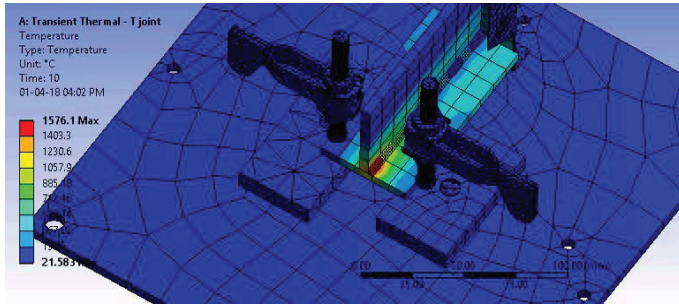
In a welding process like shielded metal arc welding (SMAW), harmful radiations, intense heat of welding, smoke etc. increases difficulty for a welder. While protecting himself from these difficulties holding heavy electrode holder and aligning metallic workpiece becomes additional task for him.

Based on obtained analysis results, it can be stated that the designed fixture is a feasible design based on considerations. Such fixtures are easy to manufacture at less cost and quite convenient to use. Thus they can be suitably implemented to ease the efforts of the welder. As well as the fixture can serve as a part of academic and experimental set up for analysis of different methods of welding over various metals. The research work in this paper shows welded joints on flat plates but the same fixture can be utilized for obtaining joints on similar profiled plates for industrial applications.

The use of fixtures discussed in this report is limited for joining of flat plates. Additional attachments can be designed so that the same fixture can be used for joining circular piece parts also. Estimation of temperature rise in fixture after a number of welding can be scope for further research.

As, human factor is the main reason of faults in welding as well as in other manufacturing processes, automation is observed as single hand solution. Despite the decrease of human factor, full automation is not always a feasible solution [8]. Initial cost of an automated system and lot size of production are main factors to consider before atomization of any process.

Usually each welding fixture is designed for fabrication of specific part requirement which decreases there versatility. At the same time an innovative approach of fixture design makes it versatile in use.

## REFERENCES

[1] Roy A. Lindberg, *Processes and Materials of Manufacturing*, 4th Edition, pp 623-624, 2011
[2] Lien TK, Lind M., *Instrumented fixtures for on-line correction of welding paths*. 41st CIRP conference on manufacturing systems, pp. 435–438, 2008.
[3] Sikstrom F., Ericsson M., Christiansson A.K., *Tools for simulation based fixture design to reduce deformation in advanced fusion welding*. 1st International conference on intelligent robotics and applications. Part II, pp. 398–407, 2008
[4] P H Joshi, Jigs and Fixtures, 3rd Edition, pp 169-170, 1988
[5] Kalpakjian S. and Steven R. Schmid, *Manufacturing Engineering and Technology*. Pearsion Education, 4th Edition, pp. 166 and 799-800, 1995
[6] M. Vural, H. F. Muzafferoglu, V. C. Tapici, *The Effect of Welding Fixtures on Welding Distortions*, journal of achievements in materials and manufacturing engineering. Issue 1-2, volume- 20, pp 511-514, 2007
[7] Martin L. Culpepper, *Design of a hybrid positioned fixture for six axis nanopositioning and precision fixturing*, pp 65-80, 2005
[8] M.A. Wahab, M.J. Painter, M.H. Devis, *The prediction of the temperature distribution and weld pool geometry in the gas metal arc welding process*, Journal of Material Processing Technology, Vol. 77, Issues 1-3, pp 233-239, 1998

# The Performance of Solar Powered Agriculture Sprayer: Design & Analyze

B.Sravya Reddy[1], N.Ankitha[2], Abhinay Sai Kothakonda[3]

[1]Asst. Professor, CVR College of Engineering/Mechanical Department, Hyderabad, India
Email: beeramsravya@gmail.com

[2]Asst. Professor, CVR College of Engineering/Mechanical Department, Hyderabad, India
Email: graceankitha@gmail.com

[3]B. tech Student, CVR College of Engineering/Mechanical Department, Hyderabad, India
Email: abhinayk999@gmail.com

*Abstract:* Now-a-days the concept and technology of employing the non-conventional energy have become very popular for all kinds of developmental activities. One of the major areas, which finds a number of application is in Agriculture Sectors. Solar energy plays an important role in drying agriculture products, for irrigation purpose and for pumping the well water in remote villages with no electricity. This technology on solar energy can be extended for spraying pesticides, fungicides, fertilizers and etc., using Solar Sprayers. In the present work, the performance of the solar powered agriculture sprayer is compared with the conventional fuel powered sprayer by considering the various parameters like unit cost, operating cost, weight and maintenance are compared to judge solar agricultural sprayer is better for using in the fields. The experimentation was to find the efficiency of the solar panel and for three different nozzles. The efficiency of the panel keeps on increasing till the value reaches a maximum value at 12:00 and the nozzle efficiency values of all the 3 nozzles under different conditions are greater than 80%.

*Index Terms:* fertilizer tank, solar panel, battery, motor, sprayer and charger.

## I. INTRODUCTION

Science and technology always help the mankind to improve life. Innovative human brains use their creative power and blend it with the principles of mathematics and physics to develop an ultimate range of plant protection equipments, showcasing the highest degree of human excellence. The invention of solar powered agriculture sprayer brings revolution in the agriculture/horticulture sector. Solar Operated Agriculture Sprayer is a pump runs on electricity generated by photovoltaic panels or the thermal energy available from collected sunlight.

Especially, the invention of sprayers enables farmers to obtain maximum agricultural output. They are used for garden spraying, weed/pest control, liquid fertilizing and plant leaf polishing. It is available in man-portable units, and self-propelled units to boom mounts of 60-151 feet in length. Based on the concept of high pressure, sprayer provides optimum performance with minimum efforts. There are several types of sprayers available in the market such as manual or self-propelled sprayers, tractor mounted sprayers and aerial sprayers.

## II. LITERATURE SURVEY

1) The studies include Ian F Mahaney et.al [1] who explained the phenomenon of solar energy and how we can use it for all the purposes.

2) H.P.Garg and Prakash et.al [2] explained the different applications of the solar energy in the field of agriculture and daily life. This study showed that solar energy can be put to use in agriculture industry effectively.

3) G.N Tiwari [3] mainly emphasized on the design, construction, performance and application of PV and PV/T from the electricity and thermal standpoint. It showed that the temperature is an important factor in influencing the efficiency of the panel.

4) Langsdorf Alexander Suss [4] has given a detailed picture of the AC and DC motors and their use in the industry.

5) Demis H Hill et.al [5] has studied the effects of pests on crops and how to control the pests.He suggested to use less pesticide and start using organic stuff to kill pests.

6) G.A.Mathews et.al [6] has studied and given different methods of application of pesticides.

7) Pistoia, Gianfranco [7] have studied the different kinds of the batteries according to their size, capacity, voltage, etc. They concluded that lithium ion battery is the best portable battery.

8) Furkan Dinçer, Mehmet Emin Meral et.al [8] have studied the factors affecting the efficiency of the solar panels. They concluded that temperature is an important factor that effects the efficiency of the solar panel.

9) Surawdhaniwar, Sonali; Mr. Ritesh Diwan et.al [9] have suggested the use of MPPT technology for the charging of the battery through the solar panel

## III. EXPERIMENTATION

### A. Working Principle of a Sprayer

The Solar powered agricultural sprayer works same as the normal sprayer, but the only difference is the power required to run the motor in the sprayer is taken from the solar radiation. The PV module is connected to the charge



Figure 1. Solar Powered Agriculture Sprayer

controller, from there the battery to which the charging is to be done is connected to the charge controller, thus the battery can be charged and it is stored. The energy stored in the battery is used in running the motor for spraying the pesticide/fertilizer.

The PV module is kept in sunlight at an angle of 15 degrees preferably so that maximum amount of solar energy can be tracked; the solar energy radiation is then converted into electricity i.e. DC power which is sent directly to the charge controller. The charge controller maintains the amount of electricity passing into the device, so that neither more nor less electricity can be transferred into the devices helping them to work efficiently. From the charge controller the power is transferred to the battery of the sprayer and it is stored in the battery, the charge controller will be useful in maintaining the amount of charge entering into the battery doesn't exceed too much which may defect the battery.

The power saved in the battery taken from solar radiation is used to run the sprayer, the sprayer runs in the same way as it runs if it is charged with electricity from fossil fuel. This type of energy used to run the sprayer is ecofriendly and doesn't cause any pollution to the users. This is the working of the Solar Powered Agricultural Sprayer

### B. Types of Agricultural Sprayers

There are various types of sprayers available in the market. Some of them are:

1. Hand compression Sprayer
2. Power Sprayer
3. Electric Sprayer
4. Backpack/Knapsack Sprayer
5. Motorized mist blower

### C. Technical Specifications of Sprayer

The following are specifications of solar agriculture sprayer:

➢ Capacity of fuel tank = 15 liter
➢ Pump = Electric Feed Pump 12 volt.
➢ Material of construction = Plastic Diaphragm.
➢ Once the battery is recharged fully the sprayer can work up to 4 hours.
➢ Operating voltage of motor = 12 volts.
➢ Battery = 12-volt, 12 Ah (ampere-hour)
➢ Discharge = 1500 ml. /min at 30 PSI (max)
➢ Weight of solar panel = 1200gms
➢ Size of panel = 42cm*84cm
➢ Power output from panel = 20 Watt (max)
➢ Working Pressure:
   Low pressure = 30 psi
   High Pressure = 40 psi



Figure 2. Complete view of the internal assembly

The study was done by comparing the following parameters between a solar powered agricultural sprayer and an I.C engine sprayer.

➢ **Unit Cost**

Unit cost of the total product is Rs 4000/- which is a thousand less than a conventional sprayer.

➢ **Operating Cost**

Operating cost is nil as solar power is freely available, whereas in conventional system costs Rs100/- for 1 acre of land.

➢ **Maintenance Cost**

Maintenance cost is also nil as the components used are of good quality which have a life of 5 years whereas in conventional system, it needs continuous maintenance.

➢ **Weight**

Before adding the solar panel and solar charger to the sprayer the weight was 7.1kg after adding the weight of the system was 8.2kg and after filling it with fertilizer it weighs 11kg. For a conventional system it weighs around 15kg.

➢ **Charging Time**

The charging time of the battery is 5hrs(9:00-2:00) the sun's intensity of radiation is high between these timings.

➢ **Running Time**

The running time is 4hrs when the solar panel is disconnected after charging. If it is not disconnected it can keep charging the battery for use.

➢ **Running time with continuous charging**

The running time is 7hrs when the solar panel is connected with the battery even after charging.

➢ **Efficiency of the solar panel**

The efficiency of the panel is found by measuring the open circuit voltage and short circuit current of the solar panel at intervals of 20mins from 9:00 am to 12:30 pm using multimeter

[9] efficiency of the solar panel $= V_{oc} \times I_{sc} / P_{IN}$

$V_{oc}$ = Open circuit voltage of the panel

$I_{sc}$ = current of solar panel

$P_{IN}$ = Incident radiation from sun which according to STC is 1000W/m$^2$.



Figure 3. Open Circuit Voltage Measurement of a Solar Panel

TABLE I.
VOLTAGE, CURRENT AND EFFICIENCY VALUES OF SOLAR
PANEL AT DIFFERENT TIME INTERVALS

| Time | Voltage(Voc) (V) | Current(Isc) (A) | Efficiency (%) |
|------|------|------|------|
| 9 | 19.48 | 1.899 | 10.48 |
| 9:20 | 20 | 1.9 | 10.76 |
| 9:40 | 20.3 | 1.90 | 10.93 |
| 10:00 | 20.6 | 1.91 | 11.15 |
| 10:20 | 20.6 | 1.91 | 11.09 |
| 10:40 | 20.5 | 1.91 | 11.10 |
| 11:00 | 20.7 | 1.91 | 11.2 |
| 11:20 | 20.6 | 1..89 | 11.10 |
| 11:40 | 20.6 | 1.88 | 11.08 |
| 12:00 | 21 | 1.87 | 11.29 |
| 12:20 | 21.1 | 1.87 | 11.35 |
| 12:30 | 20.7 | 1.86 | 11.10 |

➢ **Flow rate**

   The variation of flow rate with respect to time is measured. The values of flow rate at their corresponding times for three different nozzles such as extended range nozzle, standard flat fan nozzle, and even flat fan nozzle are shown in the table and a graph is plotted.



Figure 4. Measuring the flow rate of standard flat fan nozzle using a measuring flask

TABLE II.
FLOW RATE VALUES OF EXTENDED RANGE NOZZLE AT
DIFFERENT TIME INTERVALS

| Time(min) | Flow Rate(ml/min) |
|------|------|
| 0 | 2000 |
| 30 | 2000 |
| 60 | 1995 |
| 90 | 1990 |
| 120 | 1880 |
| 150 | 1850 |
| 180 | 1840 |
| 210 | 1820 |
| 240 | 1805 |

TABLE III.
FLOW RATE VALUES OF STANDARD FLAT FAN NOZZLE AT
DIFFERENT TIME INTERVALS

| Time(min) | Flow Rate(ml/min) |
|------|------|
| 0 | 1510 |
| 30 | 1515 |
| 60 | 1499 |
| 90 | 1490 |
| 120 | 1480 |
| 150 | 1450 |
| 180 | 1422 |
| 210 | 1420 |
| 240 | 1410 |

TABLE IV.
FLOW RATE VALUES OF EVEN FLAT FAN NOZZLE AT DIFFERENT
TIME INTERVALS

| Time(min) | Flow Rate(ml/min) |
|------|------|
| 0 | 1200 |
| 30 | 1200 |
| 60 | 1192 |
| 90 | 1185 |
| 120 | 1170 |
| 150 | 1155 |
| 180 | 1150 |
| 210 | 1125 |
| 240 | 1100 |

➢ **Nozzle Efficiency:**

   In this test, we calculate the efficiency of the nozzle by using the actual flow rate in the formula. The values are shown in the table V, VI and VII.

Efficiency = Actual mass flow rate/ Ideal mass flow rate (standard values)

TABLE V.
EFFICIENCY VALUES OF EXTENDED RANGE NOZZLE AT DIFFERENT
FLOW RATES

| S.No | Actual flow rate(ml/min) | Ideal flow rate(ml/min) | Efficiency (%) |
|------|------|------|------|
| 1 | 2000 | 2100 | 95.23 |
| 2 | 1880 | 2100 | 89.50 |
| 3 | 1805 | 2100 | 85.95 |

TABLE VI.
EFFICIENCY VALUES OF EVEN FLAT FAN NOZZLE AT DIFFERENT
FLOW RATES

| S.No | Actual flow rate(ml/min) | Ideal flow rate(ml/min) | Efficiency (%) |
|------|------|------|------|
| 1 | 1200 | 1300 | 92.30 |
| 2 | 1170 | 1300 | 90.00 |
| 3 | 1100 | 1300 | 84.6 |

| S.No | Actual flow rate(ml/min) | Ideal flow rate(ml/min) | Efficiency (%) |
|---|---|---|---|
| 1 | 1510 | 1600 | 94.37 |
| 2 | 1480 | 1600 | 92.75 |
| 3 | 1410 | 1600 | 88.12 |

## IV. RESULTS AND DISCUSSIONS

1. A graph is plotted between time and efficiency indicating the efficiency of the panel keeps on increasing till the value reaches a maximum value at 12:00 as shown in the Figure 5.
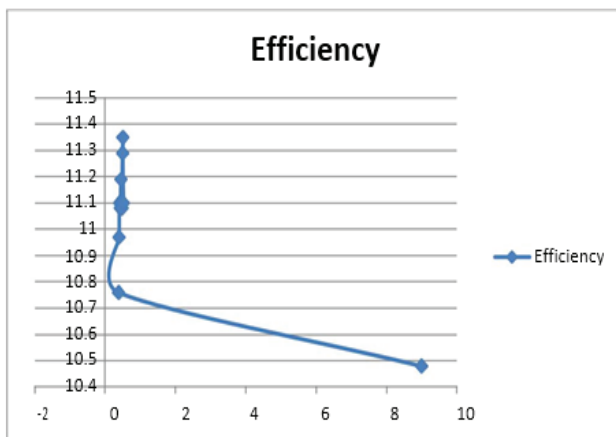


Figure 5. Graph between time and efficiency

2. A graph is plotted between flow rate and time intervals of extended flat nozzle indicate that the flow rate is initially constant and then starts decreasing w.r.t time. The flow rate is the highest in the starting (2000ml/min) and the lowest at the end (1805ml/min) of the running time as shown in the Figure 6.
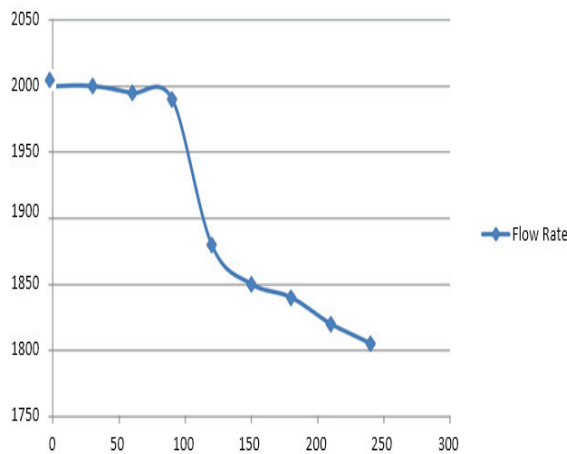


Figure 6. Graph between flow rate and time of extended flat nozzle

3. A graph is plotted between flow rate and time intervals of standard flat fan nozzle indicate that the flow rate is continuously decreasing w.r.t time. The flow rate is the highest in the starting (1510ml/min) and the lowest at the end (1410ml/min) of the running time as shown in the Figure 7.
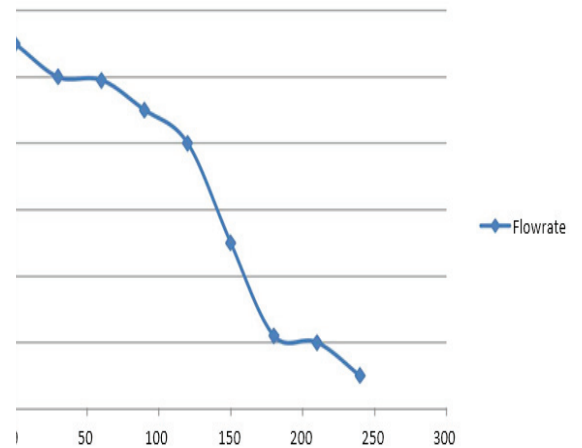


Figure 7. Graph between flow rate and time of Standard flat fan nozzle

4. A graph is plotted between flow rate and time intervals of even flat fan nozzle indicate that the flow rate is continuously decreasing w.r.t time. The flow rate is the highest in the starting (1200ml/min) and the lowest at the end (1100ml/min) of the running time as shown in the Figure 8.
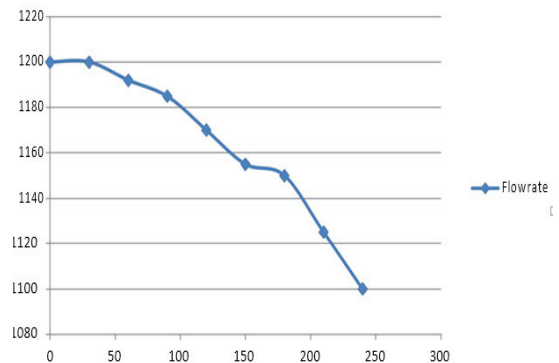


Figure 8. Graph between flow rate and time of even flat fan nozzle

## V. CONCLUSIONS

The experiments and analysis conducted on the system have given good results while measuring the flow rate, efficiency and nozzle height to range.

1) The V-I characteristics also show that the efficiency of the panel keeps on increasing till the value reaches a maximum value at 12:00.
2) The flow rate of the extended range flat fan nozzle is initially constant and then starts decreasing w.r.t time and the flow rate of the nozzle is2000ml/min which is closer to the ideal value of 2100ml/min.
3) The flow rate of even flat fan nozzles is continuously decreasing w.r.t time and flow rate of nozzle is around 1200ml/min which is closer to the ideal value of 1300ml/min.
4) The flow rate of Standard flat fan nozzles is continuously decreasing w.r.t time and flow rate of nozzle is around

1500ml/min which is closer to the ideal value of 1600ml/min.

5) The nozzle efficiency values of all the three nozzles under different conditions are greater than 80%.

## REFERENCES

[1]   Ian F Mahaney, "The Boon of Solar Energy" World Science, Vol. 1, 2002, pp. 1-42.

[2]   Garg, Prakash, "Solar Energy Application in Agriculture" Proceedings of the 2006 IEEE 4th World Conference,Vol. 2, May 2006, pp. 2168-2171.

[3]   G.N Tiwari, "The Fundamentals of Photo Voltaic Cells and Applications", Published book in june 2005.

[4]   Langsdorf, Alexander Suss (1955). Theory of Alternating-Current Machinery (2nd ed.). Tata McGraw-Hill. p. 245. ISBN 0-07-099423-4.

[5]   Demis .H. Hill, "Agricultural Insect pest Control IEEE, 2006.

[6]   G.A.Mathews, "Methods of Applications of Pesticides "Proceedings of the IEEE. 86(8): 1552–1574. CiteSeerX 10.1.1.120. 4059.Pistoia, Gianfranco (2005-01-25), "Batteries for Portable Devices". Elsevier. p. 1. ISBN 0080455565. Retrieved 2016-03-18.

[7]   Furkan Dinçer, Mehmet Emin Meral, "A Detailed Picture of Battery", Proceedings of the 2007 IEEE 5th World Conference,Vol. 3, May 2007, pp. 2175-2183.

[8]   Surawdhaniwar, Sonali; Mr. Ritesh Diwan (July 2012). "Study of Maximum Power Point Tracking Using Perturb and Observe Method". International Journal of Advanced Research in Computer Engineering & Technology. 1 (5): 106–110.  Lipp, Charles W., "Practical Spray Technology: Fundamentals and Practice", 2012, ISBN 978-0-578-10090-6.

[9]   http://www.ee.sc.edu/personal/faculty/simin/ELCT566/21%20 Solar%20Cells%20II.pdf

[10]  Tom P.Hough, "Analysis of V-I Charateristics", Solid-State and Integrated Circuit Technology, October 1995, pp. 146-150.

# Design and Structural Analysis of Scissor Jack using ANSYS Workbench

C. Sai Kiran[1] and J. Sruthi[2]
[1]Asst. Professor, CVR College of Engineering/Mechanical Engg. Department, Hyderabad, India
Email: csaikiran001@gmail.com
[2] Asst. Professor, CVR College of Engineering/ Mechanical Engg. Department, Hyderabad, India
Email: sruthij02@gmail.com

*Abstract:* **In this paper, a scissor jack was designed and analyzed which can be used for lifting the vehicle in vertical direction. A scissor jack is an example of a power screw in which a small force is applied in a horizontal plane for raising or lowering a large load. The purpose of this work is to design a scissor jack for safe, easy operation and which will able to lift the car without spending much effort, by studying the total deformation and von-mises stress values of the scissor jack which are useful for assessing the safety and life prediction of the scissor jack. A detailed structural analysis of scissor jack is performed using ANSYS and this analysis helps to predict which parts of the scissor jack fails when a certain external load acts on it.**

*Index Terms:* **Scissor Jack, Power Screw, Von-mises stress, ANSYS.**

## I. INTRODUCTION

Whenever a vehicle tyre fails while travelling, the driver must lift the vehicle from the ground level and perform repair or maintenance of that vehicle. Therefore, a jack is used in case of a vehicle emergency. A jack is a mechanical device used for lifting heavy loads or to apply great forces. A jack is a device used for raising all or part of a vehicle into the air to facilitate repairs of that vehicle. A mechanical jack has screw threads for lifting heavy equipment or vehicles. A car jack has mechanical advantage which allows lifting a vehicle by manual force. The most common forms of jacks are scissor jack, screw jack, floor jack or garage jack which lifts vehicles for maintenance or repairs. Jacks are usually rated for a maximum lifting capacity. In industries, jacks are rated for carrying tons of load.

Manoj et al. [1] has created a scissor jack model for carrying actual loads of a light motor vehicle. The scissor jack is modelled in Pro-e software and analysed in ANSYS software. Welded joints are replaced with rivets for reduction of weight in the material. The main objective is to reduce the weight of the scissor jack by changing manufacturability and scissor jack should withstand the strength requirements. Loads are applied on the scissor jack and yield stress, failure strain and plastic strain values are obtained using ANSYS software and the values are within the limits.

Chetan et al. [2] has optimized scissor jack by designing and analysing the scissor jack model for different loading conditions. Different failure analysis of a scissor jack is performed to study the performance and reliability of the scissor jack. A scissor jack is tested under different loading conditions and the scissor jack failure is observed in screws, arm teeth, jack head failure etc. Therefore, a new model of screw jack is created with the maximum load carrying capacity and changing the angle between lifting arms of the screw jack.

Dhamak et al. [3] has designed, optimized and standardized a scissor jack to avoid field failure by modelling scissor jack in CATIA software and standardized by using MATLAB software. The design of scissor jack is modified based on human factor considerations and its functionality. The different failure modes of scissor jack are analysed and redesign of scissor jack is made interms of cost and quality of the scissor jack. Inclined load inspection test and stability test on vehicle is performed by using scissor jack.

Jaideep et al. [4] have taken the reference of Mahindra bolero scissor jack. The dimensions of the scissor jack were measured by using Vernier callipers. Different parts of scissor jack are modelled and assembled in CATIA and different parameters like maximum shear stress, maximum principal tensile stress, total torque required to lift the vehicle etc. are calculated for the components of scissor jack to avoid failure. To avoid failure of the scissor jack, different stresses are analysed and all the results were verified and they are within the safe limits.

Xin et al. [5] has installed damping device for the scissor jack system for good compactness. The design process and theoretical basis comparison is used for finding optimum geometry parameter. The scissor damping system uses minimum number of dampers to obtain damping coefficient. The scissor jack damper can provide a significant increase in the damping ratio while reducing both the drift and acceleration response. The relative velocities and displacements of the structure are observed, and the resulting damper force is amplified. The result shows that the force exerted on the structure is larger than the force produced by traditional diagonal braced.

Haribaskar et al. [6] has modified the conventional screw jack to remote controlled scissor jack which helps to lift the load by using motor as a source of energy. The scissor jack must be compact and light weight for storing it in an automobile trunk.

Chiang et al. [7] has summarized results from an evaluation program and tests performed by the National Highway Traffic Safety Administration which involves 120 automobile scissors jack selected from 24 models made by 14 different manufacturers. A mathematical model of different types of scissor jacks is introduced to describe the load and supporting characteristics. The four major failure

modes of the scissor jack are: unable to raise or lower the vehicle, collapsing, penetration of the vehicle frame and toppling over. The analytical result values are same as the result of the tests performed.

Jaideep et al. [8] has modelled a scissor jack for changing tyres or for maintenance purpose of a car. Scissor jack will convert the rotary motion into reciprocating motion. They have calculated the design criteria of different parts of a scissor jack analytically and the results obtained from CAE tools like ANSYS have been compared by taking three different materials for two different sections to find out which material has less deformation and to sustain high yield strength without any failure. The objective is to reduce the weight with high strength of scissor jack and to calculate the stresses like maximum principal stress, maximum shear stress, bending stress, torsion stress and crushing stresses which are induced in the scissor jack by comparing it with the analysis performed using ANSYS software. They found that the values of ASTM A36 mild steel are more equivalent in designing and modelling the scissor jack based on its minimum deformation and high load sustainable capacity without causing any type of failure in the scissor jack.

Nitinchandra et al. [9] has modelled a toggle jack which is used to lift heavy loads. The main parts are nut and screw. The nut is a stationary part and the screw is a moving part. The bearing stress induced in the materials causes the failure in the nut and stresses like shear and tensile cause the failure of the screw in the scissor jack. The objective is to select a pair of material for screw and nut which can resist the induced stresses by application of different loading conditions varying from 1KN to 5KN. The design of screw, nut and links of the scissor jack are performed by taking different combination of materials. Comparison of design stresses and calculated stresses acting on the nut and screw is performed. The results are within the limits.

Uday et al. [10] has designed a pneumatic scissor jack which can lift a car when it is placed at the bottom of the vehicle. The main parts are toggle jack with power screw, gear pair and DC wiper motor. The designed scissor jack can lift 4,000-5,000 pounds vehicle from the ground.

*A. Different Types of Jacks*

Jacks are used for lifting heavy weights by applying a force on it. The different names for the jacks are given depending upon the design, utility, technology used and customization etc. Some of the important jacks used for lifting are given below:

1. Scissor jack.
2. Hydraulic jack.
3. House jack/Screw jack.
4. Pallet jack.
5. Floor jack.
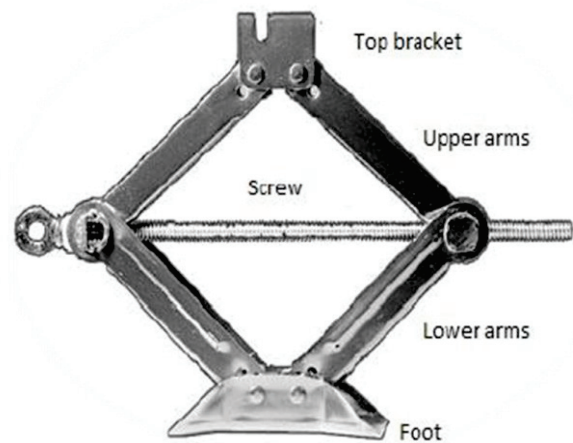6. Pneumatic jack.
7. Bottle jack.
8. Farm jack.



Figure 1.   Scissor Jack

Scissor jack is represented in Fig. 1. The main parts of a scissor jack are top bracket, foot, screw, upper and lower arms.

*B. Construction of a Scissor Jack*

All the different scissor jacks are similar in design which consists of a base plate, four lifting arms, a carrier plate, eight connection pins, two connection members, a crank and a power screw. The four metal pieces are connected to each other at the corners with a bolt. A scissor jack is having a diamond shape frame with a nut at one side and a sleeve on the other side. The nut and sleeve are supported by a screw. When the screw is rotated, the nut moves away or towards from the sleeve depending on the direction of the rotation. The rotation will either lift-up or lower down the vehicle which is supported on the scissor jack. All the different parts of the scissor jack are shown in Fig.2.
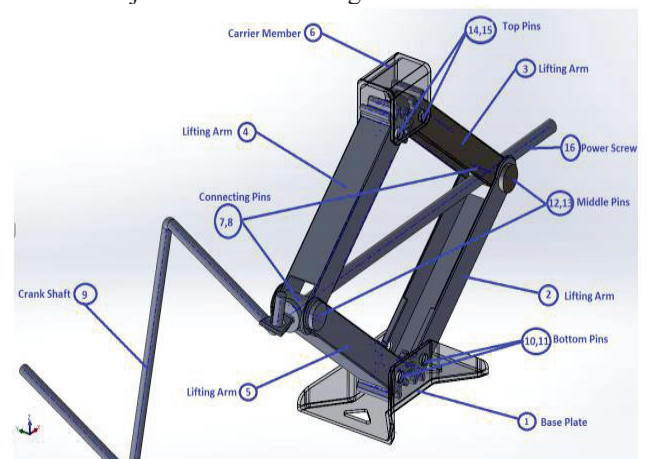


Figure 2.   Scissor jack and its parts

*C. Scissor Jack Material*

Scissor jacks are usually made of materials that are very strong and are suitable for withstanding heavier loads on it. Steel is selected as material for scissor jack because of its durability.

TABLE I.
MATERIAL PROPERTIES OF STEEL

| S. No | Properties | Steel |
|---|---|---|
| 1. | Density (Kg/m$^3$) | 7,800 |
| 2. | Young's Modulus (Mpa) | 210000 |
| 3. | Yield Strength (Mpa) | 360 |
| 4. | Tensile Strength (Mpa) | 610 |
| 5. | Poisson's Ratio | 0.3 |

## II. MODELLING AND FINITE ELEMENT ANALYSIS

### A. Scissor Jack Model

All the different parts of the scissor jack are modelled in SOLIDWORKS software by using different commands and all the individual parts of the scissor jack are assembled in the SOLIDWORKS as shown in Fig. 3
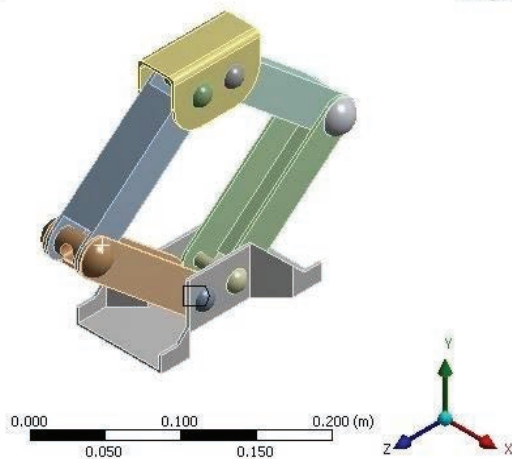


Figure 3. Assembled Model of Scissor Jack

### B. Elememt Type

The element type used is SOLID 186. SOLID 186 is a higher order 3-D with 20-node having three degrees of freedom per node, solid element that exhibits quadratic displacement behavior. This element supports large deflections, plasticity, large strain capabilities, hyper elasticity, stress stiffening and creep.

### C. Meshing

After assigning element type to the scissor jack, the created solid model is converted into IGES format and imported into ANSYS Workbench. Meshing is an important process of an analysis and it should be performed on the scissor jack model. Meshing is the process of dividing the created model in number of divisions or elements which consists of nodes. By meshing process, we can determine the efficiency and effectiveness of any analysis. An automated mesh generation is as shown in Fig. 4.
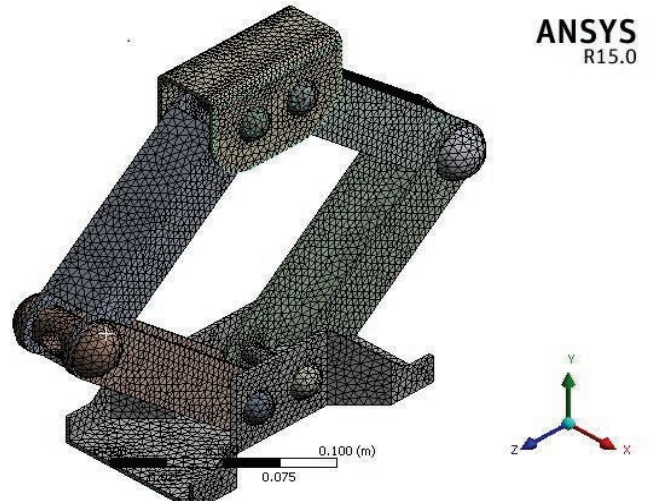


Figure 4. Meshing of Scissor Jack

Meshing is applied by using automatic mesh. Under mesh sizing, mesh was set to fine mesh to achieve accurate and precise results. Rather than using a fine mesh all over the components, coarse mesh was used on larger area and fine mesh was used at the area of stress concentration.

### D. Applying Loads

In the analysis setting, fixed support is assigned to the base plate of the scissor jack, by assigning the fixed support the base plate is constrained in all degrees of freedom and it would withstand the forces acting on the scissor jack as shown in Fig. 5.
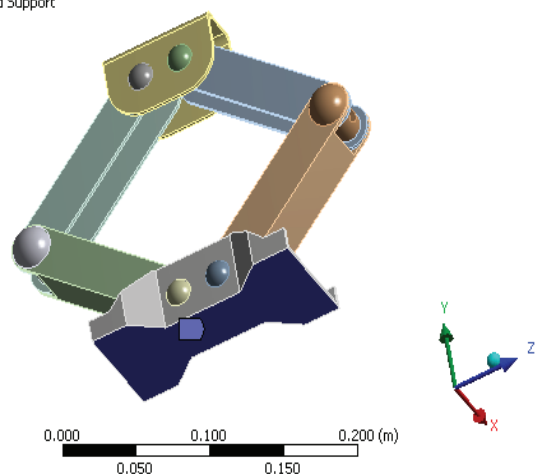


Figure 5. Fixing the base of Scissor Jack

The average weight of the car is calculated and converted into force. A force of 2943 N is applied on the top bracket of the scissor jack as shown in Fig. 6.
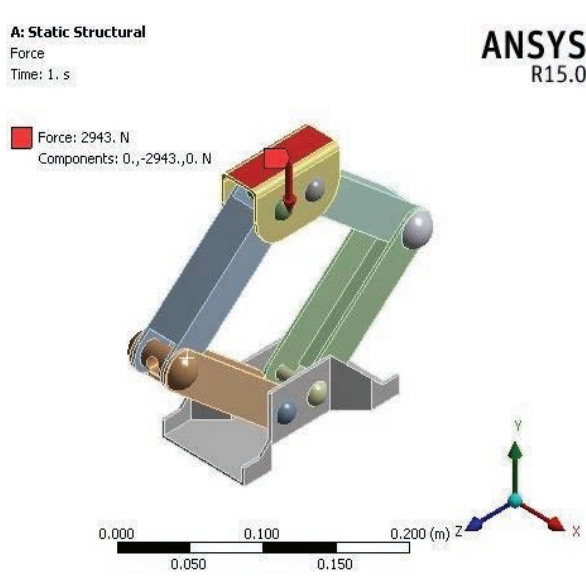
Figure 6.   Applying Force on Top Bracket

## III. RESULTS AND DISCUSSIONS

After fixing the base and applying the load on the top bracket of the scissor jack, structural analysis is performed on the scissor jack in ANSYS workbench. The following results were observed in the structural analysis.

### A. Total Deformation of Scissor Jack

After performing structural analysis on the scissor jack by applying the load on it, maximum total deformation of 0.115 mm is observed from the Fig. 7.
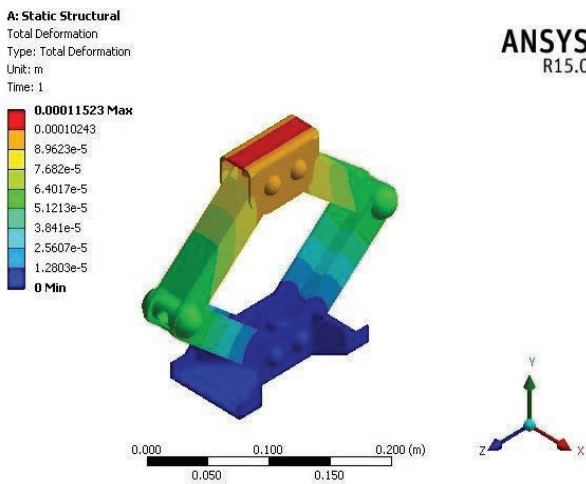


Figure 7.   Total Deformation of Scissor Jack

### B. Von-mises Stress of Scissor Jack

After performing structural analysis on the scissor jack by applying the load on it, maximum von-mises stress of 128.21 Mpa and minimum von-mises stress of 6.868 Mpa is observed in the scissor jack from the Fig. 8.
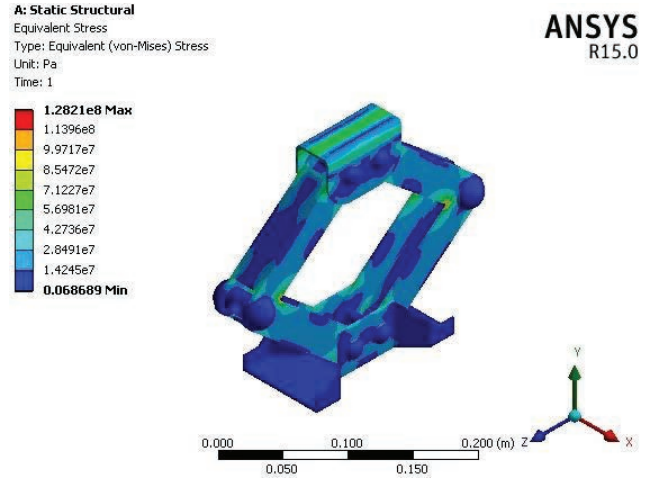


Figure 8.   Von-mises Stress of Scissor Jack

## IV. CONCLUSIONS

In this paper, a scissor jack is modelled in SOLIDWORKS and a structural analysis of scissor jack with a force of 2943 N is performed in ANSYS software. The total deformation and von-mises stress of the scissor jack is analysed. From the results, it is observed that the maximum deformation and the von-mises stress of the scissor jack are within the limits. Therefore, modelled scissor jack is safe to use and has long life.

In future scope, different types of jacks can be modelled by taking different materials and by giving different loading conditions for structural analysis.

## REFERENCES

[1] Manoj R Patil and S D Kachave, "Design and analysis of scissor jack," *International Journal of Mechanical Engineering and Robotics Research*, vol. 4, pp. 327–335, January 2015.

[2] Chetan S. Dhamak, D.S. Bajaj and V.S. Aher, "Design and optimization of scissor jack," *International Journal of Advances in Production and Mechanical Engineering*, vol. 2, pp. 29–34, 2016.

[3] C.S. Dhamak, D.S. Bajaj, V.S. Aher and G. Nikam, "Design and standardization of scissor jack to avoid field failure," *International Journal of Advance Research and Innovative Ideas in Education*, vol. 1, pp. 1–10, 2015.

[4] Jaideep Chitransh and Dilshad Hussain, "Designing and calculating the stresses induced in scissors jack for three different materials," *International Journal of Scientific and Technology Research*, vol. 5, pp. 119–123, July 2016.

[5] Xin Zhao and Zhuang MA, "Optimization of scissor-jack-damper's parameters and performance under the constrain of human comfort," *Advances in Civil, Environmental, and Materials Research*, August 2016.

[6] Haribaskar, G. Dhenesh Kumar, Arun Kumar.C, Hari Haran.P, Boobalan.M and Sadha Sivam.C, "Remote controlled scissor jack to lift the vehicle," *International Journal of Advance Research*, vol. 3, pp. 1279–1282, 2015.

[7] G. D. C. Chiang, "Test, evaluation and failure analysis of automotive scissors jack," *Journal of Vibration, Acoustics, Stress and Reliability in Design*, vol. 109, pp. 207–213, November 2009.

[8]  Jaideep Chitransh and Akash Singh Patel, "Comparing mathematical model of scissors jack analytically and by using CAE tools," *International Journal of Computational Engineering Research*, vol. 6, pp. 49–53, November 2016.

[9]  Nitinchandra R. Patel, Sankethkumar Dalwadi, Vijay Thakor and Manish Bamaniya, "Design and toggle jack considering material selection of screw – nut combination," *International Journal of Innovative Research in Science and Technology*, vol. 2, pp. 1748–1756, May 2013.

[10] Pandra Uday Kumar, and G. Ramanjulu, "Design and analysis of center jack for cars," *International Journal & Magazine of Engineering, Technology, Management and Research*, vol. 2, pp. 1476–1479, September 2015.

# Radiation Effect on MHD Stagnation-point Flow of a Nanofluid over an Exponentially Stretching Sheet in the Presence of Chemical Reaction

G. Narender[1], G. Sreedhar Sarma[2] and K. Govardhan[3]
[1]Asst. Professor, CVR College of Engineering / H & S Department(Mathematics), Hyderabad, India.
Email: gnriimc@gmail.com
[2]Assoc. Professor, CVR College of Engineering / H & S Department(Mathematics), Hyderabad, India.
Email: sarma.sreedhar@gmail.com
[3]Asst. Professor, GITAM University, Department of Mathematics, Hyderabad, India.
Email: govardhan_kmtm@yahoo.co.in

*Abstract: The effect of chemical reaction parameter on magnetohydrodynamic boundary layer flow of nanofluid past an exponentially stretching sheet is presented. An appropriate set of similarity transformations are used to transform the governing partial differential equations (PDEs) into a system of nonlinear ordinary differential equations (ODEs). The resulting system of ODEs is solved numerically by using the 4th order Adam's - Moultan method along with shooting technique. The numerical results are analyzed by graphs for different parameters which appear in the solution affecting the MHD mixed convection stagnation point.*

*Index Terms: Numerical solution, MHD, Radiation effect, stagnation-point flow, chemical reaction, Nanofluid.*

## I. INTRODUCTION

The study of heat and mass transfer on fluids with chemical reaction effect past an exponentially stretching surface have important role in chemical engineering, nuclear reactors, solar collectors, drying processes, heat exchangers, geothermal and oil recovery, building construction. Possible applications of this type of flow can be found in many industries. From technological point of view, MHD flow finds application in the field of stellar and planetary magneto-spheres, aeronautics, meteorology, solar physics, cosmic fluid dynamics, chemical engineering, electronics and induction flow merry, MHD generators, MHD accelerators and other centrifugal mechanics. Nanofluids have properties that make them potentially useful in many heat transfer applications. They exhibit enhanced thermal conductivity and convective heat transfer coefficient.

Choi [1] studied the enhancing thermal conductivity of fluid with nanoparticles. Buongiorno [2] presented a simple convective model to analyz transport in nanofluids implied that energy transfer by dispersion of nanoparticles was negligible. In the boundary layer, there may be a decrease in viscosity, which will lead to heat transfer enhancement. An excellent assessment of nanofluid physics and developments had been provided by Cheng [3]. Buongiorno and Hu [4] they analyzed the thermal conductivity in nano fluid and

gave the comparison for the enhancement heat transfer. However, Gupta et al. [5] examined the heat and mass transfer for the boundary layer flow over a stretching sheet subject to suction and blowing. Emmanuel et al. [6] has examined heat and mass transfer in a visco elastic boundary layer flow over an exponentially stretching sheet. The impact of viscous dissipation, non-uniform heat source on heat transfer in a viscoelastic boundary layer flow over a stretching sheet was studied by Subhas et al. [7]. The effect of thermal radiation on the flow was examined by Sohail Nadeem et al. [8]. Al-odat et al. [9] obtained the results on the effect of magnetic field on an exponential temperature distribution on the linear sheet. Gopi Chand et al. [10] considered an unsteady stretching surface in a porous medium and explained the viscous dissipation and radiation effects on MHD flow over it. Ishak [11] worked on the radio ative magnetohydrodynamic boundary layer flow. Flow through a porous, bounded by a vertical surface in presence of hall current was explained by Sudhakar et al. [12]. B Bidin and R Nazar [13] presented the MHD boundary layer flow with radiation effect.

Our prime objective is, we first reproduce an analytical study of [14] and then extend the MHD stagnation point flow of nanofluid past an exponentially stretching sheet with convective boundary condition." According to our information, chemical reaction effects on MHD mixed convection stagnation point flow of nanofluid over an exponentially stretching surface" is not yet examined.

## II. MATHEMATICAL FORMULATION

Consider the steady, two-dimensional boundary layer flow of a nanofluid over an exponentially stretching surface. The stretching and free stream velocities are assumed to be $u_w(x) = ae^{(x/l)}$ and $u_\infty(x) = be^{(x/l)}$ where $a$ and $b$ are constants. In addition, a magnetic field $B(x) = B_0 e^{(x/2l)}$ is applied to the plate as shown in figure 1. Temperature and concentration are denoted by $T$ and $C$ with suffix $w$ and $\infty$ for

stretching surface and free stream respectively take forms $T_w(x), C_w(x), T_\infty$ and $C_\infty$.

The governing equations of conservation of momentum, energy, mass and nanoparticle fraction, under the boundary layer approximation, are as follows:

$$\frac{\partial u}{\partial x} + \frac{\partial v}{\partial y} = 0 \tag{1}$$

$$u\frac{\partial u}{\partial x} + v\frac{\partial v}{\partial y} = v\nabla^2 u + U_\infty \frac{\partial U_\infty}{\partial x} + \frac{\sigma B_0^2}{\rho_f}(U_\infty - u) \tag{2}$$

$$u\frac{\partial T}{\partial x} + v\frac{\partial T}{\partial y} = \alpha\nabla^2 T - \frac{1}{\rho c_p}\frac{\partial q_r}{\partial y} + \frac{v}{\rho c_f}\left(\frac{\partial u}{\partial y}\right)^2 + \tau\left(D_B\nabla\varphi.\nabla T + \frac{D_T}{T_\infty}\nabla T.\nabla T\right) \tag{3}$$

$$u\frac{\partial \varphi}{\partial x} + v\frac{\partial \varphi}{\partial y} = \alpha\nabla^2 T + \frac{D_T}{T_\infty}\nabla^2 T - k_0(C - C_\infty) \tag{4}$$

where $x$ is the coordinate axis along the continuous surface in the direction of motion and $y$ is the coordinate axis along the continuous surface in the direction perpendicular to the motion. The components of velocity along $x-$ and $y-$ axis are respectively $u$ and $v$. In the above equations, $\mu$ is the kinematic viscosity, $\rho_f$ is the density, $\sigma$ is an electrical conductivity, $B(x)$ is the variable magnetic field, $\alpha = \frac{\xi}{(\rho c)_f}$ where $\xi$ is the thermal conductivity and $(\rho c)_f$ is the heat capacitance of the base fluid, $\tau$ parameter defined by $\tau = \frac{(\rho c)_p}{(\rho c)_f}$, $(\rho c)_p$ effective heat capacity of
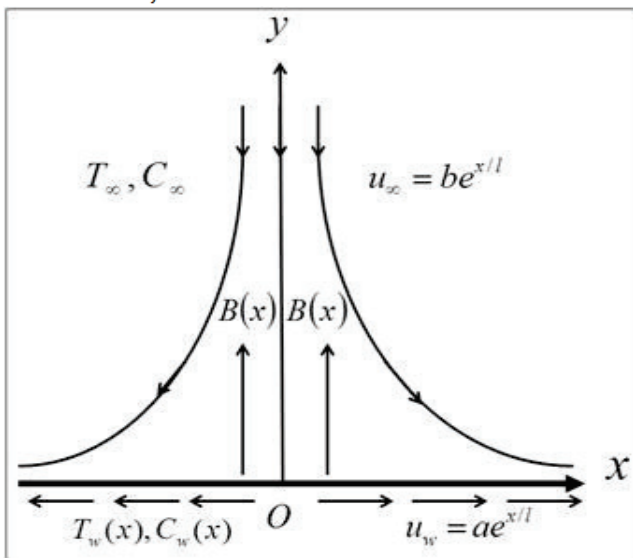


Figure 1. Geometry for the flow under consideration.

a nanoparticle, $D_B$ is the Brownian diffusion, $q_r$ is the radiation flux.

The radiation heat flux is given as

$$q_r = \frac{-4\sigma^*}{3k^*}\frac{\partial T^4}{\partial y} \tag{5}$$

where $\sigma^*$ is Stefan-Boltzmann constant and $k^*$ is mean absorption coefficient. For small temperature differences within the flow, expanding $T^4$ about $T_\infty$ by Taylor series. This after neglecting the higher order terms takes the following form:

$$T^4 = 4T_\infty^3 T - 3T_\infty^4 \tag{6}$$

Substituting (6) in (5), we get

$$\frac{\partial q_r}{\partial y} = -\frac{16\sigma^* T_\infty^3}{3\kappa^*(\rho c)_f}\frac{\partial^2 T}{\partial y^2} \tag{7}$$

Using equation (7) and the energy equation (3) becomes

$$u\frac{\partial T}{\partial x} + v\frac{\partial T}{\partial y} = \left(\alpha + \frac{16\sigma^* T_\infty^3}{3\kappa^*(\rho c)_f}\right)\nabla^2 T + \tau(D_B\nabla\varphi.\nabla T + \frac{D_T}{T_\infty}\nabla T.\nabla T) \tag{8}$$

The boundary conditions considered:

$$\begin{cases} u = u_w(x) = ae^{(x/2l)}, \quad v = 0, \quad T = T_w(x), \\ \qquad\qquad C = C_w(x) \ at \ y = 0 \\ u = u_\infty(x) = be^{(x/2l)}, v = 0, \qquad T = T_\infty, \\ \qquad\qquad C \to C_\infty \ as \ y = \infty \end{cases} \tag{9}$$

$T_w(x) = T_\infty + T_0 e^{(x/2l)}$, $C_w(x) = C_\infty + C_0 e^{(x/2l)}$ are surface temperature and concentration respectively. Now the nonlinear PDEs are converted into nonlinear ODEs. For that purpose, the stream function $\psi$ is defined by $u = \frac{\partial\psi}{\partial y}$, $v = -\frac{\partial\psi}{\partial x}$, so that the Eq.(1) will be satisfied identically. For the conversion of the mathematical model (1) - (4) into the dimensionless form, the following similarity transformation has been introduced.

$$\begin{cases} \eta = y\sqrt{\frac{a}{2vl}}e^{(x/2l)}, \quad \psi = \sqrt{2vla}e^{(x/2l)}f(\eta), \\ \theta(\eta) = \frac{T-T_\infty}{T_f-T_\infty}, \qquad \beta(\eta) = \frac{C-C_\infty}{C_w-C_\infty}. \end{cases} \tag{10}$$

The effect of stream function on the remaining three equations, the momentum Eq. (2), the temperature Eq. (3) and concentration Eq. (4) are as

$$f''' + ff'' - 2(f')^2 + M(A - f') + 2A^2 = 0 \tag{11}$$

$$\frac{\left(1+\frac{4}{3}Nr\right)\theta''}{Pr} + f\theta' - f'\theta + Nb\theta'\beta' + Nt(\theta')^2 = 0 \quad (12)$$

$$\beta'' + Lef\beta' - Lef'\beta + \frac{Nt}{Nb}\theta'' - Le\chi\beta = 0 \quad (13)$$

and the boundary conditions (9) change into the form:

$$\left. \begin{array}{l} f(\eta) = 0, f'(\eta) = 1, \ \theta(\eta) = 1, \beta(\eta) = 1 \text{ at } \eta = 0, \\ f'(\infty) \to A, \ \theta(\infty) \to 0, \beta(\infty) \to 0 \text{ as } \eta \to \infty \end{array} \right\} \quad (14)$$

Here

$Nr = \frac{-4T_\infty^3 \sigma^*}{3k^*k}$      Radiation parameter,

$Pr = \frac{v}{\alpha}$,      Prandtl number,

$Le = \frac{a}{D_B}$      Lewis number,

$M = \frac{2l\sigma B_0^2}{\rho_f a}$      Magnetic parameter,

$A = \frac{u_\infty}{u_w}$      Velocity ratio parameter,

$Nb = \frac{\rho_p D_B(C_w - C_\infty)}{\rho_f \alpha}$   Brownian motion parameter,

$Nt = \frac{\rho_p D_T(T_w - T_\infty)}{\rho_f \alpha T_\infty}$   Thermophoresis parameter, and

$\chi = \frac{\kappa_0}{a}$      reaction rate parameter.

In this problem, the desired physical quantities are the local Nusselt number $Nu_x$, and reduced Sherwood number $Sh_x$ and the skin-friction coefficient $C_f$ . These quantities are defined as

$$\left. \begin{array}{l} C_{fx}(0) = C_f\sqrt{(2l/x)Re_x}, \\ -\theta'(0) = \frac{1}{\left(1+\frac{4}{3}Nr\right)\sqrt{(2l/x)Re_x}}, \ -\beta'(0) = \frac{Sh_x}{\sqrt{(2l/x)Re_x}} \end{array} \right\} \quad (15)$$

where $Re_x = \frac{u_w(x)x}{v}$ is the local Reynolds number.

### III. NUMERICAL TECHNIQUE

The non-linear ordinary differential Equations $(11) - (13)$ with boundary conditions $(14)$ are solved using the 4$^{th}$ – order Adam's-Bashforth predictor and Moulton corrector method along a shooting technique. Equation $(11)$ is solved as an initial value problem assumed $f''(0)$ . This assumed value is found by Newton's Raphson

Method. This is followed by solving Equations $(12)$ and $(13)$ with assumed values for $\theta(0)$ and $\beta'(0)$ correct values are found by shooting method using the end conditions.

Finally, the resulting equations are solved with help of 4$^{th}$ order Adam's-Bashforth predictor and Moulton corrector method along a shooting technique for the step size of $\Delta\eta = 0.01$ and $\eta_{max} = 10$ were found to be satisfactory in obtaining sufficient accuracy.

### IV. RESULT AND DISCUSSION

The objective of this section is to analyze the numerical results displayed in the tabular and graphical form. The numerical influence of different parameters for example Brownian motion parameter $Nb$, thermophoresis parameter $Nt$, velocity ratio parameter $A$ , radiation parameter $Nr$, Prandtl number $Pr$, Lewis number $Le$, chemical reaction $\chi$ and Hartmann number $M$ are given in Tabular form (Tables 1 and 2) and displayed graphically (Figures 2 - 12). Table 1 shows a comparison of obtained results for the reduced Nusselt number $-\theta'(0)$ with the results given by [11, 13 and 14]. These comparisons show an excellent agreement between the obtained numerical results and existing results in the literature.

Table 2 shows the variations of the reduced Nusselt number $-\theta'(0)$ and the reduced Sherwood number $-\beta'(0)$ for different values of $Nb, Nt, Pr, Le, M, Nr, A$ and $\chi$ . It is observed form this table that $-\theta'(0)$ decreases with the increasing values of $Nb, Le, Nr$ and $A$. Whereas for increasing values of $Pr, Nt, N$ and $\chi$ is increasing. However, it is found that $-\beta'(0)$ decreases for the increasing value of $Nr$ whereas it increases for increasing values of $Nb, Nt, Pr, Le, M, A$ and $\chi$. Here, it is noted that for the increasing values of $M, -\theta'(0)$ and $-\beta'(0)$ show a quite opposite effect in both cases of $A < 1$ and $A > 1$.

Figure 2 shows the effects of $M$ and $A$ on the velocity profiles $f'(\eta)$ for fixed values of $Nb, Nt, Pr, Le$ when $A < 1, A = 1$ and $A > 1$. This figure shows that $f'(\eta)$ decreases for increasing values of $M$ for the case of $A < 1$. Here, the decreasing behavior in $f'(\eta)$ is justified due to the fact that larger values of $M$ increase the resistive forces on the stretching surface which result in a retardation force to slow down the nanofluid motions However, in the case of $A > 1$ , $f'(\eta)$ increases for the increasing values of $M$. It is further observed that $f'(\eta)$ increases for increasing values of $A$. It is interesting to note that in the case of $A > 1$, the momentum boundary layer thickness becomes smaller compared to the case of $A < 1$, and causes an inverted boundary layer structure. Moreover, when $A = 1, f'(\eta)$ coincide with each other and results in a degenerate inviscid flow, where the stretching matches the conditions at infinity.

**Figure 3**, represent the effect of Brownian motion parameter on the profile of temperature. So, distribution of Nano particles can be adjusted by adjusting Brownian motion parameter

**Figure 4** delineates the influence of $Nt$ on the temperature profile. When the effects of thermophoretic increase, the relocation of the nanoparticles relocate from hot part of the surface to the cold ambient fluid and consequently, at the boundary, temperature is increased. This sequels in the thickening of thermal boundary layer.

The influence of radiation parameter on profile of temperature distribution is displayed in **Figure 5**. Temperature increases with the increase of thermal radiation parameter $Nr$. The effect of radiation is to intensify the heat transfer thus radiation should be at its minimum in order to facilitate cooling process.

**Figure 6** reveals the influence of $Pr$ on dimensionless temperature profile. As expected, increasing $Pr$ leads to reduction in dimensionless temperature. Based on the definition of $Pr$ (the ratio of momentum diffusivity to thermal diffusivity), therefore, for large $Pr$ heat will diffuse more rapidly than the momentum. Consequently, thickness of thermal boundary layer reduces as $Pr$ increases. It is also noticed that higher values of $Pr$ reduce the temperature more drastically.

**Figure 7** shows that $\theta(\eta)$ increases with increasing values of $M$ when $A < 1$ while it decreases in the case of $A > 1$. It is noticed that the thermal boundary layer thickness is not much influenced by the larger values of $M$ when $A > 1$.

**Figure 8** shows the effect of the Brownian motion parameter on the concentration. It is noticed that as the Brownian motion parameter increases, the concentration decreases.

**Figure 9** shows the effect of thermal radiation on concentration profile. By increasing thermal radiation, the concentration boundary layer thickness is decreasing.

**Figure 10.** As Lewis number increases the concentration graph decreases and the concentration boundary layer thickness decreases. This is probably due to the fact that mass transfer rate increases as Lewis number increases. Moreover, the concentration at the surface of a sheet decreases as the values of $Le$ increase.

As it noticed from **Figure 11** concentration graph in response to a change in thermophoresis parameter $Nt$. The influence of thermophoresis parameter on concentration profile graph is monotonic, i.e. as the values of $Nt$ parameter increase, the concentration boundary layer thickness is also increasing.

**Figure 12.** It is discerned from this figure that the concentration profile diminishes with an increase in the chemical reaction. It is also noticed that nanoparticle concentration and layer thickness shrinkage with the destructive chemical reaction. Considerably, the presence of destructive sources and the presence of the species a cause the chemical reaction which drops the concentration profiles in the concentration boundary layer thickness

TABLE I.
COMPARISON OF $-\theta'(0)$ WHEN $Nb = Nt = Le = A = 0$.

| $Pr$ | $M$ | $Nr$ | [13] | Ishak [11] | Imran ANWAR et al. [14] | Present Results |
|------|-----|------|------|------------|-------------------------|-----------------|
|      |     |      | $-\theta'(0)$ | $-\theta'(0)$ | $-\theta'(0)$ | $-\theta'(0)$ |
| 1 | 0 | 0 | 0.9548 | 0.9548 | 0.9548 | 0.9547822 |
| 2 | 0 | 0 | 1.4714 | 1.4714 | 1.4714 | 1.4714600 |
| 3 | 0 | 0 | 1.8691 | 1.8691 | 1.8691 | 1.8690730 |
| 1 | 0 | 1.0 | 0.5315 | 0.5312 | 0.5312 | 0.5317377 |
| 1 | 1.0 | 0 | - | 0.8611 | 0.8611 | 0.8610874 |
| 1 | 1.0 | 1.0 | - | 0.4505 | 0.4505 | 0.4513935 |

TABLE II.
VALUES OF THE REDUCED NUSSELT NUMBER $-\theta'(0)$, THE REDUCED SHERWOOD NUMBER $-\beta'(0)$ AND SKIN-FRICTION COEFFICIENT.

| Nb | Nt | Pr | Le | M | A | Nr | $\chi$ | $-\theta'(0)$ | $-\beta'(0)$ | $C_{fx}(0)$ |
|----|----|----|----|---|---|----|----|-----------|-----------|----------|
| 0.1 | 0.1 | 1 | 10 | 0.1 | 0.1 | 0.1 | 0.2 | 0.5374883 | 3.4259970 | 1.2856510 |
| 0.5 | 0.1 | 1 | 10 | 0.1 | 0.1 | 0.1 | 0.2 | 0.4683891 | 3.5519440 | 1.2856510 |
| 0.1 | 0.5 | 1 | 10 | 0.1 | 0.1 | 0.1 | 0.2 | 0.5083771 | 2.9029440 | 1.2856510 |
| 0.1 | 0.1 | 10 | 10 | 0.1 | 0.1 | 0.1 | 0.2 | 1.6193550 | 2.9614960 | 1.2856510 |
| 0.1 | 0.1 | 1 | 25 | 0.1 | 0.1 | 0.1 | 0.2 | 0.5358281 | 5.6791770 | 1.2856510 |

| 0.1 | 0.1 | 1 | 10 | 2.5 | 0.1 | 0.1 | 0.2 | 0 .4688037 | 3.3257190 | 1.8976840 |
| 0.1 | 0.1 | 1 | 10 | 2.5 | 1.1 | 0.1 | 0.2 | 0.8037469 | 3.6890500 | -0 .2702405 |
| 0.1 | 0.1 | 1 | 10 | 0.1 | 0.9 | 0.1 | 0.2 | 0 .7565519 | 3.6181150 | 0 .2083470 |
| 0.1 | 0.1 | 1 | 10 | 0.1 | 1.1 | 0.1 | 0.2 | 0.7540233 | 3.6805980 | -0.2216342 |
| 0.1 | 0.1 | 1 | 10 | 0.1 | 2.0 | 0.1 | 0.2 | 0.7221949 | 3.975730 | -2.7517690 |
| 0.1 | 0.1 | 1 | 10 | 0.1 | 0.1 | 3.0 | 0.2 | 0.2762322 | 3.5029530 | 1.2881670 |
| 0.1 | 0.1 | 1 | 10 | 0.1 | 0.1 | 0.1 | -1.0 | 0.7615607 | 0.8892360 | 1.2881670 |
| 0.1 | 0.1 | 1 | 10 | 0.1 | 0.1 | 0.1 | 1.0 | 0.7819918 | 4.3453950 | 1.2881670 |
| 0.1 | 0.1 | 1 | 10 | 0.1 | 0.1 | 0.1 | 5.0 | 0.8309667 | 7.6726790 | 1.2881670 |
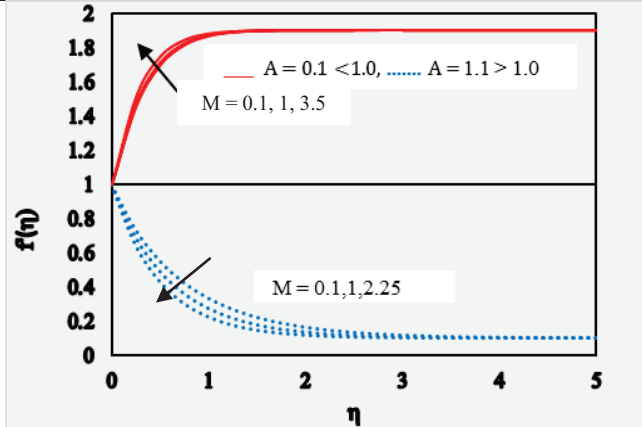


Figure 2. Velocity profiles against $\eta$ for variation values of $M$ when $Nt = Nb = 0.1, Pr = Le = 2.0, \ Nr = 1.0, \chi = 0.2$
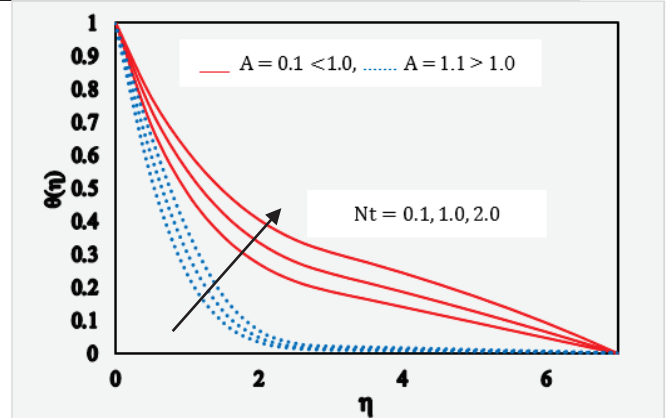


Figure 4. Temperature profiles against $\eta$ for variation values of $Nt$, when $Nb = M = 0.1, Pr = Le = 2, Nr = 1, \chi = 0.2$
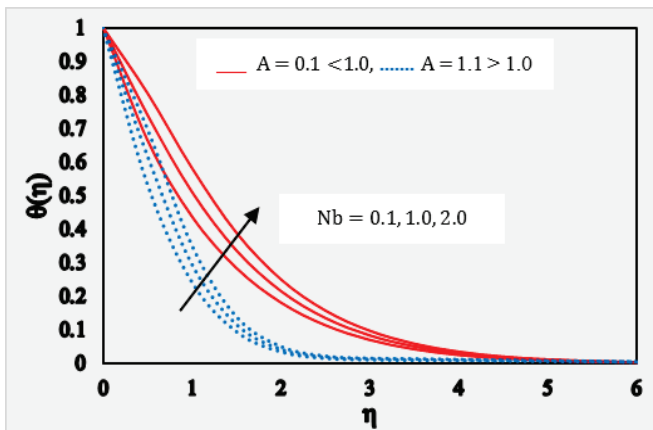


Figure 3. Temperature profiles against $\eta$ for variation values of $Nb$, when $Nt = M = 0.1, Pr = Le = 2, Nr = 1, \chi = 0.2$
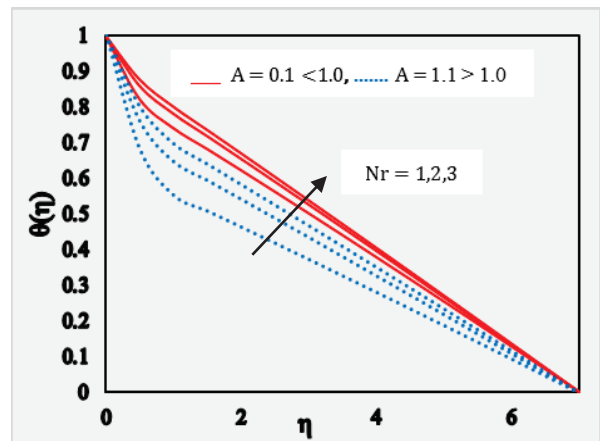


Figure 5. Temperature profiles against $\eta$ for variation values of $Nr$ when $M = Nt = Nb = 0.1, Pr = Le = 2, \chi = 0.2$
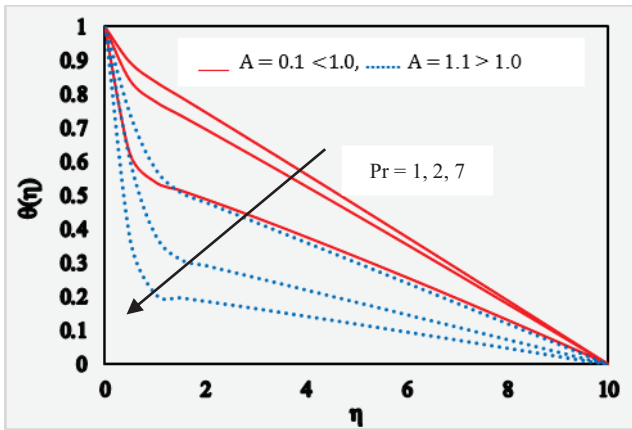
Figure 6. Temperature profiles against $\eta$ for increasing values of $Pr$, when $Nt = Nb = M = 0.1, Le = 2, Nr = 1, \chi = 0.2$
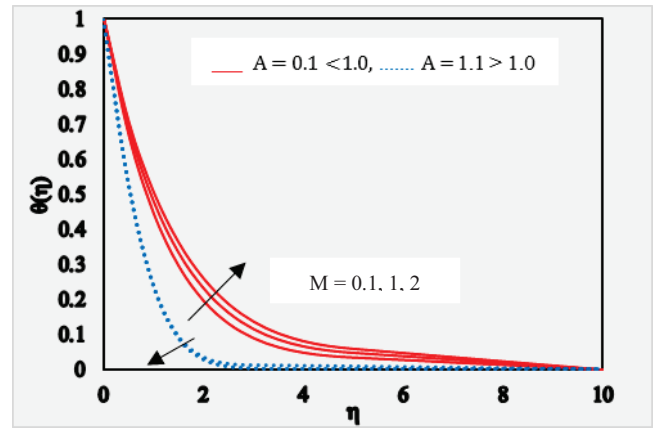


Figure 7. Temperature profiles against $\eta$ for variation values of $M$ when $Nb = Nb = 0.1, Pr = Le = 2, Nr = 1, \chi = 0.2$
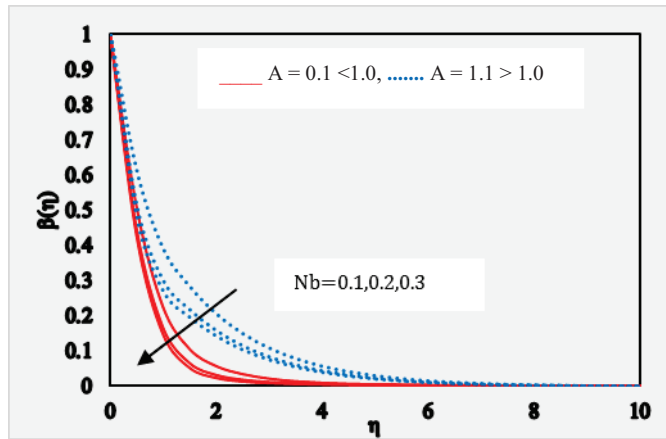


Figure 8. Concentration profiles against $\eta$ for variation values of $Nb$ when $Nt = M = 0.1, Pr = Le = 2, Nr = 1, \chi = 0.2$
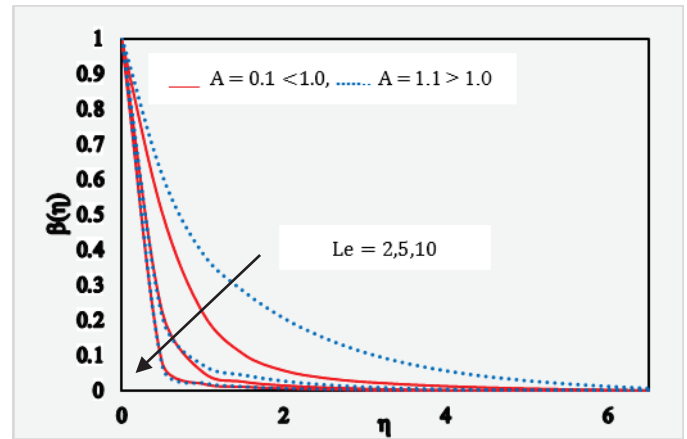


Figure 10. Concentration profiles against $\eta$ for variation values of $Le$ when $Nt = Nb = M = 0.1, Pr = 2, Nr = 1, \chi = 0.2$
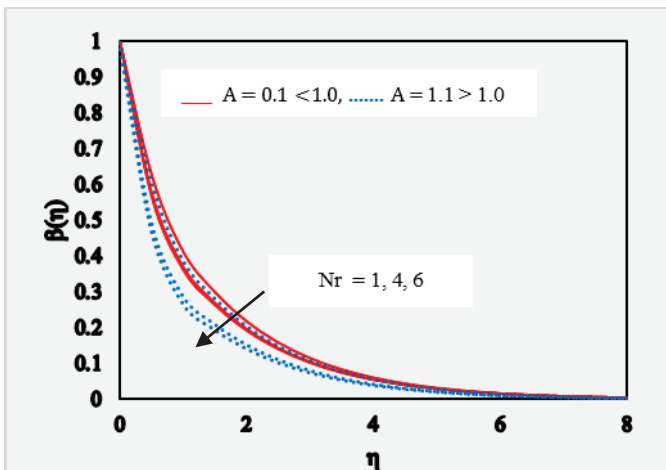


Figure 9. Concentration profiles against $\eta$ for variation values of $Nr$, when $Nt = Nb = M = 0.1, Pr = Le = 2, \chi = 0.2$.
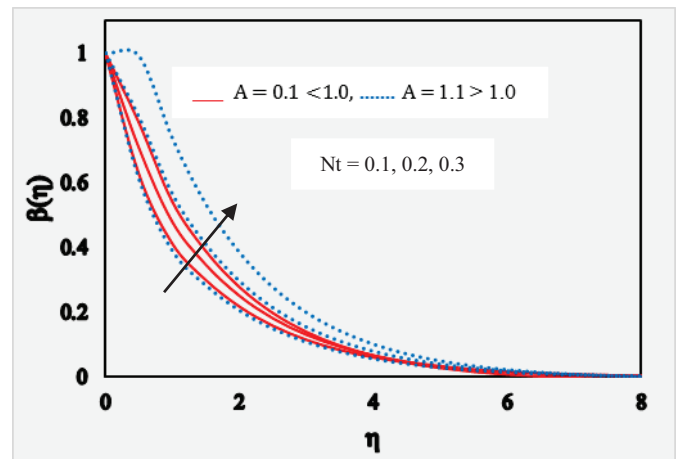


Figure 11. Concentration profiles against $\eta$ for variation values of $Nt$, when $Nb = M = 0.1, Pr = Le = 2, Nr = 1, \chi = 0.2$.
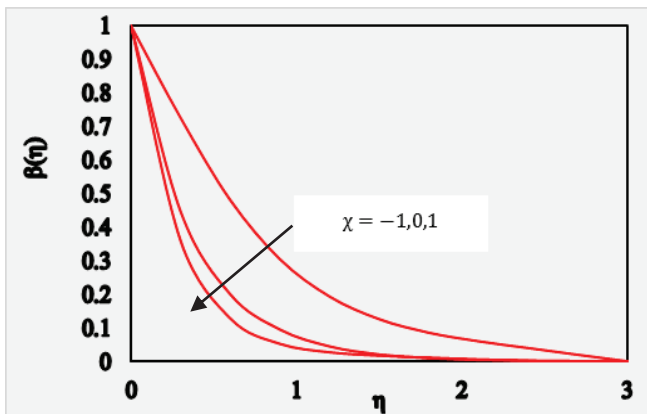
Figure 12. Concentration profiles against $\eta$ for variation values of $\chi$, when $Nt = Nb = M = 0.1, Pr = Le = 2, Nr = 1, A = 0.1$.

## V. CONCLUSIONS

Some of the important findings of this observations are given below:

➢ The velocity profiles conclude with each other if $A = 1$ and results in a degenerate inviscid flow where the strecting matches the conditions at the infinity.

➢ The external stream velocity increases compared to the stretching velocity and the momentum boundary layer thickness shortness for $A > 1$, whereas an inverted boundary layer structure is found when $A < 1$.

➢ Increasing values of $M$ has a minimal influence on velocity and temperature profiles for $A > 1$.

➢ Increase in chemical reaction Parameter decrease the concentration profile.

➢ Increasing Prandtl number decelerates the flow and strongly depresses temperatures throughout the boundary layer regime. while the opposite behavior is seen in case of enhancing the values of Brownian motion parameter, thermophores parameter and radiation parameter.

➢ We noticed that Concentration is decreased by Brownian motion, Lewis numbers.

## NOMENCLATURE

| | |
|---|---|
| $A$ | Velocity ratio parameter |
| $B$ | Transverse Magnetic field $(A.m^{-1})$ |
| $a, b, l$ | Dimensionless needle size |
| $D_B$ | Coefficient for Brownian diffusion |
| $D_T$ | Coefficient for Thermophoretic diffusion |
| $\xi$ | Thermal conductivity$(W.m^{-1}.K^{-1})$. |
| $Le$ | Lewis number |

| | |
|---|---|
| $M$ | Magnetic parameter |
| $Nb$ | Brownian motion parameter |
| $Nt$ | Thermophoresis parameter |
| $Nu$ | Nusselt number |
| $Nr$ | Radiation parameter |
| $Nur$ | Reduced Nusselt number |
| $Pr$ | Prandtl number |
| $p$ | Pressure |
| $c_f$ | Heat capacity of the fluid |
| $c_p$ | Effective heat capacity $(J.kg^{-1}K^{-1})$ |
| $q_m$ | wall mass flux |
| $q_w$ | surface heat flux |
| $Re_x$ | Local Reynolds number |
| $Shr$ | Reduced Sherwood number |
| $Sh_x$ | Local Sherwood number |
| $T$ | Fluid temperature |
| $T_w$ | Fluid Temperature at wall |
| $T_\infty$ | Ambient temperature |
| $u, v$ | Velocity vectors |
| $u_w$ | Velocity of the stretching surface |
| $x, y$ | Axial and normal coordinates |
| $\alpha$ | Thermal conductivity |
| $\beta$ | Dimensionless nanoparticle volume fraction |
| $\eta$ | Similarity variable |
| $\theta$ | Dimensionless temperature |
| $\chi$ | reaction rate parameter |
| $\rho_f$ | Density of Fluid |
| $\rho_p$ | Mass density |
| $\sigma$ | Fluid Electrical conductivity |
| $\tau$ | $\tau = (\rho c)_p/(\rho c)_f$ |

## REFERENCES

[1] Choi, S.U.S. (1995) Enhancing Thermal Conductivity of Fluids with Nanoparticles. In: Siginer, D.A. and Wang, H.P., Eds. Developments and Applications of Non-Newtonian Flows, ASME, New York, pp 99-105.

[2] Buongiorno, J. (2006) Convective Transport in Nanofluids. ASME Journal of Heat Transfer, 128, pp 240-250.

[3] Cheng, L. (2008) Nanofluid Two Phase Flow and Thermal Physics: A New Research Frontier of Nanotechnology and its Challenges. Journal of Nanoscience and Nanotechnology, 8, pp 3315-3332.

[4] Hu, W. and Buongiorno, J. Nanofluid Coolants for Advanced Nuclear Power Plants. Proceedings of ICAPP'05, Seoul, May 2005, 15-19.

[5] Gupta, P.S. and Gupta, A.S. (1997) Heat and Mass Transfer on a Stretching Sheet with Suction or Blowing. The Canadian Journal of Chemical Engineering, 55, pp 744-746.

[6] Emmanuel, S. and Khan, S.K. (2006) On Heat and Mass Transfer in a Viscoelastic Boundary Layer Flow over an Exponentially Stretching Sheet. International Journal of Thermal Sciences, 45, pp 819-828.

[7]   Subhas Abel, M. and Siddheshwar, P.G. (2007) Heat Transfer in a Viscoelastic Boundary Layer Flow over a Stretching Sheet with Viscous Dissipation and Non-Uniform Heat Source. International Journal of Heat and Mass Transfer, 50, pp 960-966.

[8]   Nadeem, S., Zaheer, S. and Fang, T.G. (2011) Effects of Thermal Radiation on the Boundary Layer Flow of a Jeffrey Fluid over an Exponentially Stretching Surface. Numerical Algorithms, 57, pp 187-205.

[9]   Al-odat, M.Q., Damseh, R.A. and Al-azab, T.A. (2006) Thermal Boundary Layer on an Exponentially Stretching Continuous Surface in the Presence of Magnetic Field Effect. International Journal of Applied Mechanics and Engineering, 11, pp 289-299.

[10]  Chand, G. and Jat, R.N. (2014) Flow and Heat Transfer over an Unsteady Stretching Surface in a Porous Medium.Thermal Energy and Power Engineering, 3, pp 266-272.

[11]  Ishak. MHD boundary layer flow due to an exponentially stretching sheet with radiation effect. Sains Malays. 2011; 40, pp 391-395

[12]  Sudhakar, K., Srinivas Raju, R. and Rangamma, M. (2013) Hall effect on an unsteady MHD flow past along a porous flat plate with thermal diffusion, diffusion thermo and chemical reaction, Journal of Physical and Mathematical Sciences,2013; 4, pp 370 − 395.

[13]  B Bidin and R Nazar. Numerical solution of the boundary layer flow over an exponentially stretching sheet with thermalradiation. Eur. J. Sci. Res. 2009; 33, pp 710-7.

[14]  Imran ANWAR, Sharidan SHAFIE and Mohd Zuki SALLEH (2014) Radiation Effect on MHD Stagnation-Point Nanofluid over an Exponentially Stretching Sheet, Walailak J Sci & Tech 2014;11(7): pp569591.

# *In the next issue (Vol 16, June 2019)*

# Template for the Preparation of Papers for Publication in CVR Journal of Science and Technology

First A. Author[1] and Second B. Author[2]
[1]Designation, Name of Institution/Department, City, Country
Email: first.author@hostname1.org
[2]Designation, Name of Institution/Department, City, Country
Email: second.author@hostname2.org

*Abstract:* **These instructions give you basic guidelines for preparing camera-ready papers for CVR College journal Publications. Your cooperation in this matter will help in producing a high quality journal.**

*Index Terms:* **first term, second term, third term, fourth term, fifth term, sixth term**

## I. INTRODUCTION

Your goal is to simulate the usual appearance of papers in a Journal Publication of the CVR College. We are requesting that you follow these guidelines as closely as possible. It should be original work. Format must be done as per the template specified. Diagrams with good clarity with relevant reference within the text are to be given. References are to be cited within the body of the paper. Number of pages must not be less than five, but not more than eight. The journal is published in colour. Colours used for

### A. Full-Sized Camera-Ready (CR) Copy

Prepare your CR paper in full-size format, on A4 paper (210 x 297 mm, 8.27 x 11.69 in). No header or footer, no page number.

*Type sizes and typefaces:* Follow the type sizes specified in Table I. As an aid in gauging type size, 1 point is about 0.35 mm. The size of the lowercase letter "j" will give the point size. Times New Roman has to be the font for main text. Paper should be single spaced.

*Margins:* Top and Bottom = 24.9mm (0.98 in), Left and Right = 16 mm (0.63 in). The column width is 86mm (3.39 in). The space between the two columns is 6mm (0.24 in). Paragraph indentation is 3.7 mm (0.15 in).

Left- and right-justify your columns. Use tables and figures to adjust column length. On the last page of your paper, adjust the lengths of the columns so that they are equal. Use automatic hyphenation and check spelling. Digitize or paste down figures.

For the Title use 24-point Times New Roman font, an initial capital letter for each word. Its paragraph description should be set so that the line spacing is single with 6-point spacing before and 6-point spacing after. Use two additional line spacings of 10 points before the beginning of the double column section, as shown above.

TABLE I.
TYPE SIZES FOR CAMERA-READY PAPERS

| Type size (pts.) | Appearance | | |
|---|---|---|---|
| | Regular | Bold | Italic |
| 6 | Table caption, table superscripts | | |
| 8 | Tables, table names, f irst letters in table captions, figure captions, footnotes, text subscripts, and superscripts | | |
| 9 | References, authors' biographies | Abstract | |
| 10 | Section titles ,Authors' affiliations, main text, equations, first letters in section titles | | Subheading |
| 11 | Authors' names | | |
| 24 | Paper title | | |

headings, subheadings and other captions must be strictly as per the template given in colour.

Each major section begins with a Heading in 10 point Times New Roman font centered within the column and numbered using Roman numerals (except for ACKNOWLEDGEMENT and REFERENCES), followed by a period, two spaces, and the title using an initial capital letter for each word. The remaining letters are in SMALL CAPITALS (8 point). The paragraph description of the section heading line should be set for 12 points before and 6 points after.

Subheadings should be 10 point, italic, left justified, and numbered with letters (A, B, …), followed by a period, two spaces, and the title using an initial capital letter for each word. The paragraph description of the subheading line should be set for 6 points before and 3 points after.

For main text, paragraph spacing should be single spaced, no space between paragraphs. Paragraph indentation should be 3.7mm/0.21in, but no indentation for abstract & index terms.

## II. HELPFUL HINTS

### A. Figures and Tables

Position figures and tables at the tops and bottoms of columns. Avoid placing them in the middle of columns. Large figures and tables may span across both columns. Leave sufficient room between the figures/tables and the

main text. Figure captions should be centered below the figures; table captions should be centered above. Avoid placing figures and tables before their first mention in the text. Use the abbreviation "Fig. 1," even at the beginning of a sentence.

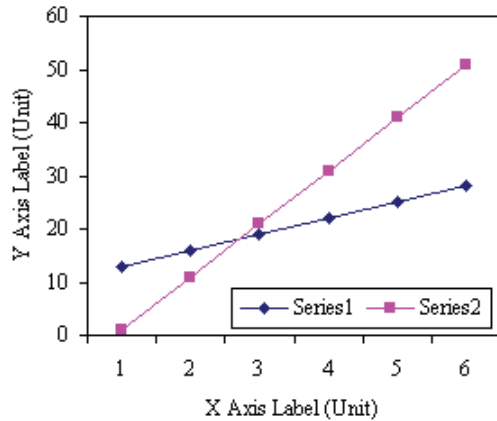To figure axis labels, use words rather than symbols. Do



Figure 2.    Note how the caption is centered in the column.

not label axes only with units. Do not label axes with a ratio of quantities and units. Figure labels should be legible, about 9-point type.

Color figures will be appearing only in online publication. All figures will be black and white graphs in print publication.

### B. References

Number citations consecutively in square brackets [1]. Punctuation follows the bracket [2]. Use "Ref. [3]" or "Reference [3]" at the beginning of a sentence:

Give all authors' names; use "et al." if there are six authors or more. Papers that have not been published, even if they have been submitted for publication, should be cited as "unpublished" [4]. Papers that have been accepted for publication should be cited as "in press" [5]. In a paper title, capitalize the first word and all other words except for conjunctions, prepositions less than seven letters, and prepositional phrases. Good number of references must be given.

### C. Footnotes

Number footnotes separately in superscripts [1, 2, …]. Place the actual footnote at the bottom of the column in which it was cited, as in this column. See first page footnote as an example.

### D. Abbreviations and Acronyms

Define abbreviations and acronyms the first time they are used in the text, even after they have been defined in the

abstract. Do not use abbreviations in the title unless they are unavoidable.

### E. Equations

Equations should be left justified in the column. The paragraph description of the line containing the equation should be set for 6 points before and 6 points after. Number equations consecutively with equation numbers in parentheses flush with the right margin, as in (1). Italicize Roman symbols for quantities and variables, but not Greek symbols. Punctuate equations with commas or periods when they are part of a sentence, as in

$$a + b = c \,. \tag{1}$$

Symbols in your equation should be defined before the equation appears or immediately following. Use "(1)," not "Eq. (1)" or "equation (1)," except at the beginning of a sentence: "Equation (1) is ..."

### F. Other Recommendations

Use either SI (MKS) or CGS as primary units. (SI units are encouraged.) If your native language is not English, try to get a native English-speaking colleague to proofread your paper. Do not add page numbers.

## III. CONCLUSIONS

The authors can conclude on the topic discussed and proposed, future enhancement of research work can also be briefed here.

## REFERENCES

[1] G. Eason, B. Noble, and I. N. Sneddon, "On certain integrals of Lipschitz-Hankel type involving products of Bessel functions," Phil. Trans. Roy. Soc. London, vol. A247, pp. 529–551, April 1955.
[2] J. Clerk Maxwell, *A Treatise on Electricity and Magnetism*, 3rd ed., vol. 2. Oxford: Clarendon, 1892, pp.68–73.
[3] I. S. Jacobs and C. P. Bean, "Fine particles, thin films and exchange anisotropy," in *Magnetism*, vol. III, G. T. Rado and H. Suhl, Eds. New York: Academic, 1963, pp. 271–350.
[4] K. Elissa, "Title of paper if known," unpublished.
[5] R. Nicole, "Title of paper with only first word capitalized", *J. Name Stand. Abbrev.*, in press.
[6] Y. Yorozu, M. Hirano, K. Oka, and Y. Tagawa, "Electron spectroscopy studies on magneto-optical media and plastic substrate interface," *IEEE Transl. J. Magn. Japan*, vol. 2, pp. 740–741, August 1987 [Digests 9th Annual Conf. Magnetics Japan, p. 301, 1982].
[7] M. Young, *The Technical Writer's Handbook*. Mill Valley, CA: University Science, 1989.

# ABOUT THE COLLEGE

CVR College of Engineering (A UGC Autonomous Institution) was established in the year 2001, and its fourteenth batch of students graduated from the College. This college is on a roll with the recent **NIRF** ranking consecutively for the II year, within the **top 3 colleges** in the state of **Telangana**, followed by record placements.

The College was the **first** college in Telangana that was promoted by NRI technology professionals resident in the US. The NRI promoters are associated with cutting-edge technologies of the computer and electronics industry. They also have strong associations with other leading NRI professionals working for world-renowned companies like IBM, Intel, Cisco, Facebook, AT&T, Google and Apple who have agreed to associate with the College with a vision and passion to make the College a state-of-the-art engineering institution.

The college has many accomplishments and to name a few, it obtained **NBA Tier 1 accreditation for all Seven UG Programs offered by the College, NAAC 'A' grade**, **UGC autonomous status**, **National Employability Award for** seventh year in a row and got a very high rating by several ranking agencies including the most recent Education World ranking of third best college in Telangana and Outlook magazine, rating CVR CE, one among the **top 100 colleges in the country.**

The college has been creating records year after year. With more than 100 companies visiting CVR and more than 650 placements for the 2017-18 academic year, it is the highest among the peer group of colleges. The highest offer is Rs. 24 Lakhs and close to 40 students got offers higher than Rs. 7 Lakhs. About 75 offers are higher than Rs. 5 Lakhs. With this, CVR becomes the leading college in entire Telangana in terms of the offers with higher salaries.  CVR has made huge progress in a short span of time and is preferred by the students and parents during the EAMCET counseling this year and is among **the top 3 colleges** in the state.

In keeping with the current global emphasis on green and eco-friendly energy generation, 360kW Solar PV plant has been installed in the campus to meet the power requirements of the college to a significant extent.

## CALL FOR PAPERS:

Papers in Engineering, Science and Management disciplines are invited for Publication in our Journal. Authors are requested to mail their contributions to Editor, CVR Journal of Science and Technology (Email Id: journal@cvr.ac.in).

Papers are to be written using a Standard Template, which may be obtained on request from the Editor. It is also available on the college website www.cvr.ac.in   under In-House Journal.

# CVR JOURNAL OF SCIENCE AND TECHNOLOGY



# CVR COLLEGE OF ENGINEERING

(UGC Autonomous- Affiliated to JNTU Hyderabad)
Mangalpalli (V), Ibrahimpatnam (M),
R.R. District, Telangana - 501510
http://cvr.ac.in